Wavelength Extension in Speciality Fibres

Burly Cumberland

Femtosecond Optics Group
Photonics Group, Department of Physics
Imperial College London
United Kingdom

May 2009

Thesis submitted for the degree of Doctor of Philosophy of Imperial College London

In memory of my Granny Mary, who sadly passed away during my write-up.
27th March 1927 - 22nd September 2008

Abstract

Since the invention of the laser and its first application, there has been an almost continuous stream of new applications - many of which require specific laser sources. These applications often require a laser source with a specific power, pulse duration, energy and wavelength. In some cases these demands are easily met, whilst in others they have proven rather more difficult to achieve. Traditionally, wavelength versatility has been limited to the regions for which rare earth or gas gain media are available. These lasers themselves can be used to generate other wavelengths through the nonlinear processes of second and third harmonic generation, as well as sum frequency generation. Despite all of this, there still exists a significant section of the visible and infrared spectrum for which no convenient sources exist. This thesis is concerned with the development of sources in these regions along with broadband sources covering significant portions of the spectrum by themselves.

These new wavelengths are generated in a variety of speciality fibres using either nonlinear processes or new gain media doped into standard silica fibres. Three types of speciality fibre are used: low concentration bismuth doped fibre which provides gain in the 1.0-1.4 μm region; photonic crystal fibres; and very high (75%) concentration germanium fibres to generate a laser source at 2.1 μm based upon stimulated Raman scattering. Photonic crystal fibres provide high nonlinearities and controllable dispersion which enables the generation of broadband supercontinuum sources based upon the interaction of many nonlinear effects. Each source will be described in depth, with particular attention given to the underlying physics that gives rise to the source. Previous and current limitations will be examined and an outlook of the future development of such sources will be discussed.

Acknowledgments

I think it is only fitting to begin my acknowledgements by thanking those who gave me the opportunity to do a PhD in the first place, Prof. Roy Taylor and Dr. Sergei Popov. Not only did they give me the opportunity to join their research group and undertake a PhD, but they provided endless support, insight and advice. Roy's phenomenal depth of knowledge, straightforward approach to all problems and generosity made the time spent within his group and my PhD remarkably enjoyable. Sergei's constantly inquisitive mind helped to push my research forward whilst often providing a perceptive take upon my work.

Thanks also have to go out to my fellow colleagues: David, Richard, John, Andrey, Anton and Edmund who not only provided company inside and outside of the lab, but were also happy to discuss all matters of my work. I would like to single out Richard for providing me with much needed support while I found my feet within the group. Thanks to Andrey for putting up with me in the same office space, sharing his astute observations and encouraging me to relax and have some beer with him. Finally a special thanks must go to John. Firstly, the vast majority of simulations in this thesis are based upon code he wrote and was kind enough to share with and explain to me. Secondly, his endless enthusiasm for the subject is infectious and helped to maintain my motivation over the years.

Thanks must also go to all of those who provided me with specialist fibres: I. Razdobreev, L. Bigot and G. Bouwmans for the Bi doped fibre; O. I. Medvedkov, S. A. Vasiliev and E. M. Dianov for the Ge doped fibre; A. Kudlinski, G. Bouwmans, Y. Quiquempois and A. Mussot for various PCFs. I'd particularly like to thank A. Kudlinski and A. Mussot for the frank and open discussions between our groups and the beer!

The chaps in the optics workshop, Paul, Martin and Simon, have my endless gratitude for making various bits and pieces of shiny metal for me over the years, normally based upon nothing more than a second-rate sketch with some vague dimensions.

I would, perhaps, have been much more reluctant to embark upon a PhD after three years in industry had it not been for the encouragement of my former colleagues: Mike Mason, Nick Hay and Duncan Parsons-Karavassilis, all of whom have been through the PhD cycle themselves. So thank you.

Of course, my family has provided me with much support and encouragement over the years, to the point where they have taken the time to enquire in detail as to what exactly I was doing. A special thanks to my grandparents who always encouraged me to simply

pursue the things I enjoyed doing in life and then attempt to make a career out of that.

Finally, I would like to thank my partner Rachel for her love and support during my PhD. When I first suggested going back to university to undertake a PhD she was very supportive and has remained so throughout all the highs and lows.

Contents

1 Introduction

1.1 Overview

Laser technology has developed at an astonishing rate since the invention of the first laser in 1960 [1]. The original Ruby laser quickly found applications in industry and medicine [2] and an almost endless list of applications was predicted. Although many of these applications, such as using lasers to fell trees, have not been realised, many others have been [3]. Additionally a wealth of unforeseen applications have been developed. The direct applicability of lasers and the commercial importance of many of those applications, coupled with academic endeavour has driven laser development forward. Today there are many types of laser operating in many different regimes and costing anything from a few pence to tens of millions of pounds.

Laser technology is now part of our everyday lives. Several lasers can be found in many households, driving optical storage systems such as CDs and DVDs. The global telecommunications backbone relies upon lasers and fibre optics to relay signals and information; in several countries fibre is now being rolled out to the home. Industrially lasers have found applications in marking, drilling, cutting and welding [3], with many car manufacturers now using lasers to weld together their cars [4]. The laser is increasingly displacing traditional manufacturing technologies, as it often provides a cleaner, faster, and more precise solution. In the research community lasers are used across so many fields in so many ways that compiling a list would be a truly daunting prospect. Applications vary from some of the world's largest laser systems, enabling the study of nuclear and quantum processes [5, 6], to optical clocks to define new time standards [7], to small tabletop systems for imaging [8, 9] and measurements [3].

Despite all of these developments, there are still many applications for which laser sources need to be developed and applied. Some examples include red, green, blue (RGB) sources for display applications, and pump lasers for extreme ultra-violet sources, which are required to deliver next generation lithograph and thus next generation computer chips [10–12]. For example RGB lasers already exist, yet they are not used for display applications. It is not enough just to have a laser of the correct wavelength and power; many other factors such as size, cost, reliability, lifetime and safety are taken into account outside of an academic laboratory. In other cases the required wavelength range is simply

not available or the required continuous wave/pulse parameters have yet to be achieved.

1.1.1 Available lasers

To illustrate the laser sources available and their output powers we can examine figure 1.1. Figure 1.1 is not a definitive list nor is it necessarily an accurate representation of the best available results; however it is intended to demonstrate the common laser media and the average power levels commonly achieved. Unfortunately it only shows the average output powers and neglects the peak powers/energies available in pulsed operation. For a more complete reference the reader should consult elsewhere [3, 13–15]. We shall briefly discuss some of the types of laser available and their relative advantages and disadvantages.

Gas lasers

The first gas laser, based upon Helium Neon [16], followed shortly after the Ruby laser in 1960. Gas lasers quickly became established commercially and dominated the market; it is estimated that half of all lasers sold in the mid nineties were gas lasers [14]. The class is characterised by narrow discreet lines with more visible laser transitions than any other class. At one point Argon ion lasers could be found, as a pump system, in many laser research laboratories while CO_2 lasers dominated industrial applications. Increasingly, semiconductor, solid-state and fibre lasers are now displacing gas lasers due to their superior reliability, higher efficiency and compact size (figure 1.2).

Gas lasers rely upon applying a voltage between two electrodes at opposite ends of the cavity to produce the necessary population inversion in the (usually low pressure) gas. In many cases the atomic gas is naturally a gas at room temperature, whereas in other cases the species needs to be heated to vaporise. For example, copper vapour lasers must be heated to approximately 1500 °C.

Due to the increasing growth of the laser market, absolute numbers of gas lasers continue to increase despite this class being slowly displaced by other classes in the majority of cases. Certain gas lasers such as excimer and copper vapour, still remain the best solution for many applications.

Chemical lasers

Chemical lasers derive sufficient energy to produce a beam via a chemical reaction. They typically operate on molecular transitions in the near to mid-infrared. They were developed for space and military applications, where electrical pumping power for the required energies may not have been available. However, they have never really broken
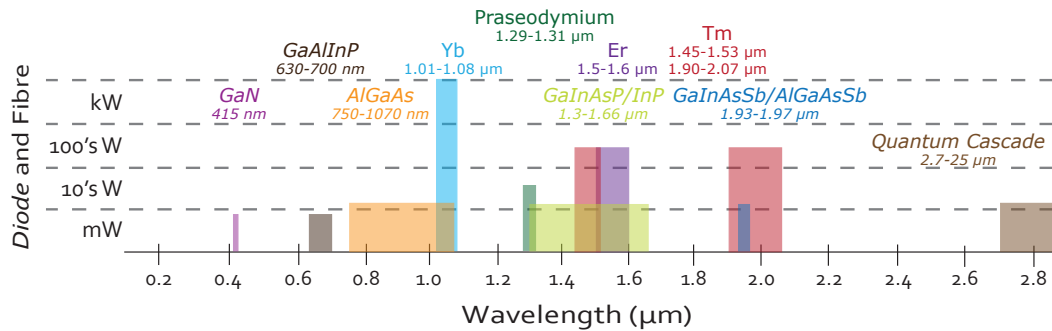
(a) Diode and fibre lasers. Diodes are in *italics*. Note that a variety of diodes are available in the 3-10 μm region which produce μW-mW of output power.
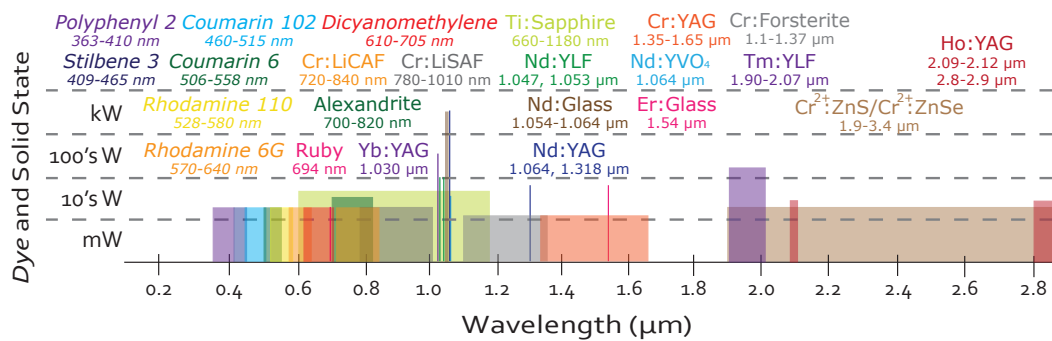
(b) Dye (in *italics*) and solid state lasers
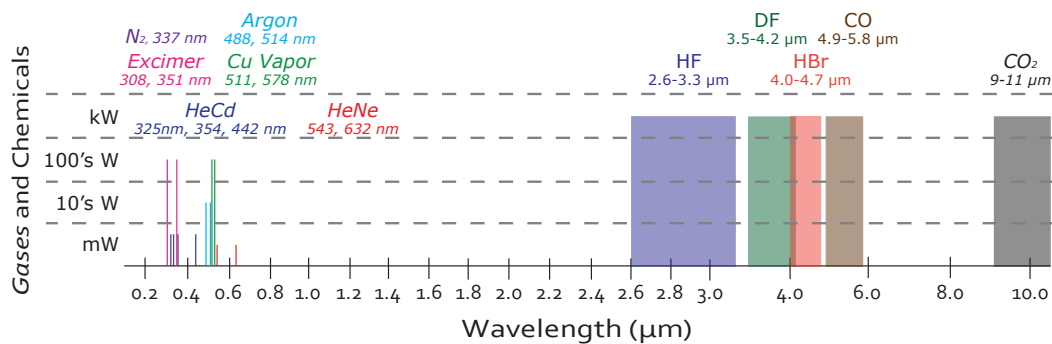
(c) Gas (in *italics*) and chemical lasers

Figure 1.1: Figures 1.1a-1.1c show many of the popular laser gain media for a variety of different classes of laser system. Powers along the *y-axis* represent the maximum average output or continuous wave output power of the laser. These numbers are intended to give a good guide and are not exhaustive.

out of this niche. This is largely due to the requirement to replace the chemicals after every use, making them relatively expensive and labour intensive.

Dye lasers

Dye lasers are based upon liquid gain media in which an organic dye is dissolved in a solvent. The dyes have very broad emission and gain spectra, enabling either tunable or short pulse (mode-locked) operation. There are over 200 dyes available covering the wavelength range from 320 nm to 1200 nm and the lasers can be operated in continuous wave, pulsed or mode-locked regimes. The gain media is pumped by either flash lamps or other lasers such as excimer and frequency doubled Nd:YAG. Importantly, dye lasers have produced ultrashort pulses as short as 6 fs as well as being able to produce high peak powers in the visible.

Unfortunately dye lasers are rather complex systems. The liquid has to be continuously pumped around the laser in order to renew the dye, and the dye itself needs to be replaced at periodic intervals. Many of the dyes are also carcinogenic, making them and their laser systems difficult to handle. These issues combined with the development of Ti:sapphire systems, for short pulse mode-locked operation, has meant that dye lasers have largely been relegated to niche applications.

Solid-state lasers

Solid-state laser materials are a class largely consisting of crystals or glasses which have been doped with an active lasing species. Host materials must fulfil a range of criteria including good optical transmission in the desired wavelength region, as well as suitable thermal, mechanical and electrical properties. Clearly, dopant ions also need to have favourable radiative properties, including suitable absorption bands and long upper state lifetimes. In general, crystals provide better performance due to superior thermal properties and a more regular structure than glasses; however, they can not be grown to very large sizes, at which point glasses are superior. In recent years a new class of ceramic host has been developed, which allow for more control during manufacture and an ability to be doped to much higher concentrations [17–19].

There are many solid-state laser materials (see figure 1.1b) but the most popular are Nd:YAG and titanium sapphire. Neodymium yttrium aluminium garnet (Nd:$Y_3Al_5O_{12}$) primarily lases at 1.064 μm and can be flash-lamp pumped or diode pumped around 0.8 μm . Today the majority of Nd:YAG lasers sold commercially are diode pumped, as a result of the higher efficiency and more compact size of the resulting lasers. They are deployed for a wide variety of applications and most commonly produce a pulsed output via Q-switching. Neodymium is a popular active ion and is used with a variety of other hosts, two examples of which are glass and yttrium vanadate (YVO$_4$).

Titanium sapphire (Ti:Al$_2$O$_3$) is the most widely tunable solid-state laser, operating in
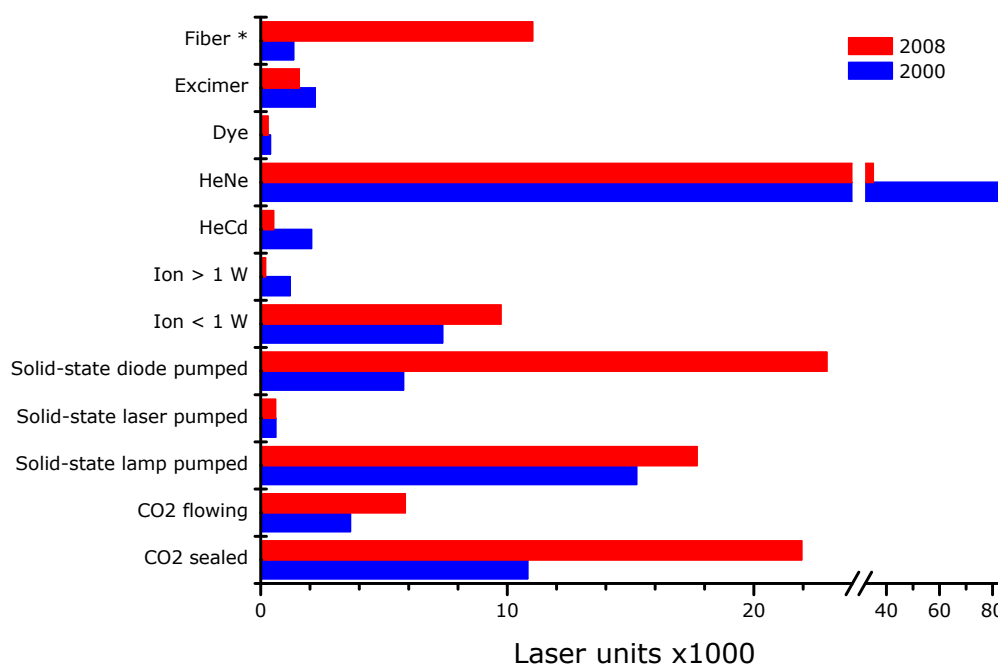
Figure 1.2: Break down of non-diode laser sales for 2000 and expected sales for 2008. Note: fibre lasers sales where so low in 2000 that they where lumped in with "others," which is what is plotted under fibre [20, 21].

the wavelength range of 660-1180 nm. This enables mode-locked operation and ultra-short pulse generation down to 6 fs. The development of Ti:sapphire lasers marked the beginning of the gradual decline for dye lasers. Whilst Ti:sapphire lasers are prevalent today, they do require another laser to act as the pump due to the short upper state lifetime, making them rather expensive and quite complex to run.

Colour-centre lasers

Colour-centre lasers are broadly tunable solid-state lasers that operate in the near infrared. Tuning is achieved by using several different colour centre crystals in sequence similar to dye lasers. The materials are made by producing point defects in an alkali-halide crystal lattice. They are pumped by other lasers but many only have an operational lifetime of weeks or months. To resolve this issue many commercial colour-centre lasers were sold in a dewar system, requiring the user to fill the laser with liquid nitrogen to extend operational lifetime. In fact many colour centre lasers will simply not lase unless held at cryogenic temperatures. Due to these difficulties very few colour centre lasers are in use today.

Diode lasers

Diode or semiconductor lasers account for just over half the laser market [21] and are unique compared with other types of lasers. They are very efficient, operate with low input powers and are very small. Diode lasers make use of *p* and *n* type semiconductors to create a *p-n* junction. When the junction is biased, electrons and holes combine releasing the energy as photons. The energy and hence frequency of the photons is governed by the energy difference between the *p* and *n* regions, which is called the bandgap. Depending upon the choice of semiconductor, different bandgaps are possible, resulting in different frequencies. The process is spontaneous but can also be stimulated by incident photons, leading to amplification and if a suitable resonator is present, laser oscillation is achieved.

A wide variety of diode lasers are available (see figure 1.1a), ranging from single mode single frequency lasers producing 10-100s mW, to water cooled diode bars producing 50-100 W of output power. The beam quality of the higher power diodes tends to suffer due to their structure and as a result they are most often used to pump other laser systems, notably solid-state ones.

Diodes offer many advantages but they are limited to continuous wave or pulsed operation. Short pulse generation through q-switching and mode locking is not possible, nor is it possible at present to build diodes capable of very high output powers.

Fibre lasers

Despite the appearance of the first fibre laser in 1961 [22] and subsequent research in the late Sixties and early Seventies [23–27], little attention was paid to fibre lasers with only a small number of researchers developing these systems. This changed in the mid-Eighties after previous results were re-demonstrated [28] and more importantly the first Erbium fibre amplifier was demonstrated [29]. The potential importance of Erbium fibre amplifiers, with their gain around 1.5 μm, to telecommunications led to the rapid development of these systems.

Work followed on Ytterbium [30, 31], Thulium [32–34] and Praseodymium [35, 36]. Of those three Ytterbium has been the most successful. During the late Nineties the first commercial high power Ytterbium fibre laser began to appear with a race between research groups and companies to achieve the highest single mode output power. Today multi-kW single mode Ytterbium fibre lasers are available [37]. Recently, development efforts have focused more on Thulium fibre lasers. Praseodymium offers the attractive possibility of providing gain around 1.3 μm, which is important for telecommunications. Despite a large development effort in the Eighties and Nineties, it proved to be largely fruitless with difficulties arising from the soft glasses used and associated reliability issues

making them unsuitable for telecommunications [36].

Fibre lasers offer several advantages over many of the other laser systems described above:

- Fibre by its nature can be coiled leading to compact systems.

- An all-fibre set-up (such as fibre Bragg gratings etc.) means that no alignment is required.

- Dust etc. is not an issue as the light travels inside the fibre.

- Fibre gain media have a large gain bandwidth, permitting wavelength tuning or ultra-short pulse generation.

- Fibre lasers have broad spectral regions with good pump absorption meaning that the exact pump wavelength is not critical. Pump diodes therefore do not require precise temperature stabilisation.

- Diffraction limited beam quality is easily obtainable from single mode fibres.

- Fibre lasers have a high power efficiency and can be made to operate with very small pump powers, due to their structure and the gain efficiency of doped fibres.

- The high surface area to volume ratio of fibre means that air cooling is usually sufficient with no need for special thermal management.

However fibre lasers are not without their disadvantages:

- Nonlinear effects often limit performance for example single frequency operation is limited by stimulated Brillouin scattering and pulse quality is often affected by effects such as self phase modulation.

- In some cases bulk elements, such as isolators, are required, introducing a critical alignment tolerance.

- Fibres traditionally have a limited gain and pump absorption per unit length, making it difficult to realise very short resonators for single frequency or multi-gigahertz mode locked operation.

Fibre lasers have also benefited from the developments, rigorous requirements and high volumes of the telecommunications industry. As a result fibre lasers have matured over the last decade and are being rapidly accepted in a broad range of fields. This effect is apparent in figure 1.2, where fibre laser sales were essentially negligible in 2000 but are expected to sell just over 11,000 fibre lasers in 2008.

Harmonic generation

Harmonic generation gives rise to new wavelengths by taking a suitable laser source and frequency doubling, tripling or another sum frequency combination to generate new wavelengths. Under the right circumstances this can be done with reasonable efficiency in a variety of nonlinear crystals and periodically poled crystals [38]. This is often used to take a robust well established source and extend it to new wavelength regions, an example of which is frequency doubling Nd:YAG, a popular way to generate a green laser at 532 nm.

A slight variation of this is the optical parametric oscillator (OPO) [14, 39]. It uses a nonlinear crystal placed within a cavity to generate parametric amplification. The signal and idler waves can be widely tuned making it possible to access wavelengths (especially in the mid-infrared) which are either impossible or difficult to achieve with any other laser system. Unfortunately OPOs require a laser pump with a high optical intensity and an excellent spatial coherence, typically resulting in a large, complex and expensive system.

1.1.2 Discussion and outline

We have seen that there is a wide variety of different classes of laser. Despite this, a quick inspection of figure 1.1 shows that no sources are available in certain wavelength regions, notably 1.6-1.9 μm. Combined with the limitations of some sources and a general desire from end users for efficient, cheap, robust, and maintenance free laser systems, various classes, such as dye, have fallen out of favour for all but a few niche applications (see figure 1.2).

This thesis is concerned with developing laser sources and understanding the underlying physics to enable wavelength diversification and point to further improvements. In chapter 2 we investigate a new fibre gain medium based upon bismuth. Bismuth doped fibres offer potentially exciting possibilities due to their broad emission spectrum between 1.1 and 1.4 μm. Successful development could open up a number of important applications, for instance providing gain in the 1.3-1.4 μm region for telecommunications. Perhaps more important would be the ability to generate sources for frequency doubling into the visible, with the laser guide star wavelength of 589 nm a key target.

In chapters 3 and 4 we will explore the development of continuous wave supercontinuum sources. Chapter 3 will focus upon the underlying physics of continuous wave supercontinuum generation and consider increasing the spectral power density, spectral flatness and controlling the bandwidth of such sources. In the following chapter we will examine the possibility of extending continuous wave supercontinuum sources into the visible.

Then in chapter 5 we will progress to the generation of sources in the 2.0-2.5 μm region. This region has proven difficult to develop sources for and we shall demonstrate a fibre Raman laser working in this region, utilising a very high concentration GeO_2 fibre in combination with a thulium pump laser. The system will be modelled and future prospects discussed. Finally in chapter 6 we will draw some conclusions.

From the above outline it is now clear that all the work in this thesis is based upon fibre technology, fibre lasers and nonlinear processes. The rest of this chapter will outline many of the fundamentals necessary to enable a fuller discussion in the later chapters. We will start in section 1.2 by looking at the variety of different fibre technologies available, concentrating on conventional fibres (1.2.1) and photonic crystal fibres (1.2.3). Doped fibres and soft glass fibres will also be discussed (1.2.2 and 1.2.4). This will be followed, in section 1.3, by a basic explanation of each of the nonlinear effects in fibre including self-phase modulation (1.3.3), stimulated Raman scattering (1.3.4), four-wave mixing (1.3.6), solitons and modulation instability (1.3.8). Although not a nonlinear effect, group velocity dispersion is also covered in this section (1.3.2) due to its relevance to many of the nonlinear processes. Finally this is followed by a section on supercontinuum (1.4) which summarises the historical development of supercontinuum sources (1.4.1) and the common regimes of operation available today (1.4.2).

1.2 Fibre technology

As already stated, the subject of this thesis involves the use of speciality fibres. It would seem sensible to spend some time examining the fibre technology upon which the work of later chapters is based. This section will therefore discuss a variety of fibres available today, their development, guidance mechanisms, advantages, disadvantages and main uses. This section is not intended to be a definitive guide but rather cover the main fibres and those of particular interest to this thesis. We will start with conventional silica fibres and highly-nonlinear fibres in section 1.2.1, then move onto doped fibres (1.2.2) and photonic crystal fibres (1.2.3) before taking a brief look at soft glass fibres (1.2.4).

1.2.1 Conventional and highly-nonlinear fibres

History

Conventional, step-index silica fibre is by far the most common fibre available, owing to its importance in enabling modern telecommunications. Indeed, it is highly unlikely that the internet would exist if it were not for fibre optics. In time, the step-index fibre may be regarded as being one of the most important inventions of the twentieth century.

The history and development of optical fibre is a long and interesting one and cannot be discussed in detail here, but is described in detail elsewhere [40]. The basic concept of modern step-index fibres, specifically the idea of cladding a core fibre with a lower index dielectric, only emerged in 1954 [40, 41]. The first fibres which applied this idea were manufactured two years later [42] with their significance to optical communications being immediately identified [43]. In the 1960s telecommunications firms began to develop optical fibres as a potential waveguide [44]. The breakthrough came from Corning in 1970 [45], when they developed the precursor to modified chemical vapour deposition (MCVD). MCVD and its precursor are manufacturing techniques which facilitate losses of less than 20 dB/km necessary to make optical communications possible. By 1978 losses had been reduced to 0.2 dB/km [46], very close to the theoretical limit, with the first significant commercial deployments appearing en masse during the early 80s. Three further decades of research driven primarily by telecommunications and its requirements have led to a variety of fibres and the field of photonics.

This has resulted in fibres which have a series of excellent properties including: extremely low attenuation; excellent material properties including chemical stability, resistance and strength; high power handling; optical confinement over 10s to 100 km; and compactness. Much of this development has benefited other types of fibre, such as photonic crystal fibres and other applications of optical fibre, notably fibre lasers.

Structure and guidance mechanism

(a) Step-index fibre　　　　(b) Guidance of a ray in a multi-mode step-index fibre
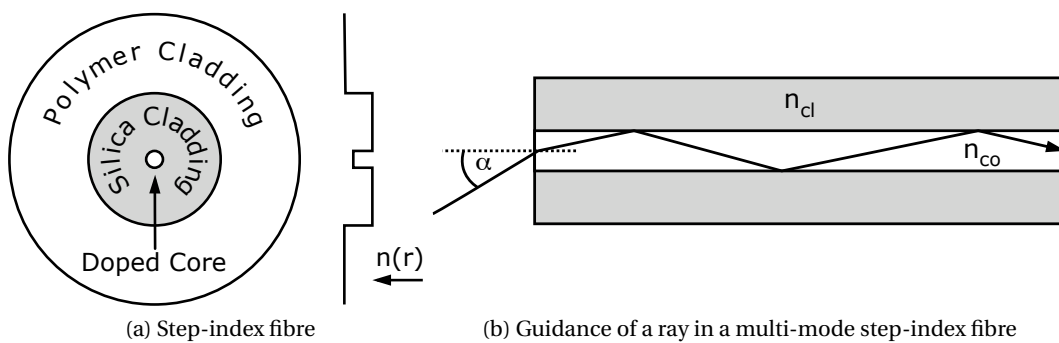
Figure 1.3: Cross-section of a step-index fibre (1.3a) and the ray picture of guidance under total internal reflection (1.3b).

The standard step-index fibre is shown in figure 1.3. It consists of a doped core (8-60 μm) , silica cladding (125 μm) and an outer protective polymer cladding (245 μm) . The core normally ranges between 8 and 12 μm for single mode fibre and is typically doped with germanium or phosphorus oxides to increase the refractive index. In some cases the

silica cladding may be doped, instead of the core, in order to reduce its refractive index.

The guidance mechanism is customarily described using the ray picture (see figure 1.3b) [47], where a ray of light is guided along the fibre due to total internal reflection. The refractive index contrast between the core, n_{co}, and the cladding, n_{cl}, determines the numerical aperture (NA) of the fibre. In physical terms the NA is the maximum acceptance angle of the fibre, such that light entering it will be guided by total internal reflection. The NA is given by

$$\text{NA} = \sqrt{n_{co}^2 - n_{cl}^2} = \sin\alpha \tag{1.1}$$

The ray picture represents a good approximation and for a full understanding we need to solve for the propagation vector of the electric field for a given frequency. Due to the cylindrical symmetry of the fibre we can express the modal fields as:

$$E_j(x, y, z) = E_j(x, y)\exp(i\beta_j z - i\omega t) \tag{1.2}$$

$$H_j(x, y, z) = H_j(x, y)\exp(i\beta_j z - i\omega t) \tag{1.3}$$

where E_j is the modal electric field distribution and H_j the corresponding magnetic field distribution. The axial position along the fibre is denoted by z and the cross-section is denoted by x and y while ω is the angular frequency. β_j is called the propagation constant or the eigenvalue of the jth mode and is the axial component of the wave vector. Generally each mode has a unique value of β_j, derived from the appropriate eigenvalue equation. If we assume that our waveguide is non-absorbing then by definition any bound modes are not attenuated and β_j is real. Thus for a given free-space wavelength λ and refractive index profile $n(x, y)$, only certain values of the propagation constant β_j are possible. This can be understood by considering the refractive index profile of the fibre at any point must satisfy $n_{co} \geq n(x, y) \geq n_{cl}$ where n_{co} and n_{cl} are the maximum and minimum indices. So we can now see that the minimum phase velocity is equal to the minimum speed of light within the core i.e. c/n_{co}. Hence, it is now clear that it is possible for the phase velocity of a mode to exceed the maximum speed of light in the cladding, c/n_{cl}, however this cannot occur without a loss of power. Accordingly a set of limits are placed upon the phase velocity and correspondingly the propagation constant takes the form:

$$kn_{cl} < \beta_j \leq kn_{co} \tag{1.4}$$

where $k = 2\pi/\lambda$ [47, 48].

The relationship in equation 1.4 makes it clear that potentially multiple solutions exist for β_j implying that the fibre may well be multi-mode. For conventional step index fibres,

this can be explored further by studying the *V* parameter (sometimes referred to as the normalised frequency). The number of modes increases with the *V* parameter and for a fibre, with a core radius *a*, it is given by:

$$V = ak\sqrt{n_{\text{co}}^2 - n_{\text{cl}}^2} \tag{1.5}$$

It transpires that provided *V* <2.405, the fibre is single mode and only the fundamental mode propagates. Thus, it is possible to calculate the single mode cut-off frequency for a given fibre. Given a short enough pump wavelength all conventional fibres are therefore multimode. Physically, the larger core size or higher refractive index difference implied by a high *V* number suggests that the fibre supports larger wavelengths or tighter confinement enabling more modes. It becomes clear from equations 1.4 and 1.5 that to maintain single mode operation the refractive index difference must be small. However to achieve strong waveguide dispersion this difference needs to be large. This conflict limits the ability to engineer the dispersion of a conventional fibre while maintaining single mode operation. Fortunately, as we shall see in section 1.2.3 photonic crystal fibres provide a solution to this problem.

So far we have described isotropic single mode fibres. Although they only sustain one transverse mode, this mode sustains both fundamental polarisations of light as they have the same propagation constant. Thus, if a polarised light source is launched into a long length of single mode fibre it will emerge in some arbitrary polarisation. To solve this problem polarisation maintaining fibres have been developed. These fibres break the rotational symmetry of the core either by the introduction of stress rods or by making the core itself elliptical (figure 1.4). This significantly increases the birefringence of the fibre permitting discrimination between the polarisations.
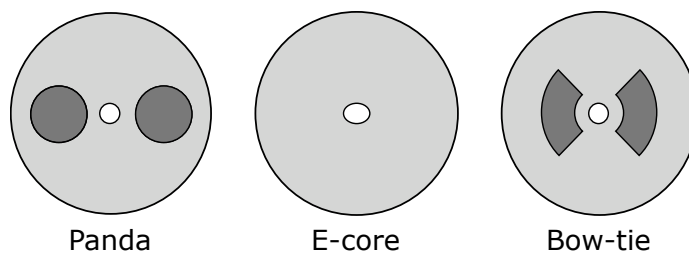

Figure 1.4: Cross section of several typical polarisation maintaining fibres.

Optical properties

Standard single mode fibre (SMF) such as Corning's SMF-28 typically has a single mode cut-off wavelength around 1.26 μm and a zero-dispersion wavelength around 1.31 μm.

The transmission window is limited by pure silica's high absorption losses in the ultraviolet and infrared beyond 2 μm. For much of the transmission window, losses are now limited by the intrinsic process of Rayleigh scattering, which is strongly wavelength dependent (λ^{-4}). Additionally losses due to impurities such as OH$^-$, responsible for the peak at 1.38 μm in figure 1.5, have been reduced further in recent years.
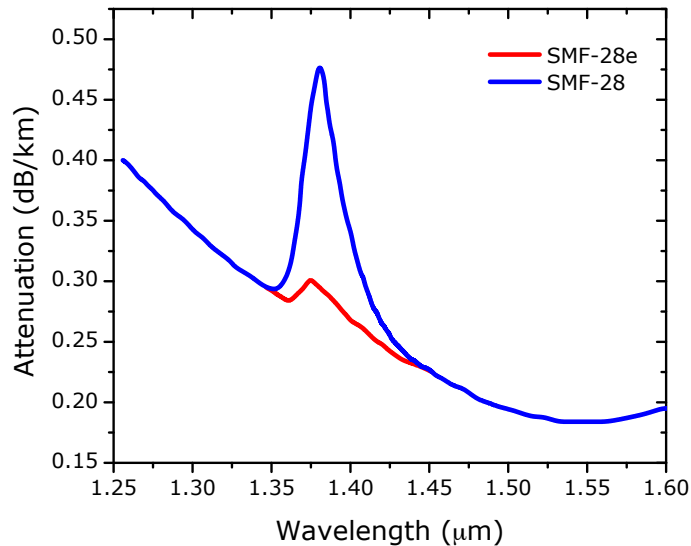
Figure 1.5: Attenuation curves for Corning SMF-28 and its successor SMF-28e.

The dispersion of SMF-28 is fairly low in the erbium band, but over the 10s-100s of kilometres used in telecommunications links it is enough to cause pulse broadening, increasing the error rate on a signal and ultimately limiting the transmission distance without compensation. It arises from two factors, the intrinsic material dispersion of the glass and the waveguide dispersion of the particular fibre design. The waveguide dispersion occurs because part of the mode propagates in the cladding which has a different refractive index from the core. The mode therefore experiences an effective refractive index n_{eff}, which is wavelength dependent. As a result, the propagation constant β varies from values close to the cladding wave vector at low frequencies to values close to the core wave vector at high frequencies as shown in figure 1.6. The variation between the extremes leads to non-zero derivatives of β and thus to waveguide dispersion.

The change of the wave vector can be controlled by the refractive index profile and a variety of more complicated refractive index profiles such as: triangular core, trapezoidal core, depressed cladding with triangular core and the W-profile have been utilised. Many of these have been designed to either shift the dispersion or flatten the dispersion for various applications [48].

The nonlinearity of SMF is also fairly low, though due to the very long interaction
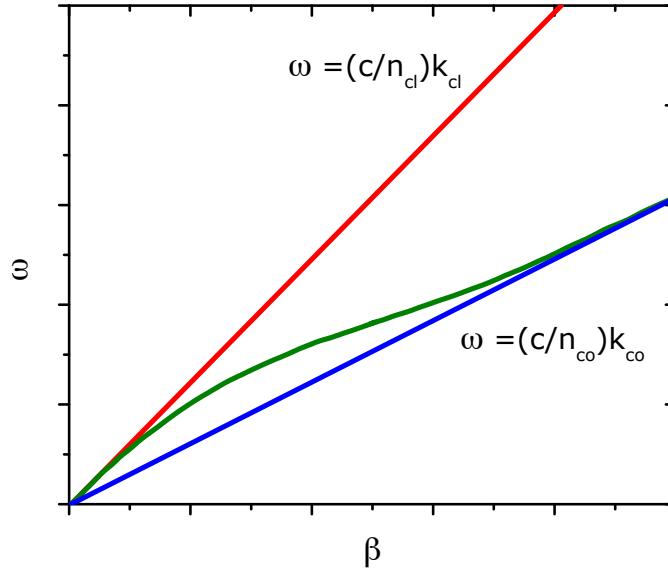
Figure 1.6: Waveguide ω versus β dispersion relation with zero material dispersion. The cladding wave vector is plotted in red, the core wave vector is plotted in blue and the resulting fibre wave vector is plotted in green. Adapted from [48].

lengths can again become a problem for many standard telecommunication schemes. Conversely, there are a large number of nonlinear process in fibre that can be very useful including Raman gain to build Raman amplifiers and self-phase modulation, which when combined with dispersion in the anomalous regime leads to solitons. Solitons can be thought of as pulses which maintain their properties and hence have potential applications to telecommunications (they are described in detail in section 1.3.8). In order to study and develop nonlinear systems, various fibres have been developed with higher nonlinearities. These highly nonlinear fibres (HNLF) as they are known, usually achieve their nonlinearity by reducing the core size, to increase the power density, and doping the core with germanium, which has a higher nonlinearity than silica. In chapter 5 we will look at a Raman laser system based upon an extremely nonlinear fibre capitalising on an almost pure GeO_2 core for the first time.

1.2.2 Doped fibres

As previously discussed in section 1.1.1 a variety of fibre lasers have been developed. All of these lasers have relied upon doping the host fibre with a rare-earth ion to provide the required gain to enable lasing or amplification. Common rare earth ions that have been used include: neodymium, ytterbium, praseodymium, erbium, thulium and holmium. Of these, fibre laser sources and amplifiers are commercially available based upon ytterbium, erbium and increasingly thulium. The dependence of praseodymium and holmium on

(a) Absorption and emission cross sections   (b) Yb^{3+} energy level structure
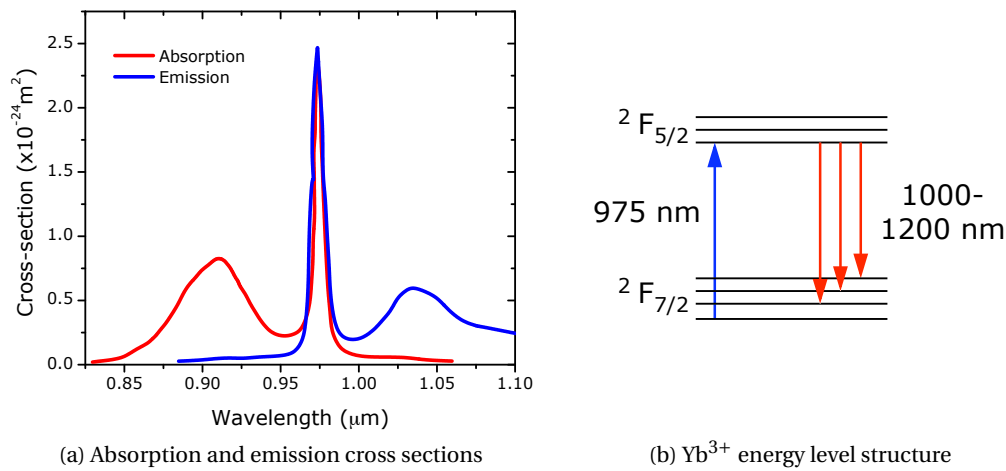
Figure 1.7: The absorption and emission cross sections for an Yb doped germanosilicate host are shown in 1.7a. 1.7b shows the energy level structure, consisting of the ground manifold $^2F_{7/2}$ with four Stark levels and the excited manifold $^2F_{5/2}$ with 3 Stark levels. Energies of the transitions are indicated. Adapted from [31].

soft glasses and the relative draw backs, which will be discussed in the next section, have prevented commercial adoption to date.

Ytterbium has become the most successful in terms of fibre laser sources. This is partly due to the fact that it has transitions in the 1.0 μm region, therefore directly competing with solid-state Nd:YAG based lasers at 1.064 μm. The absorption and emission spectrum along with the energy level structure of Yb^{3+} are shown in figure 1.7. It is clear that there is a strong absorption and emission between the lowest Stark levels of the $^2F_{7/2}$ and $^2F_{5/2}$ manifolds at 975 nm. Typically, Yb^{3+} is pumped at 975 nm due to the strong absorption leading to emission via transfer to the remaining three Stark levels of the lower manifold. This quasi-three level structure leads to a number of benefits including: no excited state absorption due to the absence of higher energy levels; and a low quantum defect leading to excellent thermal properties [31, 36]. It is also possible to pump Yb at shorter wavelengths or multiple wavelengths [49]. These factors have enabled the development of multi-kW class Yb fibre lasers [37].

Doped silica based fibres are excellent candidates for high power lasers for two reasons: they have an extremely high damage threshold; and due to the surface/volume ratio are very efficient at dissipating heat. However, in order to get high power output, high power pumping is required, which involves coupling the light into the core. For a single mode fibre laser this is most easily achieved by diodes with a single mode output which can be coupled into the core. Due to damage threshold limitations, in producing single mode diodes pumping is limited to watts, rather than 10's or 100's of watts.

Doped core (signal)

1st cladding
(pump)

2nd cladding

Coating

Index

(a) Basic configuration and index profile

(b) Offset core

(c) Rectangular
cladding

(d) D-shaped
cladding

(e) Scalloped
cladding
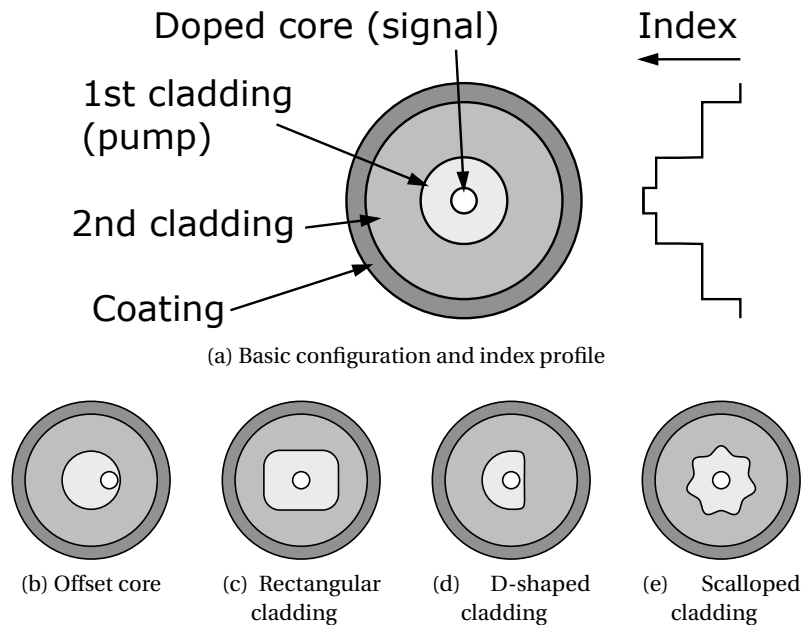
Figure 1.8: Double clad fibres. The basic double clad configuration (1.8a) and variations
designed to eliminate helical rays (1.8b-1.8e).

A solution to this problem was presented in 1987 [50, 51] when the double clad fibre
was first proposed. In this scheme, shown in figure 1.8, a single-mode doped-core is
surrounded by a cladding of lower refractive index, which is also surrounded by a second
cladding of even lower refractive index. In effect, the single-mode core is surrounded by
a large mutli-mode core. As this core is 10s to 100s of times larger than the single mode
core and has a much higher NA, much more diode light can be coupled in from a laser
diode array. As the multi-mode pump light travels down the inner cladding it overlaps
spatially with the doped core and is absorbed by the dopant. This therefore acts as a
brightness converter, increasing the low brightness multi-mode light to a high brightness
single-mode output. It also reduces the alignment tolerances of the diode. The scheme is
not perfect as it means a longer length of fibre is need to form the laser and numerous
schemes have been proposed and tried in an effort to improve the coupling efficiency
into the core (see figures 1.8b-1.8e) [32, 36, 52, 53]. Similarly, there are a wide variety of
pump configurations for launching the diode light into the inner cladding, and a detailed
description can be found elsewhere [54–57].

The absorption and emission spectra for erbium and thulium are shown in figure 1.9.
Erbium amplifiers have been very important for telecommunications applications as
previously discussed. They are often pumped in the same double clad configurations
described above. However this is difficult due to erbium's much lower absorption than
ytterbium, fortunately it is possible to use ytterbium as a sensitiser by co-doping the
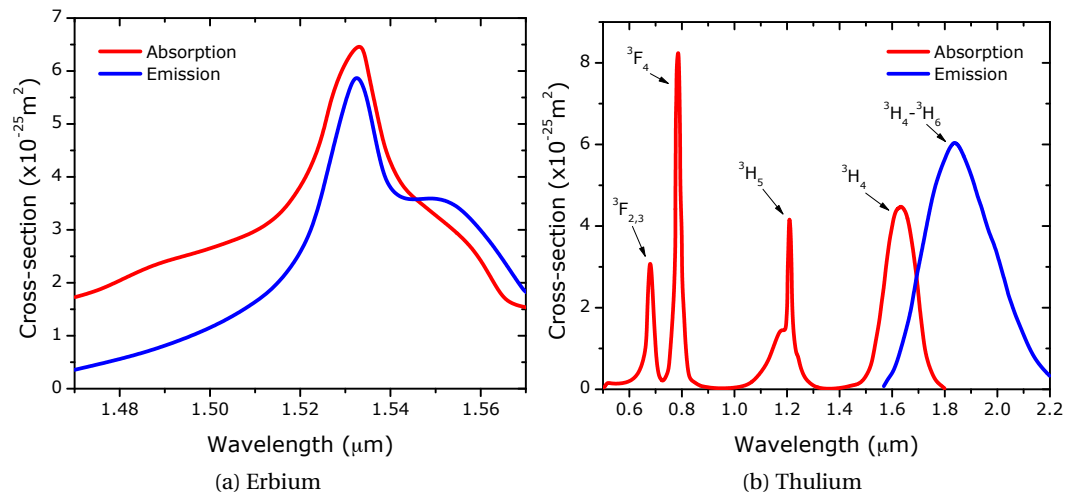
Figure 1.9: The absorption and emission cross sections for erbium in aluminium co-doped silica and thulium doped silica. Thulium's energy structure is complex and the relevant transitions have been labelled. Adapted from [58, 61].

erbium with it, improving absorption especially at 0.98 μm. Typically the concentration ratio of Er:Yb is 1:20. As erbium lasers and amplifiers are not used in this thesis we shall not discuss them further.

Thulium has a rather complicated energy structure [36, 58] which results in a number of absorption and emission lines. The important emission line in terms of commercial lasers sources is the one shown in figure 1.9b centred on 1.9 μm. It is worth noting that this emission is rather broad, allowing some flexibility in wavelength. The other important emission line is centred on 1.4 μm, unfortunately the best performance for this and upconversion to the blue is achieved by doping Tm into soft glasses [36]. Thulium lasers have been demonstrated utilising double clad fibres [59], with sources of up to 150 W available commercially [60].

In chapters 3 and 4 we make use of high power continuous-wave ytterbium fibre lasers. In chapter 5 we make use of a high power continuous-wave thulium laser. In chapter 2 we develop a fibre laser source based upon newly developed bismuth doped fibre, which as we shall see provides gain in the wavelength region 1.1-1.4 μm. .

1.2.3 Photonic crystal fibres

Photonic crystal fibres (PCF) are relatively new and have invigorated the nonlinear fibre optics community owing to their unique properties. These include highly customisable control of the dispersion and nonlinearity, having the ability to be endlessly single mode and providing new guidance mechanisms in the form of photonic bandgap fibres.

History

Photonic crystals are materials which have a periodic modulation in their refractive index on the scale of an optical wavelength. This allows them to interact unusually strongly with light at certain wavelengths. Significantly, appropriately designed structures can exhibit band gaps at optical frequencies [62]. Originally conceived in the late 80s in bulk format [63], difficulties in fabricating structures on the scale of an optical wavelength in 3D led researchers to focus on 2D structures manufactured by utilising etching techniques [64, 65]. The idea of developing a fibre based solution followed and the first photonic crystal fibre (PCF) was manufactured in 1996 [66]. This initial fibre was not a hollow core fibre, rather it had a solid core surrounded by a cladding containing a series of microscopic air holes running along the length of the fibre. The difficulty, during manufacture, is maintaining the structure of the air holes and it was not until 1999 that the first hollow core PCFs, with their high air-filling fractions were manufactured [67]. It should be stated that microstructured fibres were first invented in the 1970s during the search for suitable low loss fibres for telecommunications [68]. Ultimately, the manufacturing technology of the time was inadequate. Some time was spent revisiting the idea during the 1980s although these fibres were not designed to be photonic crystals but rather to use air to reduce the effective index of the cladding.

In recent years, hollow core band gap fibres have been demonstrated as fibre containers for gases and liquids, enabling many of the advantages of the fibre format for gas and liquid interactions [69, 70]. Hollow core PCFs were also identified as a possible replacement for SMF in telecommunications [71] due to the potential for lower losses, lower nonlinearities and a broader window of operation. In reality the losses are still significantly above those of modern SMF and splicing represents a real challenge, though some good progress has been made [72, 73].

Structure and guidance

Photonic crystal fibres are manufactured using a procedure known as stack and draw [66]. A preform is manufactured by fusing together an assembly of rods and capillaries, forming a macroscopic replica of the desired structure. The preform is then drawn on a fibre drawing tower in a similar fashion to traditional optical fibres, except for the addition of pressure being applied to the air holes. By controlling the speed of the draw and the gas pressure it is possible to exert additional control over the fibre's structure. In this way, making several PCFs with similar target parameters is possible from a single preform structure. Scanning electron microscope images for several different PCFs are shown in figure 1.10. The finished PCFs have many of the same handling properties as traditional

fibres and this is in part due to the transfer of technologies and processes from standard fibre manufacturing techniques, which are well developed.

(a) Solid core PCF with low air filling fraction

(b) Solid core PCF with high air filling fraction

(c) Hollow core band gap PCF
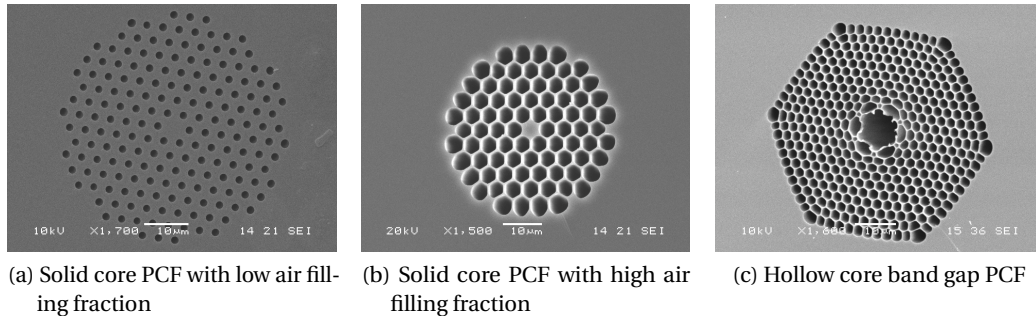
Figure 1.10: Scanning electron microscope images of several PCF structures. The small white bar corresponds to 10 μm.

As can be seen in figure 1.10 the PCF consists of either a solid or hollow core surround by a cladding structure made of several rings of air-holes. Normally these are arranged in a triangular pattern but other arrangements have been tried [71]. Two parameters define this structure, namely the hole diameter d and the pitch Λ. These are denoted in figure 1.11. A variety of PCFs have been manufactured with pitches ranging from 1-10 μm and air fractions (d/Λ) of less than 0.1 to over 0.9. This can lead to a very large refractive index difference (25%) compared with conventional fibres (4%) [74].
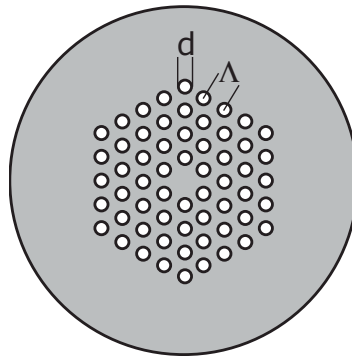
Figure 1.11: Cross section of a solid core PCF. The grey region denotes pure SiO$_2$ while the white regions are air filled. The hole diameter d and pitch Λ are marked.

As discussed, all PCFs guide by the photonic band gap effect [75]. This originates from the periodicity of the cladding, preventing transmission of frequencies which destructively interfere due to multiple reflections from the multiple air-silica interfaces. In a similar manner to step index fibres there exists a series of β values for which the existence of real transverse propagation constants are forbidden. Analogies between solid core PCFs and traditional step index fibres have been drawn [76], where the effective index of the

cladding is calculated and then used as its refractive index value. Thus guidance can be assumed as being due to total internal reflection and standard methods for calculating fibre properties applied. However this method is an approximation and perhaps leads to confusion over the guidance mechanisms.

Optical properties

As only solid core PCFs are used in this thesis, we shall concentrate upon the optical properties of these fibres over those of hollow core PCFs. Solid core PCFs can be engineered to exhibit a wide range of optical properties, not possible in conventional fibres. These include: highly controllable dispersion, high nonlinearity, strong birefringence, strong confinement and the unique property of being endlessly single mode. They also have some weaknesses compared to conventional fibres such as: higher optical losses especially around the OH^- absorption peaks; and due to their microstructured nature are difficult to splice to with low losses. We shall discuss each of the properties in a little more detail.

As discussed for conventional fibres in section 1.2.1 the dispersion of the fibre is made up from the material dispersion and waveguide dispersion. Given that most PCFs are made from the same fused silica as conventional fibres the material dispersion is identical. Dispersion control arises from the ability to control the waveguide dispersion which is due to a portion of any given mode propagating in the cladding. As the mode field diameter changes with wavelength the amount of light in the cladding region also changes. Thus the effective index, n_{eff}, varies with wavelength leading to non-zero derivatives of the propagation constant β. As previously mentioned the refractive index difference between the core and the cladding can be much greater in PCFs than conventional fibres. This in combination with the highly wavelength dependent nature of the cladding's effective index, due to its microstructure, allows for zero dispersion wavelengths shorter than 1.27 μm and the potential to have a second zero dispersion wavelength. Figure 1.12 shows control of the dispersion profile by varying d/Λ and Λ.

The strong optical confinement arises from the high refractive index contrast between the core and the cladding. This significantly enhances confinement especially at longer wavelengths and allows for smaller cores. In the extreme case where the air filling fraction is very high (such as figure 1.10b), the core can be approximated as a strand of silica in air. As a result it is possible to have very small cores, which in turn have very high nonlinearities due to the high power densities which can be maintained over a broad wavelength range. Values of the nonlinearity can be over three orders of magnitude higher than conventional fibres.

In a comparable way to conventional fibres, birefringence can be significantly enhanced

(a) Fixed pitch Λ of 3.5 μm and varying d/Λ.

(b) Fixed d/Λ of 0.5 and a varying pitch Λ.
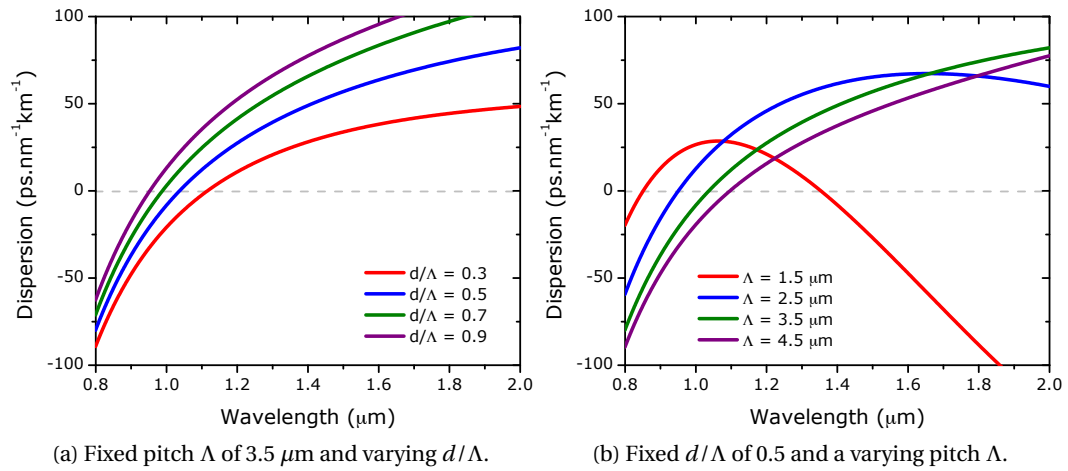
Figure 1.12: Figures 1.12a and 1.12b demonstrate some of the dispersion control available by varying the pitch, Λ and the hole diameter, d.

by breaking the rotational symmetry. For PCFs this can be done by altering the structure of the cladding, usually by leaving out or reducing the size of the air holes along one axis [77–79]. An example is shown in figure 1.13.

The final major advantage of PCFs is that they can be end-lessly single mode [80]. It can be understood by noting that the effective index of the cladding has a strong frequency dependence. This frequency dependence cancels with the frequency dependence included in the V parameter enabling the second mode to be cut-off at all frequencies for the correct cladding structures. An alternative way to envisage the endlessly single mode property is to consider the cladding structure to be a modal sieve [81]. In this case the fundamental mode cannot escape between the cladding holes whereas the higher order modes can, due to their smaller discrete field intensities. Through theoretical analysis it has been shown that a PCF will be endlessly single mode if $d/\Lambda < 0.41$ [82, 83].
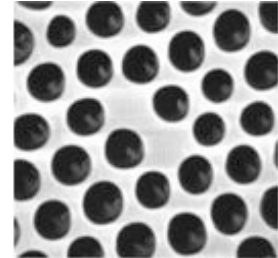
Figure 1.13: Cross section of a solid core highly birefringent PCF. Taken from [77].

Having covered some of the unique properties of PCFs which potentially offer advantages over conventional fibres, lets examine some of their main hindrances. Optical losses are generally higher, but particularly at 1.38 μm there is a very large loss due to OH^- absorption. A typical loss curve is shown in figure 1.14, where the high loss at 1.38 μm is clearly visible. In conventional fibre there is a similar peak due to OH^- absorption (figure 1.5) however it is several orders of magnitude less. The majority of losses in PCF arise from water binding to the surface of the microstructured air holes [84, 85], thus explaining the
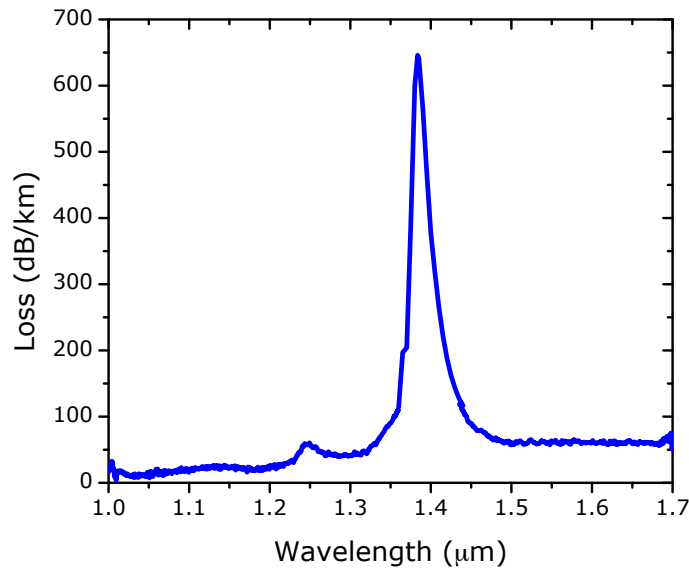
Figure 1.14: Measured loss of a solid core PCF.

very large losses. As we shall see in chapters 3 and 4 this high loss can represent a major problem for supercontinuum generation.

The other main difficultly with PCFs is splicing them to either conventional fibre or other PCFs with low losses. Two factors contribute to this problem. The first is that there is generally a mode field mismatch between the PCF and the conventional fibre, given that PCFs tend to have smaller mode field diameters. The second problem arises because splicing involves heating the fibres to melting point and then fusing them together. With PCFs the heating procedure can often lead to the collapse of the microstructured cladding region, which in turn results in a breakdown in the guidance properties and an increased loss [86–88]. Various techniques have been developed to attempt to resolve this problem and these will be discussed in chapter 3.

1.2.4 Soft glass fibres

Soft glass fibre covers a fairly large subset of fibre technology, namely any fibres based upon soft glasses such as: fluoride, chalcogenide and tellurite. Soft glasses have a much lower melting point than SiO_2 and as such are often not drawn from a preform. Instead, a method utilising a double crucible which has a reservoir for the core glass surrounded by one, or several reservoirs, for cladding glass is used. This allows the core and cladding to be simultaneously drawn from the crucible, enabling excellent control of the fibre during the draw. However, it is not possible to make ultra-pure fibres, leading to higher losses than the MCVD.
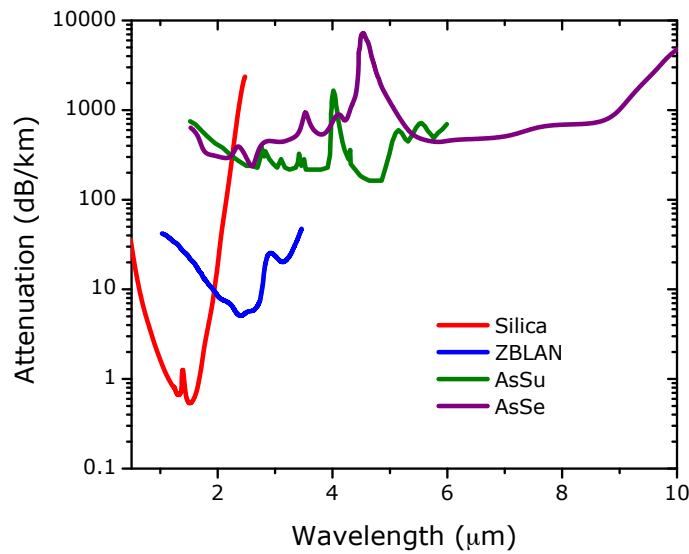
Figure 1.15: Attenuation of a variety of soft glass fibres compared to silica fibre.

Soft glasses offer some significant advantages over conventional silica-based fibre technology. These include the potential for very high nonlinearities (up to 1000 times that of SiO_2), transparency in the mid-infrared (see figure 1.15) and the ability to dope to high concentrations with rare-earth ions without clustering [89]. Unfortunately soft glass fibres also have some fairly significant limitations. Their optical attenuation is generally much greater than SiO_2 because the manufacturing process does not allow for ultra-pure fibres, as already mentioned. They are quite often structurally weak and therefore require careful handling, and their low melting points make splicing virtually impossible, forcing users to butt-couple to standard fibres or launch light into them using bulk optics. This in itself is made difficult by the typically high refractive index of the core and cladding, as the cladding may often also guide light, requiring mode stripping by metals such as Gallium. Finally their power handling is not comparable to that of conventional fibres [89].

Despite all these issues the advantages of soft glasses has led to a number of researchers continuing to work on these fibres, and although progress has been slow they continue to show promise [90–92]. Although no soft glass fibres are used in this thesis we shall discuss them briefly in some of the later chapters.

1.3 Nonlinear effects in fibre

1.3.1 Nonlinear susceptibility

In general when an electric field is applied to a dielectric material, the material becomes polarised, i.e. the electrons shift with respect to the nuclei. The resulting polarisation

depends on the strength of the electric field and the dielectric susceptibility, and can be expressed as

$$P = \varepsilon_0(\chi^{(1)}E + \chi^{(2)}E^2 + \chi^{(3)}E^3 + \dots) \tag{1.6}$$

where P is the total induced polarisation, ε_0 is the vacuum permittivity, E is the electric field and $\chi^{(j)}$ is the jth order susceptibility. When the electric field applied is much weaker than the internal electric field of the dielectric material, the higher order terms may be ignored. Equation 1.6 then reduces to $P = \varepsilon_0(\chi^{(1)}E)$ resulting in a linear response within the dielectric. The effects of $\chi^{(1)}$ are included through the description of the real part $\Re(\chi^{(1)})$ via the refractive index n, and the imaginary part $\Im(\chi^{(1)})$ via the attenuation coefficient α.

If the external field is of a similar order to or greater than the internal field strength, then the higher order terms become significant. This leads to a variety of nonlinear effects, for example, the possibility of high harmonic generation is easily shown. Considering the third order term, exposed to a field $E = E(\omega)\cos(\omega t)$ then it can be shown that

$$P^{(3)} = \varepsilon_0 \chi^{(3)} E_0^3 \cos^3(\omega t) \tag{1.7}$$

$$P^{(3)} = \varepsilon_0 \chi^{(3)} E_0^3 \left(\frac{1}{4}\cos(3\omega t) + \frac{3}{4}\cos(\omega t) \right) \tag{1.8}$$

which demonstrates that a second field of frequency 3ω is generated alongside the original field of frequency ω, which is referred to as third harmonic generation.

Similarly the second order term is responsible for nonlinear effects, such as second harmonic generation [93] and sum-frequency generation. In isotropic materials $\chi^{(2)}$ is zero under the dipole approximation. Hence in silica fibres $\chi^{(2)}$ generally vanishes as SiO_2 is isotropic. In reality these processes may still occur due to quadrupole and magnetic-dipole effects, but with very low efficiency. Thus the dominant nonlinear effects in silica fibres are due to $\chi^{(3)}$ [94].

The third order susceptibility is responsible for phenomena such as third-harmonic generation, four-wave mixing and nonlinear refraction. Its contributions originate from the electric response of the atoms, the vibrational response of the molecules, thermal effects and electrostriction effects [95]. For fibres the nonlinear processes involving third-harmonic generation and four-wave mixing are generally not efficient unless steps are taken to ensure phase matching, thus most non-linear effects in fibres originate from nonlinear refraction. Nonlinear refraction refers to the intensity dependence of the refractive index. Its origin can be understood when you consider that $\chi^{(3)}$ is dependent upon the electric field strength, which is a function of the intensity at a given point. Hence

the total refractive index n' is intensity dependent and can be expressed as

$$n'(\omega, I) = n(\omega) + n_2 I \tag{1.9}$$

where $n(\omega)$ is the linear refractive index at a frequency ω and I is the optical intensity. Hence the non-linear refractive index n_2 is given by

$$n_2 = \frac{3}{8n}\Re(\chi^{(3)}) \tag{1.10}$$

where n is the linear refractive index of the material and $\Re(\chi^{(3)})$ is the real part of the third order susceptibility. The nonlinear refractive index gives rise to self- and cross-phase modulation (SPM and XPM) [94, 96, 97]. Similarly the imaginary part gives rise to nonlinear absorption or amplification which leads to effects such as two photon absorption and Raman amplification.

Fibre would not appear an obvious choice for nonlinear processes due to its low nonlinearity. We can examine this by comparing with bulk materials, for which the optimal nonlinear interaction is achieved around the confocal focusing regime. We can define an intensity interaction-length product such that

$$IL_{\text{bulk}} = \frac{2\pi\omega_0^2 n}{\lambda}I = \frac{2Pn}{\lambda} \tag{1.11}$$

where P is the peak power, n is the refractive index of the bulk material, λ is the wavelength and ω_0 is the $1/e^2$ intensity spot size. For fibre we can define it as

$$IL_{\text{fibre}} = \frac{4L_{\text{eff}}P}{\pi\omega_{\text{MFD}}^2} \tag{1.12}$$

where $L_{\text{eff}} = [1 - \exp(-\alpha L)]/\alpha$ is the effective fibre length, α is the linear fibre loss and ω_{MFD} is the mode field diameter (MFD) of the fibre. Comparing equations 1.11 and 1.12 it becomes clear that for large values of L_{eff} and small MFDs it is possible to achieve large enhancement factors. For instance for a 100 m long PCF with a 2 μm MFD and a loss of 10 dB/km the enhancement factor is ~107 at a wavelength of 1 μm. Such large enhancement factors allow for low power sources, including continuous wave sources, to experience nonlinear effects.

1.3.2 Group velocity dispersion

Group velocity dispersion (GVD) is not a nonlinear process, instead it arises from the frequency dependence of the refractive index n. It is useful to consider GVD here because it interacts with nonlinear processes to generate effects such as solitons. The frequency

dependence arises because the medium absorbs energy at different frequencies via oscillations of bound electrons. GVD gives rise to temporal pulse broadening, as any given pulse of light will see its various spectral components travelling at different speeds as a result of the frequency dependence of the refractive index. It is useful to introduce a dispersion length L_D

$$L_D = \frac{T_0^2}{|\beta_2|} \tag{1.13}$$

where T_0 is initial pulse width and β_2 is the GVD parameter. If the length of the fibre is much less than L_D then the pulse maintains its shape during propagation. If the length of the fibre is similar to L_D then the pulse is broadened and positively or negatively chirped by GVD. Positive chirp emerges from the normal dispersion regime ($\beta_2 > 0$) while negative chirp emerges from the anomalous dispersion regime ($\beta_2 < 0$). Both chirped and unchirped Gaussian pulses maintain their shape during broadening. Other initial pulse shapes tend to broaden and change shape as they do so [94, 98–101].

1.3.3 Self-phase modulation

Self-phase modulation (SPM) is the induced spectral broadening of light pulses. It was first experimentally reported and identified in 1967 by Shimizu [102] who used a Q-switched ruby laser to observe filaments formed by CS_2 when excited by single pulses. The author noted that, "The structure of the frequency spectrum shows a pattern which can be explained by phase modulation through intensity-dependent refractive index."

For fibres we can explain SPM by defining a nonlinear length L_{NL} and effective length L_{eff}. The nonlinear length provides us with the length scale over which nonlinear effects become important. The effective length provides us with a length shorter than L that takes account of fibre losses.

$$L_{NL} = \frac{1}{(\gamma P_0)} \tag{1.14}$$

$$L_{eff} = \frac{1 - \exp(-\alpha L)}{\alpha} \tag{1.15}$$

$$\gamma = \frac{n_2 \omega_0}{c A_{eff}} \tag{1.16}$$

where γ is the nonlinear parameter, P_0 is the peak power, α accounts for fibre losses, n_2 is the nonlinear refractive index, ω_0 is the frequency, c is the speed of light and A_{eff} is the effective core area of the fibre. It can be shown that the nonlinear phase change ϕ_{NL} is given by

$$\phi_{NL}(L, T) = |U(0, T)|^2 \left(\frac{L_{eff}}{L_{NL}} \right) \tag{1.17}$$

where $U(0, T)$ is the field amplitude at $z = 0$. Thus the maximum phase shift ϕ_{max} occurs

when the pulse centre is located at $T = 0$. If U is normalised so that $|U(0,0)| = 1$ then

$$\phi_{\text{max}} = \frac{L_{\text{eff}}}{L_{\text{NL}}} = \gamma P_0 L_{\text{eff}} \tag{1.18}$$

As ϕ_{NL} is time dependent this results in a temporally varying phase which in turn causes the optical frequency to vary with time. Hence as a pulse of light propagates down a fibre new frequency components are generated by SPM, spectrally broadening the pulse and positively chirping it [94, 97]. It should be noted that the extent of the spectral broadening is dependent upon the initial pulse shape and chirp. Figures 1.16a-1.16d show how the spectral broadening changes for a variety of chirps and for a Gaussian pulse verses a super-Gaussian pulse. The maximum phase shifted is fixed for all cases at $\phi_{\text{max}} = 4.5\pi$. For an unchirped Gaussian pulse the maximum spectral broadening factor $\delta\omega_{\text{max}}$ is given by

$$\delta\omega_{\text{max}} = 0.86\Delta\omega_0\phi_{\text{max}} \tag{1.19}$$

where $\Delta\omega_0$ is the initial $1/e$ bandwidth of the pulse. Using typical values for picosecond laser pumping a PCF: $P_0 = 10\,\text{kW}$, $\gamma = 50\,\text{W}^{-1}\text{km}^{-1}$, $L_{\text{eff}} = 10\,\text{m}$, $T_{\text{FWHM}} = 8\,\text{ps}$, $\lambda = 1.06\,\mu\text{m}$; we find that a pulse of width 0.21 nm will increase to 895 nm (56 GHz to 234 THz). This is a very significant spectral broadening but not as large as those seen during supercontinuum formation.

1.3.4 Simulated Raman scattering

Spontaneous Raman scattering occurs when a photon of frequency ω_p is downshifted or upshifted to a frequency ω_s when incident on a molecule. The downshift is determined by the transition to a higher vibrational energy state by the molecule generating a phonon wave. If the medium is pumped continuously, frequency shifted radiation may be generated. This frequency-shifted radiation is called a Stokes wave [95]. In 1962 Woodbury discovered that for intense pump fields, a nonlinear effect exists such that the Stokes field grows rapidly to the point where the majority of the pump energy has been transferred to it. This is known as stimulated Raman scattering (SRS) [94, 103–107]. In 1972 Stolen reported SRS in fibre for the first time, noting that despite a small Raman cross-section a "relatively low threshold for Raman emission can be achieved because high optical power densities are maintained over long lengths of waveguide." SRS is important in fibre for a variety of reasons. Firstly, the waveguiding nature means that high power densities can be maintained over 100s of metres making SRS very efficient, to the extent that it can cascade to create many Stokes orders. Secondly, given that silica is amorphous, there are many available vibrational states resulting in very broad gain: about 40 THz for a 1 μm pump beam with the maximum gain at 13 THz, see figure 1.17 [108, 109]. It should be noted that
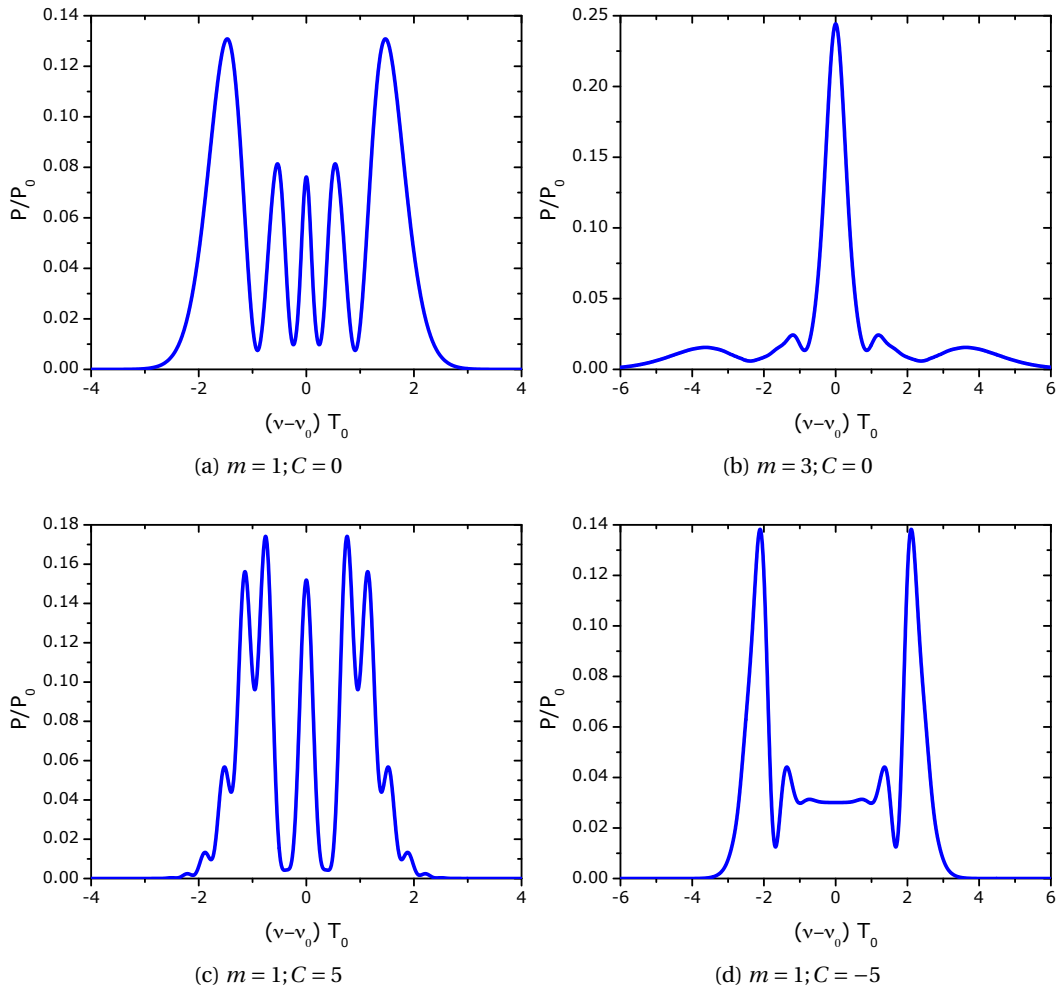
Figure 1.16: Comparison of SPM-broadened spectra for unchirped Gaussian (1.16a), super-Gaussian (1.16b) and chirped Gaussian pulses with $C = 5$ (1.16c) and $C = -5$ (1.16d). In all cases $\phi_{\max} = 4.5\pi$.

it is possible for a molecule in a high vibrational state to combine with a lower energy photon to upshift the photon producing an anti-Stokes wave. However the requirement for a pre-existing phonon tends to make this process extremely inefficient, unless very high populations of the correct energy phonons are generated by exceptionally strong Stokes generation.

Mathematically the initial growth of the Stokes wave can be described by

$$\frac{dI_s}{dz} = g_R I_p I_s \tag{1.20}$$

where I_s is the Stokes intensity, I_p is the pump intensity, z is the length and g_R is the
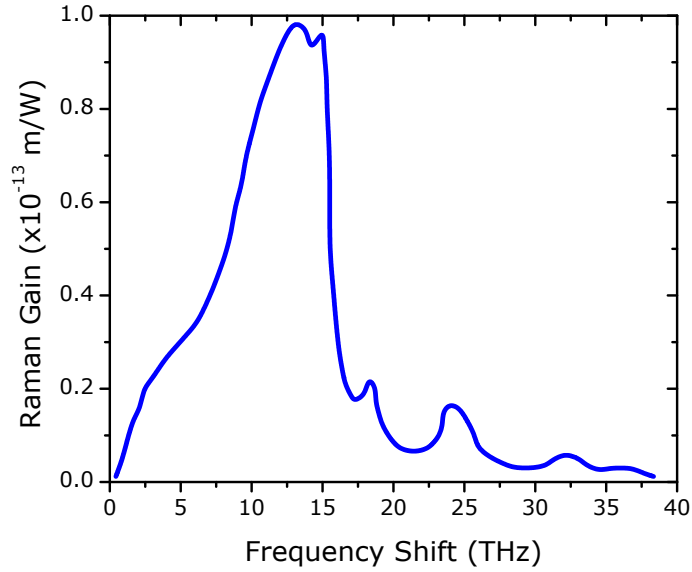
Figure 1.17: Raman gain spectrum for fused silica at a pump wavelength of $\lambda_p = 1$ μm.

Raman gain coefficient. The Raman gain coefficient originates from the imaginary part of the third order nonlinear susceptibility and is related to the spontaneous Raman scattering cross-section. Equation 1.20 holds true for the CW and quasi-CW case where pulse durations are greater than 1 ns. It can also be shown that the critical pump power, P_0^{cr}, for the Raman threshold is given by

$$P_0^{cr} \approx \frac{16A_{\text{eff}}}{g_R L_{\text{eff}}} \tag{1.21}$$

where A_{eff} is the effective core area and L_{eff} is the effective length of the fibre. Thus for a single mode fibre with an effective core of 10 μm^2 and 100 m long at a wavelength of 1 μm we get a critical pump power of ~16 W.

1.3.5 Stimulated Brillouin scattering

Stimulated Brillouin scattering (SBS) is a nonlinear process similar to stimulated Raman scattering in that it manifests itself though the generation of a frequency downshifted Stokes wave; the distinction is that the wave propagates backwards in the case of SBS. It can be explained by considering the formation of an acoustic wave in the fibre, generated by the electric field of the pump forming a pressure wave in the material through electrostriction [110]. The acoustic wave modulates the refractive index of the fibre, setting up the conditions for Bragg reflection which scatters and reflects the light. The light is downshifted in frequency because of the Doppler shift associated with the travelling

acoustic wave. The process can become stimulated at low powers, which can become a significant problem for high power fibre lasers and telecommunications. Fortunately, as the pump power must be within a very narrow bandwidth for the effect to dominate, a variety of schemes are possible to negate this. Stimulated Brillouin scattering does provide gain and can be used for Brillouin fibre lasers [94], however we make no use of SBS in this thesis and we will only be concerned with limiting the effect in latter chapters.

1.3.6 Four-wave mixing

Four-wave mixing (FWM) transfers energy from two photons at separate frequencies ω_1 and ω_2 by annihilation whilst creating two new photons at frequencies ω_3 and ω_4 ensuring energy conservation.

$$\omega_3 + \omega_4 = \omega_1 + \omega_2 \tag{1.22}$$

Additionally there is a phase-matching requirement for this process such that

$$\Delta k = k_3 + k_4 - k_1 - k_2 \tag{1.23}$$

where k is the wave number. It is easier to meet the phase-matching condition in the more common case of degenerate mixing where $\omega_1 = \omega_2$. Under such conditions a suitably strong pump wave will generate an upshifted and downshifted wave. The amount of frequency shift, Ω_s, is given by

$$\Omega_s = \omega_1 - \omega_3 = \omega_4 - \omega_1 \tag{1.24}$$

If a weak signal is launched into the fibre at ω_3, together with the pump at ω_1, the signal is amplified, and a new wave is generated at ω_4, in accordance with the conservation of energy. Thus, the process is stimulated, and the resulting gain is called parametric gain. In the absence of an initial signal, the Stokes and anti-Stokes waves can still be generated from noise.

Four-wave mixing was first demonstrated in silica fibres by Stolen *et al.* in 1974 when they launched a 100 W pump and 10 mW signal into a 9 cm multimode fibre and got a 4 μW idler signal out [111]. This work was followed up by demonstrations of CW degenerate FWM in single mode fibres at low powers and later cascaded orders of FWM in multimode fibres with kW pumps [112, 113].

For perfect phase matching the maximum gain attainable is given by

$$g_{\text{max}} = \gamma P_0 = g_p \left(\frac{P_0}{A_{\text{eff}}} \right) \tag{1.25}$$

where $g_p = 2\pi n_2'/\lambda$ at the pump wavelength. Comparing this to the Raman gain (figure 1.17) for typical values of $n_2' \approx 3\text{x}10^{-20}$ m^2/W at 1 μm we get $g_p = 2\text{x}10^{-13}$ m/W which is twice that of the Raman gain. In practice, the difficulty of maintaining phase-matching over long lengths of fibre means that SRS tends to prevail as the dominant nonlinear effect [94].

1.3.7 Cross phase modulation

We have seen that nonlinear refraction gives rise to a variety of nonlinear effects in fibre for any given field. We have also seen that it is possible to generate new fields and transfer energy between them through four-wave mixing. Another related effect is cross phase modulation (XPM) which couples two fields together without inducing any energy transfer between them. It is always accompanied by SPM and occurs because the refractive index seen by the beam depends not only on the intensity of that beam but also on the intensity of any co-propagating beams. The end result is an additional phase modulation due to the co-propagating wave which is twice as strong as that generated through SPM.

XPM gives rise to a variety of spectral and temporal effects depending on the group-velocity mismatch between the two pulses and the dispersion length L_D. If we introduce the walk off length L_W such that

$$L_W = \frac{T_0}{|d|}, \qquad d = \frac{\nu_{g1} - \nu_{g2}}{\nu_{g1}\nu_{g2}} \tag{1.26}$$

where T_0 is the width of the first pulse, ν_g is the group velocity of each pulse, and L_D is as defined in 1.13. If we have a fibre of length L such that L is small compared to L_W and L_D then the nonlinear effects can be neglected. In the case $L_W < L$ and $L_D \gg L$ then the pulse shape is maintained but the spectrum can alter drastically with the XPM normally resulting in asymmetric spectral broadening. In the final case when both $L_W \gg L$ and $L_D \gg L$ both the spectrum and pulse shape are changed [94, 114].

1.3.8 Solitons

Previously the effects of GVD and SPM were considered independently. When operating in power and length regimes where both dispersive and nonlinear effects are significant, the combination of the two can give rise to solitons. A soliton is a special kind of wave packet that can propagate undistorted over long distances. Their existence in fibre was predicted by Hasegawa *et al.* in 1973, however it wasn't until 1980 that Molenauer *et al.* reported their observation experimentally [115–117]. Soliton formation occurs in the anomalous dispersion regime where the negative chirp generated by GVD cancels the positive chirp generated by SPM, and as a result creates a temporally stable pulse known as a soliton.

Mathematically we need to start from the nonlinear Schrödinger equation.

$$i\frac{\partial U}{\partial \xi} = -\frac{1}{2}\frac{\partial^2 U}{\partial \tau^2} - N^2 \exp(-\alpha z)|U|^2 U \qquad (1.27)$$

where U is a normalised field amplitude, ξ and τ are normalised distance and time variables such that

$$U = \frac{A}{\sqrt{P_0}} \qquad (1.28)$$

$$\xi = \frac{z}{L_D} \qquad (1.29)$$

$$\tau = \frac{T}{T_0} \qquad (1.30)$$

and N is defined as

$$N^2 = \frac{L_D}{L_{\mathrm{NL}}} = \frac{\gamma P_0 T_0^2}{|\beta_2|} \qquad (1.31)$$

where A is the field amplitude, T_0 is the pulse duration, P_0 is the peak power, z is the distance and everything else is as previously defined. By using the inverse scattering method [118, 119] the equation can be solved and the simplest solution for $N = 1$ is given by

$$u(\xi, \tau) = \mathrm{sech}(\tau) \exp\left(\frac{i\xi}{2}\right) \qquad (1.32)$$

where $u = NU = \sqrt{\gamma L_D}A$.

Physically in equation 1.27 the first term on the right represents the dispersion and the second term represents the SPM. N governs the relationship between the effects of SPM and GVD on a pulse as it travels down a fibre. If $N \ll 1$ then GVD dominates, if $N \gg 1$ SPM takes over. For integer values of N equal to or greater than 1, solitons are formed with the value of N relating to the soliton order.

From equation 1.31 it emerges that there is a reciprocal relationship between the amplitude of a soliton and its width. Thus should a soliton lose power due to absorption, or other fibre effects, its width will increase: as this occurs the dispersive length (L_D) will also increase and the soliton will decay. Similarly, should a soliton gain power, via available gain, its width will decrease. Consequently it is possible to generate solitons in fibre and compress them down to produce an ultrafast pulse source.

Figure 1.18 shows the evolution of optical spectra and pulse shape for an initially unchirped Gaussian pulse propagating in a fibre under the anomalous regime. It can be seen that the pulse broadens initially and reaches a steady state by $z/L_D > 4$ while at the same time the spectrum narrows as the SPM and GVD chirps cancel each other out. A soliton of order $N = 1$, is formed. The pulse is reshaped as the initial pulse is Gaussian
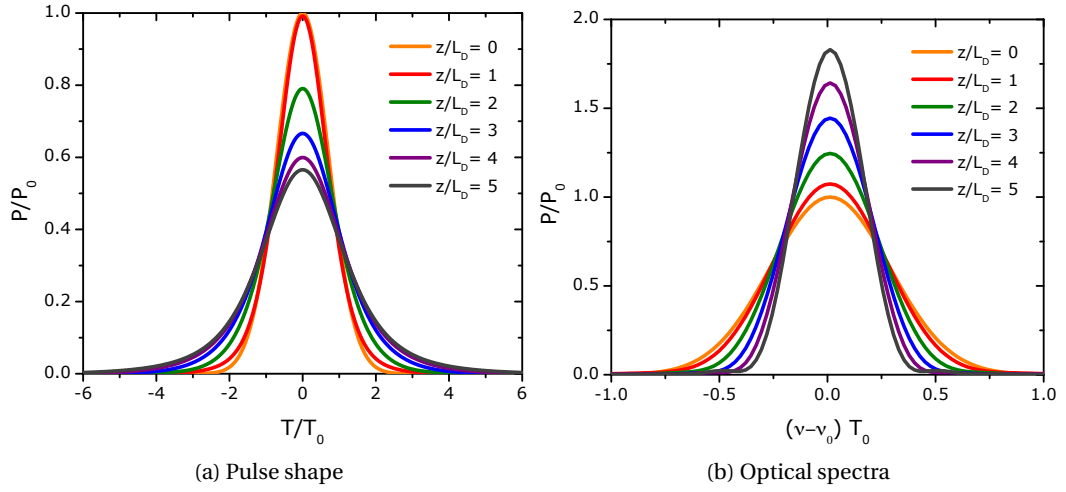
(a) Pulse shape

(b) Optical spectra

Figure 1.18: Evolution of a Gaussian pulse propagating in the anomalous dispersion regime.

and as equation 1.32 shows, the solution is in the form of a hyperbolic secant shaped pulse. Thus the Gaussian pulse is transformed to a secant pulse in order to meet the required conditions. In the normal regime the pulse broadens rapidly while the spectral components broaden more slowly than would be expected in the absence of GVD.

A soliton of order $N = 3$ is shown in figure 1.19. It can be seen from figure 1.19 that the soliton's propagation can be characterised as periodic in ξ with a period $\xi_0 = \pi/2$. As $\xi = z/L_D$ then the soliton period z_0 can be defined as

$$z_0 = \frac{\pi}{2} L_D = \frac{\pi}{2} \frac{T_0^2}{|\beta_2|} \approx \frac{T_{\text{FWHM}}^2}{2|\beta_2|} \tag{1.33}$$

As the high order soliton propagates down the fibre, it initially contracts then expands and splits into two distinct pulses at $z_0/2$, before recombining and contracting again. The process occurs because the SPM and GVD generated chirps do not perfectly cancel each other out and as such a set of coupled equations govern the soliton leading to the periodic variations.

Modulation instability

It is possible to generate solitons from CW or quasi-CW beams in fibres via a process know as modulation instability. Modulation instability (MI) had been studied in other fields of physics [119] before Hasegawa and Brinkman applied it to optical fibres in 1980 [120]. Modulation instability arises from a non-stable solution to the nonlinear Schrödinger equation (equation 1.27) under perturbation in the anomalous dispersion regime. It can
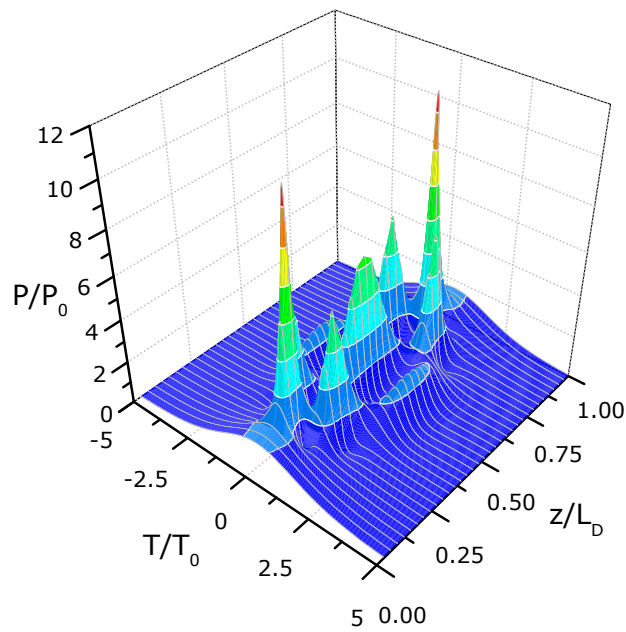
(a) Temporal Evolution
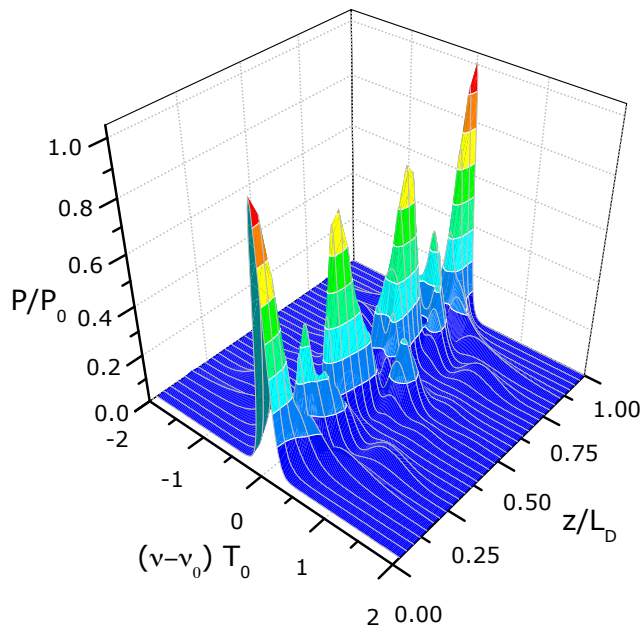
(b) Spectral Evolution

Figure 1.19: Evolution of a third order soliton over one soliton period.

also be interpreted in terms of a four-wave mixing process that is phase matched by SPM. If a probe wave at frequency $\omega_1 = \omega_0 + \Omega$ co-propagates with a CW beam at frequency ω_0

(a) Calculated gain spectra

(b) Experimental spectrum showing MI
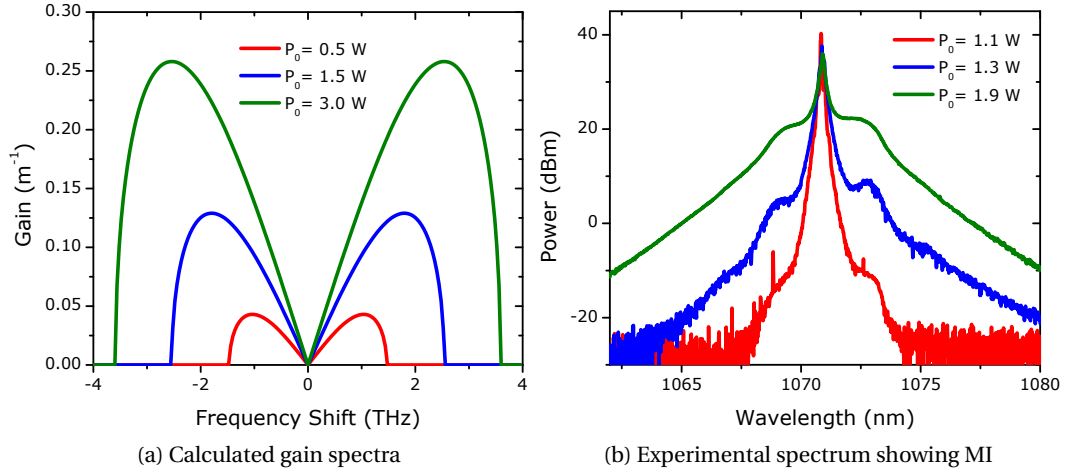
Figure 1.20: 1.20a shows the calculated gain spectra for three different pump powers for a fibre with β_2= 0.040 ps^2/m and γ= 0.043 (W m)$^{-1}$. 1.20b shows the same fibre pumped at three different pump powers. The spectral wings of MI are visible.

then it can experience gain provided $|\Omega| < \Omega_c$ where Ω is the frequency of perturbation and Ω_c is the critical frequency given by

$$\Omega_c^2 = \frac{4\gamma P_0}{|\beta_2|} \tag{1.34}$$

For a CW beam, photons generated through noise act as the probe-beam leading to its spontaneous breakup into a soliton pulse train with maximum growth occurring at $\Omega_{\text{max}} = \pm\Omega_c/\sqrt{2}$ [94, 119]. The first experimental report was made by Tai *et al.* [121] in 1986 using a Nd:YAG laser mode-locked at 1.32 μm producing 100 ps pulses with a 100 MHz repetition rate. Experimental results for a pure CW beam propagating in a PCF, along with the calculated gain, are shown in figure 1.20.

Soliton self-frequency shift

A remarkable and important feature of solitons is soliton self-frequency shift (SSFS) also referred to as intra-pulse Raman scattering. It was discovered shortly after the soliton [122, 123] and is caused by Raman self-pumping of the soliton, where the blue edge of the pulse amplifies the red edge via Raman shifting the central frequency of the pulse towards the red side [119]. A theoretical model developed by Gordon [124] predicts that the downshift in the central frequency of the pulse is proportional to the inverse fourth

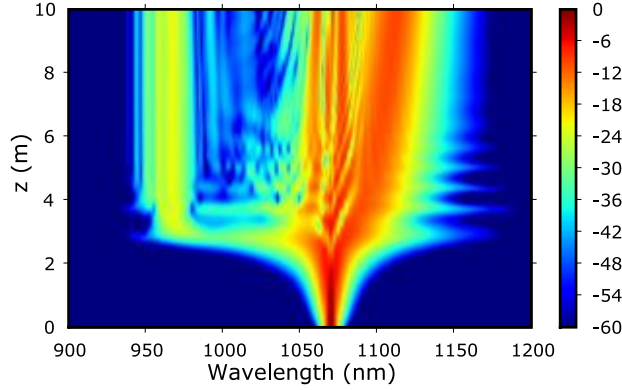Figure 1.21: A 250 fs pulse with a 150 W peak power is launched into 10 m of PCF with a zero-dispersion wavelength of 1.038 μm. The pulse broadens and then undergoes fission ($\sim$ 2 m in) creating a dispersive wave. Scale on the right hand side is logarithmic.

power of the pulse width (or soliton power squared) such that:

$$\Delta\omega_R(z) = -\frac{8|\beta_2|T_R}{15\tau_0^4}z \qquad (1.35)$$

where T_R= 3 fs and is the first moment of the Raman response function [94]. The Raman shifting of solitons leads to several things including soliton fission, soliton collisions and perhaps most importantly extreme spectral broadening. The result of this process is often called a soliton Raman continuum and was first demonstrated by Gouveia-Neto *et al.* [125, 126] who showed that solitons could form though modulation instability and then SSFS, in the anomalous region, to producing a continuum. This is the key process for the formation of supercontinua from CW laser sources and will be dealt with in depth in chapters 3 and 4.

Soliton fission

Soliton fission describes the process where a high order soliton splits into a collection of fundamental solitons. The propagation of a high order (N = 3) soliton has already been shown in figure 1.19. Although fundamental solitons are very robust against perturbations, high order solitons are not. Hence effects such as high order dispersion often prevent the periodic oscillation of a high order soliton. Typically, the soliton will undergo its initial temporal compression, and at the same time it will expand spectrally [127, 128], transferring energy to a dispersive wave if the spectrum overlaps into the normal dispersion region [122, 129]. As a result of the energy transfer, the central frequencies of the constituent fundamental solitons shift by different amounts, resulting in fission as they no longer have identical group velocities. Similarly, any process which can drive this change will lead to

fission, so intra-pulse Raman scattering will also lead to fission [130]. An example of this process is shown in figure 1.21. The initial transfer of energy to the dispersive wave can be quite efficient [131] and it is possible for the dispersive wave to be continually amplified as it propagates along the fibre. This fission and amplification process can be used to generate broadband continua, though an ultra-short (sub 500 fs) pulse is required which must be launched close to the zero dispersion wavelength on the anomalous side [132]. Although the work in chapters 3 and 4 is concerned with supercontinuum generation under CW pumped conditions, we will also draw comparisons with femtosecond pumped continua. In chapter 4 we will take a step further by showing that in order to generate a CW pumped continuum which extends short of the pump wavelength, we need to set up a similar dispersive wave on the short wavelength side.

Soliton trapping

Soliton trapping is an effect which involves the generation of a dispersive wave in the normal regime, which gets shifted to shorter wavelengths as the soliton that is trapping the dispersive wave, shifts to longer wavelengths via intra-pulse Raman scattering. The process requires that the group velocity of the dispersive wave and soliton are matched. The effect was first noticed and reported by Beaud *et al.* in 1987 [133]. They referred to the soliton as being on the Stokes side while the dispersive wave was on the anti-Stokes side stating that, "A possible explanation would be the trapping of the anti-Stokes pulse through an index well created by the much stronger Stokes pulse." Despite being a great insight at the time, it was ignored until 2002 when Nishizawa *et al.* revisited the matter [134, 135]. Even these results were neglected until recently when Gorbach *et al.* used it to explain the short wavelength edge of several supercontinuum results [136, 137].

(a) Spectral evolution with length

(b) Spectrogram taken at the end of the fibre (z = 10 m).
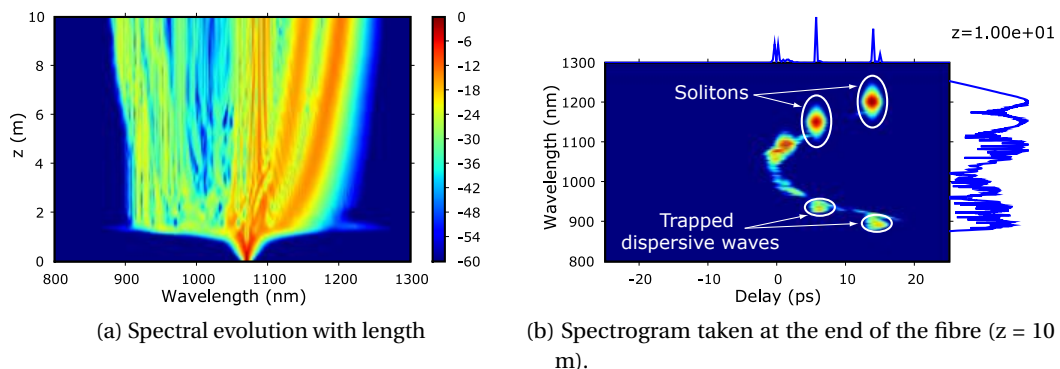
Figure 1.22: 1.22a shows the evolution of a 600 W 250 fs pulse along 10 m of PCF with a zero dispersion wavelength of 1.038 μm. 1.22b shows the spectrogram taken at the end of the fibre. The solitons and trapped dispersive waves are clearly visible.

The effect can be seen in figure 1.22 where a 600 W 250 fs pulse is launched into a PCF with a zero dispersion length of 1.038 μm. Figure 1.22a shows the evolution of the pulse with length along the fibre. After a little more than a metre of propagation the pulse rapidly expands and fissions in the way described above. A dispersive wave is generated in the normal dispersion region and several solitons can be seen shifting to longer wavelengths in the anomalous region. After 6 m of propagation it is clear that some of the energy in the dispersive wave is being shifted to shorter wavelengths as the continuum broadens (compared to figure 1.21). Careful examination shows that the trapped energy originated in the region between the pump and 1 μm. This can be seen in detail in 1.22b which shows the spectrogram (or XFROG [138]) trace for the same pulse after it has propagated through the 10 m of fibre. The spectrogram clearly shows two solitons which have self-frequency shifted to longer wavelengths, with corresponding trapped dispersive waves. We will show that this mechanism is also important when attempting to generate a CW pumped continuum which extends short of the pump wavelength in chapter 4.
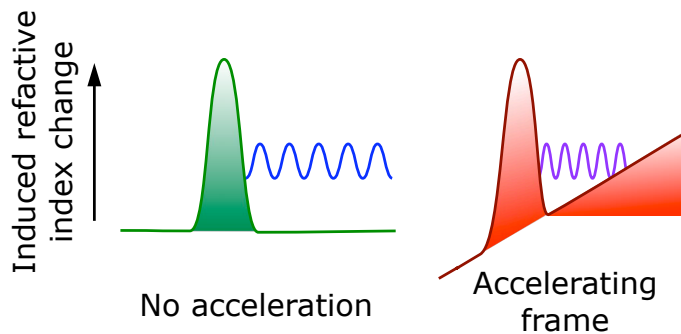
Figure 1.23: Pictorial representation of the trapping effect demonstrating the need for an accelerating force.

The process requires a high intensity red-shifting soliton and the generation of a dispersive wave. The red-shifting soliton creates a refractive index well on the leading edge of the dispersive wave, which prevents further dispersion of the dispersive wave. Cross-phase modulation between the dispersive wave and the soliton induces a blue-shift on the dispersive wave, causing it to decelerate as it shifts into a region of lower group velocity. At the same time the soliton continues to red-shift into a region of lower group velocity as well. Therefore, as the soliton slows it maintains the dispersive wave trap so that the dispersive wave is constantly blue-shifted as the soliton red-shifts. The accelerating force, in this case a deceleration provided by the SSFS, is essential for the process to occur. Without it there is no mechanism to trap the dispersive wave as denoted pictorially in figure 1.23. A changing GVD via a fibre taper has also been shown to provided the required accelerating force [139]. In either case, the trapping effect can be maintained as long as

the group velocity of the soliton and dispersive wave remain matched, as governed by the fibre's parameters.

1.4 Supercontinuum generation

During the last decade, the development of supercontinua sources has emerged as an interesting and active research field. This is largely due to new technological developments, which have allowed more controlled and accessible generation of supercontinua. This renewed research has created a variety of new light sources which are finding applications in a diverse range of fields, including optical coherence tomography [9, 140], frequency metrology [7, 141, 142], fluorescence lifetime imaging [8], optical communications [143–145], gas sensing [146–148] and many others. The application of these sources has created a feedback loop whereby the scientists utilising the supercontinua are demanding better customisable continua to suit their particular applications. This has driven researchers to develop novel methods to produce these continua and to develop theories to understand their formation and aid future development. As a result rapid progress has been made in developing these sources since 2000. In this section we will briefly define a supercontinuum, discuss their historical development and the two common regimes for generation.

As has been already alluded to in previous sections, a supercontinuum is formed when a collection of nonlinear processes act together upon a pump beam in order to cause severe spectral broadening of the original pump beam. The result is a smooth spectral continuum (figure 1.24). There is no definitive explanation of how much broadening constitutes a supercontinuum; however researchers have published work claiming as little as 60 nm of broadening as a supercontinuum [145]. Nor is there any agreement on the spectral flatness required to define the bandwidth of the source, with authors using anything from 5 dB to 40 dB or more. As we shall show, the term supercontinuum itself did not gain widespread acceptance until this century, with many authors using alternative phrases to describe their continua.

1.4.1 Historical overview

The 1960s and 1970s

In 1964 Jones and Stoicheff [149] reported using a continua generated by a maser to study induced Raman absorption in liquids at optical frequencies. It had been noted by Stoicheff in an early publication [150] that "when the maser emission was in a single sharp spectral line, all the Raman emission lines were sharp; whenever the maser emission
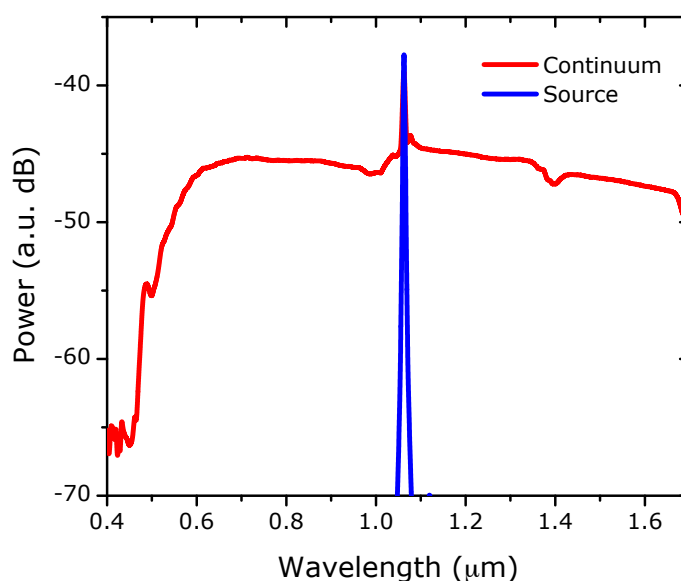
Figure 1.24: Spectral output of a pump source and a supercontinuum generated from the
source in a photonic crystal fibre.

contained additional components, all of the Raman emission lines, with the exception
of the first Stokes line, were considerably broadened, sometimes up to several hundred
cm^{-1}." [149] These weak continua, as they were described, allowed the first Raman
absorption spectroscopy measurements to be made.

In 1970 Alfano and Shapiro reported the first measurements of frequency broadening
in crystals and glasses using a frequency doubled Nd:Glass mode-locked laser. The output
pulses were approximately 4 ps and had a pulse energy of 5 mJ. The filaments formed
produced the first white light spectra in the range from 400-700 nm and the authors
explained their formation though self-phase modulation and four-wave mixing. The
filaments themselves were of no real use as a source; nevertheless the authors suggested
that the crystals might prove useful as ultrafast light gates [151, 152].

The study of atomic vapours, organic vapours and liquids by Raman absorption spec-
troscopy through the 1960s and 1970s drove the development of continua sources. By the
early 1970s, continua formed by nanosecond duration flash lamps and laser-triggered
breakdown spark in gases, along with laser excited fluorescence continua from scintillator
dyes, were being used to study the excited states [153]. These sources all had problems;
what was required was a source that produced broad continua at high power levels with
a reasonable efficiency. In 1976 Lin and Stolen reported a new nanosecond source that
produced continua with a bandwidth of 110-180 nm centred on 530 nm at output powers
of around a kW [153]. The system used a 10-20 kW dye laser producing 10 ns pulses with
15-20 nm of bandwidth to pump a 19.5 m long, 7 μm core diameter silica fibre (see figure

1.25 for the setup). They could only manage a coupling efficiency in the region of 5-10 %, stating "quite often the input end of the fibre was damaged if the full pump power was applied before good coupling to the fibre had been obtained." Nevertheless, it was noted that 90 % of the energy launched into the fibre was converted into the continuum. The continuum was identified as a result of sequential stimulated Raman scattering generating a series of Stokes lines. These were smoothed out by self-phase modulation. This fibre laser represented the first useful super continuum source.
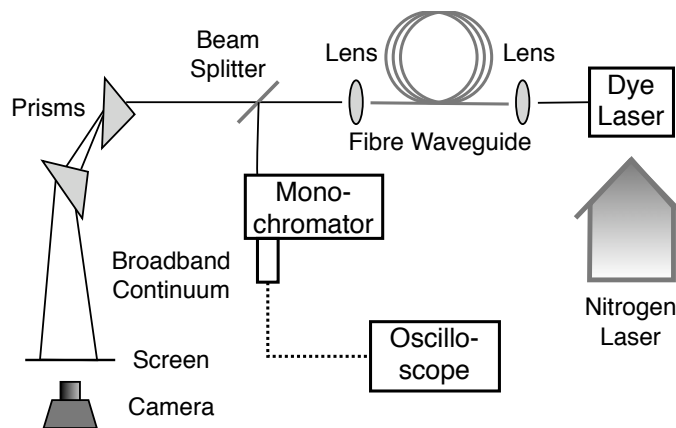
Figure 1.25: Lin and Stolen's setup, adapted from [153]

By 1978 Lin and Nguyen reported several continua, most notably one stretching from 0.7-1.6 μm using a 315 m long GeO$_2$ doped silica fibre with a 33 μm core [154]. The optical setup was similar to Lin's previous work with Stolen, except in this instance the pump source was a 150 kW, 20 ns, Q-switched Nd:YAG laser. Indeed, they had so much power available to them that two thirds was attenuated away to prevent damage to the fibre. The 50 kW coupled into the fibre emerged as a 12 kW continuum as shown in figure 1.26. Stokes lines are clearly visible up to 1.3 μm , at which point the continuum begins to smooth out, except for a large loss due to water absorption at 1.38 μm. As they increased the launch power beyond 50 kW they noted that the continuum extends down into the green part of the visible spectrum. However, the higher power levels quickly damaged their fibre. In the same paper they also pumped a single mode fibre with a 6 μm core diameter and "a few 100 m in length." It generated a similar continuum spanning from 0.9 μm to 1.7 μm with reduced launch and output powers. Without realising it, they had also generated optical solitons for the first time.

The 1980s

In 1980 Fujii *et al.* repeated Lin's 1978 setup with a mode-locked Nd:YAG [155]. The peak power of the pulses was reported as being greater than 100 kW and they achieved better

Figure 1.26: Spectra of the continuum obtained in a GeO$_2$ doped silica core multimode fibre by Lin and Nguyen in 1978. Two 7-56 Corning glass filters and a 0.3 neutral density filter where used for the measurements above 0.9 μm. Shorter wavelengths where unfiltered. Adapted from [154]
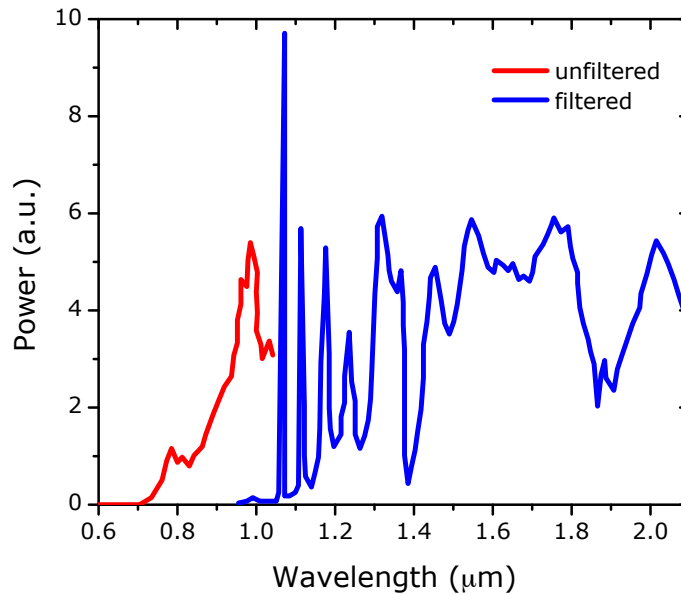
than 70 % coupling efficiency into a 10 μm core single-mode Ge doped fibre. Unusually, they did not report their pulse duration. Their spectrum spanned the entire spectral window in silica from 300 nm to 2100 nm. The authors concerned themselves with the visible side of the spectrum and identified the main mechanism for generation to be four-wave mixing of the pump and Raman generated Stokes. However there were some higher order modes, which were attributed to sum-frequency generation between the pump and Stokes lines. The phase-matching condition was met by coupling of the up-converted light and the quasi-continuum of cladding modes.

A further advance was reported by Wshio *et al.* [156] in 1980 when they pumped 150 m of single-mode fibre with a 1.34 μm Q-switched Nd:YAG laser. This was just inside the anomalous dispersion regime for their fibre. The result was a continua which stretched from 1.15 to 1.6 μm and showed no discrete Stokes lines.

Up to this point no one had really provided a suitable explanation why the continuum smoothed out between the Stokes lines at longer wavelengths in fibres. In the majority of cases this is explained by soliton mechanisms; but as solitons were not reported in fibres until 1985 [123, 157]. It was realised that self-phase modulation could not account for the broad continua seen, but for the most part little else was offered as an explanation.

In 1982 Smirnov *et al.* [158] reported similar results to that achieved by Lin in 1978. Using multimode phosphosilicate fibres pumped at 0.53 and 1.06 μm , they saw the normal

Stokes components and a spectrum which extended from the ultraviolet to the near infrared. They calculated that the spectral broadening due to self-phase modulation should have been 910 cm^{-1}, but their continuum was greater than 3000 cm^{-1}. They concluded that "an optical continuum cannot be explained by self-phase modulation alone." They continued by pointing out the difficulties of phase-matching over long lengths of fibre to maintain four wave mixing, and reported an unusual damage mechanism (with hindsight this would probably be considered a very short fibre fuse). Interestingly, they note a much earlier suggestion by Loy and Shen [159] that if the nanosecond pulses consisted of sub-nanosecond spikes in a nanosecond envelope, it would explain the broad continuum.

This idea of very short pulses resulting in the broad continuum was studied a year later when Fork *et al.* [160] reported using 80 fs pulses from a colliding mode-locked laser [161]. The laser's wavelength was 627 nm and they used it to pump a jet of ethylene glycol. They collimated the resulting continuum and measured the pulse duration at different wavelengths, noting that the red part of the continuum was at the front of the pulse and the blue at the rear. They reported very small chirps across the continuum. These observations and others led them to state that self-phase modulation was the dominant effect by some margin. However they also noted that their calculations showed that the continuum remained much larger than self-phase modulation would allow, suggesting that four-wave mixing processes must also be present. They stated that it was much easier to produce a reliable, repeatable continuum using a femtosecond source. Over the ensuing years this source was developed further and used to examine other liquids [162].

In the same year Nakazawa and Tokuda reported using the two transitions in Nd:YAG at 1.32 and 1.34 μm to pump a multimode fibre simultaneously at these wavelengths. They attributed the continuum spectrum to a combination of forced four wave mixing and a superposition of sequential stimulated Raman scattering. The main advantage of this was that they were able to generate a continuum at the relatively low pump powers of a few kW, compared to previous work [163].

During the early to late 1980s Alfano, Ho, Corkum, Manassah and others carried out a wide variety of experiments, though very little of it involved fibres. The majority of the work centred around using faster sources (10 ps and below) to pump various crystals, liquids, gases and semiconductors in order to generate continua mostly in the visible region [107]. Self-phase modulation was normally used to explain the processes although from the mid-1980s other explanations were offered, including second harmonic generation cross-phase modulation [164] and induced phase modulation [165]. Indeed, efforts were made to explain why self-phase modulation might well result in much broader continua, mostly through modifications to theory by including factors such as a slowly varying amplitude envelope amongst others [166, 167].

In 1987 Gomes *et al.* [168] reported cascaded stimulated Raman scattering in a single mode phosphosilicate based fibre. They pumped the fibre with a Q-switched and mode-locked Nd:YAG, which produced 130 ps pulses with 700 kW peak power. They launched up to 56 kW into the fibre and as a result of the phosphorus achieved a much broader and flatter continuum than had been achieved to that point with silica fibre. A year later Gouveia-Neto *et al.* [126] from the same group published a paper describing the formation and propagation of soliton waves from modulation instability. They used a 1.32 μm Nd:YAG which produced 100 ps pulses with 200 W peak power to pump 500 m of single mode fibre with a 7 μm core diameter. The zero dispersion of the fibre was at 1.30 μm , placing the pump just inside the anomalous dispersion regime. They noted pulses emerging with durations of less than 500 fs (solitons) and as they increased the pump power a continuum was formed stretching from 1.3 to 1.5 μm .

The 1990s

Gross *et al.* in 1992 published a paper modelling the formation of supercontinua (in the anomalous group velocity dispersion region) when generated by femtosecond pulses in fibre. It was easily the most complete model, to that date, with fundamental solitons and soliton self-frequency shift emerging as solutions to the equations [169].

The applicability of supercontinua for use in wavelength division multiplexed (WDM) systems for optical communications was investigated heavily during the 1990s. In 1993 Morioka *et al.* [143] reported a 100 wavelength channel multiplexing scheme which simultaneously produced one hundred 10 ps pulses in the 1.224-1.394 μm spectra region with a 1.9 nm spectral spacing. They produced a supercontinuum using a Nd:YLF pump centred on 1.314 μm which was mode-locked to produce 7.6 ps pulses. They then filtered the resulting continuum with a birefringent fibre to generate the channels.

Morioka and Mori continued development of telecommunications technologies utilising supercontinuum generation throughout the 1990s up to the present day. Their research included: using a supercontinua to measure the group velocity dispersion in optical fibres [170]; the demonstration of a 1 Tbit/s based WDM system [144]; and more recently a 1000 channel dense wavelength division multiplexed (DWDM) system capable of 2.8 Tbit/s using a supercontinuum fractionally more than 60 nm wide [145].

The first demonstration of a fibre-based supercontinuum pumped by a fibre-based laser was reported by Chernikov *et al.* [171] in 1997. They made use of distributed back-scattering to achieve passive Q-switching in single-mode ytterbium and erbium-doped fibres. The passive Q-switching produced pulses with a 10 kW peak power and a 2 ns duration. The resulting continuum stretched from 1 μm to the edge of the silica window at 2.3 μm. The first three Stokes lines were visible and the continuum stretched down to

about 0.7 μm but at significantly reduced power levels.

Progress since 2000

Advances made during the 1980s meant that it had become clear that to get the broadest continua in fibre, it was most efficient to pump in the anomalous dispersion regime. However it was difficult to capitalise upon this with high power 1 μm lasers as it had proven extremely difficult to achieve a zero dispersion wavelength of much less than 1.3 μm in conventional silica fibre. A solution appeared with the invention of photonic crystal fibres (PCF) in 1996 by Knight *et al.* [66]. We have already discussed many of the properties of PCFs in detail in section 1.2.3, but clearly their high nonlinearity and customisable zero dispersion wavelength makes PCF an excellent medium in which to generate supercontinua. It was some time though before supercontinua were first generated in PCFs. Amongst the first was Ranka *et al.* in 2000 [141], who used a 75 cm PCF with a zero dispersion at 767 nm and a 1.7 μm core diameter. They pumped the fibre with 100 fs, 800 pJ pulses at 790 nm to produce a flat continuum from between 400 and 1450 nm.

This work was followed by others pumping short lengths of PCF with zero dispersions around 800 nm with high power femtosecond Ti:sapphire lasers. Lehtonen *et al.* [172] studied the effect of polarization on the formation of the continua in a birefringent PCF, as well as varying the pump wavelength (728-810 nm) and pulse duration (70-300 fs). They found that the best continua were formed just inside the anomalous region with 300 fs pulses. Shorter pulses resulted in clear separation of the solitons which were visible in the spectral output. Herrmann *et al.* provided a convincing explanation of the development of femtosecond supercontinua, specifically the reduction of solitons from high orders down to the fundamental and the production of dispersive waves during this process [173, 174]. Needless to say, fully fibre integrated femtosecond sources have since been developed and demonstrated [175, 176].

Other areas of development in since 2000 have included: supercontinua sources that operate in the picosecond, nanosecond and CW regimes; the development of fibres to include new materials, production techniques and tapers; novel methods for generating broader continua, and the development of numerical models to explain and aid understanding of supercontinuum generation. Many of these will be discussed in chapters 3 and 4 though the reader is also referred to a recent review article [132].

1.4.2 Regimes

In this final section of the introduction we will briefly discuss the two main regimes in which supercontinua are generated in fibre. As previously stated a supercontinuum occurs

through the interaction of many nonlinear processes to cause extensive spectral broadening. Many of these processes were discussed individually in section 1.3 and on their own are well understood. The breakthroughs in recent years have involved understanding and modelling how all these processes interact together to generate supercontinua and how parameters can be engineered to enhance and control continuum formation.

Soliton fission regime

The soliton fission regime is essentially the same as the soliton fission described in section 1.3.8. A short, high power, femtosecond pulse is launched into the PCF or other highly nonlinear fibre. As previously discussed, the femtosecond pulse may be considered as a high order soliton, consequently it rapidly broadens and then fissions into fundamental solitons. During the fission process excess energy is shed as dispersive waves on the short wavelength side. Generally these dispersive waves will undergo no further shifting [132] and thus the extension short of the pump is dependent on how broadly the soliton expands as it breathes [177]. The fundamental solitons then undergo intra-pulse Raman scattering and shift to longer wavelengths, generating the long wavelength side of the continuum. It is possible for the soliton Raman continuum to interact with the dispersive radiation via four-wave mixing [178] and cross-phase modulation [179]. Under certain circumstances, it is possible for these dispersive waves to be coupled with the solitons via the soliton trapping affect [133, 136] (also described in section 1.3.8). This means that as the soliton self-frequency shifts (SSFS) to longer wavelengths, the coupled dispersive wave is shifted to shorter wavelengths as dictated by the group velocity matching conditions. Generally, this soliton trapping mechanism allows for the continuum to extend to shorter wavelengths than is possible via any other mechanism.

The first supercontinuum generated in PCF operated in this regime [141] and many of the subsequent experiments also made use of ultra-short pulsed femtosecond systems as a pump source [132]. One of the main advantages of this regime is that the continuum often exhibits a high degree of coherence [132], in addition it is possible to generate broad supercontinua in very short lengths of PCF. Disadvantages include an inability to scale to very high average powers in the continuum, although the limiting factor here is the available pump sources; and typically the spectrum is not smooth due to the localised nature of the spectral components which generate it. Figure 1.27 shows the evolution of an ultra-short pulse in a short length of PCF.

Whether this regime is dominant can be worked out from the pulse and fibre parameters. We can define a soliton fission length, L_{fiss}, to estimate the length at which the highest
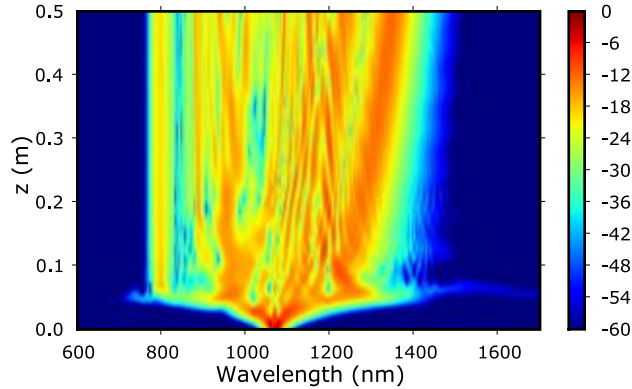
Figure 1.27: A 50 fs pulse with a 20 kW peak power is launched into 0.5 m of PCF with a zero-dispersion wavelength of 1.038 μm. The pulse broadens and then undergoes fission ($\sim$ 5 cm in) creating a dispersive wave. Scale on the right hand side is logarithmic.

soliton compression is achieved, such that

$$L_{\text{fiss}} = \frac{L_D}{N} = \sqrt{\frac{\tau_0^2}{|\beta_2|\gamma P_0}} \tag{1.36}$$

where L_D is the characteristic dispersion length (defined in equation 1.13) and N is the soliton order. As fission tends to occur at this length then provided that L_{fiss} is shorter than the length of the fibre and other characteristic length scales such as the MI length L_{MI}, fission will dominate.

Modulation instability regime

We previously covered modulation instability as a mechanism for generating solitons in section 1.3.8. Modulation instability (MI), leads to the break up of a continuous wave (CW) or quasi-continuous wave fields, which becomes a train of fundamental solitons. It is important to stress that the solitons generated in this regime are fundamental, as several papers on CW and quasi-CW supercontinuum formation have accredited short wavelength generation to soliton fission and dispersive wave generation as described above [180, 181]. In a similar manner to the soliton fission regime, the long wavelength side of the continuum is generated by the solitons undergoing intra-pulse Raman scattering and self-frequency shifting to longer wavelengths. As the MI process is noise driven, a distribution of solitons with different energies are created, resulting in different rates of self-frequency shifting. The net result is that MI driven soliton-Raman continua tends to be spectrally much smoother than those generated in the fission regime. Short wavelength generation is driven by four-wave mixing, especially for higher peak powers in

the quasi-CW regime. In the pure CW regime, short wavelength generation has not been achieved at wavelengths shorter than those of a 1 μm pump and we demonstrate the first results of this in chapter 4. We will also show that soliton trapping potentially plays a role in short wavelength generation in the MI driven regime.

A continuum will only occur in the MI regime if the fibre and field parameters are such that MI forms and dominates over other processes such as fission. In a similar fashion to the fission regime it is constructive to develop a characteristic length scale for MI, L_{MI}.

$$L_{\text{MI}} = \frac{n_{\text{dB}}}{20\gamma P_0 \lg 10} \sim \frac{4}{\gamma P_0} \tag{1.37}$$

where n_{dB} is the level of the background noise below the peak power level. Equation 1.37 is essentially a measure of the length required for the MI gain to amplify the background quantum noise into solitons. Typically this shot noise is taken to be ~200 dB down. So provided $L_{\text{MI}} \ll L_{\text{fiss}}$ then MI will dominate over soliton fission in the quasi-CW case and this condition may be expressed as

$$4^2 \ll \frac{\gamma P_0 \tau_0^2}{|\beta_2|} = N^2 \tag{1.38}$$

The middle term of equation 1.38 is simply the soliton equation as defined in 1.31. For MI to dominate we need the left hand side to be much less than the right hand side which implies that the soliton order must be much greater than 4. In practice this boundary has been established as being approximately $N = 16$ [132]. Therefore we can see that it is predominantly ultra-short pulses that lead to the soliton fission mechanism.

1.4.3 Pumping in the normal dispersion regime

The two regimes outlined above assume that the pump is in the anomalous dispersion region. It is possible to create supercontinua in the normal region and in fact many of the early results discussed in section 1.4.1 were pumped in the normal. If the input pulses are short enough then SPM can lead to significant broadening which is temporally coherent. However, if the pulses are not ultra-short then SRS tends to dominate and typically a series of cascaded discrete Stokes lines will appear until the zero dispersion wavelength is reached. At this point a soliton Raman continuum may form. As pumping in the anomalous is much more efficient for continuum generation, all the work in this thesis, with regards to supercontinuum generation, involves pumping in the anomalous regime.

1.5 Summary

We have seen that there is a great variety of laser sources available, yet despite this, important wavelength regions are still not easily accessible. The next four chapters of this thesis will be concerned with trying to enable wavelength diversification in fibre based sources. To this end we have covered the basic principles of various fibres including conventional, doped and soft glass fibres. We also discussed photonic crystal fibres which are used extensively in chapters 3 and 4. These chapters will focus on supercontinuum generation which we described in the previous section. Supercontinuum generation involves many nonlinear processes, each of which has been explained individually in section 1.3; their complex interactions will be discussed further in later chapters. One of these nonlinear processes, stimulated Raman scattering, is used by itself to build a Raman laser which will be explored in detail in chapter 5. Initially, we shall consider a new bismuth doped fibre for providing gain around 1.2 μm in the next chapter.

Bibliography

[1] T. H. Maiman, "Optical and microwave-optical experiments in ruby," Phys. Rev. Lett. **4**, 564–566 (1960).

[2] J. W. Goodman, D. W. Jackson, M. Lehmann, C. S. Weaver, and W. H. Huntley, *Laser Applications* (Stanford University, 1965).

[3] T. T. Basiev and R. C. Powell, *Handbook of Laser Technology and Applications* (Institute of Physics Publishing, UK, 2003).

[4] H. Schlueter, K. Mann, and T. B. Morris, "Remote welding applications in high-volume automotive manufacturing lines," in "Conference on Lasers and Electro-Optics/Quantum Electronics and Laser Science Conference and Photonic Applications Systems Technologies," (Optical Society of America, 2006), p. PTuE3.

[5] M. Andre, "Laser megajoule project status," Current Trends in International Fusion Research: Proceedings of the Fourth Symposium (2007).

[6] E. Moses, "The national ignition facility: Status and plans for laser fusion and high-energy-density experimental studies," 19th Symposium on Fusion Engineering pp. 487–492 (2002).

[7] J. Ye, H. Schnatz, and L. Hollberg, "Optical frequency combs: from frequency metrology to optical phase control," IEEE J. Sel. Topics Quant. Elect. **9**, 1041–1058 (2003).

[8] C. Dunsby, P. M. P. Lanigan, J. McGinty, D. S. Elson, J. Requejo-Isidro, I. Munro, N. Galletly, F. McCann, B. Treanor, B. Onfelt, D. M. Davis, M. A. A. Neil, and P. M. W. French, "An electronically tunable ultrafast laser source applied to fluorescence imaging and fluorescence lifetime imaging microscopy," J. Phys. D: Applied Physics **37**, 3296–3303 (2004).

[9] P. Hsiung, Y. Chen, T. H. Ko, J. G. Fujimoto, C. J. S. de Matos, S. V. Popov, J. R. Taylor, and V. P. Gapontsev, "Optical coherence tomography using a continuous-wave, high-power, Raman continuum light source," Opt. Express **12**, 5287–5295 (2004).

[10] J. E. Bjorkholm, "EUV Lithography—the successor to optical lithography?" Intel Technology Journal **2**, 1–8 (1998).

[11] T. Ito and S. Okazaki, "Pushing the limits of lithography," Nature **406**, 1027–1031 (2000).

[12] V. Bakshi, "High power lasers for generation of EUV light," in "Conference on Lasers and Electro-Optics/Quantum Electronics and Laser Science Conference and Photonic Applications Systems Technologies," (Optical Society of America, 2007), p. PThB4.

[13] A. E. Siegman, *Lasers* (University Science Books, 1986).

[14] W. T. Silfvast, *Laser Fundamentals* (Cambridge University Press, 2004).

[15] M. J. Weber, *Handbook of Lasers* (CRC Press, 2000).

[16] A. Javan, W. R. Bennett, and D. R. Herriott, "Population inversion and continuous optical maser oscillation in a gas discharge containing a He-Ne mixture," Phys. Rev. Lett. **6**, 106–110 (1961).

[17] C. Greskovich and J. P. Chernoch, "Improved polycrystalline ceramic lasers," J. Appl. Phys. **45**, 4495–4502 (1974).

[18] I. Shoji, S. Kurimura, Y. Sato, T. Taira, A. Ikesue, and K. Yoshida, "Optical properties and laser characteristics of highly Nd^{3+}-doped $Y_3Al_5O_{12}$ ceramics," App. Phys. Lett. **77**, 939–941 (2000).

[19] R. Won, "View from...ASSP 2008: Ceramic future," Nat. Phot. **2**, 216–217 (2008).

[20] S. G. Anderson, "Review and forecast of the laser markets Part I: Nondiode lasers," Laser Focus World **37** (2001).

[21] K. Kincade and S. G. Anderson, "Laser marketplace 2008: Innovation opens the door for the next wave of success," Laser Focus World **44** (2008).

[22] E. Snitzer, "Optical maser action of Nd^{+3} in a barium crown glass," Phys. Rev. Lett. **7**, 444–446 (1961).

[23] C. J. Koester and E. Snitzer, "Amplification in a fiber laser," Appl. Opt. **3**, 1182–1186 (1964).

[24] G. Holst, E. Snitzer, and R. Wallace, "High-coherence high-power laser system at 1.0621 μm," IEEE J. Quant. Elect. **5**, 342–342 (1969).

[25] G. Holst and E. Snitzer, "Detection with a fiber laser preamplifier at 1.06 μm," IEEE J. Quant. Elect. **5**, 319–320 (1969).

[26] B. Ross and E. Snitzer, "Optical amplification of 1.06-μ InAs$_{1-x}$P$_x$ injection-laser emission," IEEE J. Quant. Elect. **6**, 361–366 (1970).

[27] J. Stone and C. A. Burrus, "Neodymium-doped silica lasers in end-pumped fiber geometry," App. Phys. Lett. **23**, 388–389 (1973).

[28] R. J. Mears, L. Reekie, S. B. Poole, and D. N. Payne, "Neodymium-doped silica single-mode fibre lasers," Elect. Lett. **21**, 738–740 (1985).

[29] R. J. Mears, L. Reekie, S. B. Poole, and D. N. Payne, "Low-threshold tunable CW and Q-switched fibre laser operating at 1.55 μm," Elect. Lett. **22**, 159–160 (1986).

[30] D. C. Hanna, R. M. Percival, I. R. Perry, R. G. Smart, P. J. Suni, J. E. Townsend, and A. C. Tropper, "Continuous-wave oscillation of a monomode ytterbium-doped fibre laser," Elect. Lett. **24**, 1111–1113 (1988).

[31] H. M. Pask, R. J. Carman, D. C. Hanna, A. C. Tropper, C. J. Mackechnie, P. R. Barber, and J. M. Dawes, "Ytterbium-doped silica fiber lasers: versatile sources for the 1-1.2 μm region," IEEE J. Sel. Topics Quant. Elect. **1**, 2–13 (1995).

[32] B. J. Ainslie, S. P. Craig, and S. T. Davey, "The absorption and fluorescence spectra of rare earth ions in silica-based monomode fiber," J. Lightwave Tech. **6**, 287–293 (1988).

[33] L. Esterowitz, R. Allen, and I. Aggarwal, "Pulsed laser emission at 2.3 μm in a thulium-doped fluorozirconate fibre," Elect. Lett. **24**, 1104 (1988).

[34] D. C. Hanna, I. M. Jauncey, R. M. Percival, I. R. Perry, R. G. Smart, P. Suni, J. Townsend, and A. Tropper, "Continuous-wave oscillation of a monomode thulium-doped fibre laser," Elect. Lett. **24**, 1222–1223 (1988).

[35] R. Percival, M. Phillips, D. Hanna, and A. Tropper, "Characterization of spontaneous and stimulated emission from praseodymium (Pr^{3+}) ions doped into a silica-based monomode optical fiber," IEEE J. Quant. Elect. **25**, 2119–2123 (1989).

[36] M. J. F. Digonnet, *Rare-Earth-Doped Fiber Lasers and Amplifiers* (CRC Press, 2001).

[37] V. Fomin, A. Mashkin, M. Abramov, A. Ferin, and V. Gapontsev, "3 kW Yb fibre lasers with a single-mode output," in "International Symposium on High-Power Fiber Lasers and their Applications," (I.P.G. Germany, 2006).

[38] W. Koechner, *Solid-State Laser Engineering* (Springer, 1999).

[39] I. T. Sorokina and K. L. Vodopyanov, *Solid-State Mid-Infrared Laser Sources* (Springer, Berlin, 2003).

[40] J. Hecht, *City of Light: The Story of Fiber Optics* (Oxford University Press, USA, 2004).

[41] A. V. Heel, "A new method of transporting optical images without aberrations," Nature **173**, 39–39 (1954).

[42] L. E. Curtiss, "Glass fiber optical devices," US Patent 3589793 (Filled 1956. Issued 1971.).

[43] J. W. Hicks, E. Snitzer, and H. Osterberg, "Optical energy transmitting devices and method of making same," US Patent 3,157,726 (1964).

[44] K. C. Kao and G. A. Hockham, "Dielectric-fiber surface waveguides for optical frequencies," Proc. IEE **113**, 1151–1158 (1966).

[45] D. B. Keck and P. C. Schultz, "Method of producing optical waveguide fibers," US Patent 3711262 (1970).

[46] T. Miya, Y. Terunuma, T. Hosaka, and T. Miyashita, "Ultimate low-loss single-mode fibre at 1.55 μm," Elect. Lett. **15**, 106–108 (1979).

[47] A. W. Snyder and J. D. Love, *Optical Waveguide Theory* (Kluwer Academic Publishers, 1983).

[48] J. A. Buck, *Fundamentals of Optical Fibers* (Wiley-Interscience, 2004).

[49] J. Limpert, A. Liem, H. Zellmer, and A. Tünnermann, "500 W continuous-wave fibre laser with excellent beam quality," Elect. Lett. **39**, 645–647 (2003).

[50] J. D. Kafka, "Laser diode pumped fiber lasers with pump cavity," US Patent 4829529 (1987).

[51] E. Snitzer, H. Po, F. Hakimi, R. Tumminelli, and B. McCollum, "Double clad, offset core Nd fiber laser," in "Optical Fiber Sensors," (Optical Society of America, 1988), p. PD5.

[52] A. Liu and K. Ueda, "The absorption characteristics of circular, offset, and rectangular double-clad fibers," Opt. Commun. **132**, 511–518 (1996).

[53] A. Bertoni and G. Reali, "A model for the optimization of double-clad fiber laser operation," Appl. Phys. B: Lasers and Optics **66**, 547–554 (1998).

[54] D. Ripin and L. Goldberg, "High efficiency side-coupling of light into optical fibres using imbedded v-grooves," Elect. Lett. **31**, 2204–2205 (1995).

[55] D. J. DiGiovanni and A. J. Stentz, "Tapered fibre bundles for coupling light into and out of cladding pumped fiber devices," US Patent 5864644 (1999).

[56] V. P. Gapontsev and I. Samartsev, "Coupling arrangement between a multi-mode light source and an optical fiber through an intermediate optical fiber length," US Patent 5999673 (1999).

[57] A. B. Grudinin, D. N. Payne, P. W. Turner, L. Johan, A. Nilsson, M. N. Zervas, M. Ibsen, and M. K. Durkin, "Multi-fibre arrangement for high power fibre lasers and amplifiers," US Patent 7221822 (2007).

[58] S. D. Jackson and T. A. King, "Theoretical modeling of Tm-doped silica fiber lasers," J. Lightwave Tech. **17**, 948–956 (1999).

[59] S. D. Jackson and T. King, "High-power diode-cladding-pumped Tm-doped silica fiber laser," Opt. Lett. **23**, 1462–1464 (1998).

[60] I.P.G. Photonics, "TLR series: 1-150 W single mode thulium fiber lasers," `http://www.ipgphotonics.com/products_2micron_lasers_cw_tlr-series.htm` (2008).

[61] C. Giles and E. Desurvire, "Modeling erbium-doped fiber amplifiers," J. Lightwave Tech. **9**, 271–283 (1991).

[62] J. D. Joannopoulos, S. G. Johnson, J. N. Winn, and R. D. Meade, *Photonic Crystals - Molding the Flow of Light* (Princeton University Press, 2008), 2nd ed.

[63] S. John, "Strong localization of photons in certain disordered dielectric superlattices," Phys. Rev. Lett. **58**, 2486–2489 (1987).

[64] R. J. Tonucci, B. L. Justus, A. J. Campillo, and C. E. Ford, "Nanochannel array glass," Science **258**, 783–785 (1992).

[65] P. L. Gourley, J. R. Wendt, G. A. Vawter, T. M. Brennan, and B. E. Hammons, "Optical properties of two-dimensional photonic lattices fabricated as honeycomb nanostructures in compound semiconductors," App. Phys. Lett. **64**, 687–689 (1994).

[66] J. C. Knight, T. Birks, P. Russell, and D. Atkin, "All-silica single-mode optical fiber with photonic crystal cladding," Opt. Lett. **21**, 1547 (1996).

[67] R. Cregan, B. Mangan, J. Knight, T. Birks, P. Russell, P. Roberts, and D. Allan, "Single-mode photonic band gap guidance of light in air," Science **285**, 1537 (1999).

[68] P. Kaiser, E. A. J. Marcatili, and S. E. Miller, "A new optical fiber," The Bell System Technical Journal **52**, 265–269 (1973).

[69] F. Benabid, F. Couny, J. C. Knight, T. A. Birks, and P. S. J. Russell, "Compact, stable and efficient all-fibre gas cells using hollow-core photonic crystal fibres," Nature **434**, 488–491 (2005).

[70] A. Bozolan, C. J. S. de Matos, C. M. B. Cordeiro, E. M. dos Santos, and J. C. Travers, "Supercontinuum generation in a water-core photonic crystal fiber," Opt. Express **16**, 9671 (2008).

[71] J. C. Knight, "Photonic crystal fibres," Nature **424**, 847–851 (2003).

[72] P. Roberts, F. Couny, H. Sabert, B. Mangan, D. Williams, L. Farr, M. Mason, A. Tomlinson, T. Birks, J. Knight, and P. S. J. Russell, "Ultimate low loss of hollow-core photonic crystal fibres," Opt. Express **13**, 236–244 (2005).

[73] R. Amezcua-Correa, F. Gèrôme, S. G. Leon-Saval, N. G. R. Broderick, T. A. Birks, and J. C. Knight, "Control of surface modes in low losshollow-core photonic bandgap fibers," Opt. Express **16**, 1142–1149 (2008).

[74] P. S. Russell, "Photonic-crystal fibers," J. Lightwave Tech. **24**, 4729–4749 (2006).

[75] A. Ferrando, E. Silvestre, J. J. Miret, P. Andrés, and M. V. Andrés, "Donor and acceptor guided modes in photonic crystal fibers," Opt. Lett. **25**, 1328–1330 (2000).

[76] J. C. Knight, T. A. Birks, P. S. J. Russell, and J. P. de Sandro, "Properties of photonic crystal fiber and the effective index model," J. Opt. Soc. Am. A **15**, 748–752 (1998).

[77] T. Hansen, J. Broeng, S. Libori, E. Knudsen, A. Bjarklev, J. Jensen, and H. Simonsen, "Highly birefringent index-guiding photonic crystal fibers," IEEE Phot. Tech. Lett. **13**, 588–590 (2001).

[78] A. Ortigosa-Blanch, J. Knight, W. Wadsworth, J. Arriaga, B. Mangan, T. Birks, and P. Russell, "Highly birefringent photonic crystal fibers," Opt. Lett. **25**, 1325–1327 (2000).

[79] K. Suzuki, H. Kubota, S. Kawanishi, M. Tanaka, and M. Fujita, "Optical properties of a low-loss polarization-maintaining photonic crystal fiber," Opt. Express **9**, 676–680 (2001).

[80] T. A. Birks, J. C. Knight, and P. S. Russell, "Endlessly single-mode photonic crystal fiber," Opt. Lett. **22**, 961–963 (1997).

[81] P. Russell, "Photonic crystal fibers," Science **299**, 358–362 (2003).

[82] B. Kuhlmey, R. McPhedran, C. de Sterke, P. Robinson, G. Renversez, and D. Maystre, "Microstructured optical fibers: where's the edge?" Opt. Express **10**, 1285–1290 (2002).

[83] N. A. Mortensen and J. R. Folkenberg, "Low-loss criterion and effective area considerations for photonic crystal fibres," J. Opt. A: Pure and Applied Optics **5**, 163–167 (2003).

[84] A. Monteville, D. Landais, O. L. Goffic, D. Tregoat, N. J. Traynor, T.-N. Nguyen, S. Lobo, T. Chartier, and J.-C. Simon, "Low loss, low OH, highly non-linear holey fiber for Raman amplification," in "Conference on Lasers and Electro-Optics/Quantum Electronics and Laser Science Conference," (Optical Society of America, 2006), p. CMC1.

[85] J. Zhou, K. Tajima, K. Nakajima, K. Kurokawa, C. Fukai, T. Matsui, and I. Sankawa, "Progress on low loss photonic crystal fibers," Optical Fiber Technology **11**, 101–110 (2005).

[86] B. Park, J. Kim, U. Paek, and B. Lee, "The optimum fusion splicing conditions for a large mode area photonic crystal fiber," IEICE Trans. on Elec. **E88-C**, 883–888 (2005).

[87] R. Thapa, K. Knabe, K. L. Corwin, and B. R. Washburn, "Arc fusion splicing of hollow-core photonic bandgap fibers for gas-filled fiber cells," Opt. Express **14**, 9576–9583 (2006).

[88] L. Xiao, W. Jin, and M. S. Demokan, "Fusion splicing small-core photonic crystal fibers and single-mode fibers by repeated arc discharges," Opt. Lett. **32**, 115–117 (2007).

[89] J. S. Sanghera and I. D. Aggarwal, *Infrared Fiber Optics* (CRC Press, 1998).

[90] R. E. Slusher, G. Lenz, J. Hodelin, J. Sanghera, L. B. Shaw, and I. D. Aggarwal, "Large Raman gain and nonlinear phase shifts in high-purity As_2Se_3 chalcogenide fibers," J. Opt. Soc. Am. B **21**, 1146–1155 (2004).

[91] S. D. Jackson and G. Anzueto-Sanchez, "Chalcogenide glass Raman fiber laser," App. Phys. Lett. **88**, 221106 (2006).

[92] J. Hu, C. R. Menyuk, L. B. Shaw, J. S. Sanghera, and I. D. Aggarwal, "Raman response function and supercontinuum generation in chalcogenide fiber," in "Conference on Lasers and Electro-Optics/Quantum Electronics and Laser Science Conference," (Optical Society of America, 2008), p. CMDD2.

[93] P. A. Franken, A. E. Hill, C. W. Peters, and G. Weinreich, "Generation of optical harmonics," Phys. Rev. Lett. **7**, 118–119 (1961).

[94] G. P. Agrawal, *Nonlinear Fiber Optics* (Springer, 2001), 3rd ed.

[95] Y. R. Shen, *The Principles of Nonlinear Optics* (New York, Wiley-Interscience, 1984).

[96] R. Hellwarth, J. Cherlow, and T. Yang, "Origin and frequency dependence of nonlinear optical susceptibilities of glasses," Phys. Rev. B **11**, 964–967 (1975).

[97] R. H. Stolen and C. Lin, "Self-phase-modulation in silica optical fibers," Phys. Rev. A **17**, 1448–1453 (1978).

[98] D. Marcuse, "Pulse distortion in single-mode fibers," Appl. Opt. **19**, 1653–1660 (1980).

[99] D. Marcuse, "Pulse distortion in single-mode fibers. Part 2," Appl. Opt. **20**, 2969–2974 (1981).

[100] D. Marcuse, "Pulse distortion in single-mode fibers. Part 3: Chirped pulses," Appl. Opt. **20**, 3573–3579 (1981).

[101] C. G. B. Garrett and D. E. Mccumber, "Propagation of a Gaussian light pulse through an anomalous dispersion medium," Phys. Rev. A **1**, 305–313 (1970).

[102] F. Shimizu, "Frequency broadening in liquids by a short light pulse," Phys. Rev. Lett. **19**, 1097–1100 (1967).

[103] R. W. Hellwarth, "Theory of stimulated Raman scattering," Phys. Rev. **130**, 1850–1852 (1963).

[104] R. W. Hellwarth, "Analysis of stimulated Raman scattering of a giant laser pulse," Appl. Opt. **2**, 847–853 (1963).

[105] G. Eckhardt, R. W. Hellwarth, F. J. McClung, S. E. Schwarz, D. Weiner, and E. Woodbury, "Stimulated Raman scattering from organic liquids," Phys. Rev. Lett. **9**, 455–457 (1962).

[106] E. J. Woodbury and W. K. Ng, "Ruby laser operation in the near IR," Proceedings of the IRE **50**, 2367 (1962).

[107] R. R. Alfano, *The Supercontinuum Laser Source: Fundamentals With Updated References* (Springer, 2006), 2nd ed.

[108] R. H. Stolen, E. P. Ippen, and A. R. Tynes, "Raman oscillation in glass optical waveguide," App. Phys. Lett. **20**, 62–64 (1972).

[109] R. Shuker and R. W. Gammon, "Raman-scattering selection-rule breaking and the density of states in amorphous materials," Phys. Rev. Lett. **25**, 222–225 (1970).

[110] R. W. Boyd, *Nonlinear Optics* (Academic Press, 2003).

[111] R. H. Stolen, J. E. Bjorkholm, and A. Ashkin, "Phase-matched three-wave mixing in silica fiber optical waveguides," App. Phys. Lett. **24**, 308–310 (1974).

[112] K. O. Hill, B. S. Kawasaki, Y. Fujii, and D. C. Johnson, "Efficient sequence-frequency generation in a parametric fiber-optic oscillator," App. Phys. Lett. **36**, 888–890 (1980).

[113] K. O. Hill, D. C. Johnson, B. S. Kawasaki, and R. I. MacDonald, "CW three-wave mixing in single-mode optical fibers," J. Appl. Phys. **49**, 5098–5106 (1978).

[114] M. N. Islam, L. F. Mollenauer, R. H. Stolen, J. R. Simpson, and H. T. Shang, "Cross-phase modulation in optical fibers," Opt. Lett. **12**, 625 (1987).

[115] L. F. Mollenauer, R. H. Stolen, and J. P. Gordon, "Experimental observation of picosecond pulse narrowing and solitons in optical fibers," Phys. Rev. Lett. **45**, 1095–1098 (1980).

[116] A. Hasegawa and F. Tappert, "Transmission of stationary nonlinear optical pulses in dispersive dielectric fibers. I. Anomalous dispersion," App. Phys. Lett. **23**, 142–144 (1973).

[117] A. Hasegawa and F. Tappert, "Transmission of stationary nonlinear optical pulses in dispersive dielectric fibers. II. Normal dispersion," App. Phys. Lett. **23**, 171–172 (1973).

[118] A. Hasegawa and M. Matsumoto, *Optical Solitons in Fibers* (Springer, 2003).

[119] J. R. Taylor, *Optical Solitons: Theory and Experiment* (Cambridge University Press, 1992).

[120] A. Hasegawa and W. Brinkman, "Tunable coherent IR and FIR sources utilizing modulational instability," IEEE J. Quant. Elect. **16**, 694–697 (1980).

[121] K. Tai, A. Hasegawa, and A. Tomita, "Observation of modulational instability in optical fibers," Phys. Rev. Lett. **56**, 135–138 (1986).

[122] E. M. Dianov, A. Karasik, P. Mamyshev, A. Prokhorov, V. Serkin, M. Stel'makh, and A. Fomichev, "Stimulated-Raman conversion of multisoliton pulses in quartz optical fibers," JETP Lett. **41**, 294 (1985).

[123] F. M. Mitschke and L. F. Mollenauer, "Discovery of the soliton self-frequency shift," Opt. Lett. **11**, 659 (1986).

[124] J. P. Gordon, "Theory of the soliton self-frequency shift," Opt. Lett. **11**, 662 (1986).

[125] A. Gouveia-Neto, M. Faldon, and J. R. Taylor, "Spectral and temporal study of the evolution from modulational instability to solitary wave," Opt. Commun. **69**, 325–328 (1989).

[126] A. Gouveia-Neto, A. Gomes, and J. Taylor, "Femto soliton Raman generation," IEEE J. Quant. Elect. **24**, 332–340 (1988).

[127] L. F. Mollenauer, R. H. Stolen, J. P. Gordon, and W. J. Tomlinson, "Extreme picosecond pulse narrowing by means of soliton effect in single-mode optical fibers," Opt. Lett. **8**, 289 (1983).

[128] R. H. Stolen, L. F. Mollenauer, and W. J. Tomlinson, "Observation of pulse restoration at the soliton period in optical fibers," Opt. Lett. **8**, 186 (1983).

[129] P. K. A. Wai, C. R. Menyuk, Y. C. Lee, and H. H. Chen, "Nonlinear pulse propagation in the neighborhood of the zero-dispersion wavelength of monomode optical fibers," Opt. Lett. **11**, 464 (1986).

[130] W. Hodel and H. P. Weber, "Decay of femtosecond higher-order solitons in an optical fiber induced by Raman self-pumping," Opt. Lett. **12**, 924 (1987).

[131] F. Lu, Y. Deng, and W. H. Knox, "Generation of broadband femtosecond visible pulses in dispersion-micromanaged holey fibers," Opt. Lett. **30**, 1566–1568 (2005).

[132] J. Dudley, G. Genty, and S. Coen, "Supercontinuum generation in photonic crystal fiber," Rev. Mod. Phys. **78**, 1135 (2006).

[133] P. Beaud, W. Hodel, B. Zysset, and H. Weber, "Ultrashort pulse propagation, pulse breakup, and fundamental soliton formation in a single-mode optical fiber," IEEE J. Quant. Elect. **23**, 1938–1946 (1987).

[134] N. Nishizawa and T. Goto, "Pulse trapping by ultrashort soliton pulses in optical fibers across zero-dispersion wavelength," Opt. Lett. **27**, 152–154 (2002).

[135] N. Nishizawa and T. Goto, "Characteristics of pulse trapping by ultrashort soliton pulse in optical fibers across zero-dispersion wavelength," Opt. Express **10**, 1151–1160 (2002).

[136] A. Gorbach and D. Skryabin, "Theory of radiation trapping by the accelerating solitons in optical fibers," Phys. Rev. A **76**, 053803 (2007).

[137] A. Gorbach and D. Skryabin, "Light trapping in gravity-like potentials and expansion of supercontinuum spectra in photonic-crystal fibres," Nat. Phot. **1**, 653 (2007).

[138] R. Trebino, *Frequency-Resolved Optical Gating: The Measurement of Ultrashort Laser Pulses* (Kluwer Academic Publishers, 2002).

[139] J. C. Travers, S. V. Popov, and J. R. Taylor, "Trapping of dispersive waves by solitons in long lengths of tapered PCF," in "Conference on Lasers and Electro-Optics/Quantum Electronics and Laser Science Conference," (Optical Society of America, 2008), p. CThGG2.

[140] I. Hartl, X. D. Li, C. Chudoba, R. K. Ghanta, T. H. Ko, J. G. Fujimoto, J. K. Ranka, and R. S. Windeler, "Ultrahigh-resolution optical coherence tomography using continuum generation in an air-silica microstructure optical fiber," Opt. Lett. **26**, 608–610 (2001).

[141] J. K. Ranka, R. S. Windeler, and A. J. Stentz, "Visible continuum generation in air-silica microstructure optical fibers with anomalous dispersion at 800 nm," Opt. Lett. **25**, 25–27 (2000).

[142] D. J. Jones, S. A. Diddams, J. K. Ranka, A. Stentz, R. S. Windeler, J. L. Hall, and S. T. Cundiff, "Carrier-envelope phase control of femtosecond mode-locked lasers and direct optical frequency synthesis," Science **288**, 635–639 (2000).

[143] T. Morioka, K. Mori, and M. Saruwatari, "More than 100-wavelength-channel picosecond optical pulse generation from single laser source using supercontinuum in optical fibres," Elect. Lett. **29**, 862–864 (1993).

[144] T. Morioka, H. Takara, S. Kawanishi, O. Kamatani, K. Takiguchi, K. Uchiyama, M. Saruwatari, H. Takahashi, M. Yamada, T. Kanamori, and H. Ono, "1 Tbit/s (100 Gbit/s × 10 channel) OTDM/WDM transmission using a single supercontinuum WDM source," Elect. Lett. **32**, 906–907 (1996).

[145] H. Takara, T. Ohara, T. Yamamoto, H. Masuda, M. Abe, H. Takahashi, and T. Morioka, "Field demonstration of over 1000-channel DWDM transmission with supercontinuum multi-carrier source," Elect. Lett. **41**, 270–271 (2005).

[146] H. Delbarre and M. Tassou, "Atmospheric gas trace detection with ultrashort pulses or white light continuum," in "Conference on Lasers and Electro-Optics Europe.", (2000), p. CWF104.

[147] S. Sanders, "Wavelength-agile fiber laser using group-velocity dispersion of pulsed super-continua and application to broadband absorption spectroscopy," Appl. Phys. B: Lasers and Optics **75**, 799–802 (2002).

[148] M. Ere-Tassou, C. Przygodzki, E. Fertein, and H. Delbarre, "Femtosecond laser source for real-time atmospheric gas sensing in the UV–visible," Opt. Commun. **220**, 215–221 (2003).

[149] W. J. Jones and B. P. Stoicheff, "Inverse Raman spectra: Induced absorption at optical frequencies," Phys. Rev. Lett. **13**, 657–659 (1964).

[150] B. P. Stoicheff, "Characteristics of stimulated Raman radiation generated by coherent light," Phys. Lett. **7**, 186–188 (1963).

[151] R. R. Alfano and S. L. Shapiro, "Observation of self-phase modulation and small-scale filaments in crystals and glasses," Phys. Rev. Lett. **24**, 592–594 (1970).

[152] R. R. Alfano and S. L. Shapiro, "Direct distortion of electronic clouds of rare-gas atoms in intense electric fields," Phys. Rev. Lett. **24**, 1217–1220 (1970).

[153] C. Lin and R. H. Stolen, "New nanosecond continuum for excited-state spectroscopy," App. Phys. Lett. **28**, 216–218 (1976).

[154] C. Lin, V. Nguyen, and W. French, "Wideband near-I.R. continuum (0.7-2.1 μm) generated in low-loss optical fibres," Elect. Lett. **14**, 822–823 (1978).

[155] Y. Fujii, B. S. Kawasaki, K. O. Hill, and D. C. Johnson, "Sum-frequency light generation in optical fibers," Opt. Lett. **5**, 48 (1980).

[156] K. Washio, K. Inoue, and T. Tanigawa, "Efficient generation of near-I.R. stimulated light scattering in optical fibres pumped in low-dispersion region at 1.3 μm," Elect. Lett. **16**, 331–333 (1980).

[157] E. Golovchenko, E. M. Dianov, A. Prokhorov, and V. Serkin, "Decay of optical solitons," JETP Lett. **42**, 87–91 (1985).

[158] V. Grigor'yants, V. I. Smirnov, and Y. Chamorovski, "Generation of wide-band optical continuum in fiber waveguides," Sov. J. Quant. Elect. **12**, 841–847 (1982).

[159] M. Loy and Y. Shen, "Study of self-focusing and small-scale filaments of light in nonlinear media," IEEE J. Quant. Elect. **9**, 409–422 (1973).

[160] R. L. Fork, C. V. Shank, C. Hirlimann, R. Yen, and W. J. Tomlinson, "Femtosecond white-light continuum pulses," Opt. Lett. **8**, 1 (1983).

[161] R. L. Fork, B. I. Greene, and C. V. Shank, "Generation of optical pulses shorter than 0.1 psec by colliding pulse mode locking," App. Phys. Lett. **38**, 671–672 (1981).

[162] W. H. Knox, M. C. Downer, and R. L. Fork, "Amplified femtosecond optical pulses and continuum generation at 5-kHz repetition rate," Opt. Lett. **9**, 552 (1984).

[163] M. Nakazawa and M. Tokuda, "Continuum spectrum generation in a multimode fiber using two pump beams at 1.3 μm wavelength region," Jpn. J. Appl. Phys. **22**, L239–L241 (1983).

[164] R. R. Alfano, Q. Z. Wang, T. Jimbo, and P. P. Ho, "Induced spectral broadening about a second harmonic generated by an intense primary ultrashort laser pulse in ZnSe crystals," Phys. Rev. A **35**, 459–462 (1987).

[165] R. R. Alfano, Q. X. Li, T. Jimbo, J. T. Manassah, and P. P. Ho, "Induced spectral broadening of a weak picosecond pulse in glass produced by an intense picosecond pulse," Opt. Lett. **11**, 626 (1986).

[166] J. Manassah, R. Alfano, and M. Mustafa, "Spectral distribution of an ultrafast supercontinuum laser source," Phys. Lett. A **107**, 305–309 (1985).

[167] J. Manassah, M. Mustafa, R. Alfano, and P. Po, "Induced supercontinuum and steepening of an ultrafast laser pulse," Phys. Lett. A **113**, 242–247 (1985).

[168] A. S. L. Gomes, V. L. Dasilva, J. R. Taylor, B. J. Ainslie, and S. P. Craig, "Picosecond stimulated Raman scattering in P_2O_5-SiO_2 based single mode optical fibre," Opt. Commun. **64**, 373–378 (1987).

[169] B. Gross and J. T. Manassah, "Supercontinuum in the anomalous group-velocity dispersion region," J. Opt. Soc. Am. B **9**, 1813–1818 (1992).

[170] K. Mori, T. Morioka, and M. Saruwatari, "Ultrawide spectral range group-velocity dispersion measurement utilizing supercontinuum in an optical fiber pumped by a 1.5 μm compact laser source," IEEE Trans. Instrumentation and Measurement **44**, 712–715 (1995).

[171] S. V. Chernikov, Y. Zhu, J. R. Taylor, and V. Gapontsev, "Supercontinuum self-Q-switched ytterbium fiber laser," Opt. Lett. **22**, 298–300 (1997).

[172] M. Lehtonen, G. Genty, H. Ludvigsen, and M. Kaivola, "Supercontinuum generation in a highly birefringent microstructured fiber," App. Phys. Lett. **82**, 2197–2199 (2003).

[173] A. V. Husakou and J. Herrmann, "Supercontinuum generation of higher-order solitons by fission in photonic crystal fibers," Phys. Rev. Lett. **87**, 203901 (2001).

[174] J. Herrmann, U. Griebner, N. Zhavoronkov, A. Husakou, D. Nickel, J. C. Knight, W. J. Wadsworth, P. S. J. Russell, and G. Korn, "Experimental evidence for supercontinuum generation by fission of higher-order solitons in photonic fibers," Phys. Rev. Lett. **88**, 173901 (2002).

[175] R. E. Kennedy, A. B. Rulkov, J. C. Travers, S. V. Popov, V. P. Gapontsev, and J. R. Taylor, "High-power completely fiber integrated super-continuum sources," in "Proceedings SPIE: Fiber Lasers II: Technology, Systems, and Applications: Lase: Photonics West," , vol. 5709 (SPIE, 2005), vol. 5709, pp. 231–241.

[176] A. V. Tausenev, P. G. Kryukov, M. M. Bubnov, M. E. Likhachev, E. Y. Romanova, M. V. Yashkov, V. F. Khopin, and M. Y. Salganskii, "Efficient source of femtosecond pulses and its use for broadband supercontinuum generation," Quant. Elect. **35**, 581–585 (2005).

[177] I. Cristiani, R. Tediosi, L. Tartara, and V. Degiorgio, "Dispersive wave generation by solitons in microstructured optical fibers," Opt. Express **12**, 124–135 (2004).

[178] A. V. Gorbach, D. V. Skryabin, J. M. Stone, and J. C. Knight, "Four-wave mixing of solitons with radiation and quasi-nondispersive wave packets at the short-wavelength edge of a supercontinuum," Opt. Express **14**, 9854–9863 (2006).

[179] G. Genty, M. Lehtonen, and H. Ludvigsen, "Effect of cross-phase modulation on supercontinuum generated in microstructured fibers with sub-30 fs pulses," Opt. Express **12**, 4614–4624 (2004).

[180] A. Abeeluck and C. Headley, "Continuous-wave pumping in the anomalous- and normal-dispersion regimes of nonlinear fibers for supercontinuum generation," Opt. Lett. **30**, 61 (2005).

[181] F. Vanholsbeeck, S. Martin-Lopez, M. González-Herráez, and S. Coen, "The role of pump incoherence in continuous-wave supercontinuum generation," Opt. Express **13**, 6615–6625 (2005).

2 Bismuth Doped Fibre

2.1 Introduction

The search for new laser gain media is ongoing and potentially never-ending. As we discussed in the introduction, there are many wavelength regions for which it is difficult to produce compact, efficient laser sources due to a lack of suitable gain media. Other criteria such as ultrashort pulses or high average powers may not be achievable from a given gain medium; hence due to the multitude of potential applications, it becomes clear why this search is important. In this chapter we will examine some very early results from a new fibre gain medium of Bismuth doped silica.

We will start by examining the development of Bi doped fibre. This will be followed in section 2.3 by a series of experimental results. Firstly we will look at the properties of the fibre in section 2.3.1, before building and examining several lasers based upon the Bi doped fibre in section 2.3.2. We will then survey progress since this work in section 2.4, before discussing possible future directions and then concluding.

2.2 Development of bismuth doped fibre

The first infra-red luminescence from Bismuth based glass was reported by Fujimoto *et al.* in 2001. They reported a spectrum centred on 1140 nm with a full width half maximum (FWHM) bandwidth of 200 nm under 500 nm pumping, as shown in figure 2.1a [1]. The lifetime was measured as 630 μs making the glass potentially useful as a laser gain material. The glass itself was made by sintering spectroscopic grade bismuth oxide (Bi_2O_3), aluminium oxide (Al_2O_3) and silica powder (SiO_2) at 1760 °C. The composition of the resulting glass was measured as Bi_2O_3: 0.3 mol.%, Al_2O_3: 2.2 mol.%, and SiO_2: 97.5 mol.%; by X-ray fluorescence analysis. The glass's transmission was 30 % at maximum, due to a large number of air bubbles and it exhibited 4 absorption bands at (A) 300, (B) 500, (C) 700 and (D) 800 nm as shown in figure 2.1b. The authors noted that luminescence was not observed in the absence of the Al_2O_3 co-doping, and suggested that the emission may originate from Bi^{5+}.

The potential importance of this discovery becomes clear when the currently available infrared fibre gain media are examined. Figure 2.2 shows the emission spectrum for Yb, Er,
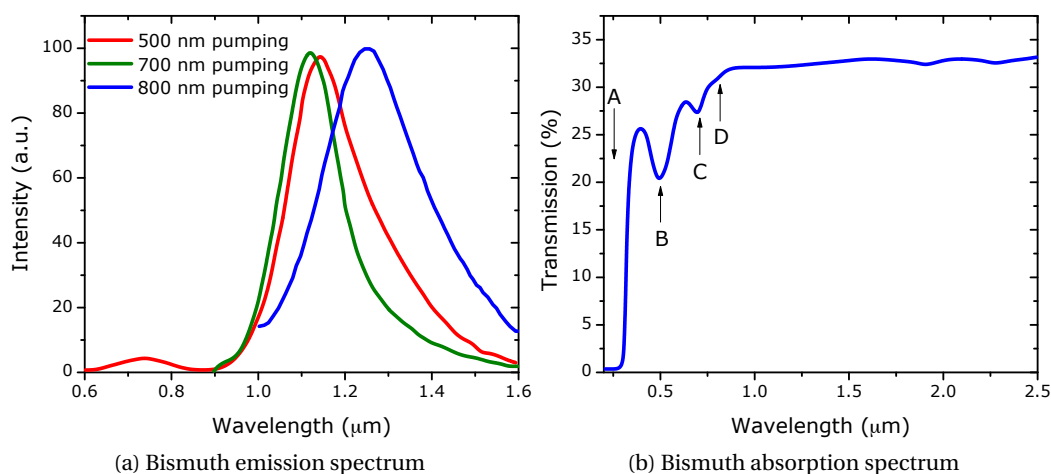
(a) Bismuth emission spectrum

(b) Bismuth absorption spectrum

Figure 2.1: 2.1a shows the emission spectrum of the Bismuth based glass made by Fujimoto *et al.* pumped at three different wavelengths. 2.1b shows the absorption spectrum of the same glass. Both figures adapted from [1].

Pr, Tm and Bi normalised to one. While Yb and Er doped silica fibres are well-established gain media, both Pr and Tm tend to operate best in soft glass fibres at the wavelengths shown. This has proven to be somewhat inconvenient, both in terms of the mechanical properties of these fibres, and in interfacing them with standard silica fibres. Thus, despite some good results [2–4] these fibre gain media have not seen wide adoption to date. Even if Pr is included, there remains a large spectral gap in the 1.1-1.3 μm region. Although it is possible to cover this region with Raman lasers or amplifiers, and there have been some exceptionally broad Raman amplifiers demonstrated [5], Raman as a gain medium has its limitations. For instance, modelocked operation is yet to be demonstrated (though ultrashort pulse generation has [6, 7]), and single frequency operation is extremely difficult. As figure 2.2 demonstrates, Bi covers a large part of the spectral gap between Yb and Er, potentially enabling this wavelength region and several important applications. The obvious use is in telecommunications: as the internet continues to grow and the amount of data being transferred increases, it is clear that extending the telecommunication windows into the 1.3 μm region will become increasingly important [8]. Generating efficient laser sources in the 1.1-1.3 μm region would also enable frequency doubling into the orange/red wavelength region, for which there are several important applications including biomedical [9, 10] and laser guide star [11].

Given the potential uses for laser sources in this wavelength region, other researchers quickly sought to investigate this new gain medium. Perhaps unsurprisingly, Fujimoto *et al.* were the first to follow up their own results [12], purssued by a series of papers by Peng *et al.* which looked at Bi luminescence in a whole series of glass hosts including: GeO$_2$,
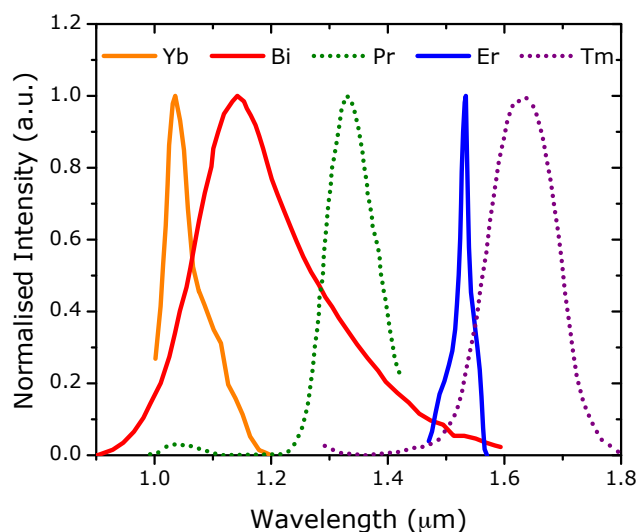
Figure 2.2: The emission spectrum for Yb, Bi, and Er doped silica fibres (solid lines). Also shown is the emission spectrum for Pr and Tm doped fluoride fibres (dotted lines).

BaO, $Li_2O-Al_2O_3-ZnO-SiO_2$ and P_2O_5 [13–17]. Optimum luminescence was achieved with low levels of Bi doping in the region of 0.5 - 2.0 mol. %. The authors argued that the luminescence may be due to Bi^+ or clusters of Bi atoms, though the authors themselves admitted that much more evidence would be needed before firm conclusions could be drawn.

Further work on Bi doped glass was carried out by Ren *et al.* who combined alkaline-earth metal oxides with Bi and silica [18]. Comparable results were achieved, and the authors put forward that the lasing may be due to Bi^{2+}.

Taking an important step forward towards realising a Bi based laser, Dvoyrin *et al.* produced the first Bi doped fibre via modified chemical vapour deposition (MCVD) [19, 20]. The fibre exhibited optical losses of less than 0.1 dB/m in the range of 1200-1800 nm and broadband luminescence spectra of up to 200 nm FWHM with the maximum in the region of 1050-1200 nm, depending upon the glass composition and excitation wavelength. The authors suggested yet another possible mechanism for the lasing based upon $\{[AlO_{4/2}]^-,Bi^+\}$ complexes. These fibres were used to demonstrate the first Bi based fibre laser. CW lasing was demonstrated at 1146, 1215, 1250 and 1300 nm under 1064 nm pumping. The cavity was formed between two fibre Brag gratings (FBG). For 5 W of pump power 460 mW of emission was achieved at 1146 nm [21].

In 2007 several results were published demonstrating Bi based silica fibre lasers exhibiting CW operation [22–24], pulsed operation [25] and mode-locked operation [26]. The second published CW result, though third by submission, came from Razdobreev *et al.* who became the second group to demonstrate luminescence from Bi doped fibre and a

CW laser cavity based upon 80 m of fibre using two FBGs, a high reflector (HR) with R = 99.8 % and an output coupler (OC) with R = 10-20 %. The gratings were written in standard silica fibre and spliced with low loss to the Bi fibre (0.1 dB). The Bi was pumped with a 3 W Yb fibre laser producing ~550 mW (slope efficiency of 24 %) at 1200 nm and ~320 mW (slope efficiency 12 %) at 1150 nm [22]. Using the same fibre, Rulkov *et al.* demonstrated a 6.4 W CW laser at 1178 nm pumped by a 55 W Yb fibre laser. They took the unpolarised 0.2 nm wide 1178 nm output and frequency doubled it using a MgO doped periodically poled lithium niobate crystal to produce 125 mW of average power at 589 nm [24].

The second submitted result was by Dianov *et al.*, who demonstrated up to 15 W of power at 1160 nm using a 70 W Yb fibre laser as the pump source for an 80 m length of Bi fibre. They also demonstrated frequency doubling to 580 nm producing 300 mW from just under 6 W of 1160 nm light. Importantly, they also noted that approximately one third of the Bi absorption is accounted for by unsaturable optical losses and that these losses have a temperature dependance [23].

These results were followed up by the first pulsed Bi laser source, demonstrated by Dvoyrin *et al.* This was achieved by using a 35 m length of Bi doped fibre as a saturable absorber in an Yb fibre laser, to produce 1 μs duration pulses at 1066 nm. Operation at 1160 nm was achieved by adding a pair of FBGs to the 35 m length of Bi, producing a weak pulsed signal at 1160 nm. This was then amplified by a second 90 m length of Bi doped fibre to produce 1.5 μs pulses at a repetition rate of 43.5 kHz with 400 mW of average power [25].

Finally, an extremely brief paper from Dianov *et al.* demonstrated mode-locked operation of a 6 m Bi doped fibre in a linear semiconductor saturable absorber mirror (SESAM) based cavity. The output FBG had a reflectivity of 75 % and a bandwidth of 0.02 nm; the high reflectivity was necessary to support the low gain of the Bi fibre. The cavity was pumped with an 800 mW Yb fibre laser at 1064 nm while residual pump light was filtered after the FBG using a wavelength division multiplexer (WDM). The cavity produced 50 ps pulses with a 13 MHz repetition rate and 2 mW of average power at 1162 nm [26].

2.3 Experimental results

In this section we will examine the properties of a bismuth doped fibre including the absorption, lumenscence, gain and lifetime. We will then go onto use the fibre to construct several CW fibre lasers before examining the possibility of mode-locked and single frequency operation.
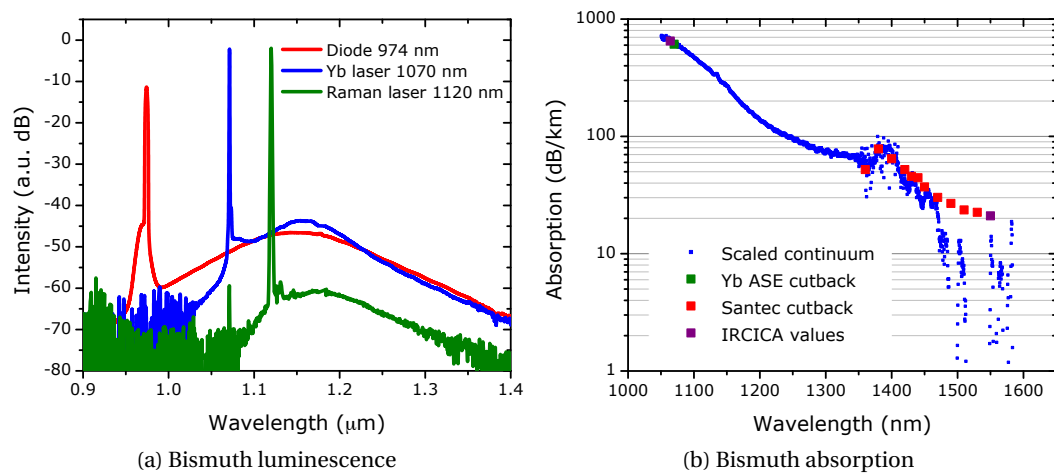
(a) Bismuth luminescence

(b) Bismuth absorption

Figure 2.3: 2.3a shows the luminescence spectrum of the Bi doped fibre pumped at three different wavelengths. 2.3b shows the residual absorption spectrum of the Bi doped fibre above 1 μm measured using a variety of methods.

2.3.1 Fibre properties

A length of Bi doped fibre was provided by our collaborators based at the IRCICA and CNRS in France. The Bi doped fibre perform was fabricated by the MCVD process with the Bismuth ions solution-doped into a porous silica layer before sintering. The $SiO_2-Al_2O_3-GeO_2-P_2O_5$ fibre had a Bi concentration of ~0.005 mol.%. The fibre was comparable to those detailed in [22]. A 37 m length of Bismuth doped fibre was used. Typically much shorter lengths of gain fibre are used with other high gain dopants such as Yb for instance. As the gain demonstrated from Bismuth has been signifigantly lower, a longer length of fibre was required. This length had to be balanced with the pump absorption, suggesting that tens of meters of fibre should be optimal.

Absorption and luminescence

The luminescence was recorded for a 37 m length of the fibre, pumped by a laser diode at 974 nm, an Yb fibre laser at 1070 nm and a Raman fibre laser at 1120 nm. The luminescence is shown in figure 2.3a. Pumping at 974 nm results in the broadest emission spectrum centred at 1150 nm with a FWHM bandwidth of 128 nm. For pumping at 1070 nm the emission is centred at 1160 nm with a FWHM of 81 nm and for pumping at 1120 nm the emission is centred at 1170 nm with a FWHM of 57 nm. With respect to the Raman pumped emission, we should ask whether the fluorescence was due to the residual 1070 nm pump light? This seems unlikely, as the residual 1070 nm pump light of the Raman cavity is of the same order of magnitude as the fluorescence, a feature not seen with direct
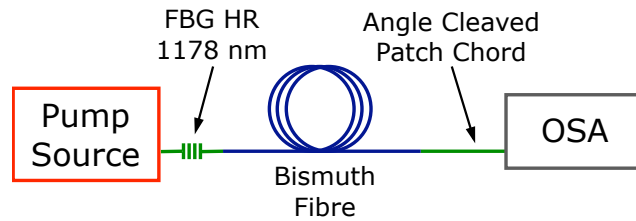
Figure 2.4: Experimental set-up used for gain measurements. Measurements made on a optical spectrum analyser (OSA).

pumping at 1070 nm. Hence, it would appear that pumping at any wavelength where there is significant absorption will lead to fluorescence, though this may be extremely weak. The mechanism for this is not clear, partly because we do not understand what gives rise to the luminescence in the Bi doped fibre.

To try to understand the emission spectrum and assess the potential use of this fibre as a laser gain medium, the absorption spectrum was measured above 1050 nm using a variety of sources. A picosecond based supercontinuum source was used to measure the spectral absorption up to 1600 nm. Unfortunately, due to pulse to pulse variations in the continuum, this proved rather unreliable in the short (50 cm) length of Bi for low attenuation values, i.e. above 1450 nm. The results were combined with a series of traditional cutback measurements made using an Yb fibre laser and various tunable diode lasers (Santec TSL-210), and are shown in figure 2.3b. Each of the methods can be seen to be in good agreement. We can see that the absorption steadily declines, bar a peak at 1380 nm which is due to OH^- induced loss. The absorption loss at 1060 nm is 650 dB/km while at 1160 nm it is still 230 dB/km. This high residual loss is clearly going to be detrimental to lasing.

Gain

In order to discover the gain available, a simple experiment was constructed as shown in figure 2.4. A FBG with a reflectivity greater than 99.9 % (HR) was spliced to the input side of the Bi fibre, while an angle-cleaved patch cord was spliced to the output side. The fibre was pumped by all three sources. Splice losses were < 0.1 dB and the output spectrum was measured on a high resolution optical spectrum analsyer (OSA) (Advantest Q8384). It was expected that spontaneous emission would lead to light being emitted in all directions, some of which would be guided in the forward and backward directions of the fibre. The forward travelling light may be amplified further and leads to the amplified spontaneous emission (ASE) spectrum as shown in figure 2.3a. A similar spectrum evolves for the backward propagating light, some of which is reflected by the FBG HR in the forwards

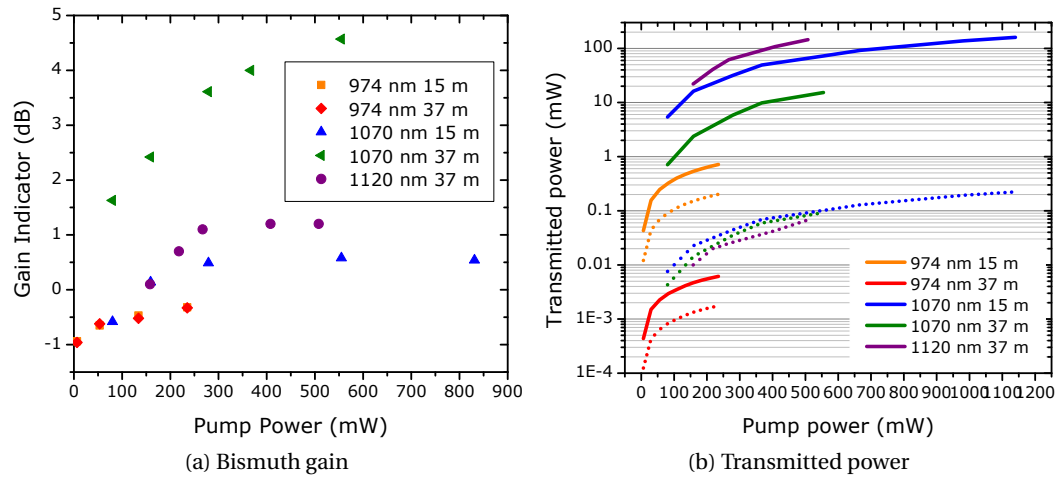(a) Bismuth gain

(b) Transmitted power

Figure 2.5: 2.5a shows the indicative gain for two lengths of the Bi doped fibre pumped at three different wavelengths. 2.5b shows the transmitted power through the Bi fibre including the residual pump (solid lines) and emission (dotted lines).

direction. Thus without any additional gain we would expect a peak which is 3 dB higher than the surrounding ASE spectrum. With the effects of gain we can expect the peak to be amplified further above the surrounding ASE spectrum. Thus the magnitude of this peak gives an excellent indication of the gain available at that wavelength in the given length of fibre.

The inferred gain measurements are shown in figure 2.5a; pumping at 1070 nm was found to produce the highest gain ~4.5 dB. In general, while there is relatively strong absorption of the pump, the fluorescence is rather weak with much of the pump energy disappearing as unsaturable loss. Indeed, the majority of the emission spectrum is made up of residual pump light. It is also evident that the gain saturates out at fairly low pump powers. In the case of pumping at 974 nm, extremely weak fluorescence is recorded while the reflected signal is below the 3 dB level expected. This suggests that the available gain is dominated by a loss process, possibly by excited state absorption. For both 974 nm and 1070 nm pumping, cutting back the fibre results in less absorption and lower residual loss, resulting in a higher transmitted power (see figure 2.5b) but reduced gain for 1070 nm pumping and no improvement for 974 nm pumping. The results also establish that it is possible to achieve gain from the fibre when pumping at 1120 nm. It is clear that 1070 nm pumping is the best option from the sources available, although shifting to a slightly longer wavelength where the residual losses are potentially lower may lead to a further gain in efficiency. The most important thing to note is that the vast majority of the pump power is absorbed and appears to be lost to unsaturable non-radiative transitions.

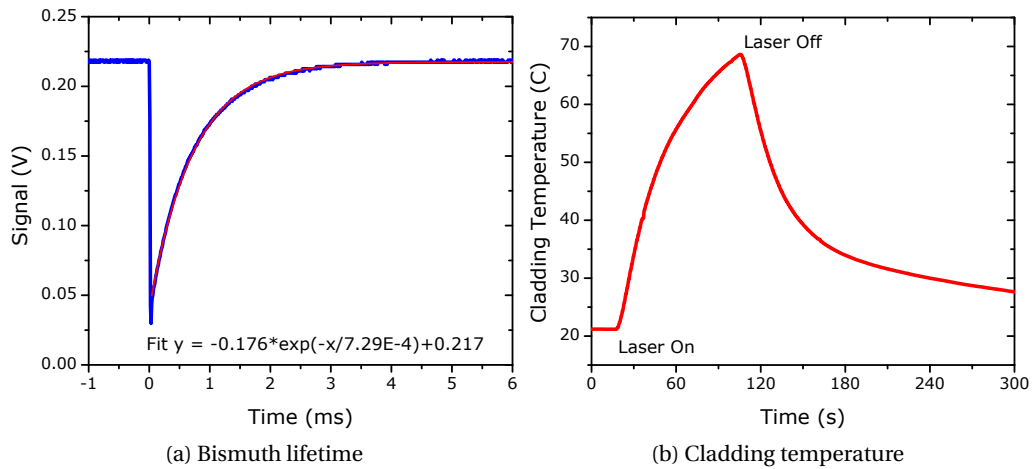Dual wavelength pumping was also investigated with the use of a WDM to couple pump

(a) Bismuth lifetime   (b) Cladding temperature

Figure 2.6: 2.6a shows the decay lifetime of the emission spectrum including an exponen-
tial fit. 2.6b shows the evolution of the cladding temperature when pumping with 54 W
at 1.07 μm for 90 seconds.

light at 974 nm and 1070 nm into the Bi doped fibre. This did not offer any improvement
over pumping with 1070 nm light alone.

It is therefore evident that the available gain in the Bi doped fibre is extremely low
compared to established fibre gain media such as Yb, Er and Tm, where the gain is orders
of magnitude greater. It is also clear, for this particular Bi fibre at least, that pumping
at 1070 nm combined with optimisation of the fibre length presents the best option for
building a fibre laser. The potential to pump with a high power single mode CW fibre laser
at 1.07 μm should enable the production of a source with reasonable output power in the
spectral region around 1178 nm.

Lifetime and temperature dependance

The upper-state lifetime was measured by modulating the 974 nm laser diode via a TTL
signal sent to the power supply. The 974 nm pump light was launched into the Bi fibre via a
fibre coupler which coupled the backwards travelling optical signal into a photodiode with
a 10 ns response time. Due to the weak optical signal the photodiode signal was amplified
with a suitable current amplifier before being captured on an oscilloscope. An example of
the measured signal is shown in figure 2.6a, along with the corresponding exponential fit.
The fit is in excellent agreement suggesting that the emission is from a single transition.
The lifetime, τ, is 730 μs which is similar to values measured elsewhere [20, 22]. From
the Fuchtbauer-Ladenburg equation it is possible to estimate the stimulated emission
cross section (σ_e) by assuming a Gaussian shaped emission band [27]. The Fuchtbauer-

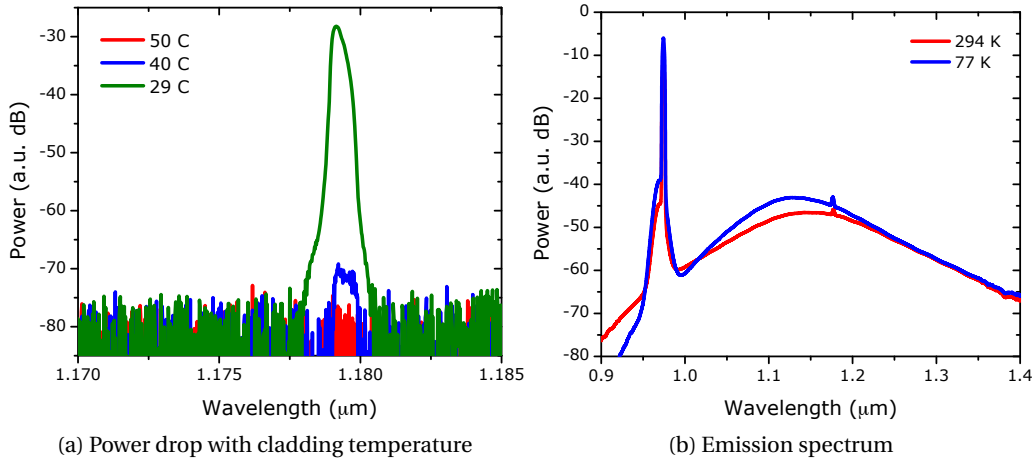(a) Power drop with cladding temperature

(b) Emission spectrum

Figure 2.7: 2.7a shows the drop in output power from a simple laser cavity at 1.178 μm as the measured cladding temperature increases. 2.7b shows the emission spectrum from 22 m of Bi fibre at room temperature and when cooled with liquid N_2 under 974 nm pumping.

Ladenburg equation is:

$$\sigma_e = \frac{\lambda_0^4}{4\pi n^2 c\tau} \left(\frac{\ln 2}{\pi}\right)^{\frac{1}{2}} \frac{1}{\Delta\lambda} \tag{2.1}$$

where λ_0, n, τ and $\Delta\lambda$ denote the peak wavelength, refractive index of the host material, emission lifetime and FWHM of the emission respectively. Thus we find that $\sigma_e = 1.8$ x 10^{-20} cm^2. The threshold for laser operation is proportional to the inverse of the product of the stimulated emission cross section and the lifetime. In this case $\sigma\tau = 1.3$ x 10^{-23} cm^{2}s, which is almost ten times higher than that of Ti:Al$_2$O$_3$ ($\sigma\tau = 1.4$ x 10^{-24} cm^{2}s).

Of course, these lifetime measurements were made under 974 nm pumping and the lifetime may change when pumping at different wavelengths if the lasing mechanism is not the same.

From the results discussed to date it is clear that a large amount of pump power is not being re-emitted as light. In order to investigate where this energy was going, a 50 W CW Yb fibre laser was used to pump the Bi fibre. It quickly became clear that with high power pumping the performance was much worse than expected. The fibre was warm to the touch and measurements of the cladding temperature, using a thermocouple, showed that the cladding temperature rapidly rose as shown in figure 2.6b. The non-radiative transitions that give rise to the high residual loss clearly convert much of the energy to heat in the core of the fibre. Given the cladding temperature, the core is presumably much hotter. Measurements of the emitted power from a basic laser cavity based around two FBGs at 1.178 μm showed that as the cladding temperature increased the power quickly
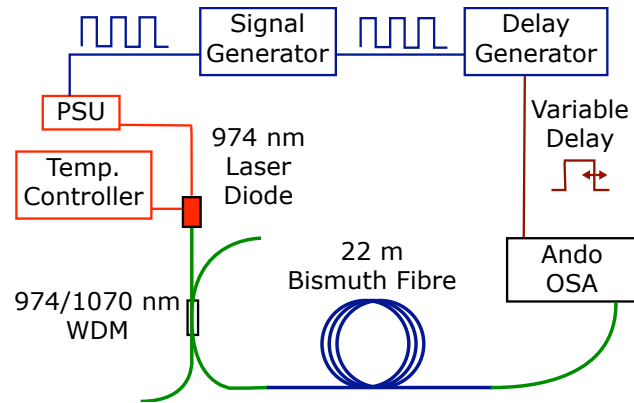
Figure 2.8: Experimental set-up used for wavelength based lifetime measurements, captured on an optical spectrum analyser (OSA).

fell off due to a drop in the available gain. This effect is clearly shown in figure 2.7a. It was found that by placing the fibre in a temperature controlled water bath, the cladding temperature can be clamped, maintaining the gain in the Bi doped fibre. As the fibre heats up, it would appear that whatever transitions are responsible for emission become less probable, resulting in a strong operational temperature dependance for the fibre.

The question that immediately arises is what happens if we cool the Bi doped fibre further. In order to do this the fibre was placed in an insulated container which was filled with liquid N_2. The emission spectrum for the fibre under 974 nm pumping in and out of the liquid N_2 is shown in figure 2.7b. From this we see that more power is transmitted through the fibre when held at 77 K while the strength of the spontaneous emission spectrum appears to have increased along with a minor change in shape.

Repeating the upper state lifetime measurements made earlier with the liquid N_2 cooled Bi fibre resulted in a shorter upper state lifetime of 680 μs, as shown in figure 2.9a. This is contrary to measurements made by Dvoyrin *et al.* [20, 28]. In order to attempt to understand this difference a more complicated set-up capable of measuring the lifetime with wavelength was used, as shown in figure 2.8. In this set-up the same signal generator was used to modulate the power supply of the laser diode to generate 150 μs pulses. However, instead of the secondary output of the signal generator being used to trigger a photodiode, it was used to trigger a delay generator which created a square wave with a given delay from the trigger signal. This signal was then used to repeatedly trigger an OSA (Ando AQ6317) so that a spectral trace could be captured at a set delay over an arbitrary spectral range. This process was then repeated 11 times for 11 different delays. By calculating the power at every wavelength for each of the delays and then fitting an exponential to the power decay at every wavelength, it is possible to derive a wavelength dependent lifetime measurement as shown in figure 2.9b. Due to the weak signal and

short integration times the data exhibited short scale fluctuations which are shown in figure 2.9b. A 50 point Savitzky-Golay smoothing method was also applied to the data to aid clarity and enable measurements of the lifetime differences [29].

(a) Bi lifetime cooled
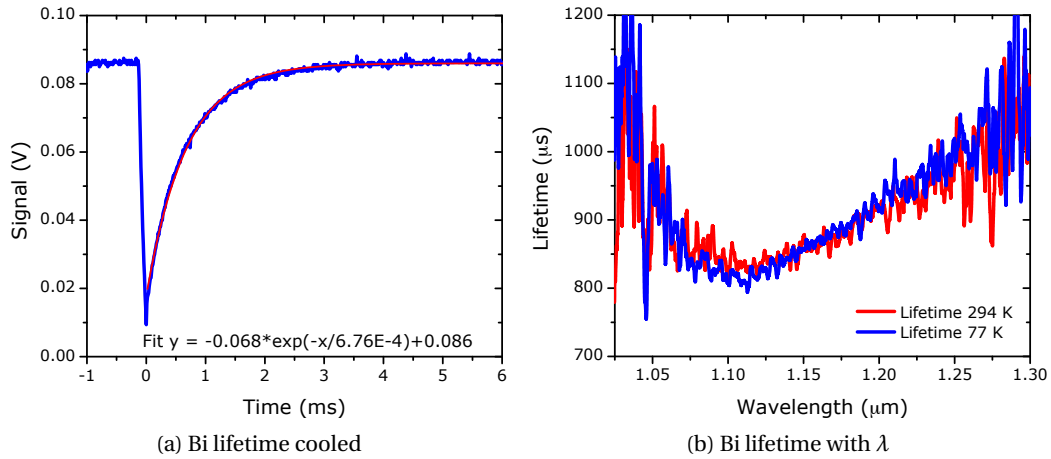
(b) Bi lifetime with λ

Figure 2.9: 2.9a shows the decay lifetime of the emission spectrum including an exponential fit when the Bi fibre is held at 77 K. 2.9b shows the upper state lifetime with wavelength (averaged over 11 measurements) for the Bi doped fibre under 974 nm pumping at room temperature and in liquid N_2.

There are several things to be noted about figure 2.9b. Firstly, the lifetimes are ∼130 μs longer than those measured by the simpler method. It is difficult to explain where this discrepancy may arise, however measurements of an Yb doped fibre confirmed its upper state lifetime using the simpler method. Unfortunately, the same measurement was not made with second set-up, therefore we do not know if the error arises from this set-up or from the Bi fibre in some way. Possible sources for the discrepancy may be: the complicated timing set-up, stimulated emission from the Bi fibre shortening the lifetime or unsaturable losses in the Bi fibre effecting the fluorescence lifetime. A better method, albeit much harder measurement, would be to measure the emission radiating from the cladding as any effect due to stimulated emission and the unsaturable losses could be removed from the measurement. Hence the lifetime numbers are best considered indicative rather than absolute.

The cooled Bi does still have a shorter lifetime, at the emission peak, than at room temperature as previously found. The difference is much smaller, 20 μs versus 50 μs, measured after smoothing the data. Arguably, the wavelength dependent lifetime is the same given the measurement noise for the two temperatures. With such a broad emission spectrum it also becomes clear that the spectral response curve of the photodiode may potentially influence the lifetime measurements. It is not possible to draw any meaningful

conclusions at the extremities of the measurement due to the significant noise present. For the central wavelength region it is clear, that the lifetime varies with wavelength and is shortest at luminescence peak.

So the key remaining question is what happens to the gain as the Bi fibre is cooled in liquid N_2? An indicative measurement of the gain was again made as before in 22 m of the Bi doped fibre. The results for the fibre at room temperature and when submerged in liquid N_2 are shown in figure 2.10. There is a significant improvement in the gain, by ~3 dB when cooled in liquid N_2. It is likely that this improvement can be explained via a reduction in the unsaturable losses when cooled to such extremely low temperatures.

The improvement in gain when cooled would naturally imply that the upper state lifetime increases as the Bi is cooled. This casts further doubt over the previous measured change of lifetime when cooled.
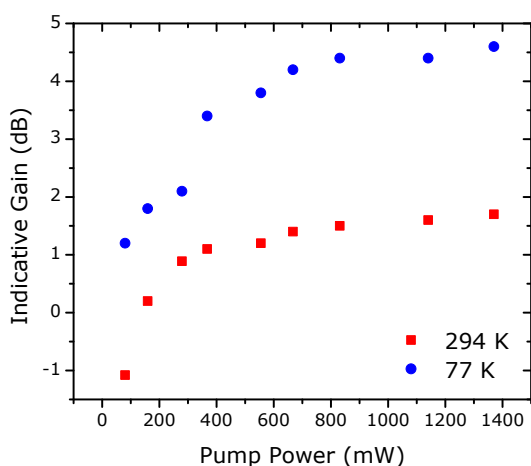

Figure 2.10: Gain measured for 22 m of Bi doped fibre under 1.07 μm pumping at 77 K and 294 K.

2.3.2 Bi based lasers

In this section we will look at the results from some laser cavities based upon the Bi doped fibre. All of the cavities were pumped at 1.07 μm as previous experiments had shown that this wavelength provides the highest available gain. The CW fibre laser cavities were straightforward, consisting of two FBGs and a length of Bi doped fibre as illustrated in figure 2.11. Due to the strong temperature dependance, the Bi fibre was either submersed in a water bath held at 294 K by a heat exchanger (Neslab RTE-210) or submersed in liquid N_2. Two pump lasers were used, a 55 W Yb CW fibre laser from IPG Photonics, and a home made Yb ASE source producing just over 1 W of pump power.
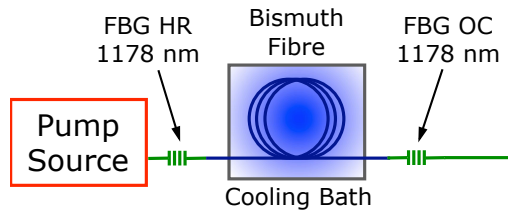
Figure 2.11: Schematic of the Bi doped fibre laser.

Output Coupler Reflectivity (%)	Slope Efficiency (%)	Grating Bandwidth (nm)	Laser Bandwidth (nm)	
			11 W Pump	56 W Pump
5	5.1	0.84	0.16	0.68
20	9.6	0.16 D	0.012	0.16 D
50	8.3	0.10	0.02	0.13
80	8.6	0.08	0.076 D	0.23 D
90	8.7	0.06	0.012	0.22 D

Table 2.1: Gives the slope efficiency, grating bandwidth and bandwidth of the laser at two pump powers for the output couplers used. Bandwidths quoted are measured at FWHM (3 dB) level. A double peaked spectrum is denoted by a 'D'.

High power pumping

The full 37 m length of Bi doped fibre was incorporated into a fibre laser cavity with a FBG HR with a reflectivity of 99 %, and a FWHM bandwidth of 0.84 nm and a variety of FBG based output couplers (OC) with much narrower bandwidths typically around ~0.1 nm (see table 2.1). As previously discussed, it was necessary to place the fibre in a water bath in order to control the temperature of the core and maintain lasing. The laser performance for different output coupler reflectivities is illustrated in figure 2.12, showing both the output power and residual pump power at 1.07 μm. The best performance was achieved using an output coupler with a reflectivity of 20 %, generating 5 W of power at 1178 nm with 1.2 W of residual pump power. The pump power was 56 W, thus over 48 W (87 %) of the pump light is converted to heat or other non-optical radiative events. This makes it obvious why the fibre heats up so quickly.

The slope efficiency for the cavity with the 20 % output coupler is 9.6 %. This is rather low for a fibre laser but can be understood by the poor gain and high unsaturable losses. Nevertheless, we would typically expect the output power to rise until the optimal output coupling is reached, at which point the output power should peak before reducing as the reflectivity is increased further. From figure 2.12a it is evident that the output power for the 50-90 % output couplers is broadly similar along with their slope efficiencies. This can be understood by considering figure 2.13 and table 2.1. From figure 2.13 it can be
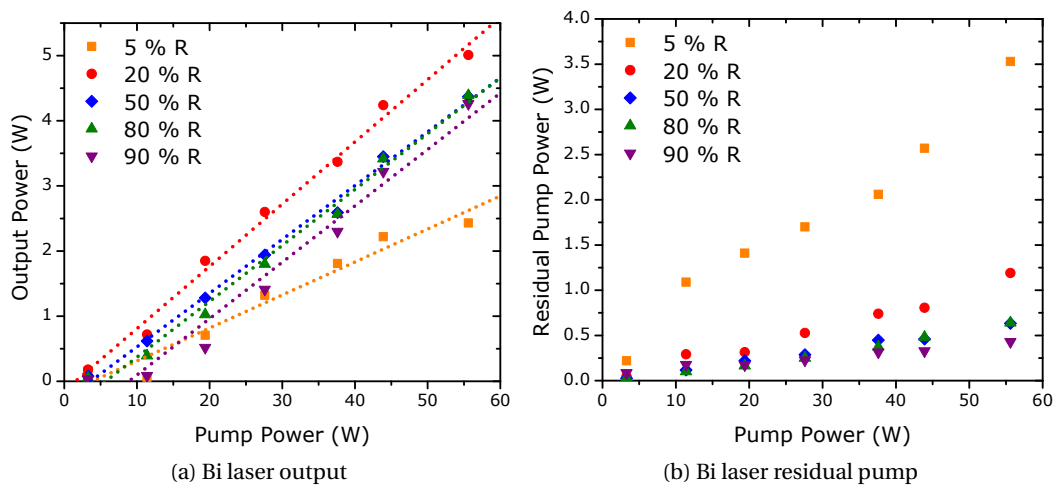
(a) Bi laser output
(b) Bi laser residual pump

Figure 2.12: 2.12a shows the output power at 1178 nm from 47 m of Bi doped fibre with pump power for various output couplers. Dotted lines are linear fits to the data points. 2.12b shows the residual pump power at 1.07 μm from the laser cavity for the various cavity configurations.

seen that the power rolls over with reflectivity as expected at low pump powers but not at higher pump powers. If we consider the cases of pumping at 11 W and 56 W, we see from table 2.1 that the laser stays within the bandwidth of the gratings at 11 W but exceeds the bandwidth of the output coupler gratings at 56 W. This broadening is partially supported by the broad high reflector and results in the cavity seeing a lower average reflectivity. It is therefore likely that the output power is being limited by the output coupler grating bandwidth in addition to the poor gain and unsaturable losses.
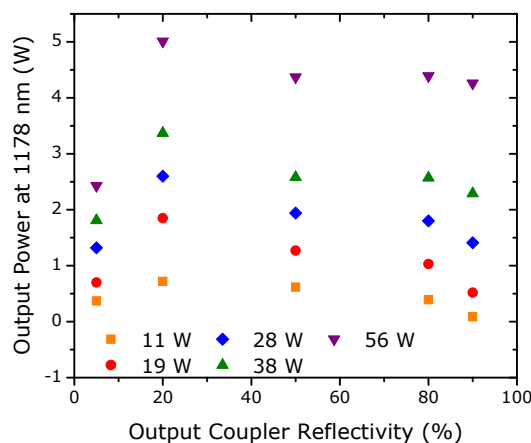

Figure 2.13: Output power with output coupler reflectivity for a variety of pump powers.

Liquid N$_2$ cooling

In section 2.3.1, we showed that the gain from the Bi doped fibre was significantly enhanced by cooling the fibre in liquid N$_2$. Here we will examine the operation of a laser cavity at room temperature and when submersed in liquid N$_2$. The cavity setup is the same as that denoted by figure 2.11, except that the cooling bath is replaced by an insulated box which could be filled with liquid N$_2$ to cool the fibre to 77 K. Further changes are brought about by the use of 22 m of Bi doped fibre combined new FBGs with a much broader bandwidth (> 1 nm). The pump source was an Yb CW fibre laser.

Output Coupler Reflectivity (%)	Grating Bandwidth (nm)	Slope Efficiency (%)		Laser Bandwidth (nm)	
		294 K	77 K	294 K	77 K
27	1.29	3.6	23.0	0.43	0.11
37	1.37	6.6	23.8	0.50	0.20
52	1.21	4.9	16.3	0.44	0.21
82	1.05	1.1	-	0.47	-

Table 2.2: Gives the slope efficiency, grating bandwidth and bandwidth of the laser at 294 K and 77 K for the output couplers used at full pump power. Bandwidths quoted are measured at the 10 dB level.

The broader gratings prevented the extracted power from being bandwidth limited. As a result the expected rollover in output power with output coupler reflectivity can be seen through the varying slope efficiencies in figure 2.14a. When cooled to 77 K the maximum output power increases from 66 mW to 241 mW, as the slope efficiency improves from 6.6 % to 23.8 %. This represents a substantial improvement in performance. The residual pump powers (shown in figure 2.14) suggest that more of the pump light is absorbed when the fibre is cooled to 77 K. For the cavities built around the 37 % output coupler, 88 % of the pump light is absorbed at 294 K whereas 92 % is absorbed at 77 K. It is highly unlikely that a 4 % improvement in pump absorption accounts for a 3.6 fold increase in slope efficiency. Some explanation may be offered by examining the linewidth of the laser emission given in table 2.2. We see that when cooled, not only does the laser produce more power, but it also does so in a narrower line. Figure 2.15 shows typical spectra from the laser when warm and cold. The room temperature spectrum consists of a series of discrete lines as if the cavity is lasing at each of these separate wavelengths independently. While there are signatures of similar discrete lines when cooled to 77 K, the spectrum is much more homogenised. This combined with a reduction of the unsaturable losses may be the main reason for the dramatic improvement in efficiency as the fibre is cooled.

It should be noted that there are distinct similarities in behaviour between this Bi doped fibre laser and those of colour centre based lasers. Both exhibit very broad fluorescence,
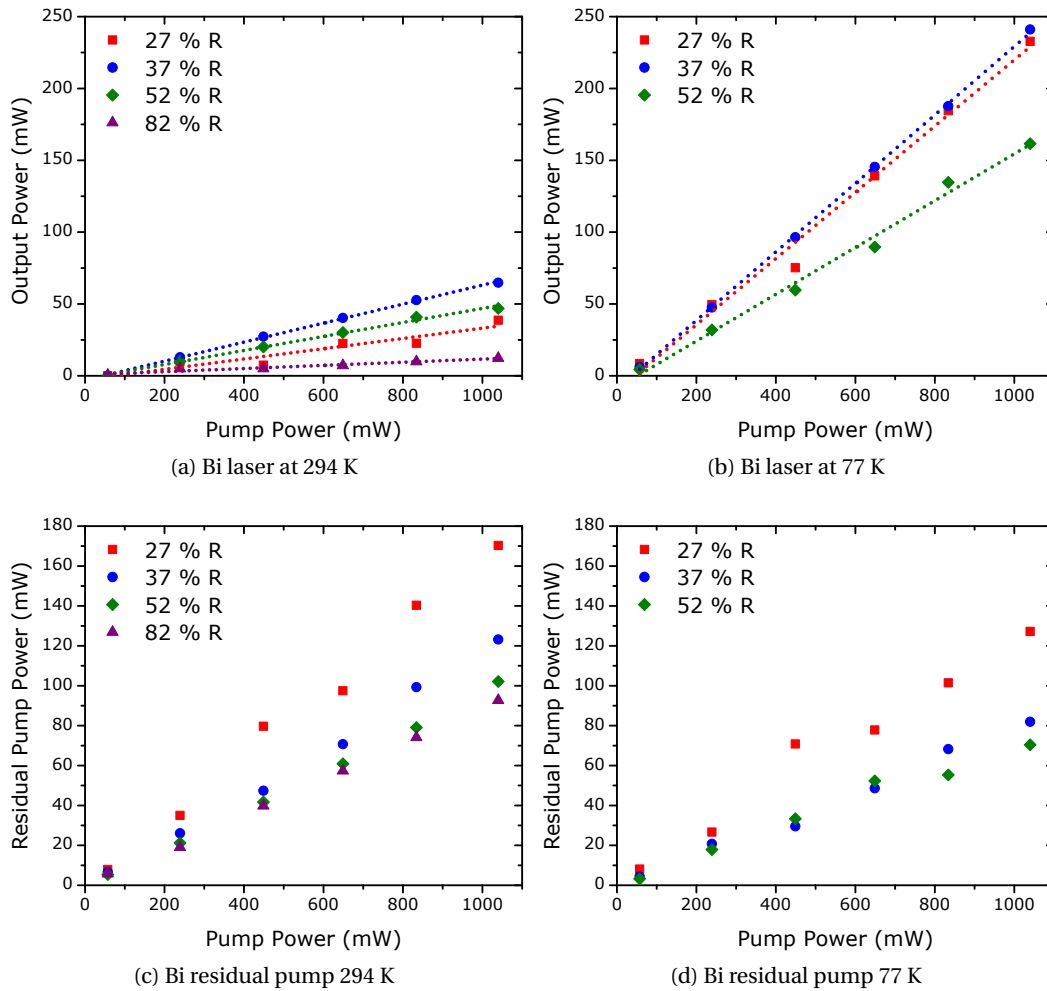
Figure 2.14: 2.14a and 2.14b show the output power at 1178 nm from the same laser cavity using 22 m of Bi doped fibre at 294 K and 77 K. 2.14c and 2.14d shows the residual pump powers for the cavities at 294 K and 77 K.

strong absorption across an extremely large spectral region (including the visible), and a steep fall off in performance as the gain medium gets hotter, resulting in best operation at liquid N_2 based temperatures. Unfortunately, it is currently impossible to state that a mechanism similar to that responsible for the gain in colour centre lasers may be at play in Bi doped silica fibre, although recent results suggest that point defects in the structure could be a suitable candidate [30].
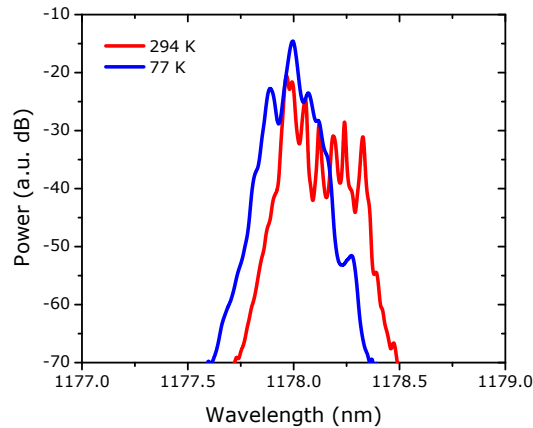
Figure 2.15: Spectrums from the Bi laser based upon the 27.9 % output coupler with 1.04 W of pump power at 294 K and 77 K.

Ring cavities and single frequency operation

Several ring cavities were constructed in order to achieve mode-locked or single frequency operation at 1178 nm. These are shown schematically in figure 2.16. Due to the low gain available, the full 37 m of Bi fibre was used in the cavity in an attempt to compensate for the insertion loss of the isolator amongst other components. The WDM used to couple light in and out, coupled 95 % of the pump light at 1.07 μm into the fibre whilst circulating 97.5 % of the light at 1.18 μm. Thus only 2.5 % of the emission was coupled out. The isolator was designed for 1.06 μm operation and had an insertion loss of 1.5 dB at this wavelength.

An attempt to achieve mode-locked operation via the nonlinear polarisation evolution effect [31] was carried out by adding an air gap with a Polar Cor polariser, designed for operation at 1.3 μm, after the isolator in figure 2.16a. The air gap had a 2.1 dB insertion loss, which combined with the isolator led to a round trip loss of > 3.6 dB. Adjusting the polarisation controllers and monitoring the signal on a fast oscilloscope with a photodiode (which had a response time of several nanoseconds) showed clear signs of pulsing, but mode-locked operation could not be achieved. It is likely that the cavity loss and long length of Bi fibre with its high loss prevented mode-locking.

Attempting to operate the laser in a single frequency regime using the basic ring cavity shown in figure 2.16a resulted in a series of distinct laser lines, as shown in figure 2.17a, which could be controlled by adjusting the polarisation controllers. The spectrum is dominated by the inhomogeneous nature of the bismuth doped gain medium and the fact that differing bismuth doped environments contribute to the overall gain spectrum over the long fibre gain length. It is also possible that birefringence could contribute to the modulation of this spectrum, which is affected by the polarization controllers. It would be

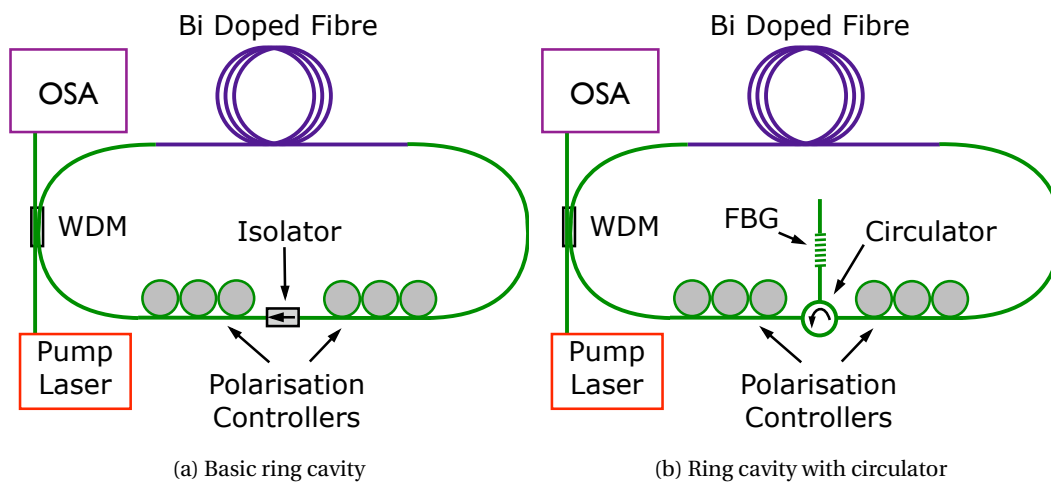(a) Basic ring cavity   (b) Ring cavity with circulator

Figure 2.16: 2.16a shows the schematic for the basic ring cavity used. For mode-locked operation an air gap with a polariser was added after the isolator. 2.16b shows a variation of 2.16a using a circulator and narrow FBG to try and encourage single frequency operation.

expected, however, that the birefringent contribution would be strongly periodic and the observed modulation deviates significantly from a single harmonic component. This may be due to spectral pulling of the lasing components by the gain inhomogeneity. Typically this would be investigated with pump power but this was not possible with the low powers available but could be undertaken with an improved setup. It was not possible to produce a source with a single line without an additional filter. This was achieved by adding a circulator to the cavity with a 0.23 nm wide FBG with a reflectivity of 99.9 %. By controlling the polarisation state and keeping the power levels low (2.7 W of pump light at 1.07 μm), it was possible to obtain a single laser line which had a spectral width of 0.009 nm. As the spectral resolution of the OSA was 0.01 nm, the actual spectral width of the laser can be described as ≤0.01 nm. Regrettably, as the WDM was not designed for operation around 1.18 μm, only 10.3 mW was coupled out which consisted of 10.1 mW of residual pump light at 1.07 μm. The use of additional filters to remove the residual pump typically left ~100 μW of light at 1177 nm.

In order to try to establish the linewidth of the laser, two methods were used. The first made use of a tunable Fabry-Pérot interferometer. After the beam was collimated and launched into the interferometer, the signal was simply too weak to detect on the photodiode. The second measurement made use of a home-made self-hetrodyne setup [32, 33], measured on an RF spectrum analyser via a photodiode. Yet again the signal was too weak to enable a reliable measurement. The use of components designed for 1.18 μm would allow significant optimisation of the source and should result in significantly more
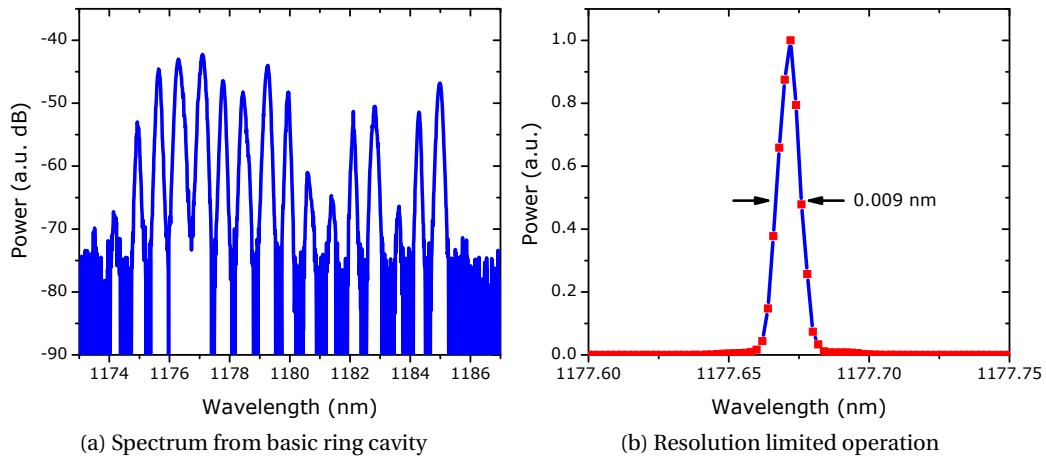
(a) Spectrum from basic ring cavity

(b) Resolution limited operation

Figure 2.17: 2.17a shows the spectral features typical of the basic ring cavity shown in 2.16a. 2.16b shows a single laser line achieved by adding a circulator and narrow FBG to the ring cavity as shown in figure 2.16b. The optical spectrum analyser has a resolution limit of 0.01 nm.

power with much less residual pump. Hence we anticipate that this would allow accurate linewidth measurements.

2.4 Progress since this work

The research work described in this chapter was largely carried out in the period between late 2007 and early 2008. During 2008 the number of researchers studying the emission of Bi doped fibre and glasses increased significantly with a corresponding increase in the number of journal publications. Some of these results have already been mentioned but many of the other results were not immediately relevant and therefore not discussed. Thus in the interests of completeness we will briefly touch on many of these results now.

Since 2005, between four and five journal papers have been published each year in mainstream journals on the subject of Bi doped glasses. In 2008, 12 papers were published, which may indicate the beginning of a wider push by the optics community to establish the potential usefulness of Bi doped glasses. As we discussed in the last section, the lasing mechanism is far from clear, and at present unsaturable losses, low gain and poor efficiency all hinder Bi based lasers. The research work can be broadly divided into two areas: studies of the luminescence of Bi doped glasses, and laser operation of Bi doped fibres. We will examine each in turn.

2.4.1 Bi doped glass studies

Several more studies of Bi based glasses have been made. One of the first and most interesting in 2008 was published by Truong *et al.* who produced fibres from Bi doped SiAlGeP and SiGeP preforms. They noted that the Al free preform showed signs of luminescence around 1.3 μm which disappeared when drawn into a fibre. This conflicted with the previous view that Al co-doping was necessary for luminescence. Further studies involving hydrogen loading and annealing of the fibres showed that it was possible to eliminate the luminescence completely. They concluded that the bismuth must be reduced to a lower valence state and that this should explain the quenching [34].

Several authors looked at co-doping with various other materials, for instance Qian *et al.* showed that co-doping Bi-doped germania based glasses with CeO_2, As_2O_5, or Y_2O_3 could enhance the luminescence intensity by a factor of 4, 12, or 23 respectively. The authors suggested that this perhaps favoured the idea that emission was from higher valence Bi ions. They also measured much shorter lifetimes of $\sim$ 270 μs [35]. Pursuing a similar line, Hughes *et al.* co-doped with PbO. They found that this decreased the strength of absorption, suggesting that less of the Bi was optically active. Whilst the 500, 700 and 1000 nm absorption bands behaved in a broadly similar way with PbO concentration, they found that the 800 nm band did not, leading them to suggest that it was due to a separate centre. Finally, they discovered that the addition of 3-4 % PbO resulted in a 50 % increase in lifetime and a 20 fold improvement in the quantum efficiency [36].

The theme of looking at alternative glass hosts was continued by Ren *et al.* who studied Bi doped lime silicate glasses. They found luminescence bands at 400, 650 and 1300 nm and suggested that they were due to Bi^{3+}, Bi^{2+} and Bi^{+} ions respectively. They also found that the intensity of the emission fell off with increments in the CaO content [37]. They measured the lifetime of their Bi doped glass as $\sim$ 400 μs.

In an insightful paper, Qiu *et al.* demonstrated that Al free fibres could be made to demonstrate luminescence. They manufactured Bi doped silica fibres with and without Al co-doping via MCVD. In the case of Al free Bi doped fibre, strong emission was seen at 1300 nm, whereas Al co-doping led to emissions at 750 and 1100 nm, which they attributed to different centres. They also noted strong up-conversion luminescence in both fibres [38].

Perhaps the most interesting study on Bi luminescence in the last year was performed by Sharonov *et al.*. They studied the optical centres formed in Bi-, Pb-, Sn-, Te-, and In-doped germanate glasses. They showed that glasses doped with 6p (Bi, Pb) and 5p (Sn, Sb) ions exhibit very similar behaviour, characterised by distinct peaks on an excitation-emission plot. The lifetime of the NIR emission was $\sim$ 400 μs. Thus the authors showed that the luminescence is not unique to Bi, and suggested that the emission was due to point defects in the glasses caused by the dopants during heat treatment of the glass as

a possible candidate for the optical centres. They also stated that the "*p* orbitals of the dopants should not be considered as a major part of the energy level model," and the "four bands observed in the absorption and excitation spectra are most likely to be assigned to different centres." [30]

2.4.2 Bi doped fibre lasers

In the first of two papers Bufetov *et al.* manufactured Bi doped fibres using surface-plasma chemical vapour deposition (SPCVD) technology as an alternative to the more established MCVD process. During the SPCVD process the halides' conversion occurs at reduced temperature and pressure in the microwave induced plasma. This allows for finer control of the manufacturing process and allows the synthesis of glasses under reducing conditions by the means of oxygen deficiency. The resulting 20 m length of Bi:Al$_2$O$_3$:SiO$_2$ fibre demonstrated optical gains as high as 10 dB at 1130 nm under 1058 nm pumping. The gain was wavelength-dependent with the much higher gain values ascribed to an increase in the Bi doping. A CW laser cavity built around this fibre had an efficiency of 8 % producing ~1.1 W for 14 W of pump light [39].

In their second paper they demonstrated gain and lasing from a Al free Bi doped phosphogermanosilicate fibre. The absorption bands were located at 450, 800 and 950 nm, with a complex band in the 1100-1500 nm region. They pumped at 1230 nm and achieved gain from 1310 through to 1470 nm, making the fibre particularly applicable for telecommunications. However, the slope efficiencies of the laser cavities were poor, with the best being 3.4 % for emission at 1470 nm [40].

Very similar results to those presented in section 2.3.2 were published by Dvoyrin *et al.* in September. They manufactured a Bi doped fibre with Al$_2$O$_3$ using the MCVD method. Bi doping was less that 0.02 at.%. The standard absorption bands were recorded along with the fluorescence spectrum at 77, 300, 465 and 600 K, showing a marked improvement as the fibre was cooled. A CW laser was formed in 64 m of the fibre and pumped at 1064, 1075 and 1090 nm with slope efficiencies of 10, 21 and 28 % at room temperature and 27, 52 and 50 % at 77 K. Thus they demonstrated significant improvements by pumping at longer wavelengths and when cooling the fibre to 77 K. The best cavity produced 8.4 W at 1160 nm for 20 W of pump at 1090 nm. The linewidth of the emission was noted to increase linearly with pump power. Finally, they discussed that the main limiting factor of Bi doped fibre lasers was the unsaturable loss. They suggested that the fluorescence band consists of two bands belonging to two different energy terms of the active centre to explain the behaviour witnessed [28].

Further progress was made by Kivistö *et al.* on modelocked Bi doped fibre lasers. They used a 12 m length of Bi doped fibre manufactured by SPCVD in a linear cavity

configuration. A GaInNAs SESAM was used in combination with a pair of transmission gratings, to provide dispersion compensation, allowing them to operate in the soliton modelocked regime. Their laser generated 0.9 ps pulses with a repetition rate of 7.5 MHz and was wavelength tunable between 1153-1170 nm. The average pulse energy was ~0.2 nJ [41].

Published at the very end of 2008, Kalita *et al.* demonstrated their first Bi doped Ge:Al:SiO$_2$ fibre. Adding to the number of demonstrations of varying CW cavity performance based upon temperature of the fibre, they showed ~1.5 W and ~2.0 W of output power at 22 °C and 10 °C (in ice water) for ~14 W of pump power. The slope efficiencies were 10 % and 15 % respectively in the 25 m length of fibre. They pumped the fibre at 1080 and 1090 nm, finding a slight improvement in efficiency for the 1090 nm pumping. They also showed that the fibre had significant unsaturable losses and that excited state absorption was a significant problem for all wavelengths when pumping at 800 nm but not a problem above 1000 nm when pumping at 1047 nm. However, it should be noted that the authors did not consider up-conversion as a possible explanation of the results. Fluorescence lifetimes were found to vary with pump wavelength from 750 μs to 670 μs for 1090 and 915 nm pumping respectively. Finally, the authors noted that their fluorescence lifetime decays were best fitted with continuous exponential fitting rather than single exponential fitting, suggesting that the Bi ions were located at different sites [42].

2.5 Future directions

It is still very early on in the development of Bismuth as a fibre gain medium. Its broad luminescence in an important spectral region makes it of great interest to the research community. Yet the current generation of Bi doped fibres suffers from high unsaturable losses and low gain. In addition to this, none of the proposed mechanisms for the lasing action has gained acceptance within the community, signifying a general lack of consensus in understanding the dynamics of this new gain medium. Much work remains to be done to understand the mechanisms, drive up the efficiency and to construct laser sources and amplifiers from this new gain material.

We believe the focus will be two fold going forward; part of the community will concentrate on the gain mechanism and producing better fibres, as well as potentially looking at developing solid state Bi based gain media. Others will take the current state-of-the-art fibres and attempt to make higher efficiency CW lasers, amplifiers, single frequency lasers and mode-locked lasers. As a result of the current poor performance of Bi based fibres and the likelihood that improvements will be incremental, many inital demonstrations will be at very low power levels. This is not necessarily the problem that it might otherwise

be, as the potential combination of new sources (such as single frequency or mode-locked sources) with established Raman amplifiers should allow the power to be scaled to useful levels. Indeed, such power-scaling may also be demonstrated via Bi based amplifiers. The number of researchers involved in Bi doped experiments will no doubt steadily increase, unless evidence emerges that the efficiency cannot be improved further.

It is too early to predict whether Bi lasers will make a significant commercial impact, but given the wavelength region covered by Bi gain media, it is certainly possible that Bi based lasers and amplifiers could make such an impact.

2.6 Conclusions

In this chapter we have characterised a Bi doped fibre which has a broad luminescence in the region from 1.1 to 1.3 μm. We showed that the fibre gain depended upon the pump wavelength and temperature of the fibre. The temperature is important as much of the power is transferred to heat rather than light, thus when pumping with high power sources the fibre quickly warms and the gain rapidly drops. The gain itself is currently very low but can be improved by cooling the fibre in liquid N_2. Several CW laser cavities were built with the most efficient cavity having a slope efficiency of 23.8 % when cooled in liquid N_2. This cavity represented a significant step forward in efficiency for Bi doped fibre lasers. Attempts were made to operate the laser in a single frequency regime, whilst the operation was at the resolution limit of the optical spectrum analyser used, technical limitations limited a more accurate measurement of the linewidth. This initial demonstration and the suggested optimisations are a promising step towards a single frequency source.

Bismuth doped fibre is a promising new gain medium. It has the potential to provide gain in the 1.1-1.3 μm spectral region for which no convenient gain medium currently exists. Efficient operation at the 1.3 μm end of the window may enable applications in telecommunications, whereas the current peak gain region of 1180 nm could allow the development of sources which can be doubled to import wavelengths in the visible. Before any of that can happen, however, more work is required to address the low gain and unsaturable losses. The results presented in this chapter show that these issues can at least be partially addressed by cooling the fibre. Finally while the exact lasing mechanism continues to be a matter of debate amongst researchers, it is surely only a matter of time before this is resolved.

Bibliography

[1] Y. Fujimoto and M. Nakatsuka, "Infrared luminescence from bismuth-doped silica glass," Jpn. J. Appl. Phys. **40**, L279–L281 (2001).

[2] M. Yamada, M. Shimizu, T. Kanamori, Y. Ohishi, Y. Terunuma, K. Oikawa, H. Yoshinaga, K. Kikushima, Y. Miyamoto, and S. Sudo, "Low-noise and high-power Pr^{3+}-doped fluoride fiber amplifier," IEEE Phot. Tech. Lett. **7**, 869–871 (1995).

[3] T. Komukai, T. Yamamoto, T. Sugawa, and Y. Miyajima, "Upconversion pumped thulium-doped fluoride fiber amplifier and laser operating at 1.47 μm," IEEE J. Quant. Elect. **31**, 1880–1889 (1995).

[4] T. Sakamoto, M. Shimizu, M. Yamada, T. Kanamori, Y. Ohishi, Y. Terunuma, and S. Sudo, "35-dB gain Tm-doped ZBLYAN fiber amplifier operating at 1.65 μm," IEEE Phot. Tech. Lett. **8**, 349–351 (1996).

[5] S. A. E. Lewis, S. V. Chernikov, and J. R. Taylor, "Triple wavelength pumped silica-fibre Raman amplifiers with 114nm bandwidth," Elect. Lett. **35**, 1761–1762 (1999).

[6] A. S. Gouveia-Neto, A. S. L. Gomes, J. R. Taylor, B. J. Ainslie, and S. P. Craig, "Cascade Raman soliton fiber ring laser," Opt. Lett. **12**, 927–929 (1987).

[7] A. S. Gouveia-Neto, A. S. L. Gomes, and J. R. Taylor, "Soliton Raman fibre-ring oscillators," Opt. Quant. Elect. **20**, 165–174 (1988).

[8] E. Desurvire, "Optical communications in 2025," in "31st European Conference on Optical Communication," (2005), pp. 5–6 Vol.1.

[9] C. Blodi, S. Russell, J. Pulido, and J. Folk, "Direct and feeder vessel photocoagulation of retinal angiomas with dye yellow laser," Ophthalmology **97**, 791–795 (1990).

[10] R. N. S. Sadick, "The utilization of a new yellow light laser (578 nm) for the treatment of Class I Red Telangiectasia of the lower extremities," Dermatologic Surgery **28**, 21–25 (2002).

[11] C. Max, S. Olivier, H. Friedman, K. An, K. Avicola, B. Beeman, H. Bissinger, J. Brase, G. Erbert, D. Gavel, K. Kanz, M. Liu, B. Macintosh, K. Neeb, J. Patience, and K. Waltjen, "Image improvement from a sodium-layer laser guide star adaptive optics system," Science **277**, 1649–1652 (1997).

[12] Y. Fujimoto and M. Nakatsuka, "Optical amplification in bismuth-doped silica glass," App. Phys. Lett. **82**, 3325–3326 (2003).

[13] M. Peng, J. Qiu, D. Chen, X. Meng, I. Yang, X. Jiang, and C. Zhu, "Bismuth- and aluminum-codoped germanium oxide glasses for super-broadband optical amplification," Opt. Lett. **29**, 1998–2000 (2004).

[14] M. Peng, J. Qiu, D. Chen, X. Meng, and C. Zhu, "Superbroadband 1310 nm emission from bismuth and tantalum codoped germanium oxide glasses," Opt. Lett. **30**, 2433–2435 (2005).

[15] X. Meng, J. Qiu, M. Peng, D. Chen, Q. Zhao, X. Jiang, and C. Z. Zhu, "Infrared broadband emission of bismuth-doped barium-aluminum-borate glasses," Opt. Express **13**, 1635–1642 (2005).

[16] M. Peng, J. Qiu, D. Chen, X. Meng, and C. Zhu, "Broadband infrared luminescence from Li_2O-Al_2O_3-ZnO-SiO_2 glasses doped with Bi_2O_3," Opt. Express **13**, 6892–6898 (2005).

[17] X. Meng, J. Qiu, M. Peng, D. Chen, Q. Zhao, X. Jiang, and C. Zhu, "Near infrared broadband emission of bismuth-doped aluminophosphate glass," Opt. Express **13**, 1628–1634 (2005).

[18] J. Ren, L. Yang, J. Qiu, D. Chen, X. Jiang, and C. Zhu, "Effect of various alkaline-earth metal oxides on the broadband infrared luminescence from bismuth-doped silicate glasses," Solid State Communications **140**, 38–41 (2006).

[19] V. V. Dvoyrin, V. M. Mashinsky, E. M. Dianov, A. A. Umnikov, M. V. Yashkov, and A. N. Guryanov, "Absorption, fluorescence and optical amplification in MCVD bismuth-doped silica glass optical fibres bismuth-doped silica glass optical fibres," 31st European Conference on Optical Communication **4**, 949–950 (2005).

[20] V. V. Dvoyrin, V. M. Mashinsky, L. I. Bulatov, I. A. Bufetov, A. V. Shubin, M. A. Melkumov, E. F. Kustov, E. M. Dianov, A. A. Umnikov, V. F. Khopin, M. V. Yashkov, and A. N. Guryanov, "Bismuth-doped-glass optical fibers - a new active medium for lasers and amplifiers," Opt. Lett. **31**, 2966–2968 (2006).

[21] E. M. Dianov, V. V. Dvoyrin, V. M. Mashinsky, A. A. Umnikov, M. V. Yashkov, and A. N. Gur'yanov, "CW bismuth fibre laser," Quant. Elect. **35**, 1083–1084 (2005).

[22] I. Razdobreev, L. Bigot, V. Pureur, A. Favre, G. Bouwmans, and M. Douay, "Efficient all-fiber bismuth-doped laser," App. Phys. Lett. **90**, 031103 (2007).

[23] E. M. Dianov, A. V. Shubin, M. A. Melkumov, O. I. Medvedkov, and I. A. Bufetov, "High-power CW bismuth-fiber lasers," J. Opt. Soc. Am. B **24**, 1749–1755 (2007).

[24] A. B. Rulkov, A. A. Ferin, S. V. Popov, J. R. Taylor, I. Razdobreev, L. Bigot, and G. Bouwmans, "Narrow-line, 1178nm CW bismuth-doped fiber laser with 6.4W output for direct frequency doubling," Opt. Express **15**, 5473–5476 (2007).

[25] V. V. Dvoyrin, V. M. Mashinsky, and E. M. Dianov, "Yb-Bi pulsed fiber lasers," Opt. Lett. **32**, 451–453 (2007).

[26] E. M. Dianov, A. A. Krylov, V. V. Dvoyrin, V. M. Mashinsky, P. G. Kryukov, O. G. Okhotnikov, and M. Guina, "Mode-locked Bi-doped fiber laser," J. Opt. Soc. Am. B **24**, 1807–1808 (2007).

[27] W. L. Barnes, R. I. Laming, E. J. Tarbox, and P. R. Morkel, "Absorption and emission cross section of Er^{3+} doped silica fibers," IEEE J. Quant. Elect. **27**, 1004–1010 (1991).

[28] V. V. Dvoyrin, V. M. Mashinsky, and E. M. Dianov, "Efficient bismuth-doped fiber lasers," IEEE J. Quant. Elect. **44**, 834–840 (2008).

[29] A. Savitzky and M. J. E. Golay, "Smoothing and differentiation of data by simplified least squares procedures." Analytical Chemistry **36**, 1627–1639 (1964).

[30] M. Y. Sharonov, A. B. Bykov, V. Petricevic, and R. R. Alfano, "Spectroscopic study of optical centers formed in Bi-, Pb-, Sb-, Sn-, Te-, and In-doped germanate glasses," Opt. Lett. **33**, 2131–2133 (2008).

[31] M. Hofer, M. Ober, F. Haberl, and M. Fermann, "Characterization of ultrashort pulse formation in passively mode-locked fiber lasers," IEEE J. Quant. Elect. **28**, 720–728 (1992).

[32] T. Okoshi, K. Kikuchi, and A. Nakayama, "Novel method for high resolution measurement of laser output spectrum," Elect. Lett. **16**, 630–631 (1980).

[33] P. Horak and W. H. Loh, "On the delayed self-heterodyne interferometric technique for determining the linewidth of fiber lasers," Opt. Express **14**, 3923–3928 (2006).

[34] V. G. Truong, L. Bigot, A. Lerouge, M. Douay, and I. Razdobreev, "Study of thermal stability and luminescence quenching properties of bismuth-doped silicate glasses for fiber laser applications," App. Phys. Lett. **92**, 041908 (2008).

[35] Q. Qian, Q. Y. Zhang, G. F. Yang, Z. M. Yang, and Z. H. Jiang, "Enhanced broadband near-infrared emission from Bi-doped glasses by codoping with metal oxides," J. Appl. Phys. **104**, 043518 (2008).

[36] M. Hughes, T. Suzuki, and Y. Ohishi, "Advanced bismuth-doped lead-germanate glass for broadband optical gain devices," J. Opt. Soc. Am. B **25**, 1380–1386 (2008).

[37] J. Ren, J. Qiu, D. ping Chen, X. Hu, X. Jiang, and C. Zhu, "Luminescence properties of bismuth-doped lime silicate glasses," Journal of Alloys and Compounds **463**, L5–L8 (2008).

[38] Y. Qiu and Y. Shen, "Investigation on the spectral characteristics of bismuth doped silica fibers," Optical Materials **31**, 223 – 228 (2008).

[39] I. A. Bufetov, K. M. Golant, S. V. Firstov, A. V. Kholodkov, A. V. Shubin, and E. M. Dianov, "Bismuth activated alumosilicate optical fibers fabricated by surface-plasma chemical vapor deposition technology," Appl. Opt. **47**, 4940–4944 (2008).

[40] I. A. Bufetov, S. V. Firstov, V. F. Khopin, O. I. Medvedkov, A. N. Guryanov, and E. M. Dianov, "Bi-doped fiber lasers and amplifiers for a spectral region of 1300–1470 nm," Opt. Lett. **33**, 2227–2229 (2008).

[41] S. Kivisto, J. Puustinen, M. Guina, O. G. Okhotnikov, and E. M. Dianov, "Tunable modelocked bismuth-doped soliton fibre laser," Elect. Lett. **44**, 1456–1458 (2008).

[42] M. P. Kalita, S. Yoo, and J. Sahu, "Bismuth doped fiber laser and study of unsaturable loss and pump induced absorption in laser performance," Opt. Express **16**, 21032–21038 (2008).

3 Continuous Wave Supercontinuum Generation: Part 1 the Near-Infrared

3.1 Introduction

In this and the subsequent chapter we will look at ways to improve high power supercontinuum sources. As we mentioned in section 1.4 of the introduction, supercontinuum sources have developed at an astounding rate since 2000. During this period a wide variety of sources were developed and found various applications, mostly in research laboratories. The vast majority of these sources are based upon pulse pumped systems, notably femtosecond and picosecond laser sources. Continuum sources based upon nanosecond and CW pump sources have also been demonstrated. Whilst short pulse driven systems have many advantages, it is difficult to scale them to the very high average power levels required for some applications. In such instances it is best to use CW pump sources to generate the required supercontinua. As we discussed in section 1.4.2, the mechanisms involved in generating a CW based supercontinuum differs from that in the short pulse regime. This raises a variety of problems which must be understood and overcome in order to develop excellent sources. In this and the next chapter we will be concerned with describing, understanding and solving these issues.

This chapter will begin by discussing recent work on CW pumped supercontinua up to the point where this work commences. This will be followed by a brief discussion of the advantages, limitations, and disadvantages of CW pumped supercontinua, along with outlining possible solutions to some of these issues in section 3.1.2. Section 3.2 will look at a series of brief experimental results complete with a short discussion on each covering: low water loss PCF; the relative intensity noise of the sources and continua; the effect of Raman oscillations; and the effects of dispersion and nonlinearity. What emerges from this early experimental work is an understanding of the need for careful control of the dispersion properties of the PCF. In the subsequent section (3.3) we investigate ways to control the continuum evolution through an understanding of the processes involved and by extensively modelling a series of hypothetical PCFs to illustrate this.

Having theoretically demonstrated how to optimise the continuum formation process, we experimentally demonstrate this in section 3.4, highlighting some of the differences between our models and reality. In section 3.5, we demonstrate control over the long wavelength edge of the supercontinuum through the use of PCFs with two zero dispersion wavelengths. We then look at some recent results and future directions for this work before presenting some conculsions.

3.1.1 Literature review of CW pumped supercontinua

As we mentioned in chapter 1, supercontinuum generation may be considered to have started as far back as 1964 [1]. The field was re-energised in 2000 [2], and subsequently developed rapidly. As the field has matured many terms and conventions have been broadly adopted, which is extremely convenient but has perhaps led to some older papers being overlooked. For example, the term supercontinuum only really started to gain widespread acceptance post 2000, with many authors using alternative phrases including superbroadening, white light continuum, anomalous frequency broadening, femtosecond distributed soliton spectrum, and the Raman continuum to name a few [3]. This is partly explained by the fact that many papers were often focused on some other fundamental study, and therefore producing a continuum was often a side effect of explaining these fundamental processes. Another convention that become widespread since 2000 is to display continuum results on a logarithmic scale. This has its advantages for analysis but has perhaps led to some older results being ignored or overlooked, as it was common to present results on a linear scale which led to much smaller reported bandwidths. As a consequence, it seems that the first CW pumped continuum result has been passed over in the literature. It was reported by Persephonis *et al.* in 1996 [4]. Based upon a CW Raman fibre laser, a continuum extending from 1.55-1.95 μm was produced with a 20 dB spectral flatness in 2.3 km of highly nonlinear fibre (HNLF), shown in figure 3.1a. The Raman laser was pumped by a 5 W Nd:YAG and the continuum produced 100 mW of output power.

This work was followed up by Prabhu *et al.* in 2000 who used a 8.4 W CW ytterbium fibre laser to pump a Raman laser cavity which was coupled to a Brillouin cavity. The nonlinearity was enhanced by using 700 m of phosphorus doped fibre combined with 500 m of single mode fibre. The continuum was quite narrow, stretching from 1433 to 1533 nm containing 1.26 W of output power with a 30 dB spectral flatness [5]. This was followed by Popov *et al.* who demonstrated a 2.2 W continuum from 1.6-2.0 μm with a spectral flatness of 0.7 dB. At the 5 dB level the continuum stretched from 1.26-2.01 μm. Notably, the spectral power density was high (3.6 mW/nm) and the continuum extended significantly short of the pump. The continuum was generated in a 600 m length of Sumitomo HNLF using a 10 W CW pump at 1.56 μm [6]. This early work and

(a) Persephonis *et al.* 1996 result (b) A collection of results for 2003/05
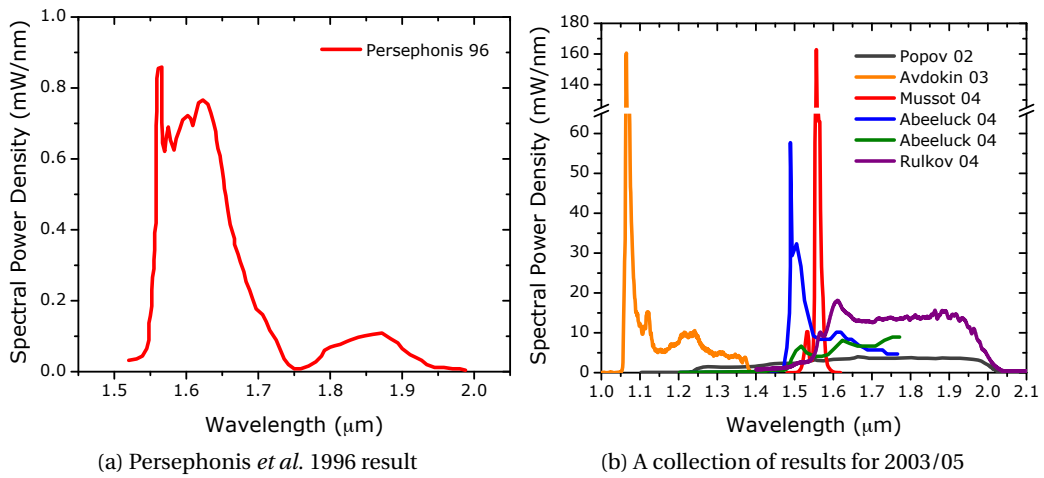
Figure 3.1: Early CW supercontinuum results which are all in conventional fibre bar
Avdokin's demonstration of the first PCF based CW result on 2003.

much of the subsequent work up to 2005 focused on generating supercontinuum sources
for potential telecommunications applications. González-Herráez *et al.* continued this
theme in 2003 by producing a supercontinuum that covered the S, C and L transmission
bands (1460-1625 nm) [7]. A 7 km long zero dispersion shifted fibre, with a zero dispersion
wavelength (ZDW) of 1453 nm was pumped by a 2.1 W Raman fibre laser at 1455 nm. At
full pump power they demonstrated complete pump depletion.

At the same time as González-Herráez's paper was published, the first CW continuum in
PCF was reported by Avdokhin *et al.* in 2003 [8]. Based upon a 15 W CW ytterbium master
oscillator power fibre amplifier (MOPFA) and 100 m of PCF, a 320 nm wide continuum
was produced with 4.1 W of output power. This result is shown in figure 3.1b along with
some of those that followed in HNLF in 2004 and 2005. Apart from the undepleted pump
the spectrum is very flat with less than 3.5 dB of variation. The spectral power density
(SPD) is in the 5-10 mW region.

A flurry of work followed in HNLF, mainly using Raman fibre lasers as the pump sources.
Prabhu *et al.* pumped essentially the same set-up as they had used before, with more
power to produce a 2 W supercontinuum spanning from 1.43 to 1.53 μm [9]. Between
2003 and 2005 Abeeluck *et al.* published several papers using HNLF in combination with
a Raman fibre laser. In their first paper, a 4.5 km fibre was pumped at 1.594 μm with 0.9
W producing a 210 mW supercontinuum between 1.43 and 1.53 μm [10]. In the second
a 4 W pump at 1.486 μm was used to pump three different HNLF with ZDW between
1.478 and 1.481 μm. The broadest continuum, from 1.5 km of NHLF, covered 544 nm
at the 20 dB level and produced 1.9 W of output power [11]. Modulation instability was
clearly visible at low pump powers. In their third paper they used the same set-up again to

make comparisons between pumping in the normal and anomalous regimes by building several Raman fibre lasers [12]. Martin-Lopez *et al.* attempted to look at the effect of pump bandwidth upon supercontinuum generation [13]. They found that there was an optimum pump bandwidth for the most efficient MI generation and that this directly translated to the broadest continuum. The experiment was carried out in dispersion shifted fibre at 1.55 μm with three different pump sources, a light emitting diode, CW laser, and CW amplified spontaneous emission (ASE) source. However, no effort was made to examine the potentially different noise signatures of each source which may well have contributed to the result.

Of all the results achieved in HNLF during this period perhaps the most impressive result in terms of SPD and spectral flatness was by Rulkov *et al.* who produced a CW continuum stretching from 1.56 μm to 2.0 μm in 300/600 m of HNLF pumped with a 10 W ytterbium/erbium laser. The spectral flatness was better than 1 dB and the SPD was 16 mW/nm [14, 15]. A very similar set-up was used by Champert *et al.* with a 5 W pump laser and 1 km of HNLF to produce a similarly broad and flat continuum with a SPD of 4.5 mW/nm [16].

Further work in PCF was reported by de Matos *et al.* They used 10 W ytterbium pump sources to pump the same fibre as used by Avodkhin *et al.* [17]. A 5.5 W supercontinuum with a SPD of 10 mW/nm was produced which extended to the water loss peak at 1.38 μm. Of particular interest in this work was the use of an ASE source to reduce the relative intensity noise from the continuum. This source was then used in an optical coherence tomography system [18].

Work to simulate CW continua was started by Nicholson, Abeeluck *et al.* in their 2003 paper where they used a super-Gaussian pulse to attempt to simulate the CW field with very limited success [10]. This was followed up by Mussot *et al.* who produced some rather narrow continua stretching from 1.52-1.60 μm and attempted to accurately model the MI and CW continua. They used the nonlinear Schrödinger equation (NLSE) in combination with a phase-diffusion model commonly used to model CW lasers [19]. In their model the field is free of amplitude fluctuations in the time domain but has a random temporal phase with a Gaussian distribution. The modelled results were in good agreement with their experimental results. A different approach was taken a year later by Kobtsev and Smirnov [20] who included quantum shot noise but neglected large temporal amplitude fluctuations. The authors realised that in order to simulate a CW continuum, a variety of simulations with random noise should be run and then averaged together to form a final spectrum which more closely resembles what was demonstrated experimentally. It was also noted that the model had a strong dependence on the initial pump power which was not reflected in the experimental results. This was attributed to the lack of intensity

fluctuations at the input of the simulation.

These intensity fluctuations were added into a model by Vanholsbeeck *et al.* [21] where they used the measured spectral power of the pump laser and added a random spectral phase to each frequency bin. This process leads to strong intensity fluctuations of the order of the coherence time, in the time domain. As a result of using this model, MI established itself much more quickly leading to solitons earlier on in the fibre. Ensemble averaging was also used by the authors in order to reflect the experimental processes. All this was used to show that pump incoherence is key to producing a CW supercontinuum.

The phase diffusion model was extended further by Frosz *et al.* who linked the statistics of the Gaussian phase noise to the bandwidth of the pump spectrum. The intensity fluctuations were yet again ignored, which may have resulted in the poor agreement between their model and experiment without artificially limiting the bandwidth of their pump spectrum. This model was used to show that soliton-soliton collisions potentially play an important role in CW continuum evolution [22].

3.1.2 Mechanism, advantages and limitations of CW supercontinuum

The basic mechanism responsible for supercontinuum generation under CW pumping conditions was outlined in section 1.4.2 and we will briefly recap it here. The key component is modulation instability (see section 1.3.8) which leads to the break up of a CW field into a train of fundamental solitons. These solitons then undergo intra-pulse Raman scattering and self-frequency shift to longer wavelengths; this generates a soliton-Raman continuum. As modulation instability (MI) is a noise driven process, the solitons are created with a distribution of energies which in turn results in varying rates of self-frequency shifting. This gives rise to the first advantage of CW supercontinua: they are spectrally smooth compared to ultra-short pulse pumped continua, due to the averaging process. The second key advantage is that the spectral power density (SPD) can be very high as a result of the high average powers of the pump source. Another advantage arises from the fact that CW pump sources are much simpler than pulsed systems. Finally, as we shall see later in this chapter, it is possible to build low intensity noise supercontinuum sources based upon suitable CW pump sources.

Continuous wave supercontinuum sources are not without their limitations. For sources pumped at 1 μm, PCF is required in order to pump in the anomalous dispersion regime, which is necessary for MI. As a result, some of the issues related to PCFs transfer directly to CW pumped supercontinuum. Most notably, the high water induced loss at 1.38 μm inhibits CW continuum evolution and the high splice losses make it difficult to launch power into the PCF efficiently. Both of these issues will be tackled in this

chapter.

To date it has proven very difficult to generate wavelengths short of the pump, which is often cited as a limitation of CW pumped supercontinua. Due to the low powers and the lack of a possible fission mechanism most CW continua evolve to wavelengths longer than the pump. Although short wavelength generation has been demonstrated with 1.5 μm pump sources, in general the mechanisms have not been well understood. Furthermore, short wavelength generation at 1 μm has not been demonstrated to date. With many potential applications in the visible this is an important spectral region and in the next chapter we will present results and explain the underlying physics necessary to achieve short wavelength generation with 1 μm CW pump sources.

The main disadvantage of CW pumped continua is a lack to temporal coherence. As CW continua are noise driven, there is a continuous stream of solitons evolving and self-frequency shifting. While this leads to smooth spectra it also results in a loss of temporal coherence [23]. This prevents compression of CW continua in order to generate ultra-short pulses. This may seem like a significant disadvantage but in reality many applications do not require highly temporally coherent sources; furthermore, such continuum sources can only be achieved by using femtosecond pump schemes.

These advantages make CW based supercontinuum particularly useful for a range of applications including: optical coherence tomography (OCT) [18], device characterisation [7], broadband Raman amplification [24], and spectroscopy [25].

3.2 Understanding and improving CW continua - bandwidth extension and noise reduction

In this section we will consider a number of initial experimental results that give us insight into the processes and limitations involved in CW continuum generation before discussing and modelling CW continua in depth in section 3.3.

3.2.1 Limits on CW continuum bandwidth

Surveying all the results covered in section 3.1.1 it is apparent that the vast majority of work on CW continuum generation has been performed in HNLF with pump sources around 1.5 μm. Furthermore, extremely flat, broad high power continua have been demonstrated in this region [14]. Options to increase the bandwidth of these continua are limited: on the long wavelength side the transmission window for silica fibre ends, while generating wavelengths short of pump has proven extremely difficult. Thus it would seem sensible to focus efforts on utilising PCF, which provides a much greater level of control over its dispersion and nonlinearity. PCF also enables the ZDW to be shifted short of 1.3

μm therefore allowing the use of 1 μm pump sources, potentially enabling continuum generation from 1 μm to 2 μm . In reality it has not been possible to generate continua spanning the full wavelength range. This has been due to the high OH^- induced loss at 1.38 μm which has prevented continuum extension beyond that point. Unlike pulsed pumped systems, the solitons formed up in the CW regime simply do not have enough energy to cross the OH^- induced loss and subsequently to continue self-frequency shifting afterwards.

As we saw in chapter 1, OH^- induced loss is a problem for conventional fibres which stems from Si-OH bonds; it is typically reduced by lowering the intrinsic OH^- content of the silica preform. The microstructured nature of PCFs leads to a very large air/silica surface interface, across which it is possible for OH^- molecules to bind to Si atoms resulting in extremely high losses. Thus using low OH^- content silica for the preforms does not significantly reduce the losses. Instead it is necessary to polish, chemically clean and dry the preform in a halogenic atmosphere at over 1000 °C to avoid OH^- related losses. The resulting preform is purged with high-purity nitrogen and is then drawn under controlled atmospheric conditions in order to prevent extrinsic contamination [26]. The losses can be reduced significantly as shown in figure 3.2. As demonstrated, the peak loss at 1.38 μm has been reduced from ~650 to ~40 dB/km. It is likely that this peak is now governed by the intrinsic losses of the silica used for the preform, as the loss corresponds to a OH^- concentration of 0.6 ppm, i.e. within the specified levels of the silica rods used. It is important to note that leaving a low water loss PCF sitting for long periods of time will result in water absorption. It is possible to protect the PCF by collapsing the microstructured holes at each end of the PCF on a fusion splicer to prevent water ingress.

3.2.2 Experimental setup

A simple experiment was set up to examine the difference a low water loss PCF makes to a CW pump continuum. Both PCFs were pumped by two CW fibre lasers: a 50 W CW laser with a collimated output, and a 20 W ASE source with a flexcore output (flexcore is a conventional fibre which has a single mode cut off wavelength at 0.97 μm). The key properties of the pump sources are given in table 3.1. The experimental setup is shown in figure 3.3.

For the 50 W source it was necessary to launch into a flexcore fibre using an aspheric lens. For the PCFs used, an intermediate high NA fibre was utilised to improve the mode field matching between the flexcore and the PCF. Splices were performed on a Vytran filament splicer. Typical splices losses of ~1.5 dB were achieved between the PCF and the high NA fibre. An additional splice loss of ~ 0.3 dB at the flexcore - high NA fibre resulted in a total splice loss of ~1.8 dB. The output power was measured on a thermal
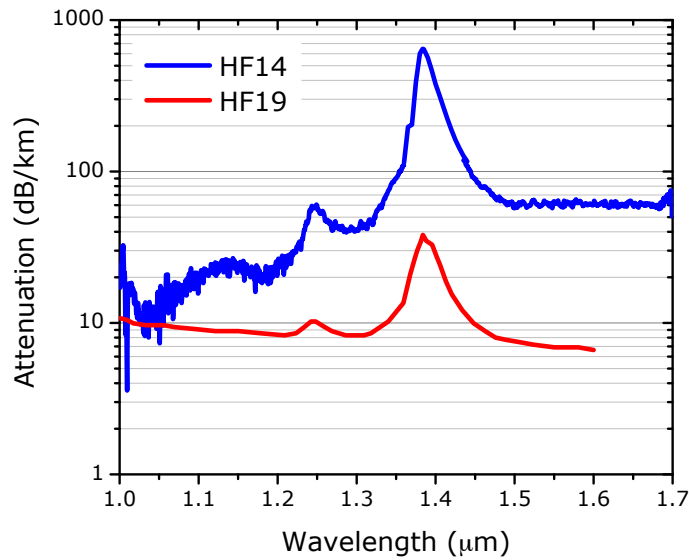
Figure 3.2: Wavelength dependent attenuation for a standard PCF (HF14) and a low water loss PCF (HF19).
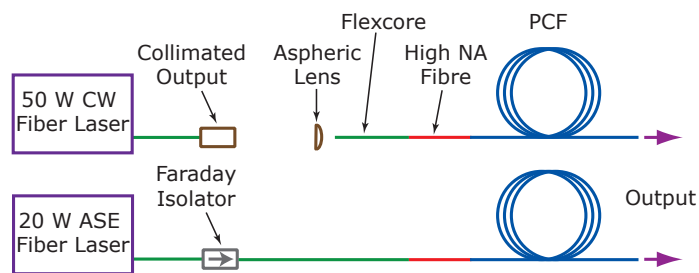

Figure 3.3: Experimental set up for pumping with a 50 W CW fibre laser and a 20 W ASE fibre laser.

power meter head (Molectron PM10), the spectrum was measured on an optical spectrum analyser (Advantest Q8384), whilst the relative intensity noise (RIN) was measured on an electrical spectrum analyser (ESA) in combination with a 2 GHz photodiode, a bias-T and a multimeter. To measure the RIN the signal was fed to the photodiode which was connected to the bias-T. The DC voltage output from the bias-T was measured on a multimeter whilst the AC signal was recorded on the ESA. The ESA is capable of measuring the frequency response between 10 kHz and 2.2 GHz. The RIN is defined as the time averaged noise power in a 1 Hz bandwidth divided by the DC power [27].

3.2.3 Low water loss PCF results

Figure 3.4 demonstrates the considerable difficultly presented by the high water loss. For HF14 the continuum evolution is stopped by the high OH$^-$ induced loss at 1.38 μm. When

Source	λ_p, μm	$\Delta\lambda$, μm	$P_{\max}$, W
CW Laser	1.071	1.15	54
ASE	1.065	5.0	23

Table 3.1: Properties of the CW pump sources used. λ_p is the pump wavelength, $\Delta\lambda$ is the bandwidth, and $P_{\max}$ is the maximum output power.

Fibre	γ_p, W^{-1}km^{-1}	D_p, ps.nm^{-1}km^{-1}	λ_{ZDW}, μm	Lengths used, m
HF5	11	10	1.038	32
HF14	44	43	0.81, 1.73	10, 100
HF19	44	72	0.88	200

Table 3.2: Properties of PCFs used. γ_p is the nonlinearity at the pump wavelength(1.07 μm), D_p is the dispersion at the pump wavelength, and λ_{ZDW} is the location of any zero dispersion wavelengths less than 2.5 μm .

the power is markedly increased the continuum evolves beyond the OH$^-$ induced loss; however a large spectral dip is present at 1.38 μm and the power on the long wavelength side of the dip is significantly reduced (figure 3.4a). Contrasting this with the low water loss PCF in figure 3.4b where the continuum extends up to 1.7 μm with no major reduction of SPD at 1.38 μm.
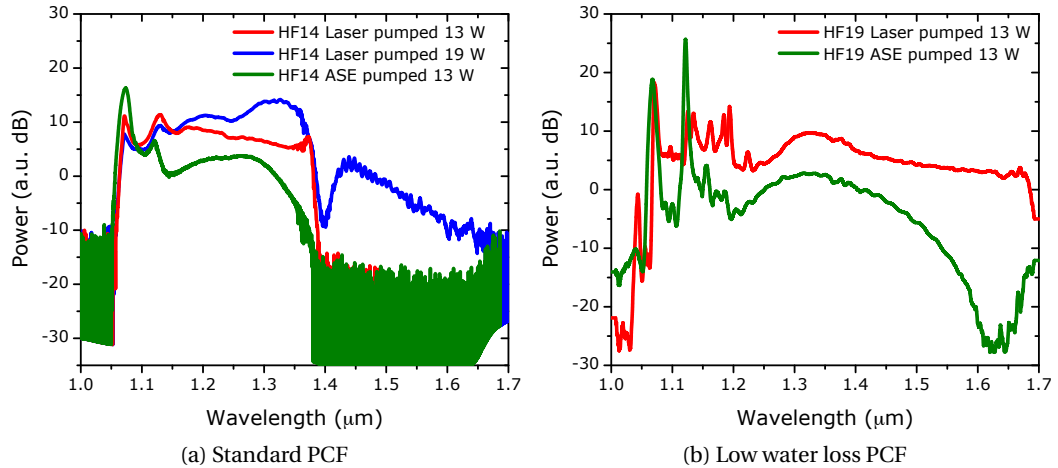
Figure 3.4: Supercontinuum evolution in 100m of standard (HF14) and 200 m of low water loss (HF19) PCF for the two pump sources. All results are for a pump power ~13 W except for the blue plot in 3.4a which is for a pump power of 19 W.

For both PCFs, the continuum expands more rapidly when pumped by the laser source over the ASE source. Several explanations for this are offered: the CW laser source may be

closer to the optimum pump bandwidth; the CW laser may have larger intensity fluctuations leading to more efficient continuum generation; and the longer pump wavelength of the CW laser may be more optimal. As mentioned in the literature review above, some work has been done to examine the effect of pump bandwidth upon continuum generation [13]. Although this work concluded that there is an optimum pump bandwidth, three different sources with different noise characteristics were used, which potentially renders these conclusions debatable.

3.2.4 Examination of relative intensity noise

The RIN describes the instability in the power level or alternatively the level of power fluctuations. The noise can arise from cavity vibrations, fluctuations in the laser gain, transfer of noise from a pump source, thermal variations, beating between longitudinal modes and between different frequencies outside of the cavity. The RIN of the laser and ASE sources used is shown in figure 3.5. In the case of the laser cavity, the characteristic oscillation of the longitudinal modes is clearly visible whilst the ASE source has a flat RIN spectrum. For the latter it can be shown that the noise of an ASE source is inversely related to its frequency bandwidth i.e. $RIN \simeq 1/\Delta\nu_{ASE}$ [27]. For our ASE source this corresponds to -121 dBc/Hz which is close to the measured value of -120 dBc/Hz in the 100 kHz region before the RIN drops to around -124 dBc/Hz in the 1-10 MHz region.
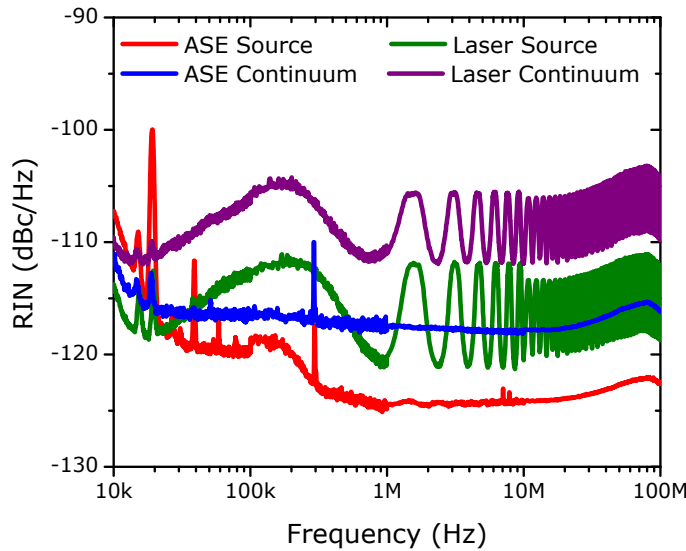

Figure 3.5: RIN from the two pump sources and supercontinuum generated by those sources in HF14.

Launching either source through the PCF to generate a supercontinuum results in a broad amplification of the RIN. The noise amplification has been shown to be due to the

nonlinear amplification of two quantum noise sources: the input shot noise and the spontaneous Raman scattering down the fibre. Of these two effects, shot noise amplification has been shown to be dominant [28, 29]. Although the RIN is independent of the power, of the source, it is not independent of the bandwidth; thus increasing the pump power to broaden the supercontinuum or filtering a broad supercontinuum down will result in a change to the RIN. As the ASE source begins with a lower overall RIN, the resulting continuum has a lower RIN than that of the laser source. The ASE source therefore offers two advantages, firstly it has a lower overall RIN than the laser source, and secondly the RIN is flat and does not have the modulations present, due to the cavity oscillations, of the laser source. This makes a big difference for several applications which are sensitive to the RIN such as LIDAR and OCT.

3.2.5 The effect of Raman oscillations

It is clear from the RIN measurements that the CW laser source has higher intensity fluctuations than the ASE source. These increased fluctuations will act as a seed for the MI process, leading to a quicker evolution of the supercontinuum. This on its own may explain the extra bandwidth of the laser pumped supercontinua. However, as already mentioned, the bandwidth of the sources as well as the change in dispersion at the different pump wavelengths may make a contribution. Before we examine the possible effects of the dispersion change, we shall investigate one particularly large effect, that of Raman generation. All of the continua generated in figure 3.4 have to a greater or lesser extent some Stokes lines. This raises two questions: are the Stokes lines inherent in continuum generation, and does the intensity of the Stokes line affect the bandwidth of the continuum? The use of PCFs to build highly efficient Raman fibre lasers has already been demonstrated [30]. A straightforward experiment in which 100 m of HF14 was pumped with the ASE source whilst the output end was either flat cleaved or angle cleaved was performed. The results shown in figure 3.6a show a strong Stokes signal, and a dramatic reduction in the continuum bandwidth for the flat cleave compared to the angle cleave. The bandwidth reduction is equivalent to a much lower pump power under angle cleaved conditions. Unfortunately as the pump power is increased, even under angle cleaved conditions, a Stokes signal becomes increasingly likely. The appearance of such Raman lasing is clear from the RIN where the frequency of oscillation is given by the cavity length (figure 3.6b). Thus it is clearly necessary to reduce the reflections at each end of the PCF in order to prevent the formation of a Raman laser, which is detrimental to continuum formation.

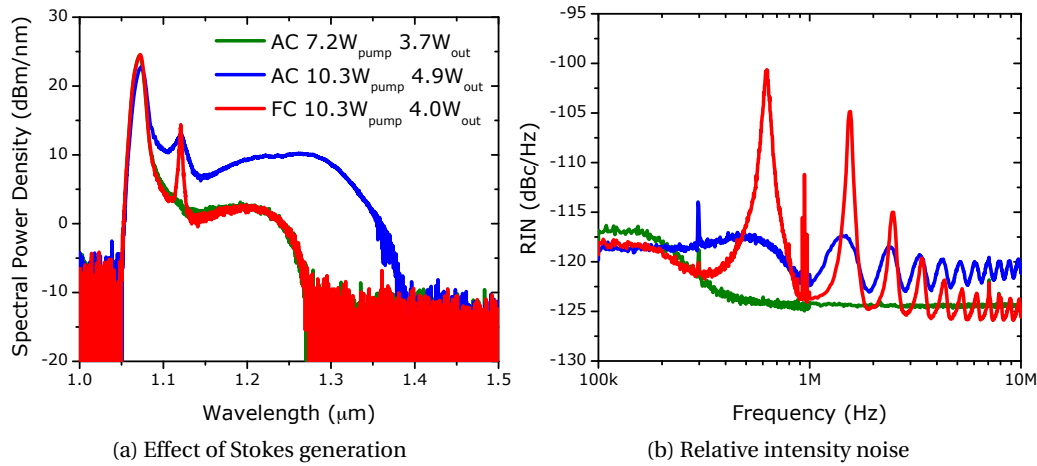(a) Effect of Stokes generation

(b) Relative intensity noise

Figure 3.6: The optical and electrical spectra for 100 m of HF14 pumped by the ASE source with a flat cleave (FC) and angle cleave (AC) at varying pump powers. Key for 3.6b is the same as 3.6a.

3.2.6 The effect of dispersion and nonlinearity

For pulse pumped supercontinuum it has been shown that the flattest, broadest supercontinuum are achieved when pumping close to the zero dispersion wavelength (ZDW) in the anomalous dispersion regime [3]. The matter has been explored to a limited extent with HNLF at 1.5 μm under CW pumping conditions and found to be in agreement with that expected from pulsed pumping [12, 31]. With PCFs pumped at 1 μm the matter is not so explicit. Figure 3.7a shows the continuum formed in two PCFs under identical pumping conditions. The 50 W CW laser was modulated by a 7.7 kHz TTL signal with an 80% duty factor, reducing the average power and thus helping to prevent thermal misalignment and fibre fuses [32]. The continuum forms up more rapidly in the shorter length of HF14 compared to the longer length of HF5. This is despite HF5 having a ZDW of 1038 nm compared to 810 nm for HF14. Examining the fibre properties in table 3.2, we see that the nonlinearity is higher for HF14 and that it has two ZDWs. The cause of this superior performance is not immediately obvious but it is clear that careful consideration needs to be given to the PCF's properties.

3.2.7 Summary

In this section we have demonstrated several things experimentally: a low OH$^-$ content PCF enables continuum extension beyond 1.38 μm; the continuum generation process leads to an amplification of the RIN of the pump source; the high nonlinearity of the PCFs allows a Raman cavity to form and negatively impacts upon continuum formation;

(a) Supercontinuum in two PCFs
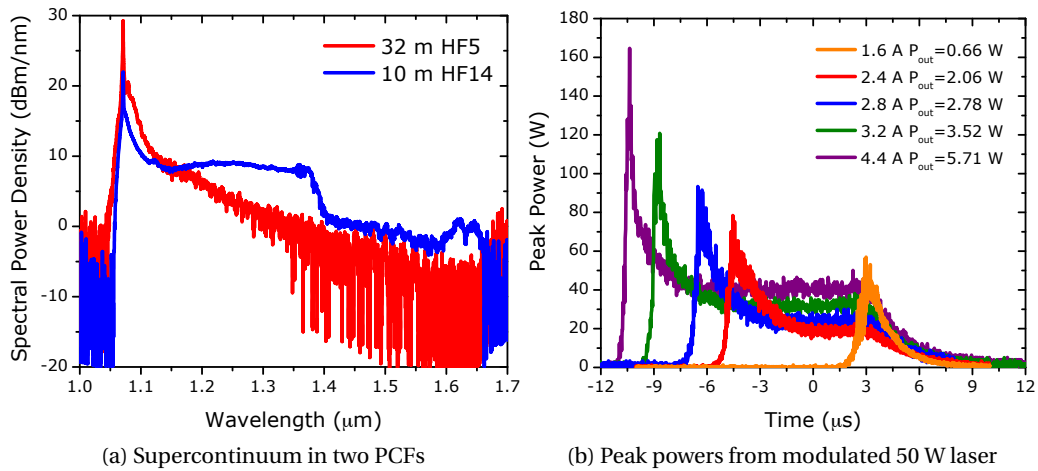
(b) Peak powers from modulated 50 W laser

Figure 3.7: Supercontinuum generated in two fibres, HF5 and HF14, when pumped by 5.7 W from the 50 W CW laser modulated. The modulation leads to a peak power enhancement shown in 3.7b.

and finally the traditional opinion of pumping close to the ZDW for the best continuum does not necessarily hold true for CW pumped continua. Whilst it is important to pay careful attention to each of these issues the final one has potentially broad and important implications for controlling CW continuum generation. Thus we shall look at this last issue in detail in the next section.

3.3 Controlling the physical processes

In this section we will examine the processes involved in CW supercontinuum generation more closely and attempt to explain how we can exert control over those processes to optimise the supercontinuum formation process.

3.3.1 Soliton formation and the self-frequency shift

We discussed supercontinuum formation in section 3.1.2, but what are the most important factors and which ones can be controlled to greatest effect? As we discussed in 1.4.2 the MI gain is dependent upon the pump power, nonlinearity and dispersion of the fibre. Therefore the solitons which emerge from this process are also related to these parameters. For a CW supercontinuum, the bandwidth extension is driven by intra-pulse Raman scattering of the solitons leading to the soliton self-frequency shift (SSFS). The SSFS is, as we shall show, strongly influenced by the energy of the solitons. Hence it is necessary to fully understand this process in order to engineer superior CW supercontinuum sources.

A CW field propagating in the anomalous dispersion regime will always break up provided that there is a suitable nonlinearity for the given length of propagation. The measurements of the RIN in the previous section indicate that the CW field consists of a series of intensity fluctuations. Such intensity fluctuations have been added to CW supercontinuum models and found to produce results in better agreement with experiment, although the continuum evolution is sensitive to the intensity of these spikes [33]. The possibility now arises that the pump can be described as a high order soliton which could undergo soliton fission. In section 1.4.2 we showed that MI dynamics will dominate if $L_{MI} \ll L_{fiss}$. If we take a fluctuation of the laser field as a pulse of duration τ_f, then the previous condition can be expressed as:

$$\tau_{cell} \ll \tau_f \tag{3.1}$$

where τ_{cell} is the MI modulation cell given by:

$$\tau_{cell} = \frac{2\pi}{\sqrt{2\gamma P_0/|\beta_2|}} \tag{3.2}$$

where γ is the nonlinearity, P_0 is the pump power and β_2 is the GVD parameter. Equation 3.1 simply conveys the fact that if the MI modulations are very short compared to the fluctuations, then the MI evolves as if the field is CW locally, giving rise to fundamental solitons. Alternatively, if the MI modulations are comparable to the fluctuations in duration then the high order soliton fission regime will take over, ejecting fundamental solitons. Thus, in the first case MI leads to the evolution of fundamental solitons from noise, in the second we have to consider the CW source as a extremely high order soliton which ejects fundamental solitons under the perturbation of MI.

In the end the field evolves into a train of fundamental solitons with randomly varying energies. In order for these solitons to self-frequency shift, they must have a short enough duration so that their bandwidth is broad enough to allow the short wavelength edge to Raman pump the long wavelength edge, leading to self-amplification. These constraints work in conjunction with the peak power of the soliton, as higher peak powers lead to more effective self-amplification and a greater rate of self-frequency shifting. Previously we showed that the self-frequency shift ($\Delta\omega_R(z)$) is dependent on the 4th power of the soliton duration (τ_0) in section 1.3.8 given by the equation:

$$\Delta\omega_R(z) = -\frac{8|\beta_2|T_R}{15\tau_0^4}z \tag{3.3}$$

where T_R= 3 fs and is the first moment of the Raman response function [34]. If we redraft

this equation in terms of the soliton energy (E_{sol}) given by:

$$E_{\text{sol}} = \frac{2|\beta_2|}{\gamma\tau_0} \tag{3.4}$$

we get:

$$\Delta\omega_R(z) = -\frac{T_R\gamma^4 E_{\text{sol}}^4}{30|\beta_2|^3}z \tag{3.5}$$

It is clear that there is a very strong dependance on the soliton energy, nonlinearity and GVD parameter. Notably the nonlinearity has a stronger influence than the GVD parameter (unless the GVD parameter is very close to zero). We can estimate the energy of the solitons produced via the MI process by making use of the concept of the energy cell developed by Kutz *et al.* [35]. In this concept, MI break-up can be viewed as a series of modulation cells from which a soliton evolves with the energy available within that cell. The energy in these cells is given by:

$$E_{\text{cell}} = \sqrt{\frac{2\pi^2|\beta_2|P_0}{\gamma}} \tag{3.6}$$

By substituting into 3.5 we can estimate how far a continuum might extend due to the SSFS for a particular set of fibre parameters and pump power:

$$\Delta\omega_R(z) = -\frac{4\pi^4 T_R}{30}\frac{\gamma^2 P_0^2}{|\beta_2|}z \tag{3.7}$$

What we find from equation 3.7 is that for the broadest continuum we need a long length of fibre, with high nonlinearity, low dispersion and a high power pump. Of these factors the length has the smallest effect. Unfortunately, the system is not this simple. The nonlinearity and GVD parameter are typically frequency dependent whilst the solitons continuously lose energy as they SSFS due to the inelasticity of the Raman process. Hence, it becomes clear that if we want to generate the broadest continuum we need to take these factors into consideration. From the above analysis we may expect that increasing the nonlinearity in combination with any measure to try and maintain the soliton duration will improve the continuum bandwidth. However, in general it is not possible to increase the nonlinearity without changing the GVD parameter, which also affects the initial MI formation and SSFS. In order to explore these effects we will simulate a series of PCFs under CW pumping conditions, and examine the supercontinuum formed.

3.3.2 Dispersion management

In the last section we showed that the nonlinearity and GVD parameter are critical in controlling the extent of the CW continuum due to the SSFS. In this section we will look at controlling the nonlinearity and GVD parameter via the use of simulations to show how to optimise the continuum. We call this optimisation dispersion management as the dispersion is directly related to the GVD parameter and is commonly used in describing a PCF's properties.

Modelling CW supercontinua

In order to examine how the continuum evolves in different PCFs we need a suitable model. Modelling pulsed supercontinuum generation has been performed by solving the nonlinear Schrödinger equation (given by equation 1.27) using the split-step Fourier method [3, 34]. While this method is perfectly valid for modelling the evolution of a CW continuum, the difficulties arise when choosing the initial conditions to represent the CW field.

Three different approaches have been widely used to date. The first is to model a pure CW beam in the time domain with additional shot noise [20]. This physically corresponds to a single frequency laser which is typically never used experimentally due to the problems of stimulated Brillouin scattering. It also fails to produce any of the intensity fluctuations inherent in a typical high power CW laser. As a result this model tends to underestimate the continuum evolution, unless a higher pump power is chosen in an attempt to include the effect of fluctuations. The second model represents the CW beam as a constant time domain intensity with correctly correlated phase to obtain a Lorentzian spectrum [22]. The downside of this model is that it tends to lead to very broad spectral wings which have much more power than seen in a real laser. This can considerably affect the simulated continuum. The third model which we use in this work takes the average spectral power and adds a random spectral phase to each frequency bin. This gives rise to fluctuations in the time domain intensity as shown in figure 3.8. We refer to this model as the VB model after Vanholsbeeck and Barviau who first described it [21, 36].

The weakness of this model is that the intensity fluctuations are dependent upon the size of your frequency bin and therefore the grid size of the simulation. Similar to the pure CW model which typically underestimates the continuum formation, it is possible for this model to overestimate it depending upon the grid size. It is therefore very difficult to get excellent agreement between experiment and simulation without developing a more accurate model of the initial CW field. Hence all the modelling performed in this work aims to reproduce the trends seen in CW continuum evolution rather than precisely
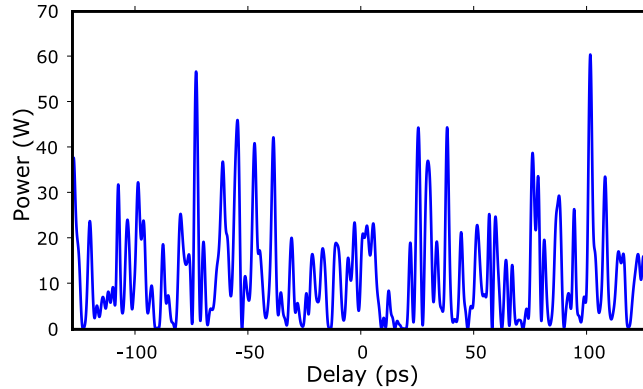
Figure 3.8: Intensity noise for a 10 W CW field using the VB model described with 2^{16} points in the grid and a time window of 256 ps.

represent experimental results. The issue of trying to improve the initial CW model of the field has recently been examined where the CW laser itself is simulated resulting in a much more accurate representation of the field [33]. Unfortunately, this process is also computationally intensive and therefore adds to the total time required for a simulation.

The code used here solves the general nonlinear Schrödinger equation (GNLSE) using a fourth order Runge-Kutta in the interaction picture method [37]. This technique leads to improved accuracy and speed over the traditional split step method. The code also makes use of a modified version of the GNLSE as described in [38]. This enables the inclusion of the wavelength dependance of the effective mode area and effective mode index while also allowing direct integration of the GNLSE without a split step technique. The model accounts for the dispersion up to arbitrary orders, the dispersion of the nonlinearity, and the Raman effect. A full description of the implementation details of the model is given elsewhere [39].

To simulate CW continuum formation within a reasonable computation time we modelled a time window of only 256 ps; however, we note that all of the physical processes involved in the spectral broadening act over much shorter time scales. The grid contained 2^{16} points, which was sufficient to cover the frequency window, and we used an adaptive spatial step size to maintain accuracy [40]. In order to produce a spectral output similar to that seen experimentally it is necessary to run the model multiple times with a different random spectral phase each time. The number of ensembles used is detailed with the simulation results.

Fibre	d/Λ	Λ μm	γ_p W^{-1}km^{-1}	D_p ps.nm^{-1}km^{-1}	λ_{ZDW} μm	Change in ratio* $|\beta_2|/\gamma$
HFa	0.47	3.4	10	6	1.039	17.8
HFb	0.52	3.2	12	13	1.008	9.8
HFc	0.55	3.0	14	20	0.982	7.4
HFd	0.57	2.7	18	30	0.946	5.6

Table 3.3: Properties of PCFs used. γ_p is the nonlinearity at the pump wavelength(1.07 μm), D_p is the dispersion at the pump wavelength, and λ_{ZDW} is the location of any zero dispersion wavelengths less than 2.5 μm . *The change in the ratio of $|\beta_2|/\gamma$ is calculated between the pump wavelength and 1.4 μm.

Increasing the nonlinearity

Let us first consider what happens when we increase the nonlinearity, which results in a corresponding increase in the dispersion. We take four hypothetical PCFs with varying pitch Λ and d/Λ as detailed in table 3.3; these have a range of nonlinearities between 6 and 30 W^{-1}km^{-1} at the pump wavelength of 1.07 μm. As a result, the ZDW is shifted from 1.039 to 0.946 μm and this is illustrated in figure 3.9a along with the wavelength dependent nonlinearity in figure 3.9b.

(a) Dispersion curves   (b) Nonlinearity
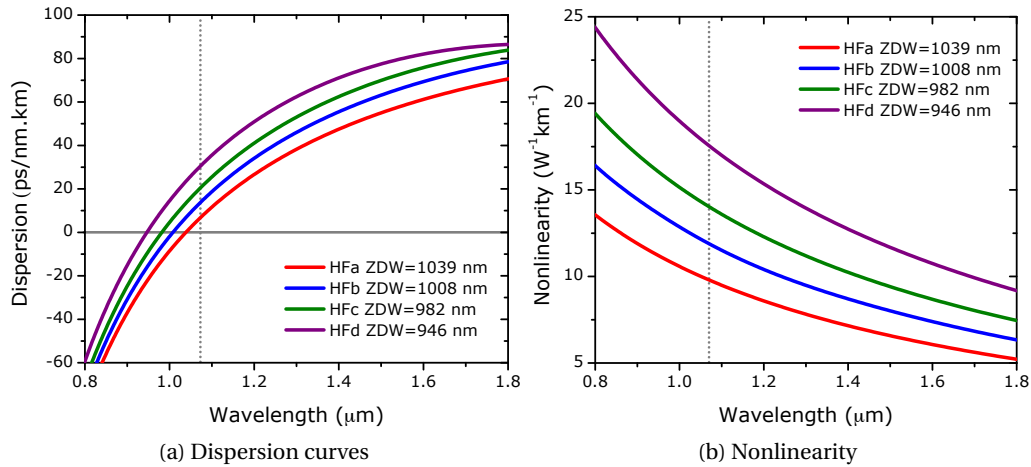
Figure 3.9: Calculated dispersion and nonlinearity for the four hypothetical PCFs detailed in table 3.3.

A 10 W CW laser with a bandwidth of 1.0 nm was simulated using the VB model and launched into 100 m of each of the PCFs. Figure 3.10 shows an intensity plot of the evolution of the field with length along PCF. Three things are immediately obvious, firstly as the nonlinearity is increased the continuum extends further into the infrared, secondly
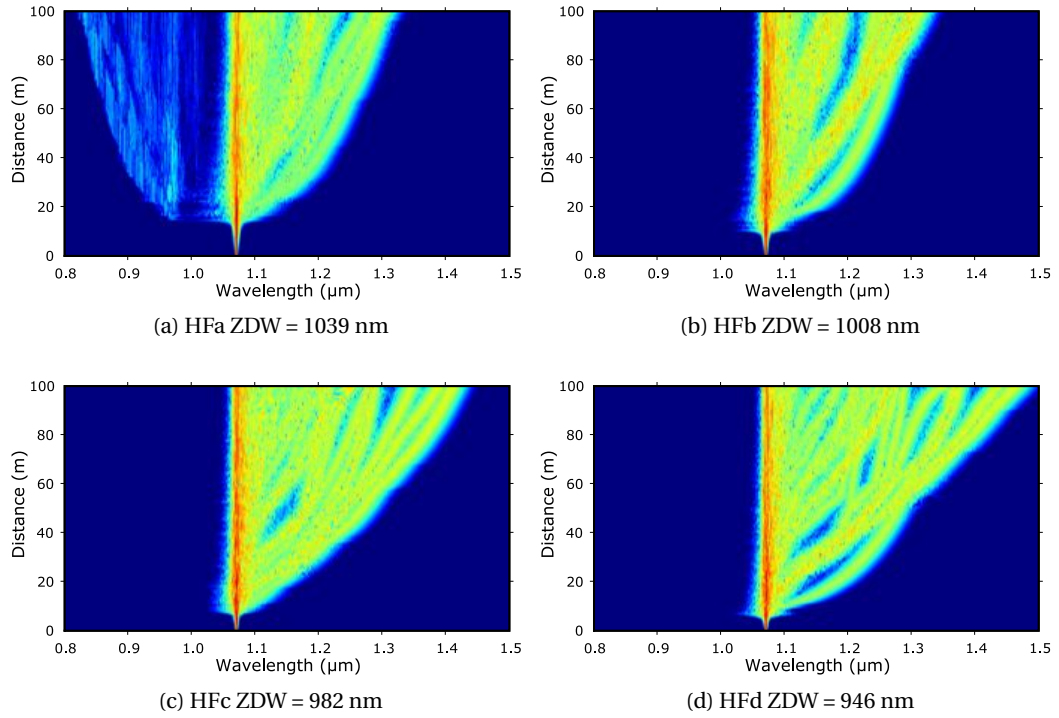
Figure 3.10: Evolution of supercontinuum with length for a single shot simulation of a 10 W CW laser. Scale: -60 dB ▬▬▬▬▬ 0 dB.

as the nonlinearity is increased the continuum forms up earlier in the PCF, and thirdly when the ZDW is closest to the pump there is a very weak continuum generated on the short wavelength side of the pump. Upon closer inspection it becomes clear that the solitons formed under the higher nonlinearities are shifting to longer wavelengths much more rapidly. While the rate of SSFS decreases as the solitons are red shifted, denoted by the inward arcs, in some cases this rate gets a boost after a significant propagation, denoted by the outward arcs of their paths.

The boost requires an increase in the soliton energy and the most likely explanation of this is via soliton-soliton collisions [22, 41]. Modulation instability leads to the generation of solitons with a range of energies and due to the strong dependance of the SSFS upon the soliton energy (E_{sol}^4) the rate of SSFS can vary dramatically between solitons. If we consider two solitons evolve from the CW field, the first at a distance z along the fibre with an energy E_{sol}, the second at a distance $z + \delta$ with a higher energy of $E_{sol} + \delta$. Both solitons begin with a frequency ω_0 but after propagating through Δz of the fibre the second soliton, which has more energy, is frequency downshifted compared to the first soliton, due to the greater rate of SSFS. So the second soliton now has a frequency of $\omega - \Delta$ compared to the first, and will eventually be passed by it (as the red shifted soliton travels slower). When
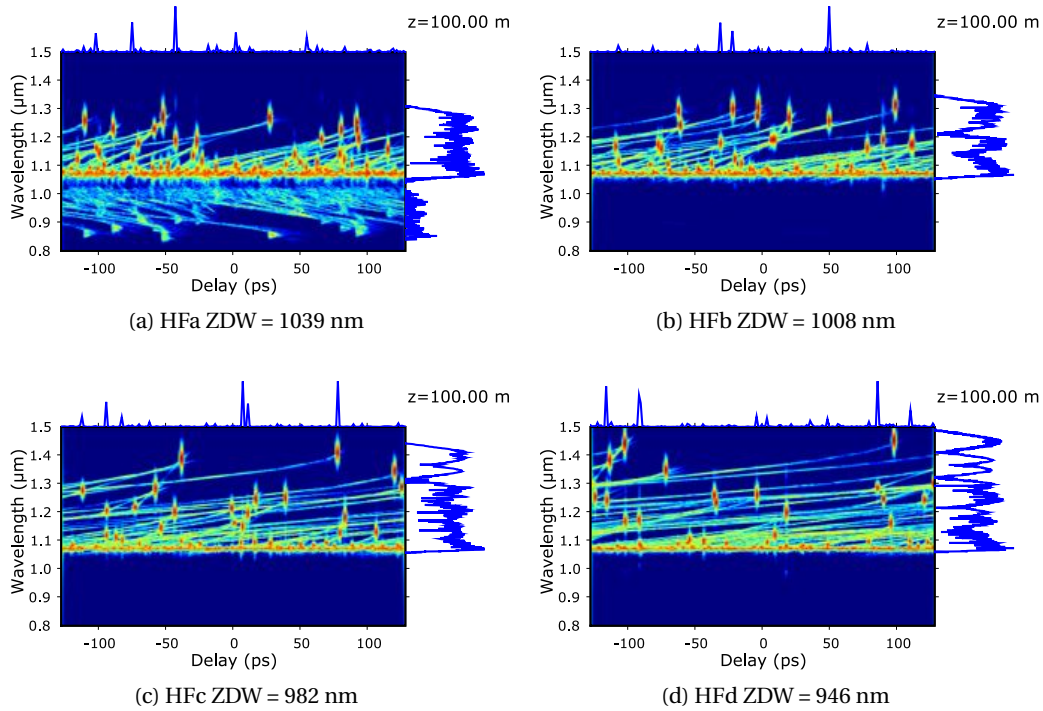
(a) HFa ZDW = 1039 nm

(b) HFb ZDW = 1008 nm

(c) HFc ZDW = 982 nm

(d) HFd ZDW = 946 nm

Figure 3.11: Evolution of supercontinuum with length for a single shot simulation of a 10 W CW laser. Scale: -80 dB ▬▬▬ 0 dB

the two solitons overlap in time, the lower frequency soliton is amplified at the expense of the first soliton via Raman gain. This process clearly results in energy being transferred to the low frequency soliton; in the process of gaining more energy, the soliton will reshape itself, resulting in a temporal compression of the soliton. Consequently, the soliton can now self-frequncy shift further into the red and its group velocity will decrease further, enabling more collisions and more energy gain for the soliton. It has been shown that for a collision between fundamental solitons, the higher frequency soliton is depleted by $\exp(-4T_R)$ once the lower frequency soliton has completely passed through [41].

The process can be clearly seen in the spectrograms (or XFROG [42]) traces. Figure 3.11 shows spectrograms for the field at the end of each fibre for a single shot. By calculating these along the fibre length it is possible to animate the continuum evolution. By examining these animations for HFa and HFd it is clear that HFd produces solitons that self-frequncy shift more rapidly and as a result collide more often, producing a greater deceleration in the solitons which have been red shifted to the greatest extent (see media files HFa_anim.gif and HFd_anim.gif [43]).

The spectrograms highlight a number of other features. Firstly the lower the dispersion the more solitons are formed. This is expected as the solitions form up from the

modulation cells, the period of which is governed by MI and is given by:

$$T_m = \frac{2\pi}{\Omega_{\text{max}}} = \frac{2\pi}{\sqrt{2\gamma P_0/|\beta_2|}} \tag{3.8}$$

where T_m is the period of the pulse train and Ω_{max} is the frequency of maximum MI gain [34]. Decreasing the dispersion decreases the period, which therefore leads to more solitons. More initial solitons means that there are more soliton-soliton collisions leading to more efficient energy transfer to the red side of the spectrum.

The second feature that is apparent from the spectrograms is that there is a reasonable amount of energy loss from the solitons in the form of dispersive waves as they self-frequency shift. These dispersive waves are actually the trails from soliton-soliton collisions. They are produced by the lower frequency soliton after it experiences amplification and then readjusts to maintain itself as a soliton by shedding excess energy. Again this can be seen in the spectrogram animations of HFa and HFd (see media files HFa_anim.gif and HFd_anim.gif [43]).

The third feature that is clear from the single shot spectrograms is that ensembled averaging is necessary to achieve agreement with experimental measurements. Each spectrogram is over a 256 ps window whilst a typical OSA has an integration time of ~1 ms. Hence, we would expect to need to average over $\sim 10^7$ ensembles. In practice, averaging over 10s-100 ensembles is often adequate to give good agreement with experiment [20, 21].

(a) Continuum generated in the 4 PCFs

(b) Ratio of $|\beta_2|/\gamma$ with wavelength
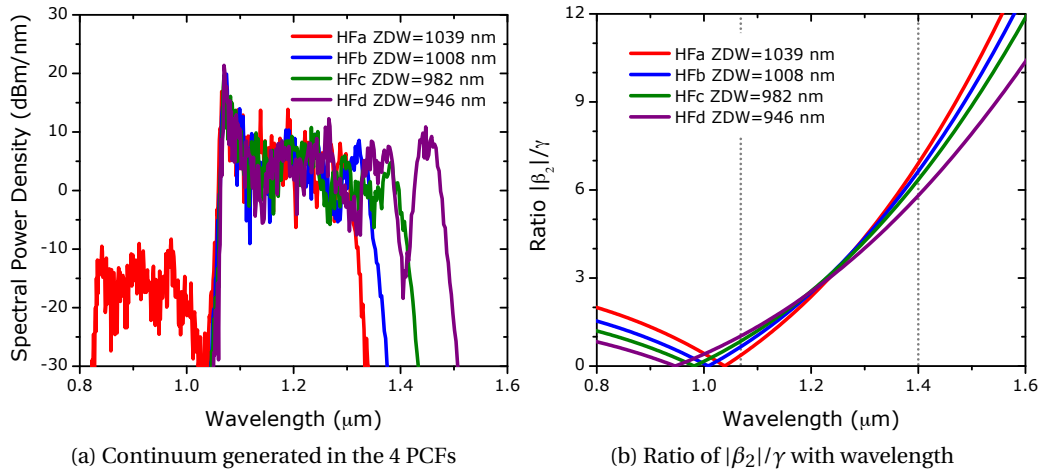
Figure 3.12: 3.12a shows the spectrum of the supercontinuum generated in the 4 PCFs with a 10 W CW pump. Each spectrum is the result of an averaging of 3 simulations each with a different random phase. 3.12b gives the ratio of $|\beta_2|/\gamma$ with wavelength. The change in the ratio between the pump (1.07 μm) and 1.4 μm is given in table 3.3.

The net result of shifting the zero dispersion to shorter wavelengths whilst increasing

the nonlinearity is summarised in figure 3.12a. Although the spectra are only the result of 3 ensembles, it is clear that as the zero moves to shorter wavelengths and the nonlinearity increases, the continuum extends further into the infrared. This is a result of the effect the dispersion and nonlinearity have on the energy of the solitons, and therefore the number of soliton collisions and the subsequent rate of SSFS. All of this can be simplified into one figure showing the ratio of $|\beta_2|/\gamma$ with wavelength (figure 3.12b). If we consider the soliton energy given in equation 3.4 and we assume there is no loss of energy, then as the ratio of $|\beta_2|/\gamma$ increases, the duration of the soliton must also increase resulting in a reduction of the soliton's bandwidth and therefore a reduction in its ability to self-frequency shift. Ultimately the ratio may become large enough to prevent any further self-frequncy shifting. Examining figure 3.12b shows that HFd has the lowest gradient for the soliton to climb and thus intuitively we would expect it to produce the broadest continuum.

In reality, matters are further complicated by PCF attenuation, which tends to increase for smaller cores and is typically very high at 1.38 μm due to OH$^-$ absorption. Taking this hypothesis to the extreme would also lead to difficulties, as the further you are from the ZDW the weaker the MI and the smaller $\Omega_{\max}$. In addition as the ZDW is moved towards the visible the PCF core size decreases, increasing the attenuation. These two factors result in a significant increase in the pump power required for continuum formation.

Comparison with femtosecond pumping - increasing the nonlinearity

As so much work on supercontinuum generation has focused on femtosecond pumping a brief investigation of what happens in the femtosecond regime with these hypothetical PCFs is useful. Using the same model as before, we propagate a 250 fs, 2 kW (peak power) pulse at 1.07 μm through 1 m of each of the PCFs. The evolution of the continuum for each PCF is shown in figures 3.13a through to 3.13d. The spectrograms for HFa and HFd are shown in figures 3.13e and 3.13f respectively.

The supercontinuum formation is governed by the soliton fission regime described in section 1.4.2. As with the CW case, when the ZDW is shifted and the nonlinearity is increased the continuum forms up earlier in the PCF. In contrast to the CW case however, there is significant power generated short of the pump wavelength. As the dispersion is shifted away from the pump and the nonlinearity is increased, the power on the short wavelength side is reduced and shifted to shorter wavelengths. The dynamics of this are complicated and we shall not discuss them in depth here, although it is clear that for HFa and HFb the soliton trapping effect (1.3.8) and FWM play a significant role in generating the short wavelengths combined with the generated dispersive wave. As the dispersion zero is shifted to shorter wavelengths these effects become less efficient and we
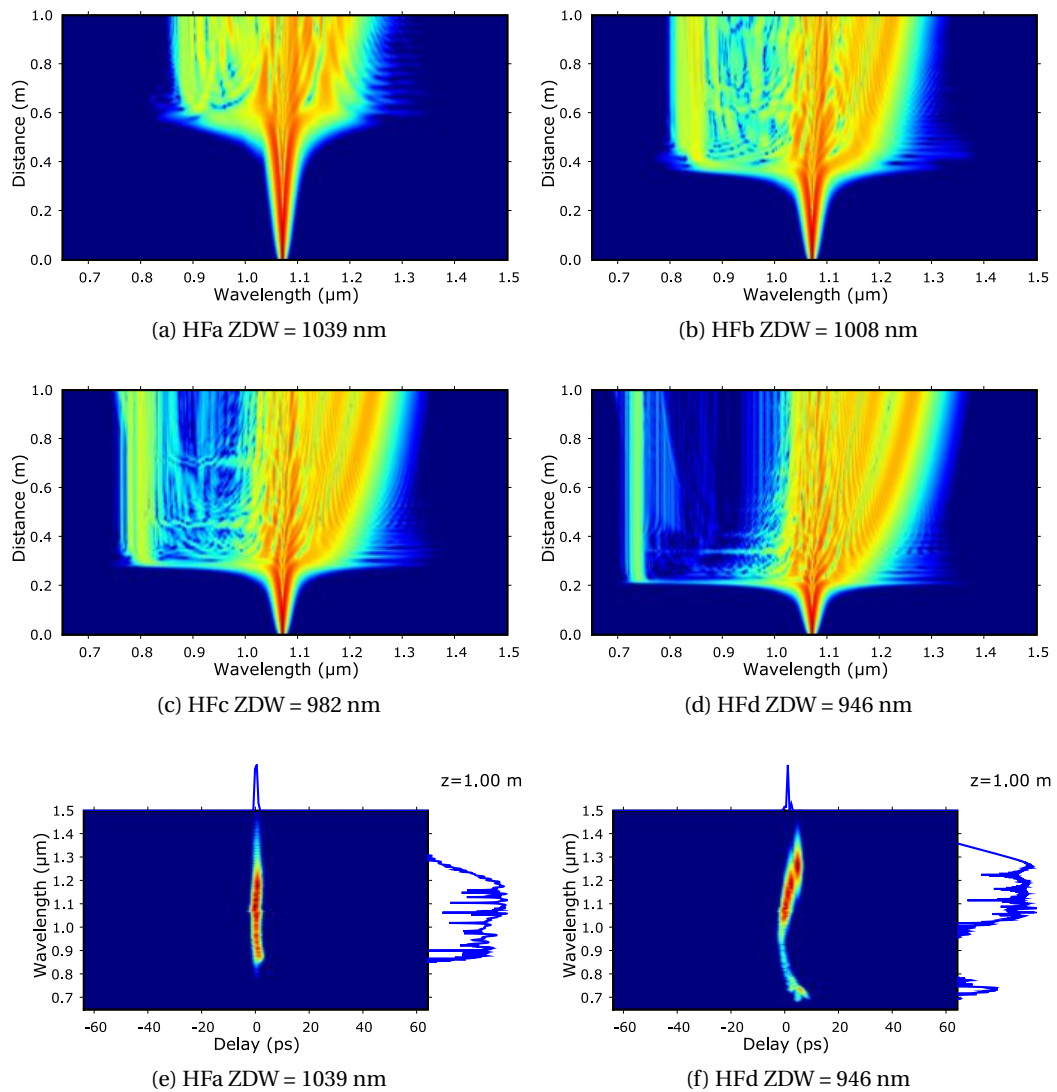
Figure 3.13: (3.13a-3.13d) Evolution of supercontinuum with length for a 250 fs 2 kW pulse through 1m of each of the PCFs. Scale: -60 dB ▰▰▰ 0 dB. (3.13e-3.13f) Spectrograms of the continuum at the end of HFa and HFd. Scale: -80 dB ▰▰▰ 0 dB.

are just left with the dispersive wave, as HFd. As a result the broadest, flattest continuous continuum is that generated in HFa. Furthermore, due to the short lengths required, simply extending the PCF length by a small amount allows the continuum to broaden further, compensating for the slightly shorter long wavelength edge compared with the higher nonlinearity PCFs.

Thus it becomes clear that pumping close to the ZDW generates the broadest continuum for femtosecond pumping [3]. If we examine the spectrograms (3.13e-3.13f) it

Fibre	d/Λ	Λ μm	γ_p W^{-1}km^{-1}	D_p ps.nm^{-1}km^{-1}	λ_{ZDW} μm	Change in ratio* $|\beta_2|/\gamma$
HFc	0.55	3.0	14	20	0.982	7.4
HFe	0.45	2.6	15	18	0.982	6.8
HFf	0.40	2.2	19	15	0.983, 2.087	5.5
HFg	0.40	1.85	25	11	0.979, 1.514	2.1

Table 3.4: Properties of PCFs used. γ_p is the nonlinearity at the pump wavelength(1.07 μm), D_p is the dispersion at the pump wavelength, and λ_{ZDW} is the location of any zero dispersion wavelengths less than 2.5 μm . *The change in the ratio of $|\beta_2|/\gamma$ is calculated between the pump wavelength and 1.4 μm.

also becomes apparent that the temporal coherence is best maintained when closest to the ZDW. If we compare these spectrograms with those of the CW pump (figure 3.11) it is very clear that CW continua are noise driven and temporally incoherent, in contrast to femtosecond pumped continua [20, 21, 44]. Hence the optimal PCF parameters for supercontinuum generation differ greatly depending upon the pump regime.

Controlling the dispersion curve

We have shown that it is desirable to increase the nonlinearity and decrease the dispersion whilst reducing the change in the ratio of $|\beta_2|/\gamma$ to potentially achieve the optimum continuum. Clearly for the PCFs we have discussed it is not possible to achieve both of these objectives concurrently. Fortunately, PCFs allow for extensive control of their dispersion properties. It is possible to have two ZDWs which results in an anomalous region surrounded by normal dispersion regions on both the short and long wavelength sides. We will now look at what effect adding a second ZDW has upon continuum formation. Several more hypothetical PCFs are simulated, which are described in table 3.4. The dispersion and nonlinearity curves for these PCFs are illustrated in figure 3.14.

Examining figure 3.14 it becomes apparent that as we pull the second ZDW in towards the first ZDW not only is the nonlinearity significantly enhanced but the dispersion (at the pump wavelength) is also reduced. As a result, based upon our previous discussions, we would expect HFg to produce a broad flat continuum. Unfortunately, solitons require anomalous dispersion to exist and therefore solitons will be confined to wavelengths shorter than the second ZDW at 1.514 μm. We can explore what happens by examining the evolution of the continuum with length (figure 3.15) and the spectrograms produced by our simulations (figure 3.16).

As expected, the continuum gets broader as the second ZDW is shifted to shorter wavelengths for PCFs HFc, HFe and HFf. For HFg with its second ZDW at 1.514 μm (figure
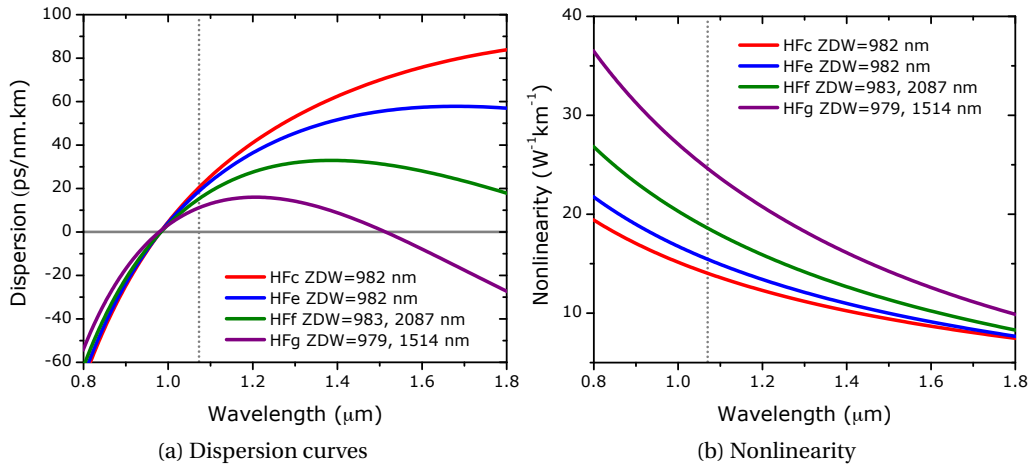
(a) Dispersion curves

(b) Nonlinearity

Figure 3.14: Calculated dispersion and nonlinearity for the four hypothetical PCFs detailed in table 3.4.

(a) HFc ZDW = 982 nm

(b) HFe ZDW = 982 nm

(c) HFf ZDW = 983, 2087 nm
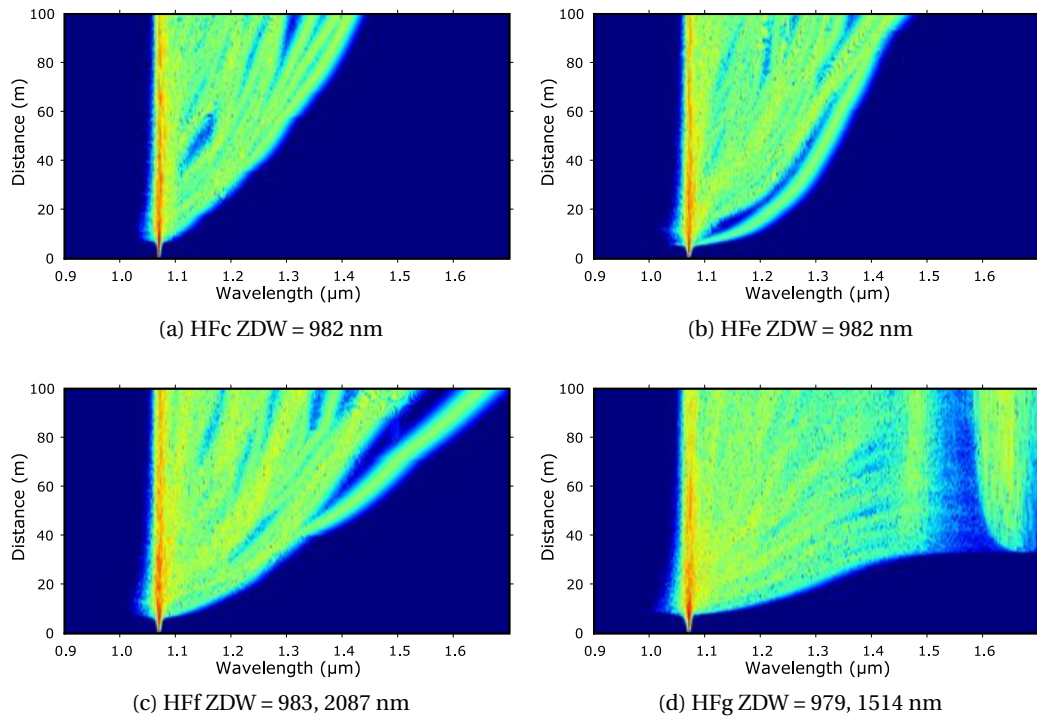
(d) HFg ZDW = 979, 1514 nm

Figure 3.15: Evolution of supercontinuum with length for a single shot simulation of a 10 W CW laser. Scale: -60 dB ▰▰▰ 0 dB.

3.15d) we see that the solitons stop spectrally shifting just before the second ZDW and a corresponding dispersive wave is generated in the normal dispersion region centred at ~1.65 μm. This soliton self-frequency shift cancellation has been explored theoretically

and demonstrated using 200 fs pulses in a PCF with a negative dispersion slope [45]. The dispersive wave is a form of Cherenkov radiation and it has been shown theoretically that solitons emitting Cherenkov radiation lose energy slowly (i.e. nonexponentially) with increasing propagation distance [46]. This transfer of energy to a resonant dispersive wave results in the soliton attempting to conserve energy by spectrally recoiling, or frequency shifting away from the dispersive wave. This analysis excludes the effect of Raman gain and the SSFS. When included it becomes clear that a soliton undergoing SSFS transfers energy exponentially to the resonant dispersive wave, as its central carrier frequency approaches the ZDW. This quickly saturates as the soliton spectrally recoils and becomes frequency locked. At this point the red-shift of the SSFS has been cancelled by the blue-shift of the Cherenkov induced recoil [45, 47].

This description is acceptable for a train of solitons from a given pulse source; however in a CW based supercontinuum, a whole range of solitons with different energies are formed. The highest energy solitons rapidly SSFS toward the second zero, generating a dispersive wave and spectrally recoil. These frequency-locked solitons continue to propagate along the fibre and thus affect the rate of SSFS of subsequent solitons. This is mediated through soliton collisions. As the number of solitons at the second ZDW increases, the probability of a shorter wavelength soliton colliding with one of these solitons increases. During this collision the higher frequency soliton loses energy to the lower frequency soliton; in the case of a soliton by the second ZDW it gains energy and thus begins to self-frequency shift towards the second ZDW again. However this shift is quickly stopped as the energy is transferred to the coupled dispersive wave and the soliton subsequently recoils back to its original position. The high frequency soliton has now been slowed and this results in a relatively even distribution of energy between the pump and the second ZDW. This effect can be seen in an animation of the spectrogram of HFg (see media file HFg_anim.gif [43]) and in figure 3.16d. Despite the collisions reducing the velocity of subsequent solitons, eventually a significant number of solitons come to rest by the second ZDW, which leads to an increase in the spectral power density at this wavelength. This is followed by a dip before the dispersive wave which has no available mechanism to extend further into the infrared. As a result the long wavelength edge of the continuum is ultimately limited by the second ZDW.

Attention should be drawn to a couple of other features in figure 3.15. The first is that as the second ZDW is moved to shorter wavelengths, the continuum broadens out more quickly, which can be understood in terms of the ratio of $|\beta_2|/\gamma$ as shown in figure 3.17b. From the figure, it is clear that as the second ZDW is moved to shorter wavelengths, this ratio begins to approach a constant, which enables solitons to maintain their duration and thus facilitating a high efficiency for the SSFS. Combined with the lower dispersion at
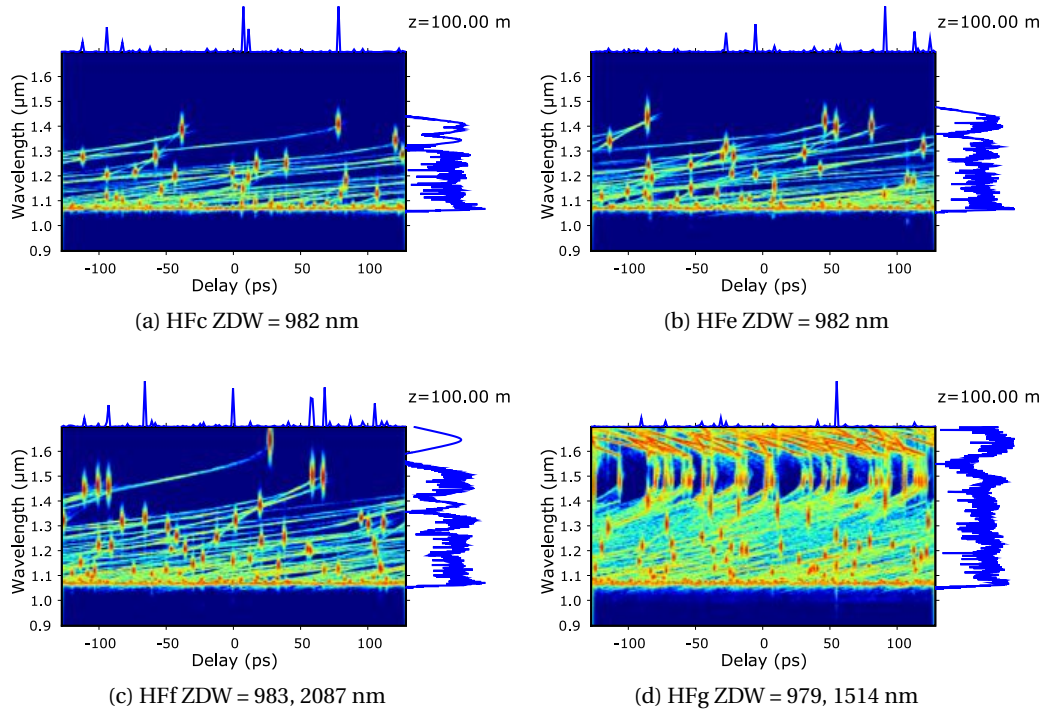
(a) HFc ZDW = 982 nm

(b) HFe ZDW = 982 nm

(c) HFf ZDW = 983, 2087 nm

(d) HFg ZDW = 979, 1514 nm

Figure 3.16: Evolution of supercontinuum with length for a single shot simulation of a 10 W CW laser. Scale: -80 dB ▬▬▬▬ 0 dB.

the pump leading to more solitons, and the higher nonlinearity resulting in higher energy solitons, we have the perfect conditions for rapidly forming a continuum. In reality, this means that a shorter length of PCF may be used, reducing the effect of attenuation upon the spectrum.

The second remaining characteristic to note in figure 3.15 is that as the nonlinearity is increased it becomes increasingly likely that occasional high energy solitons will be formed. These solitons self-frequency shift at a much higher rate (as seen in figure 3.15c) and whilst they ultimately lead to a broader continuum, they have been the focus of some recent work. Parallels have been drawn between these high energy solitons and rogue waves [48, 49], although much earlier work looks at stimulating the MI process to enhance the soliton trains formed [50]. Examination and development of this earlier work may prove to be particularly relevant to CW supercontinuum generation.

The result of introducing the second ZDW on the supercontinuum spectrum is shown in figure 3.17a. As the second ZDW is brought in towards the first ZDW the continuum extends further into the infrared for HFc, HFe and HFf. Eventually the second ZDW acts as a limit on the continuum bandwidth (as in HFg), with a dip in the spectral power density between the end of the continuum and the dispersive wave.

(a) Continuum generated in the 4 PCFs

(b) Ratio of $|\beta_2|/\gamma$ with wavelength
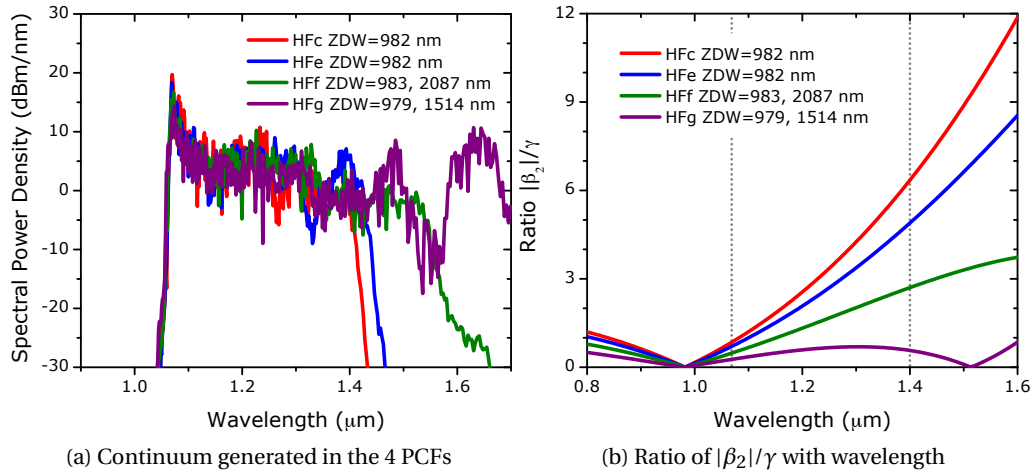
Figure 3.17: 3.17a shows the spectrum of the supercontinuum generated in the 4 PCFs with a 10 W CW pump. Each spectrum is the result of an averaging of 7 simulations each with a different random phase. 3.17b gives the ratio of $|\beta_2|/\gamma$ with wavelength. The change in the ratio between the pump (1.07 μm) and 1.4 μm is given in table 3.4.

Comparison with femtosecond pumping - controlling the dispersion curve

It is worth briefly describing what happens in the femtosecond regime with these hypothetical PCFs. As before, we propagate a 250 fs, 2 kW (peak power) pulse at 1.07 μm through 1 m of each of the PCFs. The evolution of the continuum for each PCF is shown in figures 3.18a through to 3.18d. The spectrograms for HFc and HFg are shown in figures 3.18e and 3.18f respectively.

The first thing to note from the evolution of the continuum for each PCF is that the fission event occurs at approximately the same length in all four cases. This is expected as the change in dispersion and nonlinearity approximately cancel each other out, resulting in a similar soliton order for all four cases. Hence, fission occurs after a similar distance. As the second ZDW is introduced the long wavelength edge of the continuum shifts out while the transfer of power to the region short of the pump improves. When the second ZDW becomes suitably close, a set of dispersive waves are created on the long and short wavelength sides by the fission event; at the same time, a further dispersive wave eventually forms up closer to the second ZDW as the solitons SSFS towards that zero.

The spectrograms show that as the second zero is brought closer in, the temporal coherence of the central part of the continuum is marginally improved. On the whole it is not clear that pumping a double zero PCF offers any significant benefit over a single zero PCF under femtosecond pump conditions. Of course we previously seen that the

(a) HFc ZDW = 982 nm

(b) HFe ZDW = 982 nm

(c) HFf ZDW = 983, 2087 nm

(d) HFg ZDW = 979, 1514 nm

(e) HFc ZDW = 982 nm
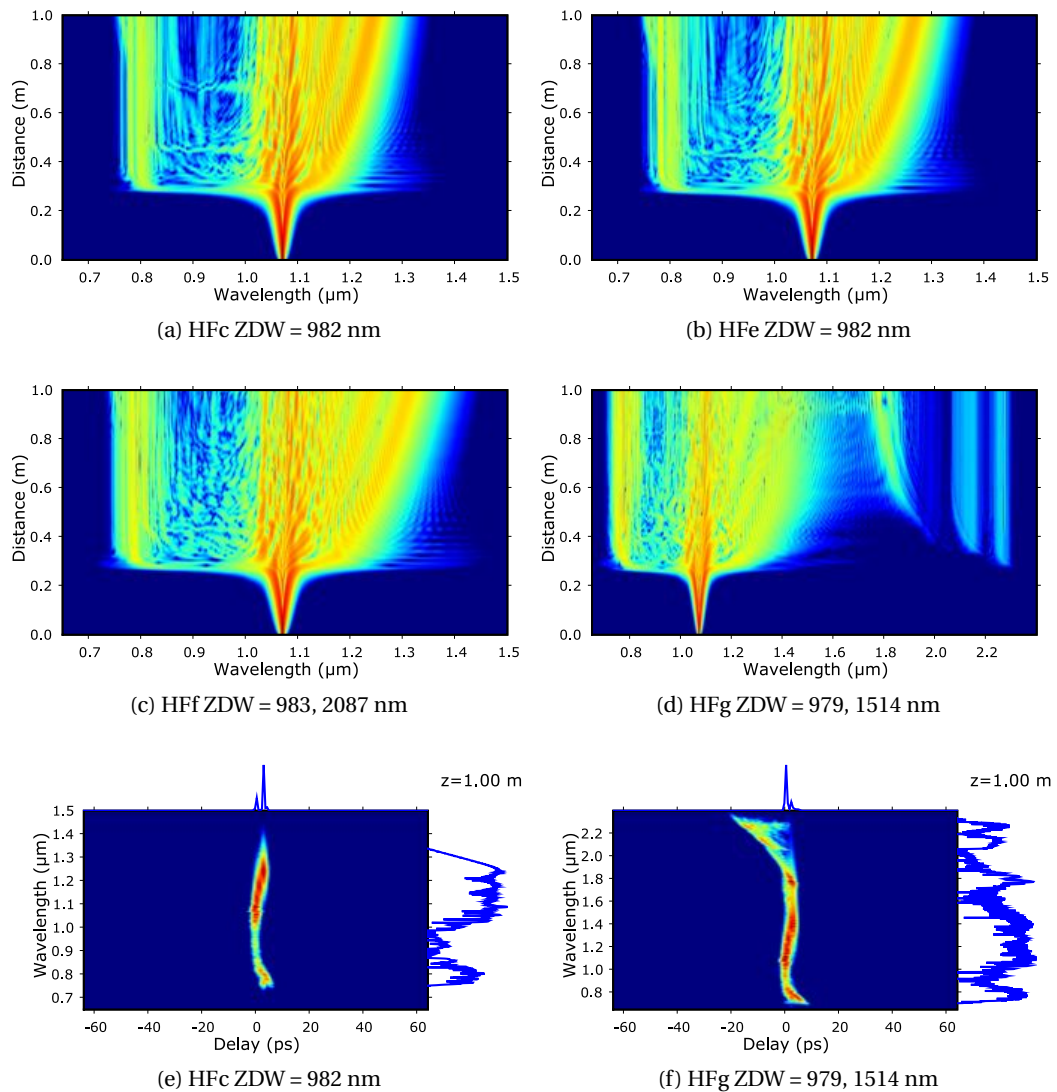
(f) HFg ZDW = 979, 1514 nm

Figure 3.18: (3.18a-3.18d) Evolution of supercontinuum with length for a 250 fs 2 kW pulse through 1m of each of the PCFs. Note the extended wavelength axis for HFg. Scale: -60 dB ▬▬ 0 dB. (3.18e-3.18f) Spectrograms of the continuum at the end of HFc and HFg. Scale: -80 dB ▬▬ 0 dB.

best femtosecond continua are generated by pumping close to the ZDW; a double zero fibre may therefore only offer benefits if one zero is close to the pump wavelength. Again the dynamics become rather complicated and various studies of femtosecond pump supercontinua in double zero PCFs have been performed [51–53].

3.3.3 Summary

We have seen that CW supercontinua are formed through MI, leading to solitons which undergo SSFS to the long wavelength side. The MI formation and SSFS are therefore critical to the process and have a strong dependance upon the pump power, dispersion and nonlinearity of the fibre. We have shown that by manipulating the dispersion and nonlinearity it is possible to control the extent of the supercontinuum, whilst adding a second ZDW enables fine control of the ratio of the GVD parameter to the nonlinearity. With this knowledge it is possible to optimise a PCF's properties to achieve the desired continuum. Indeed, not only is it possible to potentially extend a supercontinuum, but it is also possible to confine the bandwidth with a second ZDW. In the next section we will look at implementing these ideas experimentally.

3.4 Increasing SPD and enhancing the continuum

In this section we aim to apply the knowledge obtained through the preliminary work and modelling to create a broad, flat, high power supercontinuum source. As discussed in section 3.2, few CW results have been reported where the continuum has extended beyond the OH^- induced water loss at 1.38 μm; furthermore, these continua have not been particularly flat. Nor have any continua been demonstrated with spectral power densities in excess of 10 mW/nm with 1 μm pump sources. In an attempt to achieve this we pump a short (20 m) length of double zero PCF with a 50 W CW Yb fibre laser.

3.4.1 The PCF and its properties

A 20 m double zero PCF was used as the basis of this work (denoted as HF14). A scanning electron microscope (SEM) image was taken of one end of the fibre and used to calculate the dispersion, nonlinearity and mode field diameter by modeling a step index fibre using a vectorial effective index method for the cladding [54]. In order to perform this calculation the pitch (Λ) and hole diameter (d) of the PCF are required and the cladding structure is assumed to be uniform. By examination of the SEM images (inset figure 3.19b) it is clear that the hole diameter varies significantly and non-uniformly across the structure. Applying these values to the calculation leads to uncertainty in the dispersion profile especially with regards to the second ZDW. In order to try and pin point the second ZDW, the group velocity delay was measured between 1.5 and 1.6 μm. The dispersion was then calculated and the complete dispersion curve was fitted to this small subsection of real data by keeping the pitch fixed and varying the hole diameter. Using this technique the ZDWs were calculated as 0.81 μm and 1.73 μm. The complete dispersion curve is

shown in figure 3.19a along with the nonlinearity and an inset of an SEM of PCF in in figure 3.19b. At the pump wavelength of 1.07 μm the mode field diameter (MFD) is 2.2 μm with a dispersion of 65 ps/(nm.km) and a nonlinearity of 0.043 (W m)$^{-1}$. The PCF has a loss of 650 dB/km at 1.38 μm due to OH$^-$ induced absorption (figure 3.2).

(a) Dispersion curve　　　　　　　(b) Nonlinearity
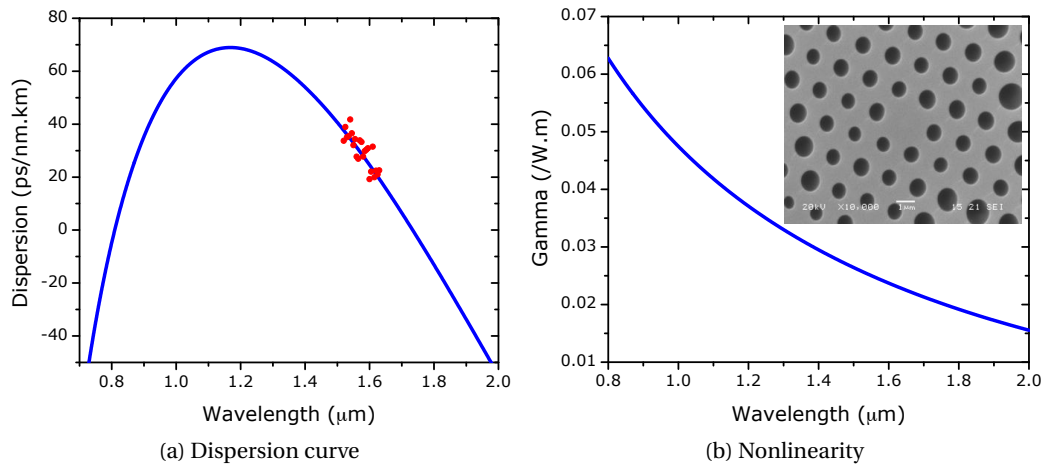
Figure 3.19: 3.19a The calculated dispersion curve (solid line) and experimental measurements (circles) of HF14. 3.19b The calculated nonlinearity. Inset an SEM of the PCF.

3.4.2 Improved splicing

Typically it is difficult to splice PCFs to conventional fibre, owing to their micro-structured nature and small mode field diameters (MFD). Over the last few years several papers have been published on splicing PCFs to standard fibres [55–57] with good results. Traditionally, high splice losses of several dB occur due to mode field mismatch and uncontrolled collapse of the micro-structure, leading to high waveguiding losses. In our experience there is no single set of fusion parameters that can be universally applied, and consequently the splice conditions need to be individually optimized for each PCF. In general we find that larger core PCFs (4 μm and above) can be spliced directly to a standard fibre similar to Flexcore with losses as low as 0.3 dB and typically of the order of 0.5-0.75 dB. These splices are often achieved using a long low power fusion arc with the electrodes offset to the side of the standard fibre. The offset is generally quite small and helps prevent hole collapse in the PCF by reducing the exposure of the PCF to the arc whilst maintaining a strong enough arc to melt the solid core fibre. For small core PCFs, as used here, an intermediated single mode high NA fibre (such as Nufern Ultra High NA fibre) allows for improved mode field matching between Flexcore and the PCF. In this regime the high NA

fibre is spliced to the Flexcore using a mode field matching technique (see section 5.4.1) and the PCF is spliced with a very short, offset, arc to the high NA fibre.

An Ericsson fusion splicer (FSU 975-PM-A) was used and typical losses of 0.15-0.30 dB were achieved for the high NA to Flexcore splice, and losses as low as 0.4 dB for the PCF to high NA fibre. Thus the total loss between the Flexcore and the PCF was typically 0.55-1.00 dB. It should be noted that the quality of the cleave, cleave angle, fusion current, duration and electrode offset are all critical to achieve low loss splices.

Unfortunately there is no easy way to know what parameters are optimal without varying them all and measuring the resulting splice losses. Splicing the same fibre several hundred times to map the parameter space (i.e. fusion time, fusion current, offset, gap, overlap etc) to splice loss is immensely time-consuming on a fusion splicer and possibly too daunting on filament splicers which generally take longer to setup and perform a single splice on. To circumvent this problem we measured the splice loss in real time during a series of test splices. This allowed quick identification of the optimal parameter region and then a series of splices with small variations around this region normally resulted in the minimum achievable splice loss. To measure the splice loss in real time a low power (-15 dBm) ASE pump was connected to the input fibre while a suitable fibre power meter with a computer interface was used to record the power through the fibre during the splicer's fusion cycle. This meant that the fibre could be fused for long durations, giving an indication of the splice loss at every given time, rapidly reducing the parameter space. An example of such an optimisation is shown in figure 3.20. It is important to note that these values are for a "hot splice" and thus only give an indication of the minimum loss. A short series of splices with fixed arc durations is necessary to find the precise loss minimum. Once the loss has been minimized in several parameter spaces and a couple of different fibres have been spliced, the operator will generally have a good understanding of what parameters will give an optimal splice for any given PCF.

Even with such low splice losses further precautions need to be taken. Optical glue is used to secure and more importantly strip and scatter stray light at the point where the fibre coating begins. Failure to do this can often result in burning of the coating as stray cladding modes created at the splice are coupled into the coating causing it to melt. Additionally, the entire splice needs to be thermally managed as build up of heat may instigate splice degradation. Imperfections in the splice leads to localised heating, which in turn results in further imperfections that increase loss; this causes further heating and eventually results in significant splice loss and often a fibre fuse [32]. Various strategies for thermal management are available [58]. Finally, the output of the PCF was angle-cleaved to reduce the reflection from the end facet. As mentioned earlier such reflections, from the output of the fibre and poor quality input splices, significantly enhance any Raman
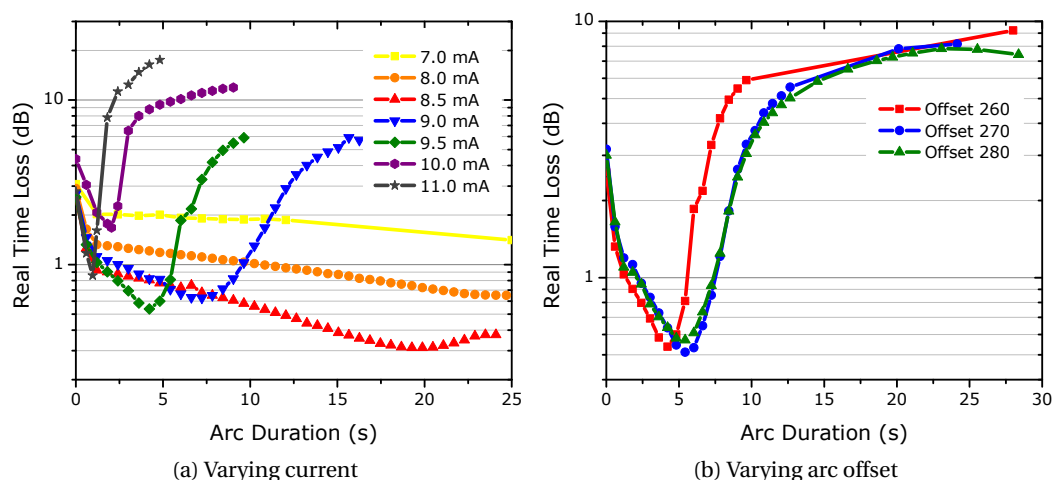
(a) Varying current

(b) Varying arc offset

Figure 3.20: 3.20a shows optimisation of PCF splice loss by measuring the real time loss for 7 different fusion currents. 3.20b shows optimisation of PCF splice loss by measuring the real time loss for 3 different arc offsets. 255 represents the centre, higher numbers offset towards the conventional fibre.

Stokes lines in the continuum and hence should be minimized.

3.4.3 Experimental setup

A 50 W CW Yb fibre laser (IPG Photonics) was spliced to 20 m of HF14 via an intermediate high NA fibre (Nufern) as described above, with a total splice loss of 0.6 dB. The output end of the PCF was angle cleaved and either coupled into an optical spectrum analyzer (Advantest Q8384, Anritsu MS9710B) via an intermediate fibre or collimated and launched into an automated Spex 500 spectrometer in combination with a PbS IR detector and lock-in amplifier for spectral measurements. Output power was measured on a thermal power meter head (Molectron). The average pulse duration was measured by spectrally slicing the supercontinuum using a Spex minimate 0.25 m monochromator followed by re-collimation and launch into an Inrad autocorrelator (Model 5-14b). In order to reduce the average power on the monochromator's gratings, several high reflector mirrors were used in reflection to perform an initial broad spectral slice. The autocorrelations were fitted assuming a sech^2 pulse shape. An outline of the experimental setup is shown in figure 3.21.

3.4.4 Results

The PCF was pumped at a variety of pump powers, under various conditions and a series of measurements was made before a cutback of the fibre was performed. We will detail
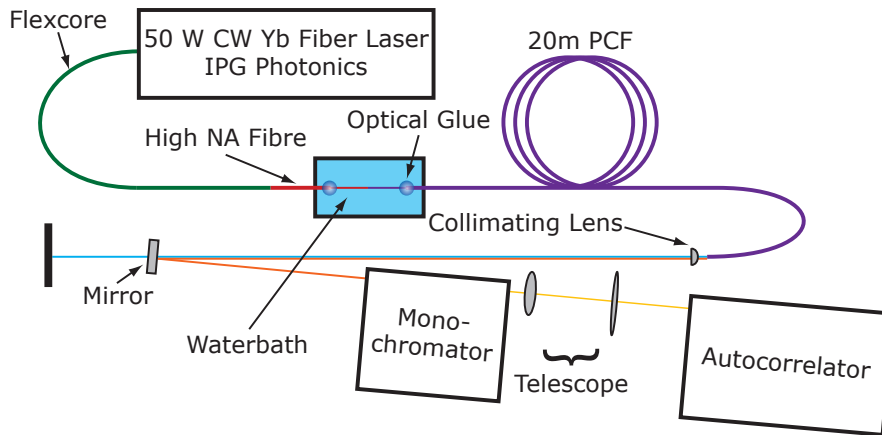
Figure 3.21: Experimental setup for high power supercontinuum generation in double zero PCF.

these results below, and compare them to some more detailed modelling. Modelling was performed using simulations as described in section 3.3.2 with a couple of minor differences. In order to try to achieve better agreement with experiment, we included the spectrally dependent loss profile of the fibre, including the water loss (experimentally measured as 650 dB/km at 1.38 μm and shown in figure 3.2). Again a time window of 256 ps was used, but this time a larger frequency window was required and the grid size was increased to 2^{17} points. Finally in order to produce a spectral output that more closely resembles the experimental results, the simulation was performed 12 times with a different initial random spectral phase each time. The results detailed are therefore the averaged results unless otherwise stated.

Experimental results

At full pump power (50 W) 44 W is launched into the PCF, producing a 29 W supercontinuum with an 8 dB bandwidth of 600 nm (1.06 to 1.67 μm) as shown in figure 3.22a. This corresponds to a SPD above 50 mW/nm between the pump and 1.38 μm as shown in figure 3.22b. The continuum is formed by modulation instability producing fundamental solitons, which then undergo SSFS to longer wavelengths, before generating dispersive waves beyond the second zero dispersion of the PCF. The output power and spectral flatness are slightly curtailed by the high water loss at 1.38 μm in the fibre (13 dB in the 20 m length) whilst the supercontinuum's bandwidth is ultimately limited by the second zero dispersion wavelength at 1.73 μm.

At lower pump powers the classic spectral wings from modulation instability are clearly visible as can be seen in figure 3.23a. It can be shown that the frequency for maximum MI gain is given by $\Omega_{\max} = \pm\sqrt{2\gamma P_0/|\beta_2|}$ where $\Omega_{\max}$ is the frequency shift for maximum gain
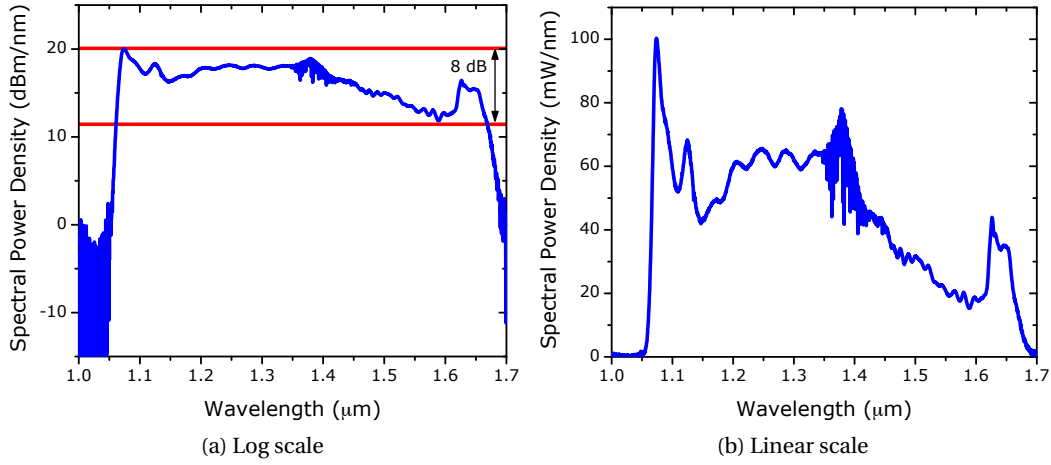
Figure 3.22: Supercontinuum generated by 44 W launched into the PCF on a log scale (3.22a) and a linear scale (3.22b).
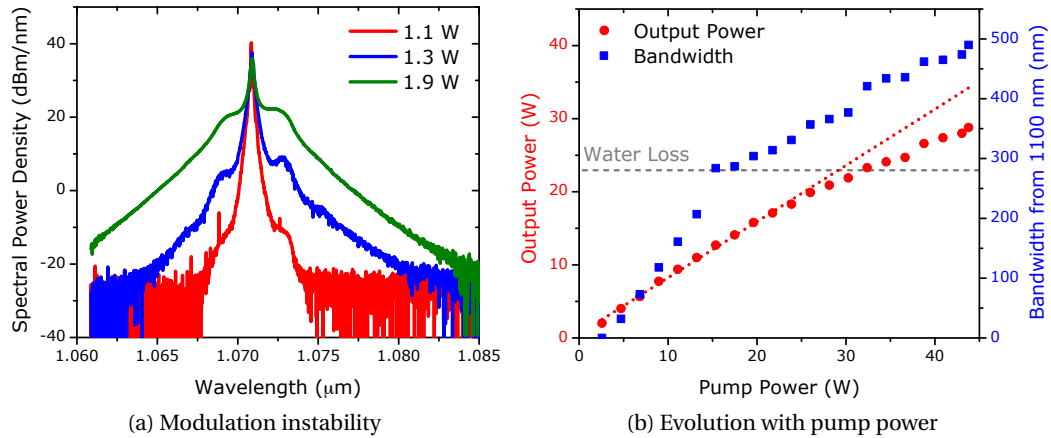

Figure 3.23: 3.23a Modulation instability sidebands at 1.1 W (red), 1.3 W (blue) and 1.9 W (green). 3.23b Evolution of output power (circles) and bandwidth (squares) with pump power.

[34]. For this PCF at the pump wavelength γ = 0.043 (W m)$^{-1}$, β_2 = -0.040 ps^2/m and for a pump power of P_0 = 1.34 W we find Ω_{max} = 1.7 THz. This corresponds to a wavelength change of 1 nm from the pump, which is slightly less than that seen in figure 3.23a (blue line). This perhaps indicates that the real value of β_2 is slightly lower.

The evolution of the continuum with pump power is shown in figure 3.23b. Here we can see progress of the continuum's output power along with the increase in bandwidth of the continuum, where the bandwidth is measured from 1.1 μm to the point where the power has dropped by a further 5 dB. It is clear that the rate of increase of the continuum bandwidth is curtailed once the water loss at 1.38 μm is reached (marked on the graph). It

(a) Pulse durations

(b) Spectra
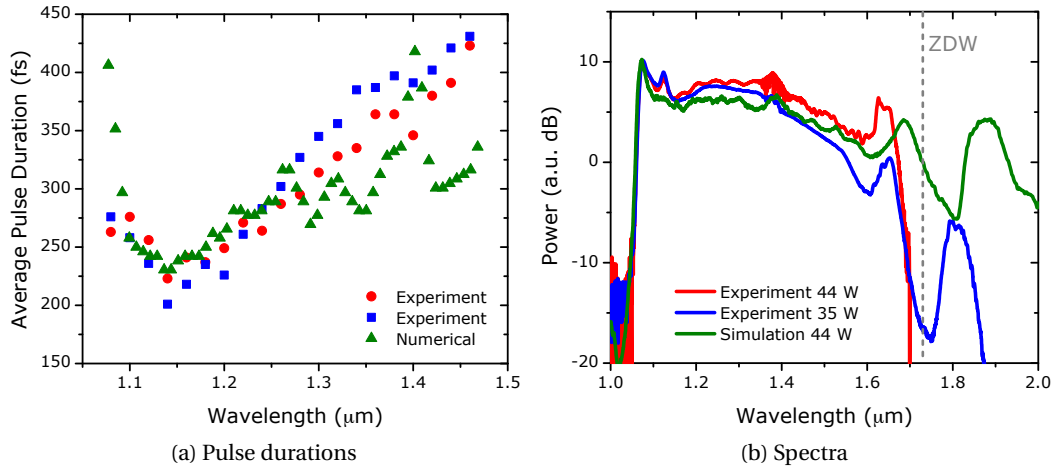
Figure 3.24: 3.24a Average soliton duration with wavelength for two sets of measurements (circles and squares) along with a numerical autocorrelation of a single shot of the simulation (triangles). 3.24b Experimental and numerical continuum results, normalized.

also shows that the power growth falls off from linear as the continuum broadens beyond 1.38 μm. Whilst the use of such a short length of PCF has enabled us to extend beyond the water loss, in contrast with earlier results [17] it is clear that the water loss still affects the continuum. From the experimental measurements (see figure 3.4) the PCF has a higher loss, 60 dB/km, on the long wavelength side of the OH^- induced loss compared to the short, 10 dB/km. It is likely that this higher loss on the long wavelength side contributes to a reduction in bandwidth growth and thus a steady fall in the SPD beyond 1.38 μm as shown in figure 3.22b.

As discussed, the efficiency of the SSFS is clearly an important factor for the generation of the continuum and this is related to the duration of the solitons. As the solitons evolve from MI we can estimate the soliton duration by calculating the frequency of maximum MI gain when P_0 = 44 W. From this we find Ω_{max} = 9.73 THz which gives a period of T_m = 0.65 ps for the pulse train. Assuming that the full-width-half-max of any soliton formed does not exceed $T_m/2$ and accounting for the $sech^2$ pulse shape of a soliton, we find that the maximum duration of a fundamental soliton would be τ_0 = 211 fs. This is slightly shorter than measured (figure 3.24a). From the figure it can be seen that the pulse duration decreases, with a minimum duration at 1.14 μm, and then steadily increases with wavelength. This may be explained by Raman amplification of the solitons followed by a slow loss of energy at longer wavelengths. Also included in figure 3.24a is a numerical autocorrelation from a single shot of the simulation, showing reasonable agreement with the experimental results.

The drawback of using a double zero PCF is that the solitons cannot travel beyond the second ZDW, which limits the long wavelength edge of the continuum. As previously discussed, from theory it is expected that the SSFS will undergo cancellation via spectral recoil and the generation of a dispersive wave beyond the second ZDW. This can be seen in figure 3.24b which shows the spectral output from an experimental measurement of the spectrum further into the infrared, with 35 W launched into the PCF. For comparison the result of a numerical simulation (which includes the fibre's water loss) and experiment both with 44 W launched into the PCF are shown. In all three traces an increase in the SPD can be seen just before the ZDW. This is due to the cancellation of the SSFS leading to a build up of solitons and hence energy just before the ZDW. On the long wavelength side of the ZDW a dispersive wave can be seen. Notably there is a difference in the location of the soliton cancellation and the dispersive wave in the numerical result compared to the experimental measurements. Explanations for this may include: inaccuracy in our calculated dispersion curve, requiring a slightly shorter ZDW; or the possibility of the solitons in our model having higher energies (shorter durations as figure 3.24a) and therefore phase-matching to a dispersive wave at a longer wavelength. The other interesting thing to note is that the dispersive wave sees a much greater amplification in the numerical simulation than our experimental measurement. This may simply be due to the lower pump power of the experiment versus the simulation, or a calibration error, which seems more likely given the results in the next section. The only remaining difference between the simulation and experiment is the presence of a Raman Stokes peak in the experimental data, which was caused by a residual weak back reflections between the angle cleaved end of the PCF and the splice. Finely tuning the cleave angle allows the Stokes line to be minimized. Splicing a multimode fibre to the end of the PCF to form an end-cap is expected to eliminate it. With regards to the numerical simulation it should be noted that using a uniform loss rather than the full spectrally dependent loss profile fails to reproduce the decrease in SPD beyond 1.4 μm seen in the experimental results.

Repeating the analysis of section 3.3.2, the soliton cancellation and dispersive wave generation is clearly seen if we examine a spectrogram of the supercontinuum generated from a single simulation of our numerical model as shown in figure 3.25. The spectrogram shows the development of solitons from MI which then shift to longer wavelengths, colliding and shedding energy before coming to rest just before the second ZDW. Beyond the second ZDW the formation of the corresponding dispersive waves can be seen. It is also clear from the spectrum (on the right side of the spectrogram) that the water loss at 1.38 μm reduces the SPD of the continuum and that the soliton cancellation results in an increased SPD just before the second ZDW.

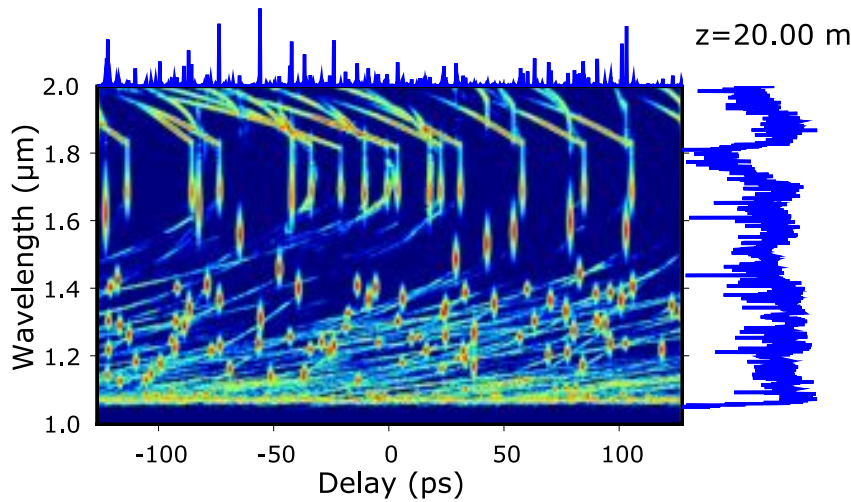Finally, the evolution of the continuum with length was measured via a cutback of the

Figure 3.25: Spectrogram from a single shot numerical simulation for 20 m of PCF and P_0 = 44 W. Scale: -60 dB ▬▬▬▬▬ 0 dB.

PCF. This is shown in figure 3.26a. We can see that the continuum does not significantly broaden beyond 1.4 μm until it has propagated through 14 m. Note the modulations visible at the long wavelengths beyond 15 m are due to a burnt patch cable, which was replaced during the cutback. It is also worth noting that several poor angle cleaves result in the temporary appearance of the first Raman Stokes line. Comparing with the numerical simulation in figure 3.26b we see the numerical simulation broadens out much faster in the first 5 m and broadens beyond 1.4 μm 3 m earlier than the experiment. It is also clear that it is a smaller number of high energy solitons that are crossing the water loss before bunching up due to SSFS cancellation. The more rapid broadening of the continuum in the simulation is probably due to intensity fluctuations, in the time domain, which are greater than that seen in reality. The intensity fluctuations arise from the random spectral phase components which are added to simulate the laser. Unfortunately, these fluctuations are dependent upon the numerical grid chosen. In order to achieve excellent agreement between simulation and reality a more accurate model of the pump laser would be required.

3.4.5 Summary

In this section we have generated a high power CW supercontinuum with a bandwidth extending from 1.06 to 1.67 μm at the 8 dB level. The continuum has the highest spectral power density demonstrated to date, producing more than 50 mW/nm up to 1.4 μm. This was made possible by significantly reducing the splice loss between a standard fibre and the PCF in order to launch high powers into the PCF. Although the use of a short
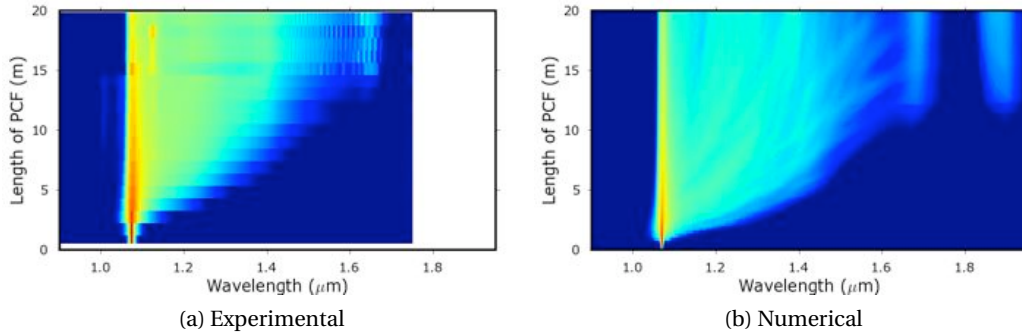
(a) Experimental   (b) Numerical

Figure 3.26: (3.26a) Experimental measurement of continuum evolution via a cutback of the PCF. Scale: -15 dB ▬ 30 dB. (3.26b) Numerical simulation of continuum evolution with length of PCF. Scale: -25 dB ▬ 20 dB.

length of PCF reduced the water loss at 1.38 μm significantly and allowed the continuum to extend beyond it, the loss still plays a dominant role in the continuum evolution. A short low water loss PCF (as demonstrated in section 3.2.1) should enable the generation of a flatter supercontinuum beyond 1.38 μm . The use of a double ZDW fibre in this work has experimentally and numerically confirmed some interesting physical processes including: efficient continuum generation; dispersive wave generation; and soliton recoil in a CW supercontinuum. In the next section we will demonstrate using the second ZDW to control the long wavelength edge of the continuum.

3.5 Control of the bandwidth via a double zero PCF

We have alluded to the possibility of using the second zero of a double zero PCF to ultimately control the extent of the supercontinuum. This idea has been explored numerically [59] and in this section we will look at experimental results based upon three more double zero PCFs made by our colleagues in Lille [60].

3.5.1 PCFs and their properties

The three PCFs are denoted as HF25, HF26, and HF27 with lengths of 60, 55, and 40 m. They have ZDWs of 0.905 & 1.541, 0.973 & 1.379, and 1.049 & 1.173 μm respectively. The dispersion and nonlinearity were calculated from SEMs by modeling a step index fibre using a vectorial effective index method for the cladding [54] as used previosuly. However, as no experimental measurement of any part of the dispersion curve has been made, the position of the second ZDW may not be accurate. This is because very small changes to the hole diameter d and pitch Λ can result in large changes to the dispersion. The

calculated dispersion curves and nonlinearity are illustrated in figure 3.27.
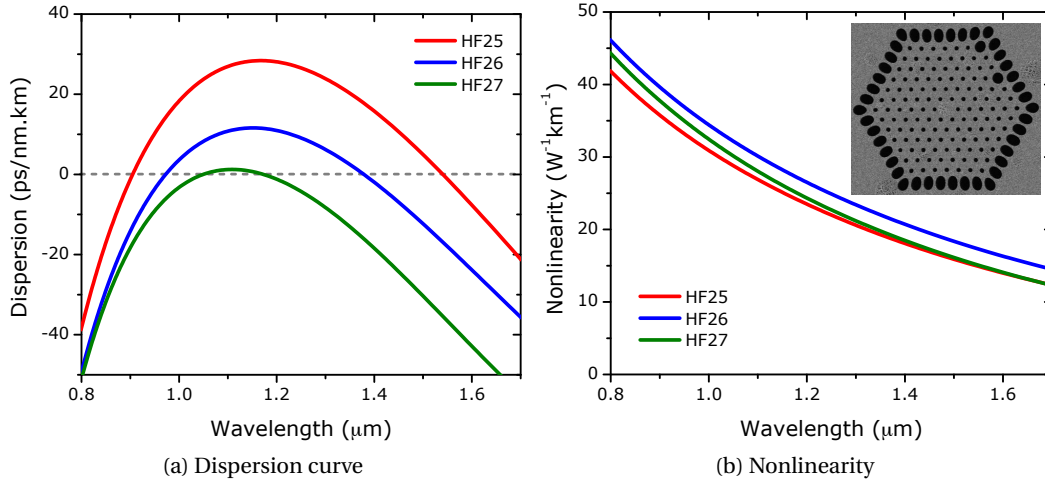

(a) Dispersion curve (b) Nonlinearity

Figure 3.27: 3.27a The calculated dispersion curves. 3.27b The calculated nonlinearity. Inset an SEM of HF25.

All three PCFs have a similar structure to that shown in the SEM inset in figure 3.27b. Of particular importance is the outer set of extra large air holes to minimise confinement loss.

3.5.2 Results

All three PCFs were spliced to the 50 W CW Yb fibre laser and pumped in an identical experimental setup to that described in section 3.4.3. The large outer air holes made splicing awkward. To prevent collapse of these holes very short arc durations of 0.6-0.8 s were used to splice the PCF to a high NA intermediate conventional fibre. The total splice loss was measured as 0.6, 0.4 and 0.4 dB respectively for each of the PCFs. These exceptionally low splice losses are thought to be partly due to the limited guiding of pump light down the large outer air holes.

The results are shown in figure 3.28. For HF25 we see the drop in SPD after 1.38 μm due to the high OH$^-$ loss in the PCF. Similarly the SPD increases just before the second zero and a corresponding dispersive wave is formed; this confirms our expectations as a result of our modelling in section 3.3.2 and from the results of HF14 in section 3.4.4. Of interest is the fact that the SPD of the self-frequency-shift cancelled solitons, and the dispersive wave are similar. This confirms what we had expected from our modelling and suggests that there was a calibration error in the spectrometer used to make the long wavelength measurements for HF14 in figure 3.24b. The remaining feature worth briefly discussing is that there is a slight increase in the SPD before the OH$^-$ induced loss at 1.38 μm. This is

(a) HF25

(b) HF26

(c) HF27
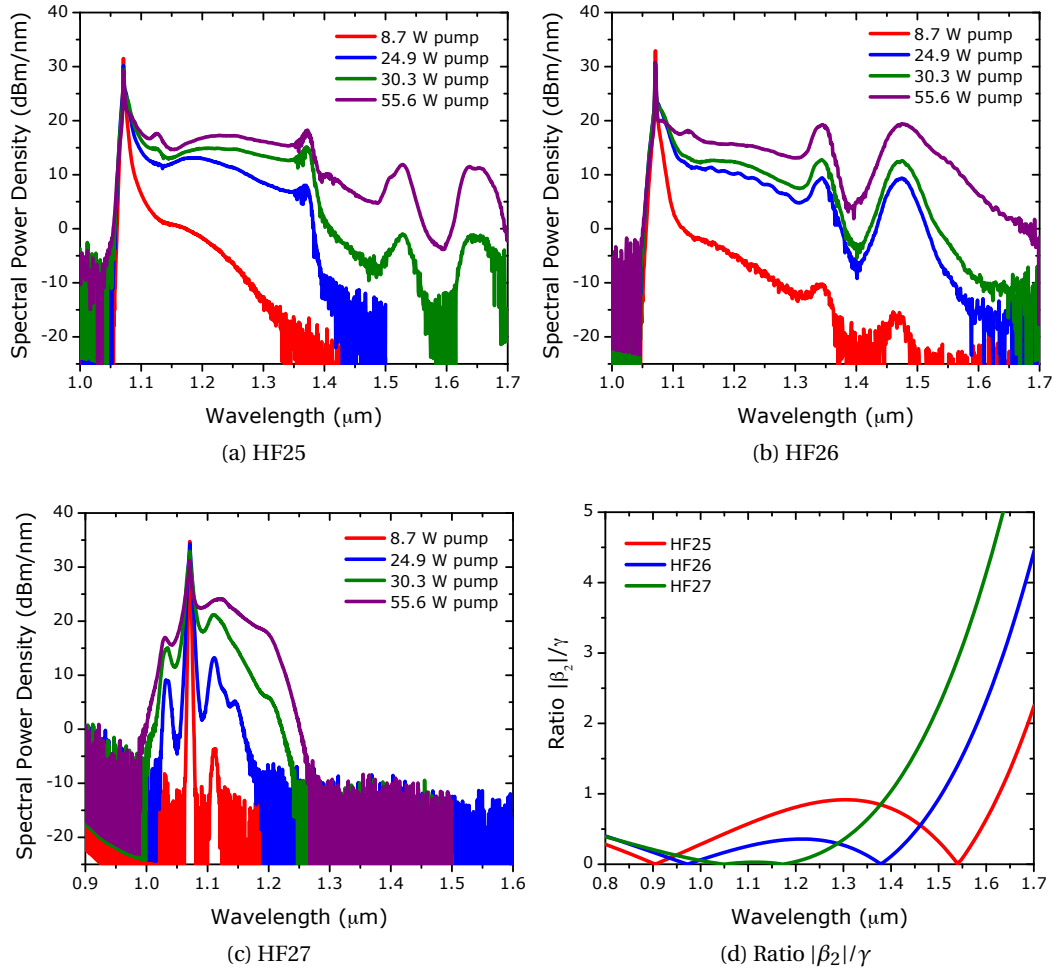
(d) Ratio $|\beta_2|/\gamma$

Figure 3.28: Experimental results for HF25 (3.28a), HF26 (3.28b) and HF27 (3.28c). Note that pump power is the power out of the 50 W CW laser and not the power into the PCF. 3.28d Shows the ratio of $|\beta_2|/\gamma$ for each of the PCFs.

also due to a SSFS cancellation brought about by the high loss.

In HF26 we see the same structure to the continuum except that as the second zero is around 1.38 μm, OH$^-$ induced loss has no effect upon the continuum. The continuum forms more readily in HF26 compared to HF25, which we expected as a result of the change in dispersion and nonlinearity. Despite the shorter region of anomalous dispersion, the SPD has not increased significantly at higher pump powers, the additional pump power is merely transferred to the dispersive wave which can be seen in figure 3.28b. In the case of HF27 the continuum generation is dominated by cascaded MI and FWM with no clear sign of a soliton Raman continuum in the spectrum shown in figure 3.28c. Finally, it is worth noting that there is still significant residual pump present for all three PCFs

compared to HF14. We speculate that a portion of this is pump light which has been guided down the large outer air holes of the cladding and therefore is not interacting in the core of the PCF.

3.5.3 Summary

We have seen that it is indeed possible to exert some control over the bandwidth of the continuum by choosing the location of the second zero. Unfortunately, as the pump power is increased, much of the extra energy is transferred to the dispersive wave. It is hard to imagine applications where this arrangement would be more useful than simple spectral slicing of a broader continuum, such as the one generated in HF14. However, the ability to tune the SPD dip at the zero between the stationary solitons and corresponding dispersive wave may prove useful. Interestingly, when the two ZDW are very close together, as is the case for HF27, then MI and FWM appears to dominate and results in some significant power transfer short of the pump wavelength. The results in these PCFs underline the importance of controlling the dispersion and nonlinearity in order to optimise the efficiency of SSFS, maximising the continuum extension, spectral flatness and SPD.

3.6 Recent results and future directions

Other groups have also recently looked at the issues surrounding double zero PCFs and CW continuum generation. Notably Mussot *et al.* carried out a numerical study [59] in parallel with our work before separate experimental demonstrations by Kudlinski *et al.* at 1 μm [61] and Martin-Lopez *et al.* at 1.5 μm [62]. Moving forward, it seems natural that double zero PCFs with low OH$^-$ losses will enable the flattest, broadest CW pumped continua possible. Similarly, the development of low loss splicing techniques should enable the use of much higher pump powers if desired to create exceptionally high spectral power densities. Further research into the effects of the spectral bandwidth of the pump upon continuum formation is required, although this may only offer limited improvements. This work only goes so far, and spectral extension beyond 2 μm will prove exceptionally difficult in silica based PCFs, so it is likely that other materials such as soft glasses will be explored for this end. The generation of such high power continua in the visible would be of great interest for many applications, however bar HF27 no significant power was generated short of the pump, which is an issue that we will examine in detail in the next chapter.

3.7 Conclusion

In this chapter we have demonstrated some of the flattest, broadest, highest power CW supercontinuum to date. With spectral power densities greater than 50 mW/nm across large portions of the continuum it is hoped that new applications for CW continua will be enabled. There has been genuine interest amongst chemists in these high power continua and hopefully such sources will be made available to them. The experiment results have been made possible through a thorough understanding of the dynamics involved in the formation of CW continua and how best to optimise these processes via control of the PCF's properties. The use of low water loss PCFs with two suitably chosen zero dispersion wavelengths should enable the production of CW continua which are spectrally flat on a linear scale. Furthermore, there is no immediate upper limit on how much pump power could be used to generate a CW continuum other than the intrinsic damage limits of silica.

Bibliography

[1] W. J. Jones and B. P. Stoicheff, "Inverse Raman spectra: Induced absorption at optical frequencies," Phys. Rev. Lett. **13**, 657–659 (1964).

[2] J. K. Ranka, R. S. Windeler, and A. J. Stentz, "Visible continuum generation in air-silica microstructure optical fibers with anomalous dispersion at 800 nm," Opt. Lett. **25**, 25–27 (2000).

[3] J. Dudley, G. Genty, and S. Coen, "Supercontinuum generation in photonic crystal fiber," Rev. Mod. Phys. **78**, 1135 (2006).

[4] P. Persephonis, S. V. Chernikov, and J. R. Taylor, "Cascaded CW fibre Raman laser source 1.6-1.9 μm," Elect. Lett. **32**, 1486–1487 (1996).

[5] M. Prabhu, N. S. Kim, and K. Ueda, "Ultra-broadband CW supercontinuum generation centered at 1483.4 nm from Brillouin/Raman fiber laser," Jpn. J. Appl. Phys. **39**, L291–L293 (2000).

[6] S. V. Popov, P. A. Champert, M. A. Solodyankinand, and J. R. Taylor, "Seeded fibre amplifiers and multi-watt average power continuum generation in holey fibres," in "Proceedings OSA Annual Meeting," (2002), p. 117.

[7] M. Gonzalez-Herraez, S. Martín-López, P. Corredera, M. Hernanz, and P. Horche, "Supercontinuum generation using a continuous-wave Raman fiber laser," Opt. Commun. **226**, 323–328 (2003).

[8] A. Avdokhin, S. V. Popov, and J. R. Taylor, "Continuous-wave, high-power, Raman continuum generation in holey fibers," Opt. Lett. **28**, 1353 (2003).

[9] M. Prabhu, A. Taniguchi, S. Hirose, J. Lu, M. Musha, A. Shirakawa, and K. Ueda, "Supercontinuum generation using Raman fiber laser," Appl. Phys. B: Lasers and Optics **77**, 205–210 (2003).

[10] J. W. Nicholson, A. K. Abeeluck, C. Headley, M. F. Yan, and C. G. Jørgensen, "Pulsed and continuous-wave supercontinuum generation in highly nonlinear, dispersion-shifted fibers," Appl. Phys. B: Lasers and Optics **77**, 211–218 (2003).

[11] A. Abeeluck, C. Headley, and C. Jørgensen, "High-power supercontinuum generation in highly nonlinear, dispersion-shifted fibers by use of a continuous-wave Raman fiber laser," Opt. Lett. **29**, 2163 (2004).

[12] A. Abeeluck and C. Headley, "Continuous-wave pumping in the anomalous- and normal-dispersion regimes of nonlinear fibers for supercontinuum generation," Opt. Lett. **30**, 61 (2005).

[13] S. Martin-Lopez, A. Carrasco-Sanz, P. Corredera, L. Abrardi, M. L. Hernanz, and M. Gonzalez-Herraez, "Experimental investigation of the effect of pump incoherence on nonlinear pump spectral broadening and continuous-wave supercontinuum generation," Opt. Lett. **31**, 3477–3479 (2006).

[14] A. B. Rulkov, S. V. Popov, and J. R. Taylor, "1.5-2.0 μm, multi-watt white-light generation in CW format in highly-nonlinear fibres," in "Advanced Solid-State Photonics," (Optical Society of America, 2004), p. TuA6.

[15] A. B. Rulkov, A. A. Ferin, J. C. Travers, S. V. Popov, and J. R. Taylor, "Broadband, low intensity noise CW source for OCT at 1800 nm," Opt. Commun. **281**, 154–156 (2008).

[16] P. Champert, V. Couderc, and A. Barthelemy, "1.5-2.0-μm multiwatt continuum generation in dispersion-shifted fiber by use of high-power continuous-wave fiber source," IEEE Phot. Tech. Lett. **16**, 2445–2447 (2004).

[17] C. J. S. de Matos, S. V. Popov, and J. R. Taylor, "Temporal and noise characteristics of continuous-wave-pumped continuum generation in holey fibers around 1300 nm," App. Phys. Lett. **85**, 2706–2708 (2004).

[18] P. Hsiung, Y. Chen, T. H. Ko, J. G. Fujimoto, C. J. S. de Matos, S. V. Popov, J. R. Taylor, and V. P. Gapontsev, "Optical coherence tomography using a continuous-wave, high-power, Raman continuum light source," Opt. Express **12**, 5287–5295 (2004).

[19] A. Mussot, E. Lantz, H. Maillotte, T. Sylvestre, C. Finot, and S. Pitois, "Spectral broadening of a partially coherent CW laser beam in single-mode optical fibers," Opt. Express **12**, 2838–2843 (2004).

[20] S. Kobtsev and S. Smirnov, "Modelling of high-power supercontinuum generation in highly nonlinear, dispersion shifted fibers at CW pump," Opt. Express **13**, 6912–6918 (2005).

[21] F. Vanholsbeeck, S. Martin-Lopez, M. González-Herráez, and S. Coen, "The role of pump incoherence in continuous-wave supercontinuum generation," Opt. Express **13**, 6615–6625 (2005).

[22] M. H. Frosz, O. Bang, and A. Bjarklev, "Soliton collision and Raman gain regimes in continuous-wave pumped supercontinuum generation," Opt. Express **14**, 9391–9407 (2006).

[23] A. Hasegawa and F. Tappert, "Transmission of stationary nonlinear optical pulses in dispersive dielectric fibers. I. Anomalous dispersion," App. Phys. Lett. **23**, 142–144 (1973).

[24] S. V. Smirnov, J. D. Ania-Castanon, T. J. Ellingham, S. M. Kobtsev, S. Kukarin, and S. K. Turitsyn, "Optical spectral broadening and supercontinuum generation in telecom applications," Optical Fiber Technology **12**, 122–147 (2006).

[25] C. Kaminski, R. Watt, A. Elder, J. Frank, and J. Hult, "Supercontinuum radiation for applications in chemical sensing and microscopy," Appl. Phys. B: Lasers and Optics **92**, 367–378 (2008).

[26] A. Monteville, D. Landais, O. L. Goffic, D. Tregoat, N. J. Traynor, T.-N. Nguyen, S. Lobo, T. Chartier, and J.-C. Simon, "Low loss, low OH, highly non-linear holey fiber for Raman amplification," in "Conference on Lasers and Electro-Optics/Quantum Electronics and Laser Science Conference," (Optical Society of America, 2006), p. CMC1.

[27] D. Derickson, *Fiber Optic Test and Measurement* (Prentice Hall, 1998).

[28] K. Corwin, N. Newbury, J. Dudley, S. Coen, S. A. Diddams, K. Weber, and R. Windeler, "Fundamental noise limitations to supercontinuum generation in microstructure fiber," Phys. Rev. Lett. **90**, 113904 (2003).

[29] K. Corwin, N. Newbury, J. Dudley, S. Coen, S. A. Diddams, B. Washburn, K. Weber, and R. Windeler, "Fundamental amplitude noise limitations to supercontinuum spectra generated in a microstructured fiber," Appl. Phys. B: Lasers and Optics **77**, 269–277 (2003).

[30] J. C. Travers, S. V. Popov, and J. R. Taylor, "Efficient continuous-wave holey fiber Raman laser," App. Phys. Lett. **87**, 031106 (2005).

[31] S. Martin-Lopez, M. González-Herráez, P. Corredera, M. Hernanz, A. Carrasco, and J. Mendez, "Temperature effects on supercontinuum generation using a continuous-wave Raman fiber laser," Opt. Commun. **267**, 193–196 (2006).

[32] S. I. Yakovlenko, "Mechanism for the void formation in the bright spot of a fiber fuse," Laser Phys **16**, 474–476 (2006).

[33] J. C. Travers, S. V. Popov, and J. R. Taylor, "A new model for CW supercontinuum generation," in "Conference on Lasers and Electro-Optics/Quantum Electronics and Laser Science Conference and Photonic Applications Systems Technologies," (Optical Society of America, 2008), p. CMT3.

[34] G. P. Agrawal, *Nonlinear Fiber Optics* (Springer, 2001), 3rd ed.

[35] J. N. Kutz, C. Lyngå, and B. Eggleton, "Enhanced supercontinuum generation through dispersion-management," Opt. Express **13**, 3989–3998 (2005).

[36] B. Barviau, S. Randoux, and P. Suret, "Spectral broadening of a multimode continuous-wave optical field propagating in the normal dispersion regime of a fiber," Opt. Lett. **31**, 1696–1698 (2006).

[37] J. Hult, "A fourth-order Runge–Kutta in the interaction picture method for simulating supercontinuum generation in optical fibers," J. Lightwave Tech. **25**, 3770–3775 (2007).

[38] J. Laegsgaard, "Mode profile dispersion in the generalised nonlinear Schrödinger equation," Opt. Express **15**, 16110–16123 (2007).

[39] J. C. Travers, "Controlling nonlinear optics with dispersion in photonic crystal fibres," Ph.D. thesis, Imperial College London, Femtosecond Optics Group, Department of Physics, Imperial College London, London, SW7 2AZ, United Kingdom (2008).

[40] O. Sinkin, R. Holzlohner, J. Zweck, and C. Menyuk, "Optimization of the split-step fourier method in modeling optical-fiber communications systems," J. Lightwave Tech. **21**, 61–68 (2003).

[41] M. N. Islam, G. Sucha, I. Bar-Joseph, M. Wegener, J. P. Gordon, and D. S. Chemla, "Femtosecond distributed soliton spectrum in fibers," J. Opt. Soc. Am. B **6**, 1149–1158 (1989).

[42] R. Trebino, *Frequency-Resolved Optical Gating: The Measurement of Ultrashort Laser Pulses* (Kluwer Academic Publishers, 2002).

[43] B. A. Cumberland, "Animations can be found on CD-ROM in bound thesis or at the following url," http://www.mtheory.co.uk/burly/thesis (2009).

[44] J. M. Dudley and S. Coen, "Coherence properties of supercontinuum spectra generated in photonic crystal and tapered optical fibers," Opt. Lett. **27**, 1180–1182 (2002).

[45] D. V. Skryabin, F. Luan, J. C. Knight, and P. S. J. Russell, "Soliton self-frequency shift cancellation in photonic crystal fibers," Science **301**, 1705–1708 (2003).

[46] N. Akhmediev and M. Karlsson, "Cherenkov radiation emitted by solitons in optical fibers," Phys. Rev. A **51**, 2602–2607 (1995).

[47] F. Biancalana, D. V. Skryabin, and A. V. Yulin, "Theory of the soliton self-frequency shift compensation by the resonant radiation in photonic crystal fibers," Phys. Rev. E **70**, 016615 (2004).

[48] D. R. Solli, C. Ropers, P. Koonath, and B. Jalali, "Optical rogue waves," Nature **450**, 1054 (2007).

[49] J. M. Dudley, G. Genty, and B. J. Eggleton, "Harnessing and control of optical rogue waves in supercontinuum generation," Opt. Express **16**, 3644–3651 (2008).

[50] E. Greer, D. Patrick, P. Wigley, and J. Taylor, "Generation of 2 THz repetition rate pulse trains through induced modulational instability," Elect. Lett. **25**, 1246–1248 (1989).

[51] K. Hilligsøe, T. V. Andersen, H. N. Paulsen, C. K. Nielsen, K. Mølmer, S. Keiding, R. Kristiansen, K. P. Hansen, and J. J. Larsen, "Supercontinuum generation in a photonic crystal fiber with two zero dispersion wavelengths," Opt. Express **12**, 1045 (2004).

[52] G. Genty, M. Lehtonen, H. Ludvigsen, and M. Kaivola, "Enhanced bandwidth of supercontinuum generated in microstructured fibers," Opt. Express **12**, 3471 (2004).

[53] M. Frosz, P. Falk, and O. Bang, "The role of the second zero-dispersion wavelength in generation of supercontinua and bright-bright soliton-pairs across the zero-dispersion wavelength," Opt. Express **13**, 6181–6192 (2005).

[54] M. Midrio, M. Singh, and C. Someda, "The space filling mode of holey fibers: an analytical vectorial solution," J. Lightwave Tech. **18**, 1031–1037 (2000).

[55] B. Park, J. Kim, U. Paek, and B. Lee, "The optimum fusion splicing conditions for a large mode area photonic crystal fiber," IEICE Trans. on Elec. **E88-C**, 883–888 (2005).

[56] R. Thapa, K. Knabe, K. L. Corwin, and B. R. Washburn, "Arc fusion splicing of hollow-core photonic bandgap fibers for gas-filled fiber cells," Opt. Express **14**, 9576–9583 (2006).

[57] L. Xiao, W. Jin, and M. S. Demokan, "Fusion splicing small-core photonic crystal fibers and single-mode fibers by repeated arc discharges," Opt. Lett. **32**, 115–117 (2007).

[58] B. Zintzen, T. Langer, J. Geiger, D. Hoffmann, and P. Loosen, "Heat transport in solid and air-clad fibers for high-power fiber lasers," Opt. Express **15**, 16787–16793 (2007).

[59] A. Mussot, M. Beaugeois, M. Bouazaoui, and T. Sylvestre, "Tailoring CW supercontinuum generation in microstructured fibers with two-zero dispersion wavelengths," Opt. Express **15**, 11553–11563 (2007).

[60] A. Kudlinski, B. A. Cumberland, J. C. Travers, G. Bouwmans, Y. Quiquempois, and A. Mussot, "CW supercontinuum generation in photonic crystal fibres with two zero-dispersion wavelengths," in "First Workshop on Speciality Optical Fibers and Their Applications," (2008).

[61] A. Kudlinski, G. Bouwmans, Y. Quiquempois, and A. Mussot, "Experimental demonstration of multiwatt continuous-wave supercontinuum tailoring in photonic crystal fibers," App. Phys. Lett. **92**, 141103 (2008).

[62] S. Martin-Lopez, L. Abrardi, P. Corredera, M. G. Herraez, and A. Mussot, "Spectrally-bounded continuous-wave supercontinuum generation in a fiber with two zero-dispersion wavelengths," Opt. Express **16**, 6745–6755 (2008).

4 Continuous Wave Supercontinuum Generation: Part 2 the Visible

4.1 Introduction

In the previous chapter we examined CW supercontinuum generation in detail. We demonstrated that careful control of the PCF's properties, specifically its dispersion and nonlinearity, enables control over the extent of the supercontinuum and how readily a continuum is formed. This understanding allowed us to demonstrate the highest spectral power density supercontinuum reported to date. This continuum was also amongst the flattest and broadest of all CW continua generated. We also showed that OH^- induced losses had the effect of limiting continuum bandwidth and spectral flatness; these losses can be overcome if suitable procedures are followed during manufacture and subsequent use. We closed the chapter by discussing the design requirements to generate flatter and broader CW supercontinua. Unfortunately, we were not able to demonstrate any significant extension short of the pump wavelength. In fact, short wavelength generation has never been demonstrated at 1μm and although a few results exist at 1.5 μm with CW pumps in conventional fibres, the mechanisms have either been wrongly identified or have not been discussed in detail in the literature.

There is already a great deal of interest in pulse based supercontinuum sources which extend into the visible. Potentially offering higher spectral powers in the visible may well enable new applications, as well as improving the performance of existing applications by easing power based constraints. If the high spectral power densities (SPD) demonstrated in the last chapter could be achieved in the visible, several possible applications would emerge. Even the development of a flat 5 mW/nm source from 0.8-1.2 μm would be potentially useful for applications such as optical coherence tomography (OCT).

In this chapter we aim to explore these issues and demonstrate the first experimental results showing the generation of CW pumped supercontinua which extends short of the pump. We will begin, in section 4.2, by explaining how short wavelengths are formed in the pulsed regime and then look at which of these mechanisms could be utilised in the CW regime. We will also examine some of the CW pumped results achieved to date in this section. In section 4.3, having gained an understanding of the basic design requirements,

we move to demonstrating the first short wavelength generation at 1 μm with a CW pump. We will then explore pumping the same PCF under varying conditions and attempt to simulate these results. These results are complemented by results utilising a 400 W CW laser, which will be examined in detail. This experimental work provides a more complete understanding of the processes involved. In section 4.4, our findings in this chapter along with the previous chapter will form the base of discussions and simulations designed to improve upon our results. Finally we will briefly discuss future possibilities for this research in section 4.5 and then conclude in section 4.6.

4.2 Theory

The mechanism involved to generate wavelengths short of the pump is determined by the pump regime. In the case of pumping with a femtosecond source in the anomalous regime, the femtosecond pulses may be considered to be high order solitons once they enter the fibre as discussed in section 1.4.2. As the high order soliton is not a stable solution, evolution is characterised by the soliton rapidly compressing (temporarily) and then fissioning, ejecting fundamental solitons (see section 1.3.8). The fission process results in excess energy being shed as dispersive waves in the normal dispersion regions. Generally these dispersive waves will undergo no further shifting [1], however under certain circumstances, it is possible that the short wavelength dispersive waves can be coupled to the solitons [2, 3]. This means that as the soliton self-frequency shifts (SSFS) to longer wavelengths, the coupled dispersive wave will be shifted to shorter wavelengths as dictated by the group velocity matching conditions. This is known as the soliton trapping effect and was discussed in section 1.3.8. The soliton trapping effect has also been demonstrated with a picosecond pump source [4].

Thus in the femtosecond regime the initial soliton fission leads to the dispersive wave and potential soliton trapping to generate the short wavelength components. This was illustrated in section 1.3.8, where the energy trapped and shifted by the solitons is clearly visible in figure 1.22, which is repeated here as figure 4.1. If we examine the group-velocity curve for this PCF in figure 4.2, we see agreement between the short wavelength edge and the long wavelength edge of the curve compared with the continuum.

In the picosecond and nanosecond regimes, phase matched four-wave mixing (FWM) can make a significant contribution to short wavelength generation. Where the dispersion curve of the fibre determines a set of phase matching conditions leading to degenerate and non-degenerate FWM [1, 5].

In the CW pump regime the supercontinuum evolves from noise. As we discussed extensively in the last chapter, the CW field is broken up by modulation instability (MI)
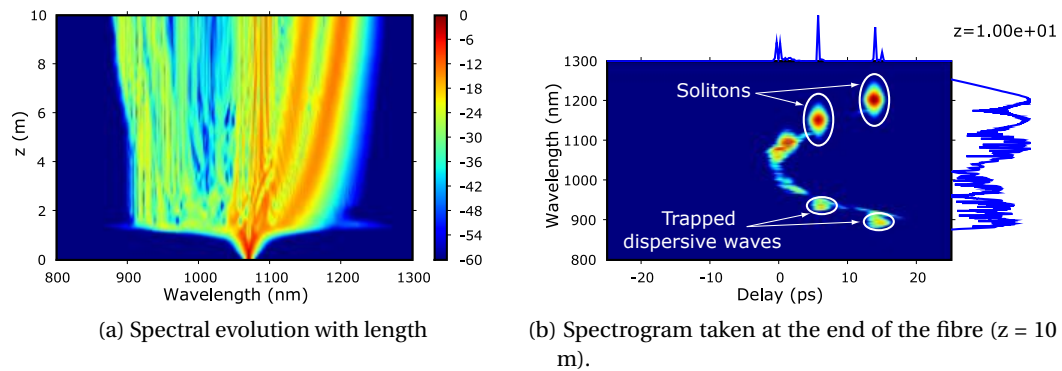
(a) Spectral evolution with length

(b) Spectrogram taken at the end of the fibre (z = 10 m).

Figure 4.1: 4.1a shows the evolution of a 600 W 250 fs pulse along 10 m of PCF (HFa) with a zero dispersion wavelength of 1.038 μm. 4.1b shows the spectrogram taken at the end of the fibre. The solitons and trapped dispersive waves are clearly visible.
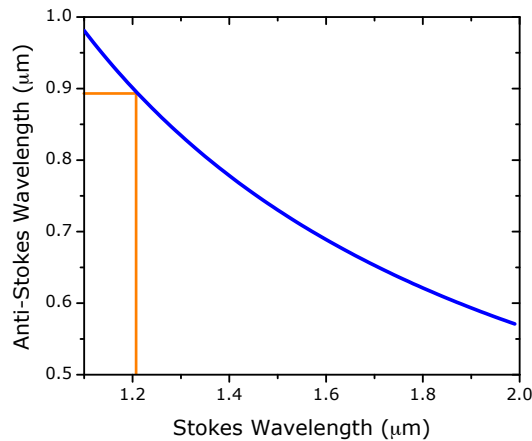

Figure 4.2: Group velocity matched curve for the Stokes and anti-Stokes sides of the pump for HFa. The orange line matches the long wavelength soliton and corresponding dispersive wave shown in figure 4.1b.

which gives rise to fundamental solitons. These solitons then undergo intra-pulse Raman scattering leading to the SSFS, generating a long wavelength soliton Raman continuum. As no high order solitons are generated, the fission process described above is clearly not a feasible mechanism for short wavelength generation. The fission mechanism has been suggested to explain short wavelength generation from a CW supercontinuum at 1.5 μm in several papers [6, 7].

The possible mechanisms to utilise for short wavelength generation from a CW pump are therefore FWM and soliton trapping. If we want to utilise soliton trapping we require a dispersive wave in the normal dispersion region which can be captured. If the trapping mechanism is to work, the soliton must have a sufficiently short duration to generate the

required index modulation in order to trap the dispersive radiation. Once trapped, this energy can be shifted to shorter wavelengths as the soliton self-frequency shifts to longer wavelengths, subject to the required group velocity matching conditions being met [3]. Thus in the CW regime, the initial solitons generated from the MI process have to be short enough (in time) so that spectrally, part of the soliton overlaps into the normal dispersion regime to generate the required dispersive wave. They must also have enough energy to generate a high enough index modulation to trap some of the dispersive wave.

In the last chapter we showed that the highest energy solitons are created when the pump is further from the ZDW for a single zero PCF, or alternatively if the pump is very close to the ZDW where β_2 is very small and dominates over the nonlinearity. If we want to make use of the soliton trapping effect, we need to generate light short of the pump. One method would be to have part of the soliton overlap into the normal dispersion regime and create a dispersive wave which could be trapped. As the solitons generated have a much lower energy than those generated in the pulsed regimes, this means that the pump will have to be very close to the ZDW to enable part of the soliton to overlap into the normal dispersion regime. This constraint can be reduced by significantly scaling up the pump power of the CW source.

Four-wave mixing may also be used for short wavelength generation, this will however be governed by the phase matching conditions. Experimental experience suggests that with low pump powers, FWM generally requires some seeding. One way to achieve this would be to have the anti-Stokes MI sideband extend into the normal dispersion regime. Thus both these mechanisms place very tight constraints on the ZDW relative to the pump, as a result of the low pump powers involved.

As an aside, it is theoretically possible to manufacture a PCF with a ZDW in the visible. Potentially we could then pump in this region to generate a supercontinuum which would extend long off the pump wavelength, which would be similar to the work described in the previous chapter. This could potentially create a CW supercontinuum through the visible region; it would certainly be possible to cover the 0.7-1.0 μm region in this way. The difficulty with this approach is that there are currently no suitable high power CW sources in the visible wavelength region, although a CW Ti:sapphire laser might be used around 0.7 μm. This limitation, combined with the difficulty of making PCFs with a ZDW in the visible and maintaining a suitably low attenuation in these PCFs, make this an unrealistic option at present.

In the next section we will experimentally explore pumping a PCF very close to the ZDW and upscaling the pump power by nearly an order of magnitude.

4.3 Experimental results

In this section we will look at a series of experimental results which are the first to demonstrate short wavelength generation from a CW pumped continuum at 1 μm in a PCF. The inital two experiments pump a PCF with a ZDW of 1.068 μm, whereas the third experiment makes use of a 400 W CW laser to pump a variety of PCFs.

4.3.1 Experiment 1: CW pumping a PCF with a ZDW of 1.068 μm

As discussed in section 4.2, in order to generate a continuum that extends short of the pump, we need to pump very close to the ZDW: this is a result of the low powers involved. To achieve this we ordered a PCF with a ZDW of 1.065 μm . Controlling the dispersion of the PCF during manufacture, to this level, is complex. As a result, it took three attempts to produce the required PCF which was 100 m long (Crystal Fiber) with a ZDW of 1.068 μm (HF23). Figure 4.3 shows the calculated dispersion and nonlinearity of HF23, and a very similar PCF with a ZDW of 1.038 μm (HF5). These values were calculated from SEM images using a free software package called MIT Photonic Bands [8, 9].

(a) Dispersion HF23   (b) Nonlinearity HF23
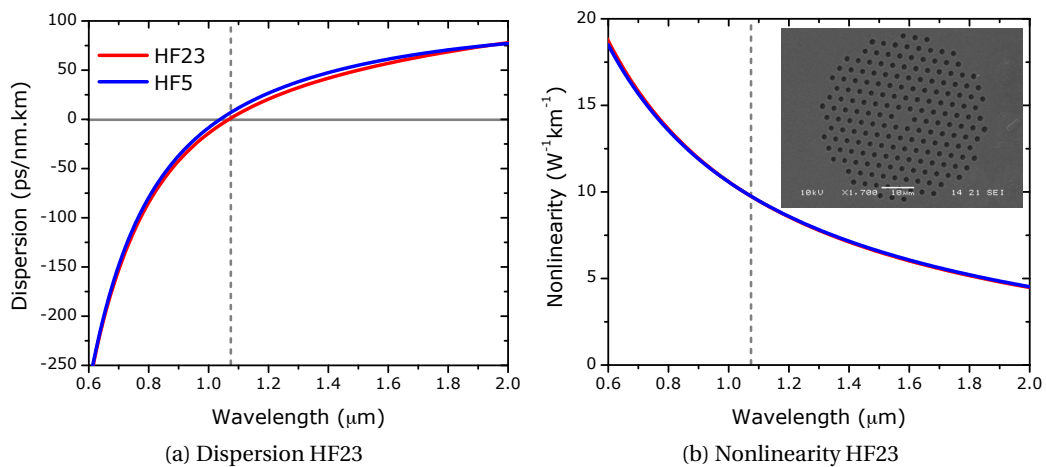
Figure 4.3: 4.3a shows the dispersion with wavelength for HF5 and HF23. The dashed line is the pump wavelength. 4.3b shows the nonlinearity for HF5 and HF23. Inset, SEM image of the PCF HF23.

The experimental set-up simply consisted of a CW pump laser with the PCF spliced to it as illustrated in figure 4.4. The pump laser was a 50 W CW Yb fibre laser (IPG Photonics) with a single-mode output fibre. The laser's emission was centred on 1.071 μm with a linewidth of 1.15 nm. The laser was directly spliced to the PCF, either 100 m of HF23 or 50 m of HF5. Both PCFs have a mode field diameter of ~5 μm. The loss for HF23 was measured as being 9 dB/km with a 130 dB/km peak at the OH$^-$ induced loss at 1.38 μm.

The splice loss was 0.6-0.85 dB and was thermally managed at high pump powers. The output end of the PCF was angle cleaved to reduce back reflections, as these can seed strong Raman-Stokes lines in the continuum. The spectra were measured on an Advantest (Q8384) and visible Anritsu (MS9030A/MS9701B) optical spectrum analyser (OSA) whilst the power was measured using a thermal power meter (Molectron PM10).
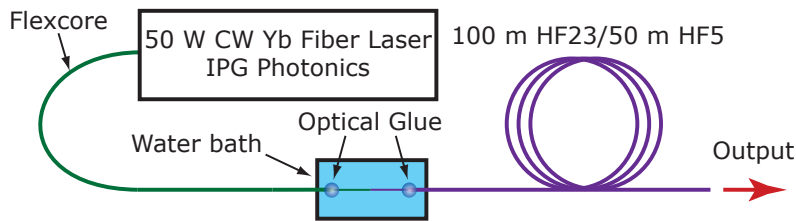

Figure 4.4: Experimental setup.

Just to illustrate the importance of the ZDW, we pumped 50 m of HF5 with the 50 W CW laser. With 49.2 W of pump power (40.9 W launched into the PCF) a rather poor long wavelength continuum was generated, as shown in figure 4.5. We can see that a small amount of energy is transferred short of the pump to 0.987 μm via a dispersive wave.
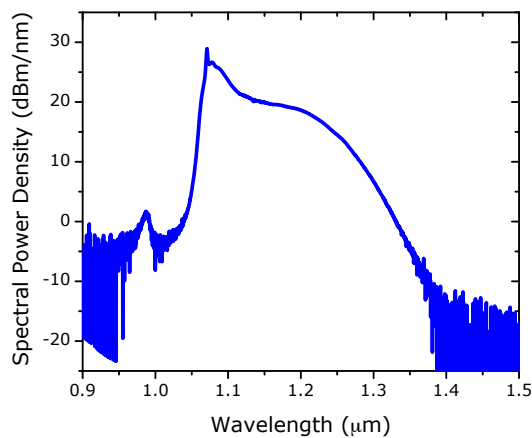
Figure 4.5: Supercontinuum from 50 m of HF5 with 40.9 W launched into the PCF. Continuum output power is 28 W.

If we now examine the results for HF23 shown in figure 4.6, we see that significant short wavelength generation is possible and that it evolves with the long wavelength edge of the continuum. The figure shows the evolution of the supercontinuum under CW pumping for several different pump powers. At maximum pump power, 47.3 W is launched into the PCF with a 32.6 W continuum produced. The SPD is very high: 141, 26, 32, 4 mW/nm at 1.10, 1.38, 1.05, 0.95 μm respectively. The MI side bands are clearly visible at low pump powers , with continuous extensions to longer and shorter wavelengths as

(a) Continuum evolution up to 25.7 W   (b) Continuum evolution up to 47.3 W
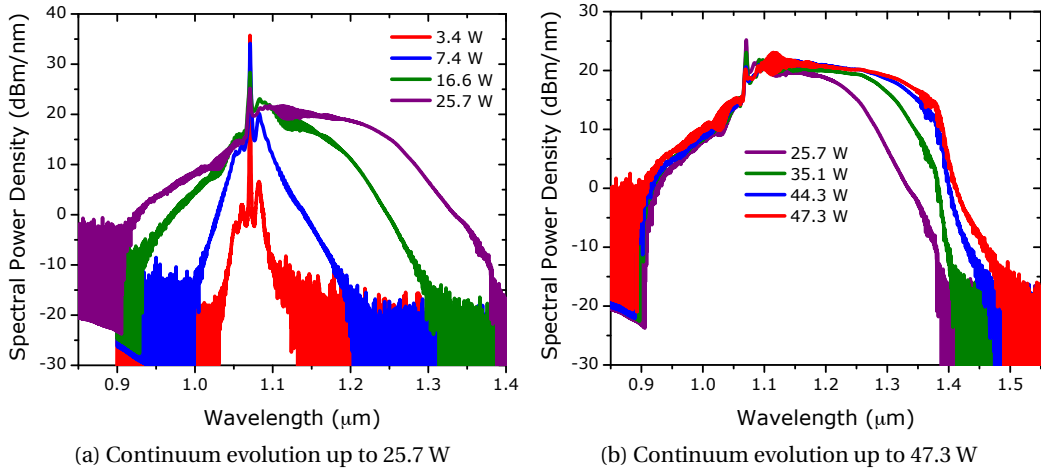
Figure 4.6: Evolution of the supercontinuum with increasing pump power. Powers marked represent the power launched after the splice. For 47.3 W the continuum output power was 32.6 W.

the pump power is increased. Eventually, the long wavelength edge of the continuum is limited by OH$^-$ loss at 1.38 μm. The anti-Stokes side is 5 dB less than the Stokes side immediately next to the pump, which may initially be due to limited energy transfer to the short wavelength side; then combined with losses due to the short wavelength side pumping the long wavelength side via Raman. It should also be noted that the noise floor of the OSA is 17 dB higher around 0.9 μm, compared with that above 1.0 μm. To understand the dynamics we need to discover whether the short wavelength side is due to FWM or soliton trapping. To do so, we can examine the phase matching curves shown in figure 4.7.

Figure 4.7 shows the phase matching curves for pump powers of 7.4 W (4.7a) and 47.3 W (4.7b). The Stokes and anti-Stokes curves are blue and green respectively. The available short pump wavelengths due to MI are denoted by the large shaded orange bar along the bottom x axis. The available long seed wavelengths, due to MI or the soliton Raman continuum, are marked on the right y axis by the large shaded green bar. The upper and lower wavelength limits available via FWM are denoted by the red lines intersecting the phase matching curve at the limiting seed wavelength. These phase matching curves were calculated for the 12 different pump powers and found to be in good agreement with the spectral evolution in every case. The most likely FWM process is given by equation 4.1.

$$\omega_{pump} + \omega_{MI_{short}} = \omega_{Stokes} + \omega_{anti-Stokes} \tag{4.1}$$

Notably, the soliton Raman continuum appears to act as the Stokes seed and is the limiting

(a) Phase matching curve for 7.4 W   (b) Phase matching curve for 47.3 W
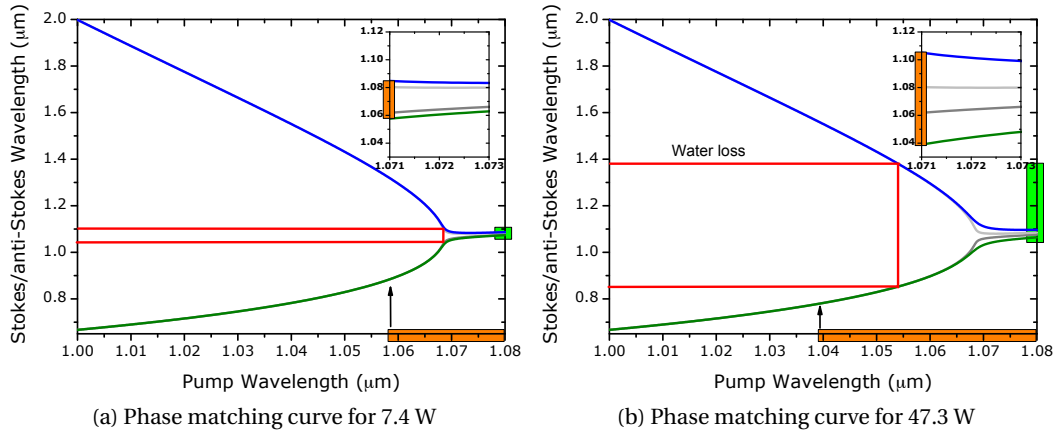
Figure 4.7: Phase matching curves for FWM. The orange bar on the x axis represents the wavelengths generated through the initial MI (shown in the inset figure). The green bar on the y axis denotes the longest wavelength available through either MI or the soliton Raman continuum. The red lines therefore represent the maximum and minimum wavelengths that can be generated through FWM.

factor on the anti-Stokes wavelength. We would expect that as the pump wavelength is shifted further from the ZDW, there will come a point when the short wavelengths generated via MI become the limiting factor on the anti-Stokes wavelength.

The phase matched FWM appears to be in excellent agreement, but what about the possibility of group velocity matched soliton trapping? Unfortunately, it is impossible to rule out soliton trapping as a mechanism in this case. As figure 4.8a shows, the matching conditions are almost identical until 1.3 μm. At longer wavelengths the curves deviate slightly and at these wavelengths the phase matched curve is in slightly better agreement with the data. Irregardless of whether it is a FWM, soliton trapping effect, or a combination of the two, it is clear that if we want to extend the continuum to much shorter wavelengths, the long wavelength edge of the continuum needs to extend beyond the OH^- induced loss at 1.38 μm. To demonstrate this, we modulated the pump to produce μs pulses.

Modulating the CW laser, via the TTL input at 7.8 kHz with a 72% duty factor, enhances the continuum beyond that expected from the peak power increase alone (previously shown in figure 3.7b). This may be due to enhanced noise driving the MI process. As a result of the peak power enhancement, figure 4.8b shows that a number of solitons now have sufficient energy to cross the OH^- loss at 1.38 μm, resulting in short wavelength generation down to 650 nm. Analysing the continuum evolution shows that the short wavelength edge appears to expand faster than that allowed by FWM alone. To explain this increased rate of expansion, one has to invoke soliton trapping as a mechanism. The dashed lines in figure 4.8b mark corresponding spectral features on the long and
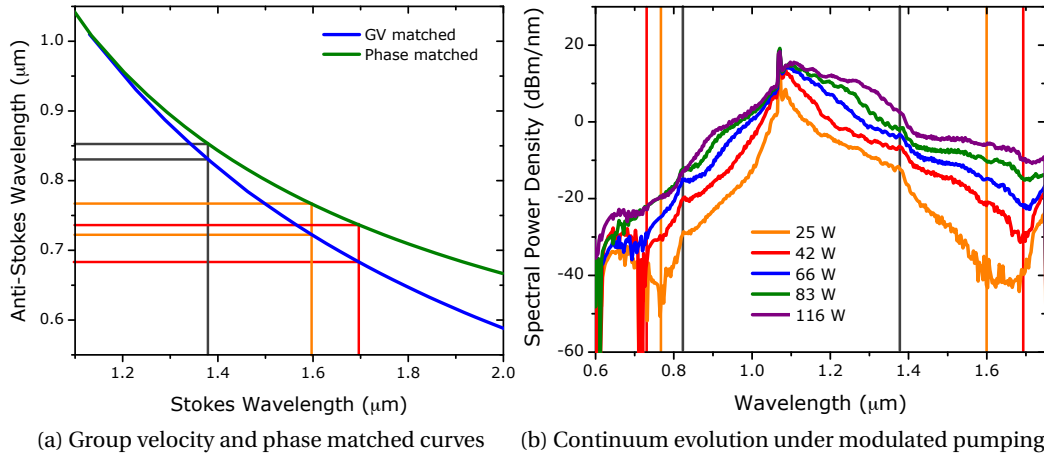
(a) Group velocity and phase matched curves   (b) Continuum evolution under modulated pumping

Figure 4.8: 4.8a Group velocity and phase matched curves for HF23. Corresponding spectral features of figure 4.8b are marked. 4.8b Supercontinuum evolution with pump power using a modulated pump source. Vertical coloured lines mark particular spectral features.

short wavelength sides. The drop due to the OH$^-$ loss at 1.38 μm has a corresponding spectral feature at 0.82 μm. Examining this on the group velocity and phase matching curves, shown in figure 4.8a, we can see that the group velocity matching curve, and thus soliton trapping, is the more convincing explanation. However, spectral features at longer wavelengths (denoted by the orange and red lines) are in much better agreement with the FWM phase matched curve. Hence it seems likely that both FWM and soliton trapping are playing an active role in the short wavelength generation. One may speculate that the OH$^-$ loss makes the solitons increase in duration, thus reducing their power; consequently the intensity dependent refractive index reduces so the cross-phase modulation effect also reduces, weakening the trapping and possibly allowing FWM to dominate. On the other hand, the loss may simply act as a barrier curtailing the number of solitons shifting to longer wavelengths and their corresponding trapped dispersive waves, reducing the power shifted short. In either case, FWM appears to become more significant at the shorter wavelengths. The short wavelength edge of the continuum is now defined by the high losses in the PCF beyond 2 μm.

Simulations

We can attempt to understand this further by simulating the experiment using the same model as described in section 3.3.2. A time window of 256 ps was used in combination with a frequency window of either 2^{16} or 2^{17} points, depending upon the spectral bandwidth required. The simulations were generally performed four times with a different

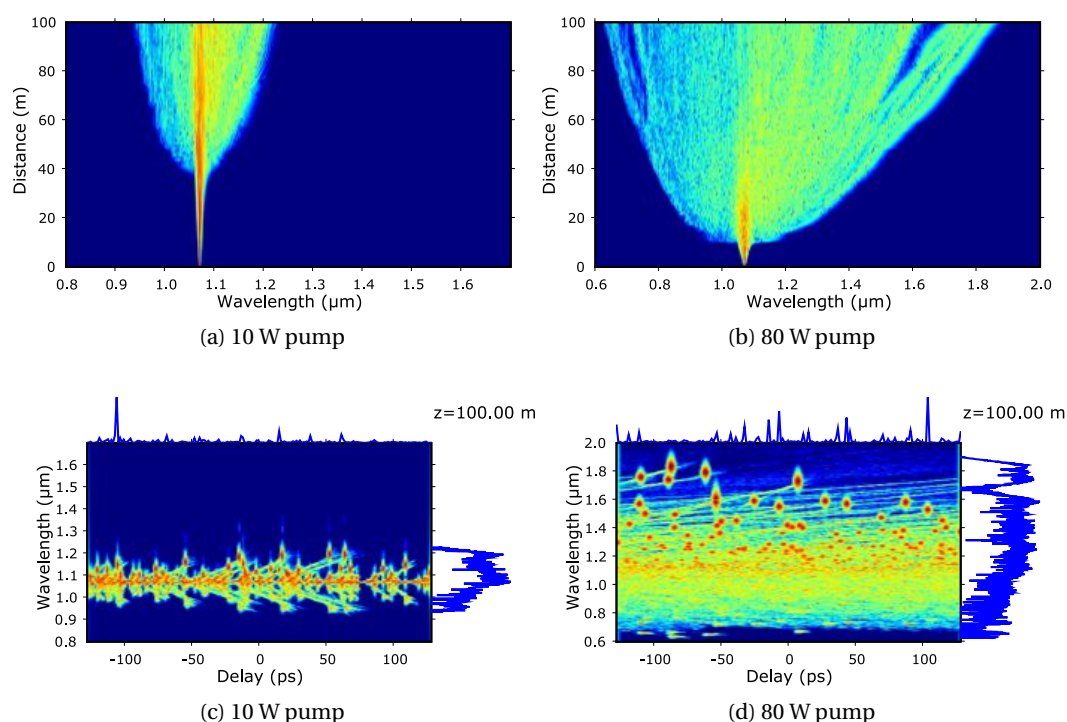(a) 10 W pump

(b) 80 W pump

(c) 10 W pump

(d) 80 W pump

Figure 4.9: 4.9a-4.9b Evolution of supercontinuum with length in HF23 for a single shot simulation of a CW laser. Scale: -60 dB ▮▮▮ 0 dB. 4.9c-4.9d Spectrograms after 100 m of propagation in HF23. Scale: -80 dB ▮▮▮ 0 dB.

initial random spectral phase each time. Although, it would be helpful to average over a much larger number of simulations, the computing resource required would dramatically increase. The results detailed are therefore the averaged results unless otherwise stated.

Propagation of a 10, 20, 40 and 80 W CW field was simulated through 100 m of HF23. The evolution with length for the 10 and 80 W pumps is shown in figure 4.9 along with the associated spectrograms. As expected, the increase in pump power results in the continuum forming earlier in the PCF, ultimately leading to a broader supercontinuum after the full 100 m of propagation. The spectrograms show clear signs of soliton trapping with the shortest wavelengths generated through trapped dispersive waves. Unfortunately, it is not so easy to identify the effects of FWM and XPM from the spectrograms. It seems likely that both of these effects probably contribute to the short wavelength generation in the supercontinuum.

Figure 4.10a shows the averaged simulated spectral for each of the pump powers. The simulations display similar spectral features to that seen experimentally, notably the initial ~ 10 dB drop in SPD on the short wavelength side followed by a gradual decline in the SPD as the wavelength decreases. As the pump power is increased not only does

(a) Simulated spectra
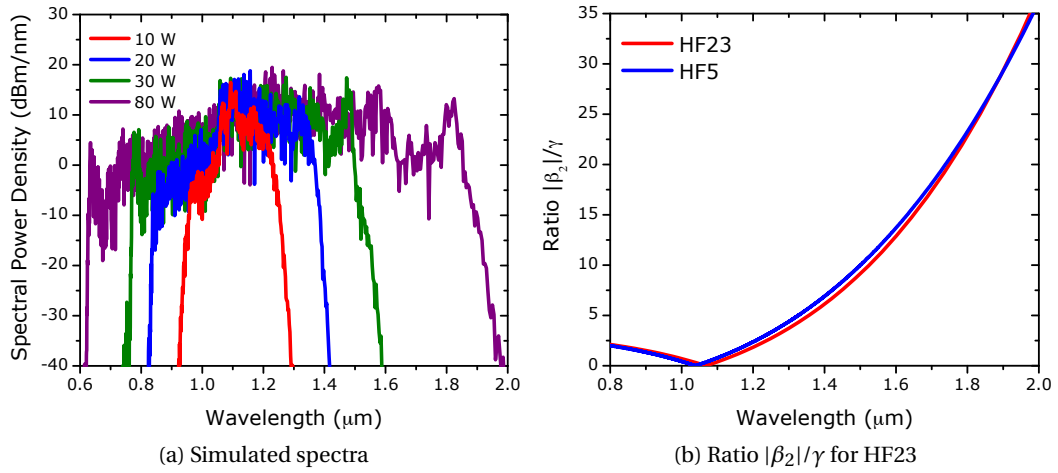
(b) Ratio $|\beta_2|/\gamma$ for HF23

Figure 4.10: 4.10a Average of 4 simulated spectra for HF23 pumped at 10, 20, 40 and 80 W. 4.10b Ratio $|\beta_2|/\gamma$ for HF23 and HF5.

the long and short wavelength sides extend as expected, but the magnitude of the initial drop on the short wavelength side and the rate of decrease of the SPD both reduce. This is easily understood if we consider the spectrograms. As the pump power is escalated both the number and energy of the solitons formed increases. This results in more dispersive energy on the short wavelength side of the pump, along with more solitons to potentially trap and transfer that energy to shorter wavelengths. Additionally, the extra short wavelength generation may act as a more efficient seed for FWM processes.

The requirement for high energy solitons arises not only from the criteria that they are broad enough spectrally to overlap with the normal dispersion region, but they must also have enough energy to continue to self-frequency shift under the increasing ratio of $|\beta_2|/\gamma$. The changing ratio is shown in figure 4.10b, and illustrates that the solitons will have a lower peak power and increased duration at longer wavelengths. Therefore their ability to self-amplify via Raman, and thus self-frequency shift is reduced.

4.3.2 Experiment 2: Tuning the pump wavelength

An immediate question which arises from the experimental results of the last section concerns the pump wavelength and its impact upon the short wavelength generation. In order to explore this issue we built a tunable 1 μm CW laser which produced up to 9 W of pump power between 1.060 and 1.076 μm. The system was based upon a 150 mW laser diode (Lumic LM-1065M150) in combination with a tunable fibre Bragg grating (FBG). As the laser diode produced a single frequency output it was necessary to modulated the drive current with a radio frequency (RF) driver to suppress stimulated Brillouin scattering

(SBS) effects. Regrettably, the 9 W of available pump power was not sufficient to generate a continuum in the 100 m length of HF23. In order to increase the peak power an acousto-optic (AO) modulator was added to the system before the final amplifier. A diagram of the setup is shown in figure 4.11.
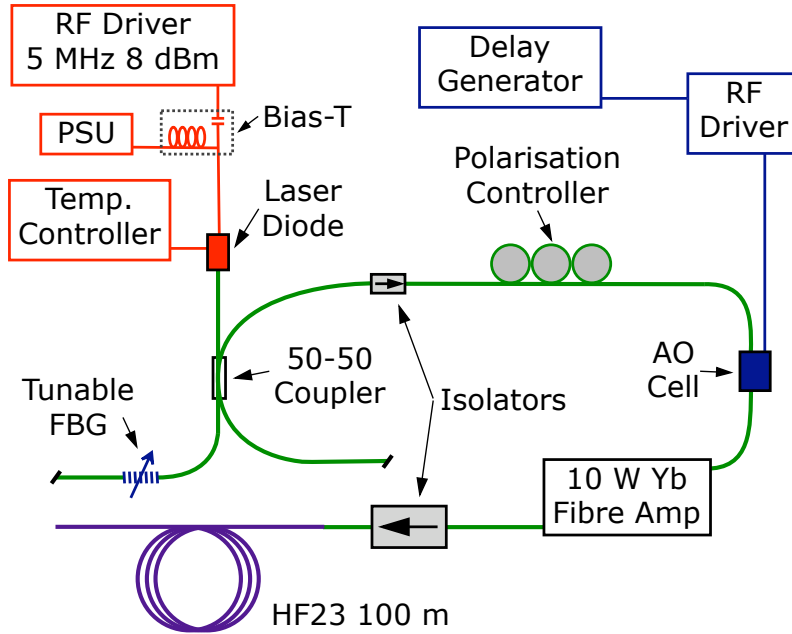

Figure 4.11: Experimental setup for tunable wavelength pumping.

The AO cell was modulated by a delay generator producing 7 ns pulses at 10 MHz. The optical pulses were measured on an oscilloscope and the duty factor, calculated via integration, was found to be 19. Thus the maximum peak pump power was 170 W. The PCF was pumped between 1.060 and 1.076 μm in 2 nm increments at a variety of pump powers. The spectra were measured on a visible Anritsu (MS9030A/MS9701B) OSA whilst the power was measured using a thermal power meter (Molectron PM10). A subset of the experimental results are shown in figure 4.12.

Pumping with 21 W at the different wavelengths leads to the spectrum broading after propagating through 100 m of HF23, with the 1068 and 1072 nm sources showing additional broadening due to MI/FWM. As the pump power is increased further it is clear that pumping between the ZDW at 1068 nm and 1072 nm produces the broadest continuum on both the long and short wavelength sides of the pump. The results for pumping at 1070 nm (not shown in figure 4.12) were marginally better than those for 1068 or 1072 nm, and comparable to those of figure 4.8b. Pumping so close to the ZDW means that $|\beta_2|$ is very small (0.04 - 0.5 ps^2/km for 1068 - 1072 nm) and dominates the formation of solitons as discussed in section 3.3. This results in high energy solitons which spectrally overlap

(a) 21 W pump

(b) 74 W pump

(c) 170 W pump

(d) Simulated results 10 W
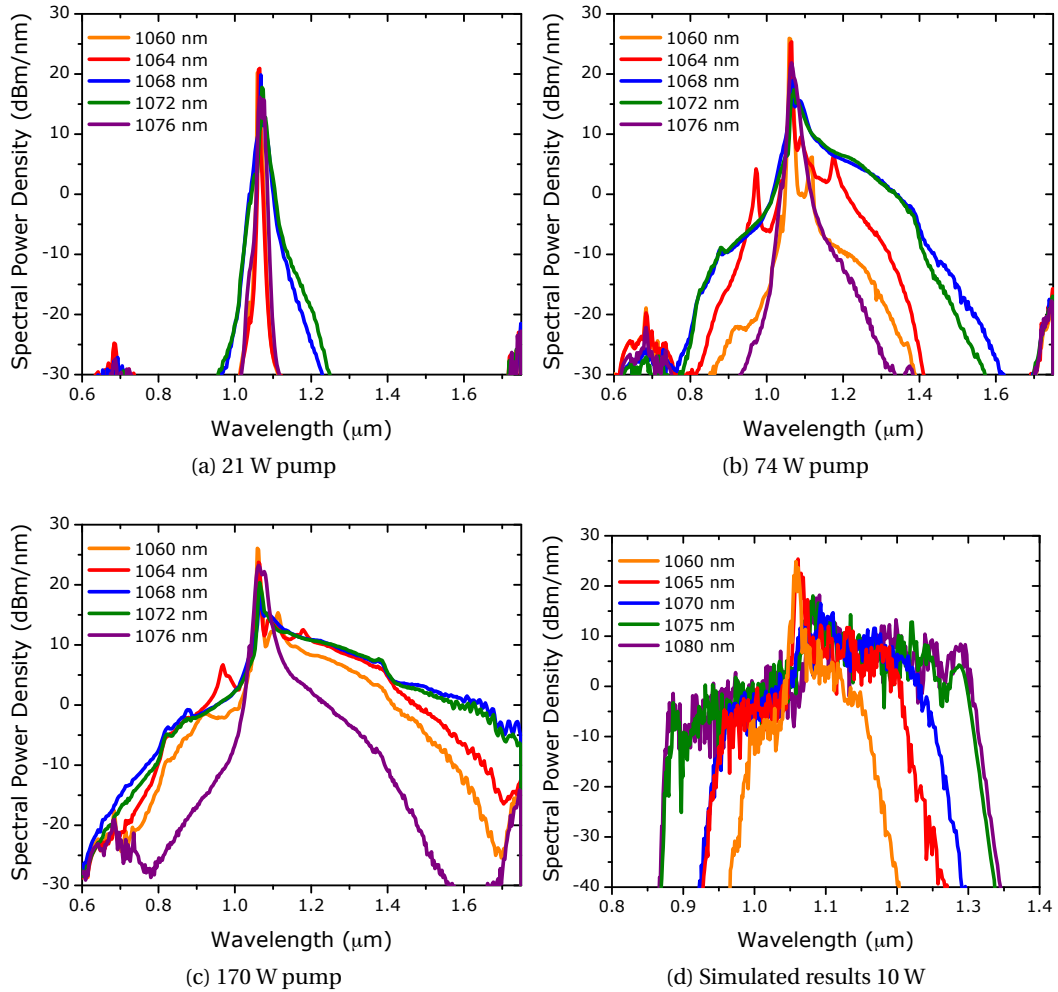
Figure 4.12: 4.12a-4.12c Spectral evolution for pumping 100 m of HF23 at varying wavelengths with the peak powers given. 4.12d Simulated results assuming a 10 W CW pump.

with the normal dispersion region creating a dispersive wave. As the pump wavelength is increased, the value of $|\beta_2|$ also increases to the extent that by 1076 nm it is no longer small enough to dominate over the nonlinearity governing the soliton formation (1 ps^2/km). As a result the solitons have less energy and the long wavelength edge of the continuum when increasing the pump wavelength from 1072 to 1076 nm reduces; as a consequence the short wavelength edge is also diminished.

Pumping close to the ZDW on the normal dispersion side (i.e. at a wavelength shorter than the ZDW) also results in a continuum which extends short and long of the pump wavelength. As the pump power is increased, a significant amount of energy is transferred via Raman to the first Stokes line which is in the anomalous region. From this point

solitons can form up to generate the long wavelength side of the continuum, while it seems likely that FWM initiates the short wavelength side. Indeed the strength of the FWM process is clearly visible in figure 4.12b where there are peaks at 972 and 1176 nm. In this case, the residual pump diode light of the 10 W Yb fibre amplifier acts as a seed for the FWM. Hence we have $2\omega_p = \omega_2 + \omega_3$ where ω_p is the pump wavelength of 1064 nm and ω_2 and ω_3 are the Stokes and anti-Stokes light respectively. The process also requires that the phase matching conditions, given by the phase matching curve (figure 4.8a) are met. What is remarkable about this is that the residual 972 nm diode light is not detectable on an OSA and is at least 50 dB below the pump power at 1064 nm. Thus it is clear that FWM is an extremely efficient process provided that some seed light is available. Finally it should be noted, that as the pump is shifted to shorter wavelengths, the bandwidth of the continuum reduces as we would expect.

Simulating the changing pump wavelength using our code fails to reproduce the experimental trends as shown in figure 4.12d. As the pump wavelength is increased from 1060 to 1070 nm the bandwidth of the continuum produced increases as we would expect. However, for 1075 and 1080 nm the bandwidth increases further. This may be a result of the linewidth difference: the experiment was based upon a source with a linewidth of < 0.07 nm but it was modulated over a 0.2 nm bandwidth in order to suppress SBS. In contrast, the simulation was based upon a 1.0 nm bandwidth, and decreasing the bandwidth requires significantly higher pump powers to form a continuum as well as taking considerably longer to simulate. The technique of adding noise to the initial conditions of the simulation becomes increasingly unsatasifactory as the bandwidth is reduced. Substantial improvements to the model may be required in order to reproduce the experimental results.

4.3.3 Experiment 3: Very high power pumping

In section 4.2 we mentioned that either very careful control of the dispersion or extremely high pump powers would be required to extend a CW pumped supercontinuum to wavelengths short of the pump. We have already demonstrated fine control of the ZDW in the previous two experiments so we shall now turn our attention to extremely high power pumping.

In the last chapter we improved the typical splice loss between a PCF and a conventional fibre. We stated our belief that it would be possible to launch significantly more power through such a splice without any problems. In this experiment we make use of a 400 W CW fibre laser (kindly leant to us by IPG Photonics for a week) to pump 50 m of HF5 which has a ZDW of 1.038 μm. HF5 is made from the same preform structure as HF23 and differs only slightly from HF23 which is clear from the dispersion and nonlinearity curves

shown in figure 4.3. We have also already demonstrated that with the 50 W pump it was not possible to generate a continuum which extended significantly short of the pump in HF 5 (see figure 4.5).

The laser emitted up to 432 W of average power at 1.07 μm , with a random polarisation and a linewidth of 3.6 nm, in a collimated output with a beam diameter of 7 mm. It was therefore necessary to re-couple the light back into a fibre. A lens was used to focus and launch into a length of large mode area (LMA) fibre, which was in turn spliced to a length of Flexcore, which was spliced to HF5, as shown in figure 4.13. Each splice was attached to a metal heat sink with optical glue being used to strip cladding modes. The free-space coupling efficiency was typically greater than 70 % and to reduce the thermal load on the launch lens, the laser was modulated with a duty factor of between 1 and 40.
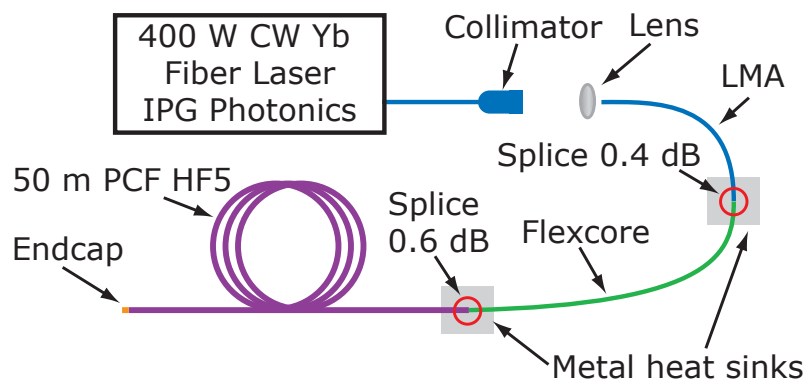
Figure 4.13: Experimental setup.

With 230 W of pump light launched into the PCF, a continuum extending from 0.6 to 1.9 μm was produced as shown in figure 4.14a. The inset photograph in figure 4.14a shows the visible part of the spectrum with a SPD of ~1 mW/nm in the red. Confirming the trends seen in the previous experiments, we see that the SPD of the short wavelength side of the continuum decreases as you move further from the pump. One new feature is a large dip in SPD at the first ZDW of the PCF. This arises from the wave vector matching conditions on either side of the ZDW.

If we examine the phase-matching and group velocity matched curves for HF5 (figure 4.14b), we see that whilst the two are initially in agreement, they diverge at longer wavelengths. If we examine the long wavelength edge of the continuum, as marked on the figure, the group velocity matched curve allows for a short wavelength edge of 594 nm whereas the phase-matched curve allows for 662 nm. Thus, it is clear that the shortest wavelengths (589 nm marked by the orange line in figure 4.14a) are generated through the soliton trapping mechanism. However, there is a 2.5 dB drop in SPD at 677 nm at the shoulder on the curve (marked by the purple dashed line in figure 4.14a). This is the
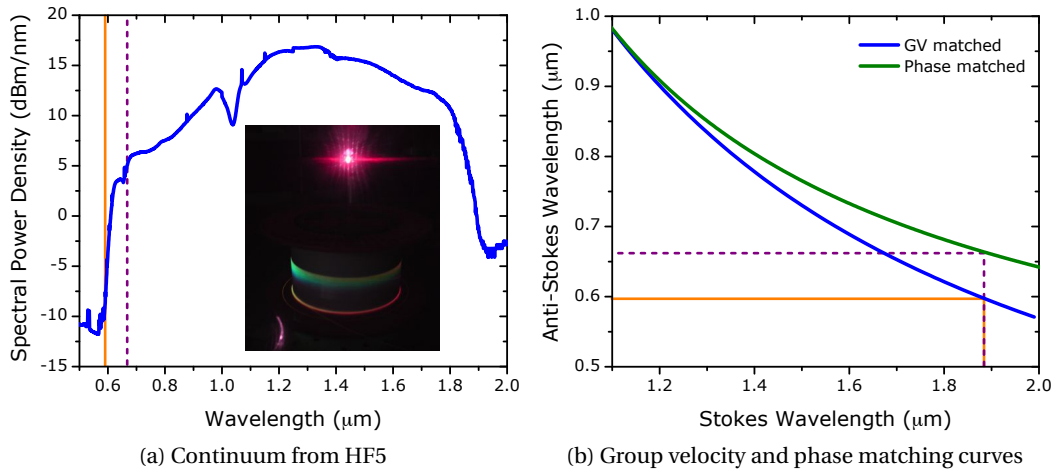
(a) Continuum from HF5

(b) Group velocity and phase matching curves

Figure 4.14: 4.14a Supercontinuum produced in 50 m of HF5 with 230 W of equivalent
pump power. Inset: Photograph of the PCF and visible output. 4.14b Group velocity
and phase matched curves for HF5. The long wavelength edge of the continuum is
marked along with the correspondingly matched short waveelengths.

short wavelength limit of the FWM process, suggesting that FWM also makes a significant
contribution to the spectral power on the short wavelength side of the pump. The slight
discrepancy in wavelengths measured and those derived from the phase-matching curves
almost certainly indicates a slight error in the calculated dispersion curve.

The long wavelength edge ultimately limits the short wavelength edge of the continuum,
and for the continuum generated in HF5 this is not governed by the edge of the silica
transmission window of the PCF. Instead the solitons gradually stop self-frequncy shifting
due to a dramatic increase in the ratio of $|\beta_2|/\gamma$ (see figure 4.10b). If the continuum
extended beyond 2 μm then the short wavelength edge would be shifted to 550 nm.
Clearly, it would be desirable to extend further into the visible; different approaches such
as cascading PCFs or long PCF tapers would be required to bring this about [5, 10].

The results in HF5 show that, given enough pump power, it is possible to extend a CW
continuum down into the visible. The results also clearly demonstrate that both soliton
trapping and FWM are involved in generating the short wavelength part of the continuum.

4.3.4 Summary

The three experiments described above have shown that it is possible to generate wave-
lengths short of the pump in CW pumped supercontinuum. The results have indicated
that both soliton trapping and FWM play a role in generating the short wavelength com-
ponents. Yet, to generate such short wavelengths, we have shown that the pump must be

Fibre	d/Λ	Λ μm	γ_p W^{-1}km^{-1}	D_p ps.nm^{-1}km^{-1}	λ_{ZDW} μm	Change in ratio* $|\beta_2|/\gamma$
HF23	0.47	3.7	10	0.4	1.068	56
HFi	0.327	2.6	12	0.3	1.068	79
HFj	0.332	2.25	15	0.1	1.069, 1.896	5.5
HFk	0.35	2.0	19	0.3	1.066, 1.515	2.5
HFl	0.36	1.9	21	0.2	1.067, 1.398	1.3

Table 4.1: Properties of PCFs used. γ_p is the nonlinearity at the pump wavelength(1.07 μm), D_p is the dispersion at the pump wavelength, and λ_{ZDW} is the location of any zero dispersion wavelengths less than 2.5 μm . *The change in the ratio of $|\beta_2|/\gamma$ is calculated between the pump wavelength and 1.4 μm.

within several nanometers of the ZDW or alternatively an exceptionally high power CW source must be utilised. These two exacting requirements are almost certainly the reason that short wavelength generation has not been seen before at 1 μm.

In all cases the short wavelength side of the continuum suffers from a gradual decrease in SPD. It would be advantageous to try and minimise this as much as possible and attempt to extend the continuum further into the visible. In the next section we are going to study some possible approaches to solve this problem.

4.4 Flatter and further

We learnt in the last chapter that by adding a second ZDW we can increase the nonlinearity, and potentially maintain a $|\beta_2|/\gamma$ ratio that approaches a constant, thus aiding the SSFS. Not only did the increased nonlinearity result in higher energy solitons, it also resulted in more solitons. This last point is perhaps key to trying to reduce the drop in SPD on the short wavelength side of the pump: more solitons should lead to more trapping and therefore more energy transferred short of the pump. In order to explore the potential of using a double zero PCF we simulate propagating a 10 W CW field through four more hypothetical PCFs (HFi-HFl) using the same methods as detailed in section 3.3.2.

The PCFs all have a ZDW of approximately 1.068 μm, which enables energy transfer to the short wavelength side of the pump. A second ZDW is gradually introduced and shifted to shorter wavelengths. The details of the PCFs are given in table 4.1, while the dispersion and nonlinearity curves are given in figure 4.15 with HF23 for comparison.

We simulated propagating a 10 W CW laser through 100 m of each of the PCFs. The plots of the spectral evolution with length and the spectrograms at the end of the PCF are shown in figures 4.16 and 4.17 respectively. The first point to note is that HFi offers a limited improvement in bandwidth over HF23 (figure 4.9a) as would be expected from

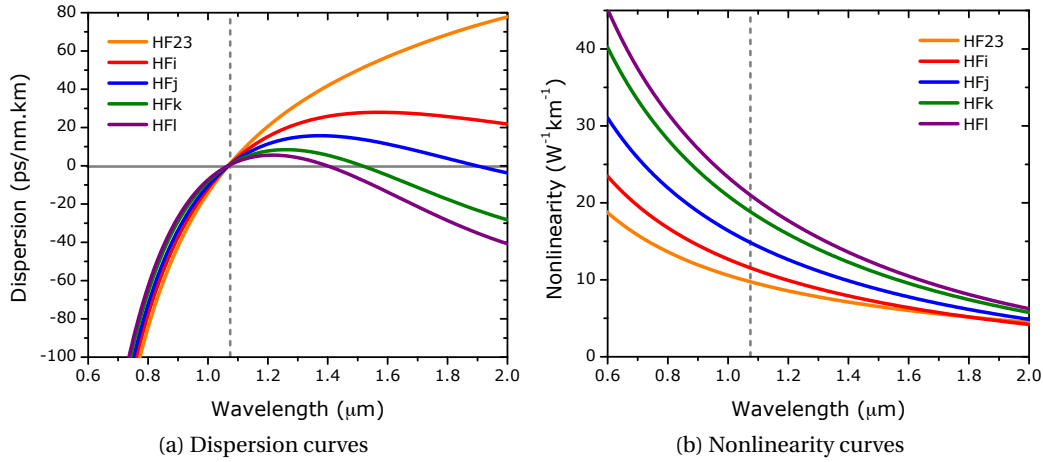(a) Dispersion curves   (b) Nonlinearity curves

Figure 4.15: 4.15a Dispersion curves for HF23 and 4 hypothetical PCFs. 4.15b Nonlinearity for HF23 and 4 hypothetical PCFs.

the dispersion curve. As we bring the second ZDW closer to the pump the bandwidth continues to improve (HFj) before the second ZDW ultimately limits the continuum (HFk); in HFl, the continuum bandwidth is reduced further as the second ZDW is moved to a shorter wavelength. It is worth noting that due to the low dispersion at the pump, the formation point of the continuum can vary appreciably between different runs of the simulation. From the evolution plots we see that the pump seems to be depleted further in HFk and HFl compared to HFi and HFj.

If we study the spectrograms we can confirm the increased pump depletion. This is brought about by a considerable increase in the number of solitons formed which self-frequency shift to the second zero, where they come to rest and transfer energy to a dispersive wave. On this occasion however, as the pump is so close to the first ZDW, energy is transferred short of the pump. Some of this energy is trapped by the self-frequency shifting solitons and shifted to shorter wavelengths in accordance with the group velocity matching conditions. Whilst the second ZDW seems to have enhanced the short wavelength processes, it does raise some limits and issues which are more clearly seen if we study the spectra from the PCFs, shown in figure 4.18a.

Figure 4.18a shows that as the continuum broadens, the pump is increasingly depleted, resulting in a reduction of the initial drop in SPD on the short wavelength side; and the rate of decrease in the SPD at shorter wavelengths reduces. For HFl the continuum bandwidth reduces due to the shorter second ZDW. If we consider the group velocity curves in figure 4.18b, we can see that as we add the second ZDW, the short wavelength edge that can be group velocity matched reduces to the extent that for HFj it is ~0.79 μm, for HFk it is ~0.88 μm, and for HFl it is ~0.92 μm. The phase-matching conditions for
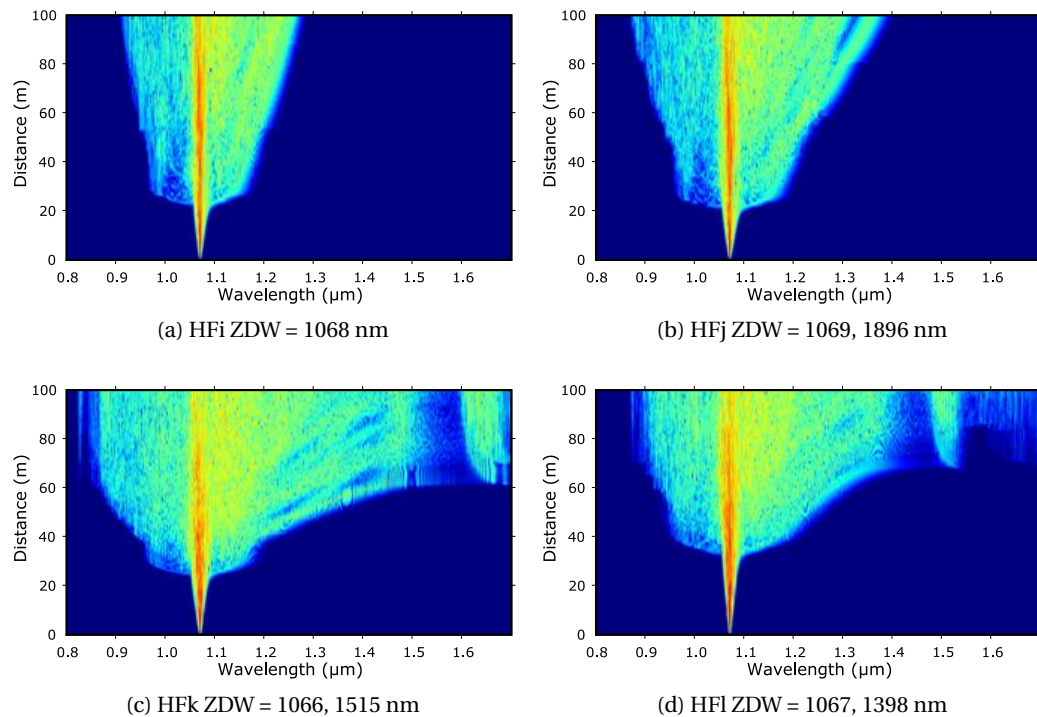
Figure 4.16: Evolution of supercontinuum with length for a single shot simulation of a 10 W CW laser. Scale: -60 dB ▬▬▬ 0 dB.

FWM mixing are limited in a similar way. Hence, unlike a single zero PCF (such as HF23) the short wavelength extension is potentially much more limited in a double zero PCF. We cannot simply increase the pump power in order to shift the short wavelength edge of the continuum further towards the visible. This is a rather significant limitation if we want to build a CW pumped supercontinuum which extends into the visible. This does not rule out the use of double zero PCFs for short wavelength generation; there are several applications, such as OCT, where a continuum extending from around 0.8 - 1.2 μm could be of use. Under these circumstances a double zero PCF would more appropriate.

4.4.1 Towards the visible

We have described how the long wavelength edge of the continuum limits the short wavelength edge. Ultimately, the long wavelength edge is itself limited by the transmission window of a silica PCF. As we require the ZDW to be very close to the pump wavelength, this means that for any given PCF with a single ZDW of approximately 1.07 μm the short wavelength side will ultimately be limited to 0.55-0.6 μm. This is a straightforward outcome from the phase matching and group velocity matching conditions. A similar

(a) HFi ZDW = 1068 nm

(b) HFj ZDW = 1069, 1896 nm

(c) HFk ZDW = 1066, 1515 nm

(d) HFl ZDW = 1067, 1398 nm
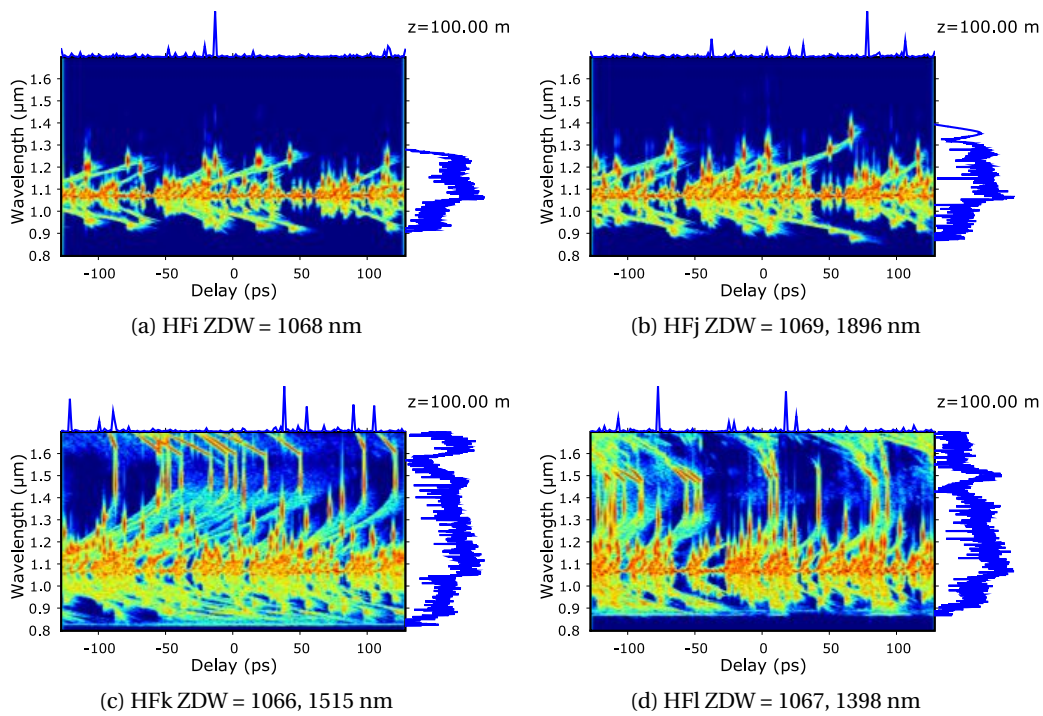
Figure 4.17: Spectrograms of supercontinuum after 100 m for a single shot simulation of a 10 W CW laser. Scale: -80 dB ▬▬▬ 0 dB.

(a) Simulated spectra
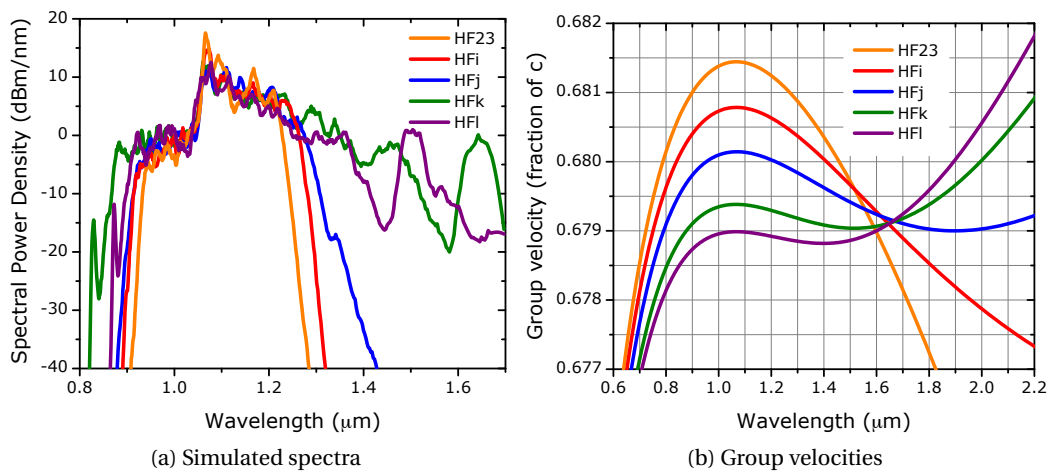
(b) Group velocities

Figure 4.18: 4.18a Simulated spectra averaged over four ensembles and smoothed using a 15 point Savitzky-Golay method to aid clarity [11]. 4.18b Group velocity curves for each of the PCFs.

short wavelength limit has been encountered under pulse pumping; this was ingeniously overcome by using either a set of cascaded PCFs [5] or a long tapered PCF [10]. Both these

methods result in the ZDW being shifted further into the visible which allows for the phase matching and group velocity matching conditions to extend to shorter wavelengths. As the tapering approach is both more elegant and more efficient, we shall consider it first.

Tapered PCFs

Fibres have been tapered on the centimetre scale for some time [12, 13], however for supercontinuum generation in the picosecond pump regime it is necessary to produce tapers which extend over several or tens of metres. In order to produce such tapers, it is necessary to manufacture them on the drawing tower. Typically, the drawing speed is gradually increased during manufacture whilst the preform is fed at a constant rate. The result is a PCF where the pitch decreases with length whilst the ratio of d/Λ is kept constant along the whole PCF. For instance if we were to reduce the overall diameter of HF23 by a factor of 1.5, then the ZDW would be shifted to 0.960 μm. The effect on the dispersion and the group velocity/phase matching curves is illustrated in figure 4.19. As the ZDW is shifted to shorter wavelengths, the shortest achievable wavelength through the soliton trapping mechanism or FWM decreases, potentially allowing extension of the continuum further into the visible. The magnitude of this change is greatest for shorter pump wavelengths (1.4 μm compared to 2.0 μm). As such, we can see from figure 4.19b, that for a long wavelength limit at the water loss (1.4 μm) the short wavelength edge could be extended from 0.82 to 0.69 μm if the diameter was reduced by a factor of 1.5.

(a) Dispersion curves   (b) Group velocities/phase matched curves
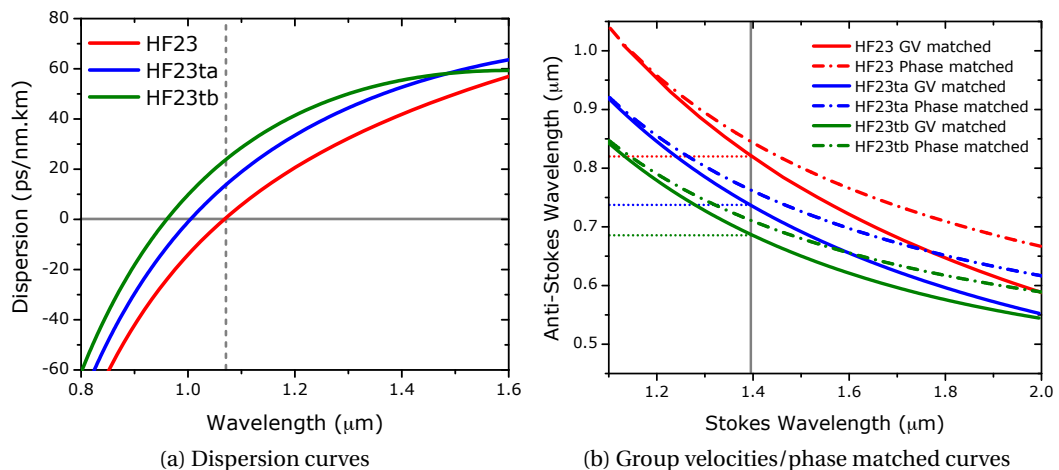
Figure 4.19: 4.19a Dispersion profile of HF23 and with a reduction in diameter by a factor of 1.25 (HF23ta) and 1.5 (HF23tb). 4.19b Group velocity and phase matched curves for each of the diameters.

The use of long PCF tapers for supercontinuum generation has been demonstrated using pulsed pumped systems [10], and since the experimental work outlined in this

chapter, with a CW pumped system [14]. In this work the authors produce a 200 m PCF. The first 100 m has a ZDW of 1.053 μm, whilst the second 100 m is tapered with a final ZDW of 0.95 μm. A 20 W CW laser at 1.064 μm was used as the pump source and a continuum extending from 0.67 to 1.35 μm was produced. The SPD initially drops by over 10 dB and then gradually declines on the short wavelength side of the pump, which is consistent with our own results. The authors attribute soliton trapping of dispersive waves as the main mechanism for short wavelength generation.

The tapering approach has several shortfalls. As we require the ZDW to be very close to the pump, this ultimately limits the short wavelength. If we examine the group velocity curves, shown in figure 4.20a, for HF23 and its scaled variants, we see that there is a fundamental short wavelength limit at 0.50 μm; this is due to the long wavelength edge of the transmission window. Tapering further does not improve the situation, as a second ZDW is introduced which confines the short wavelengths further. Hence, without adopting a more complex approach, it will be very difficult to get to the 'blue' using this technique, assuming that low water loss PCF tapers can be manufactured.

(a) Group velocity

(b) Dispersion curves
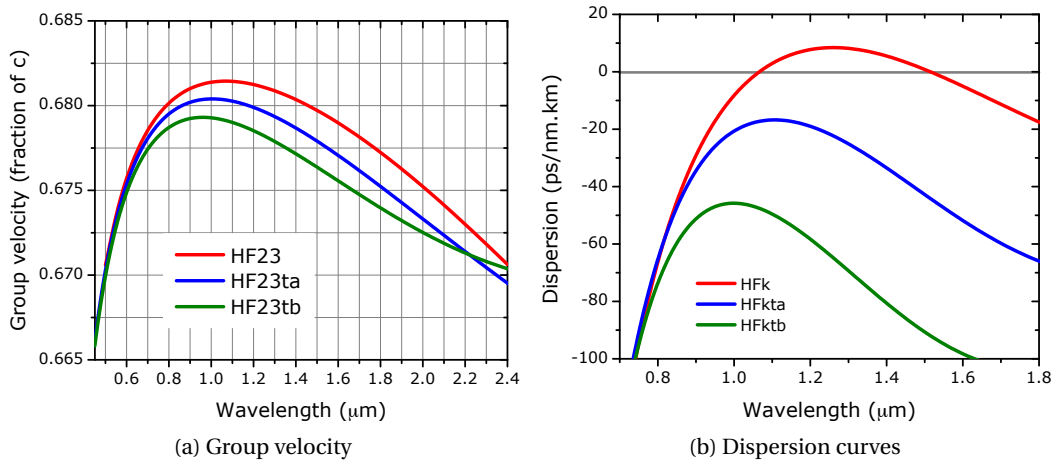
Figure 4.20: 4.20a Group velocity of HF23 and with a reduction in diameter by a factor of 1.25 (HF23ta) and 1.5 (HF23tb). 4.20b Dispersion curves for HFk and with a reduction in diameter by a factor of 1.2 (HFkta) and 1.4 (HFktb).

Tapering a double zero PCF does not offer any aid either, as the fixed d/Λ with changing pitch quickly results in a fibre which is entirely in the normal dispersion regime, as illustrated in figure 4.20b. In order to shift the ZDW of a double zero PCF, we would need to be able to control both the change in pitch as well as the hole diameter during the taper process. This is possible by controlling both the speed of the draw and the gas pressure used to maintain the microstructure during the pull. Such a technique has been demonstrated in PCF to enable pulse compression [15] and could potentially be applied to

both double zero PCFs and standard single zeros PCFs to prevent a second ZDW. In both cases the dispersion profile of the PCF would need to be carefully calculated as changes to the nonlinearity may prove detrimental the continuum processes.

Cascaded PCFs

The other approach to shifting the ZDW to shorter wavelengths is simply to splice two or more different PCFs together in a cascade. This has been demonstrated with pulsed pumped systems [5]; however this method suffers from the high splice losses that result from splicing two PCFs together. The splice loss tends to be ~1.5 dB, which under high power CW pumping may lead to a fibre fuse [16]. Nevertheless, this approach would allow two different double zero PCFs to be cascaded, potentially a more direct approach than tapering. However, simulations of several such cascades have shown no significant improvement in the bandwidth of the continuum. These simulations support the results from several quick experimental trials which also failed to demonstrate any significant enhancement to the continuum. It is likely that the steps in dispersion, between the PCFs, may need to be much smaller than those simulated and attempted. The smaller change in dispersion may help to achieve sufficient power transfer to drive the required nonlinear processes.

4.4.2 Summary

We have shown that double zero PCFs can enhance the bandwidth of a CW continuum, on both the long and short wavelength sides of the pump, over a single zero PCF up to a point where the second zero limits the long and short wavelength edges. However, it is clear that increasing the energy and number of solitons will result in more efficient short wavelength generation. Tapering of single ZDW PCFs offers some advantages, and an initial demonstration of these has recently been realised. Further improvements should be possible by potentially making use of a double zero structure and controlling both the pitch and the size of the air holes during the tapering process. Such fine control would require careful design of the parameters and extensive simulation. We have also shown that it will be extremely difficult to get into the blue region of the spectrum due to the tight requirements on the initial ZDW wavelength. Furthermore, the OH^- induced water loss at 1.38 μm will prove to be a significant obstacle unless suitable tapers can be manufactured using the techniques outlined in section 3.2.1.

4.5 Future directions

There are potentially many opportunities for high power CW pump based continuum in the visible and although we have demonstrated short wavelength extension in conventional PCFs and discussed tapered PCFs, other schemes may be worth pursuing. For example, operating in a polarisation maintaining system may offer advantages and enhance the efficiency of the supercontinuum generation processes. Another approach that could prove productive for generating short wavelengths would be to utilise the soliton fission scheme outlined by Kutz *et. al.* [17]. Unfortunately, designing a PCF cascade with the required properties is a difficult task and some ingenuity is required to execute this scheme. As a final example, it may be possible to pump with a second shorter wavelength, such as 970 nm; this light could potentially be trapped and shifted by the solitons, perhaps enhancing the spectral power density.

4.6 Conclusions

In conclusion we have shown the first short wavelength generation in a 1 μm CW pumped supercontinuum. The short wavelength generation has been shown to be due to a combination of FWM and soliton trapping. Improvements should be possible by a variety of mechanisms including pumping at much higher powers, optimisation of the PCF to aid soliton trapping [4], dispersion management via tapers[10, 15] as well as numerous schemes to enhance the gain and energy on the short wavelength side. Although these initial results are promising, it is likely that much work remains before CW pumped supercontinuum sources with high spectral power densities across the visible will be realised.

Bibliography

[1] J. Dudley, G. Genty, and S. Coen, "Supercontinuum generation in photonic crystal fiber," Rev. Mod. Phys. **78**, 1135 (2006).

[2] P. Beaud, W. Hodel, B. Zysset, and H. Weber, "Ultrashort pulse propagation, pulse breakup, and fundamental soliton formation in a single-mode optical fiber," IEEE J. Quant. Elect. **23**, 1938–1946 (1987).

[3] A. Gorbach and D. Skryabin, "Theory of radiation trapping by the accelerating solitons in optical fibers," Phys. Rev. A **76**, 053803 (2007).

[4] J. M. Stone and J. C. Knight, "Visibly "white" light generation in uniform photonic crystal fiber using a microchip laser," Opt. Express **16**, 2670 (2008).

[5] J. C. Travers, S. V. Popov, and J. R. Taylor, "Extended blue supercontinuum generation in cascaded holey fibers," Opt. Lett. **30**, 3132–3134 (2005).

[6] F. Vanholsbeeck, S. Martin-Lopez, M. González-Herráez, and S. Coen, "The role of pump incoherence in continuous-wave supercontinuum generation," Opt. Express **13**, 6615–6625 (2005).

[7] A. Abeeluck and C. Headley, "Continuous-wave pumping in the anomalous- and normal-dispersion regimes of nonlinear fibers for supercontinuum generation," Opt. Lett. **30**, 61 (2005).

[8] S. Johnson and J. Joannopoulos, "Block-iterative frequency-domain methods for Maxwell's equations in a planewave basis," Opt. Express **8**, 173–190 (2001).

[9] S. G. Johnson, J. D. Joannopoulos, and M. Soljacic, "MIT Photonic Bands," `http://ab-initio.mit.edu/wiki/index.php/MIT_Photonic_Bands` (2008).

[10] A. Kudlinski, A. K. George, J. C. Knight, J. C. Travers, A. Rulkov, S. V. Popov, and J. R. Taylor, "Zero-dispersion wavelength decreasing photonic crystal fibers for ultraviolet-extended supercontinuum generation," Opt. Express **14**, 5715 (2006).

[11] A. Savitzky and M. J. E. Golay, "Smoothing and differentiation of data by simplified least squares procedures." Analytical Chemistry **36**, 1627–1639 (1964).

[12] J. Teipel, D. Türke, H. Giessen, A. Zintl, and B. Braun, "Compact multi-watt picosecond coherent white light sources using multiple-taper fibers," Opt. Express **13**, 1734–1742 (2005).

[13] F. Lu, Y. Deng, and W. H. Knox, "Generation of broadband femtosecond visible pulses in dispersion-micromanaged holey fibers," Opt. Lett. **30**, 1566–1568 (2005).

[14] A. Kudlinski and A. Mussot, "Visible CW-pumped supercontinuum," Opt. Lett. **33**, 2407–2409 (2008).

[15] J. C. Travers, J. M. Stone, A. B. Rulkov, B. A. Cumberland, A. K. George, S. V. Popov, J. C. Knight, and J. R. Taylor, "Optical pulse compression in dispersion decreasing photonic crystal fiber," Opt. Express **15**, 13203–13211 (2007).

[16] S. I. Yakovlenko, "Mechanism for the void formation in the bright spot of a fiber fuse," Laser Phys **16**, 474–476 (2006).

[17] J. N. Kutz, C. Lyngå, and B. Eggleton, "Enhanced supercontinuum generation through dispersion-management," Opt. Express **13**, 3989–3998 (2005).

5 Infrared Laser Sources

5.1 Introduction

In this chapter we investigate ways of developing sources further into the infrared, specifically in the 2-3 μm region. As we saw in chapter 1, the variety of laser wavelengths available has been limited by the choice of gain media. In the 2-5 μm spectral region there are very few laser sources, and few of these have been commercialised because of the difficulties in engineering suitably robust sources. It is not the case that there is no demand for sources in this region, as an increasing number of applications, including medical, remote sensing, spectroscopy and military counter-measures [1] require sources in the infrared.

In section 5.1.1 we will start by looking more closely at some of the available laser sources before examining fibre laser based solutions. We will discuss the possibility of developing a high power source at wavelengths above 2 μm based upon a Raman fibre laser utilising a new type of high concentration GeO_2 fibre. In the following section we will consider high concentration GeO_2 fibres in depth covering the history of GeO_2 fibres, their development and the technologies enabling very high concentration GeO_2 fibres. The optical and non-linear properties of GeO_2 fibres will also be investigated. Section 5.3 will focus on a mathematical and physical description of a fibre Raman laser, before the examination of a series of experimental results in section 5.4. These results will be compared against a model in section 5.5 then we will look at further extension into the infrared in sections 5.6 and 5.7. Finally future prospects will be outlined in section 5.8 and conculsions drawn in 5.9.

5.1.1 Currently available sources

In chapter 1 we discussed many of the different classes of laser and the spectral regions covered by those classes. Of the rare-earth gain media, thulium and holmium both have transitions above 2 μm, with thulium's upper transition covering 1.90-2.07 μm while holmium has transitions at 2.8 μm and 2.1 μm. However none of the main laser manufacturers offer commercial thulium or holmium based solid state lasers. Fibre based thulium lasers, with emissions centred around 1.94 μm, have become available commercially since

2004 and are currently being scaled to higher output powers [2, 3]. Holmium based fibre lasers suffer from several problems, in particular the long spontaneous lifetime of the lower laser level of the 2.8 μm transition (~3 ms) makes efficient operation problematic. This hurdle along with a lack of pump diodes at 1.15 μm and the need for a soft glass host has made development complicated. Some progress has recently been made on this front with holmium based fibre lasers being demonstrated, with 55 and 162 mW of output power at 2.1 and 2.86 μm [4], and with 2.1 W of output power at 2.1 μm [5].

Looking beyond the rare-earths various options may be considered. Another important solid-state solution is that of Cr^{2+}ZnS and Cr^{2+}ZnSe based lasers. The transition metal, Cr^{2+} is broadly tunable over the 2-3 μm region and has been demonstrated in a CW regime producing several watts of output power [6–9]. Unfortunately scaling to much higher power levels is awkward due to the mechanical properties of the crystal. Several chemical lasers, notably HF (2.6-3.3 μm), can access the region but are generally not regarded as convenient sources. Semi-conductor options also exist in the form of vertical external cavity surface emitting lasers (VECSEL), which are constructed by optically pumping a semi-conductor to form a laser cavity. Recently, several watts of CW output power has been demonstrated from a AlGaIn-AsSb based system at 2.25 μm [10]. One of the most common methods to access the 2-3 μm region is via an optical parametric oscillator (OPO). As mentioned in chapter 1, OPOs use a nonlinear crystal placed within a cavity to generate parametric amplification. The signal and idler waves in these oscillators are widely tunable and are often used in the 2-3 μm region [11]. Recent work has studied the use of quasi-poled GaAs as the nonlinear crystal to produce power in the IR. Several watts from a pulse-pumped system have been demonstrated [12, 13]. Several watts has also been demonstrated in the CW regime (above 3 μm) by using periodically poled lithium niobate as the nonlinear crystal [14, 15], however scaling the power further has proven tricky.

5.1.2 Raman lasers

All the sources discussed above, except for OPOs, directly provide gain in the 2-3 μm region. Evidently, to build a laser source gain is required and a variety of nonlinear processes can provide the necessary gain. We have already briefly discussed OPOs which make use of parametric gain; the other prime nonlinear based candidate is Raman gain. The underlying physics of stimulated Raman scattering (SRS) was discussed in section 1.3.4 in chapter 1. SRS provides a broad, efficient gain mechanism which can be cascaded to longer wavelengths. The gain available is dependent upon the nonlinearity of the medium, the pump wavelength and the interaction length. As has been previously stated, the waveguiding nature of fibre enables long interaction lengths, allowing significant

enhancement of nonlinear processes such as SRS. The first SRS based fibre laser was realised in 1976 by Hill *et al.* [16], although systems based upon benzene-filled hollow core fibres had already been demonstrated [17]. A considerable amount of work on tunable Raman fibre lasers (RFL) followed [18–21] along with the development of CW Raman sources [22].

Since their invention, work has been ongoing to use RFLs to access wavelength regions for which no rare-earth gain medium exists. Much of this work has concentrated on the 1.1-1.3 μm region [23] with a narrow-linewidth 1179 nm, 23 W RFL recently demonstrated [24]. By frequency doubling these sources it is possible to access visible wavelengths for which it has proven complicated to develop sources for. One important wavelength is, 589 nm, used by guide star systems [25] and frequency doubling the above source produced over 3 W at 589 nm.

Closely related to the Raman fibre laser is the Raman fibre amplifier which provides gain for signals in the Raman gain band. These amplifiers have been developed for telecommunications as a solution for wavelength regions not covered by erbium doped fibre amplifiers [26]. Indeed, commercial systems are available for the telecommunications market [27] indicating that it is possible to build cost effective reliable laser systems based upon Raman gain.

Extending the operational wavelength of a Raman fibre laser beyond 2 μm is frought with difficulty. The rapidly increasing losses of bulk silica, a decreasing Raman gain at longer wavelengths, and an increasing waveguide loss for small core fibres, limit the long wavelength edge of conventional fibres. There are several solutions to this problem; use a medium other than fibre for the Raman interaction, make use of soft glass fibres which have much better transmission in the infrared, or attempt to make fibres from other oxide-based glasses such as germanium, boron and phosphorus. We shall deal with the relative merits of each of these options in turn starting with alternative Raman media. Raman lasers have been built and demonstrated based upon nonlinear crystals which often have much higher nonlinearities but much shorter interaction lengths often limiting overall performance [28]. An additional downside to these systems is that high power sources with an excellent beam quality are required to achieve moderate efficiency. Soft glass fibres were covered in section 1.2.4 and have the advantages of; maintaining the fibre format, good transmission in the infrared, and often a higher Raman gain coefficient than silica based fibres. Raman fibre lasers in chalcogenide have been reported, utilising a thulium pump laser, producing 0.2 W of output power at the first Stokes line at 2.102 μm [29]. There are several drawbacks for soft glass based systems: firstly it is not possible to splice the pump laser to the fibre; secondly fibre Bragg gratings cannot be used, which results in a dependance upon bulk optics, increasing cavity losses; thirdly the frequency

shift of the peak Raman gain tends to be quite small. The final option is to consider using fibres based upon other oxide-forming glass hosts such as germanium, boron and phosphorus. As we shall see in the next section, germanium has the highest Raman gain of the oxide based glasses and is aided by enhanced transmission in the infrared. This makes it an excellent candidate for building a high power Raman fibre laser in the spectral region above 2 μm.

5.2 Germania fibre

5.2.1 History

The use of alternative oxide-based glass forming hosts, such as high-concnetration GeO_2, was first suggested in 1973 by Maurer and Schultz [30]. The original intention was to produce better fibres for telecommunications with lower losses, superior mode discrimination and a simpler manufacturing procedure. Shortly after this proposal a comparison of the Raman scattering cross sections and Stokes intensities of vitreous bulk SiO_2, GeO_2, B_2O_3 and P_2O_5 was performed [31], the results for which are shown in figure 5.1. It is apparent from the diagram, that the cross section of GeO_2 is significantly higher than that of SiO_2, at some 9.2 times greater. The use of low concentrations of germanium as a dopant to modify the refractive index of silica fibres has been routine since the 1980s. Many conventional highly nonlinear fibres use slightly higher concentrations of germanium to achieve their enhanced nonlinearity. Indeed, some recent results were obtained from a 18 mol. % concentration GeO_2 fibre uesd in a Raman fibre laser at 1.17 μm [32]. In this case the Raman gain was ~3 times that of SiO_2, clearly less than what is possible. Regrettably, manufacturing high-concentration (i.e. above 20-40 mol. %, GeO_2) fibres has proven difficult.

Manufacturing high concentration germania fibres

The obstacles to producing a high concentration GeO_2 fibre stem from the mismatch of the thermal expansion coefficients of the GeO_2 core and SiO_2 cladding. This is compounded by a narrow temperature range between the nonsintering and evaporation of the GeO_2. Over the years many different approaches have been taken to resolve this problem.

Maurer and Schultz described using a multistage outside vapour deposition (OVD) technique combined with the drilling of auxiliary rods and the polishing of the preform's surfaces. The fibre produced had a pure GeO_2 core with a diameter of 68 μm and a 63-37 % GeO_2-SiO_2 cladding with a diameter of 142 μm. Losses of about 6 dB/km at 0.8 μm were reported and were determined by the Rayleigh scattering. These results were not repeated by any other researchers.
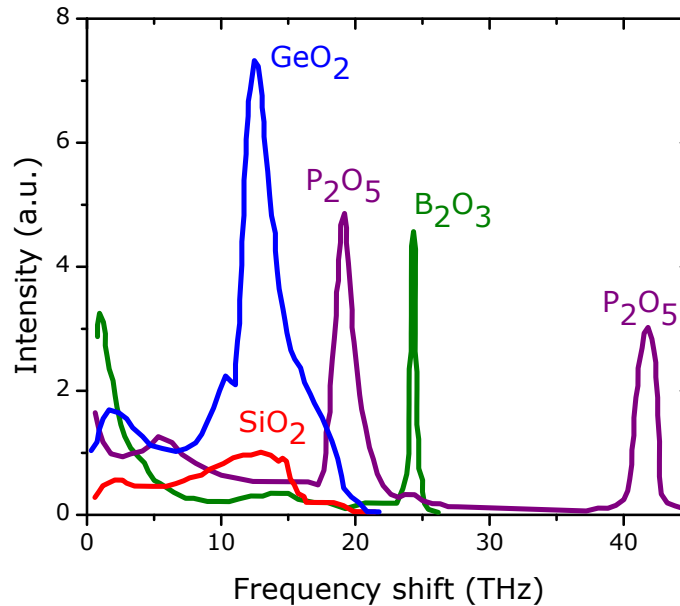
Figure 5.1: Raman gain for a variety of oxides pumped at 514.5 nm, adapted from [31].

During 1983 and 84 Takahashi *et al.* published a series of papers making incremental improvements in the production of GeO_2 fibres via a vapour-phase axial deposition (VAD) method [33, 34]. The fibres were multimode and had reported losses of 4 dB/km at 2.0 μm and 15 dB/km at 2.4 μm. Despite a significant reduction in water content to 0.5 ppm, strong OH^- absorption peaks at 1.8 and 2.4 μm of ~30 and ~120 dB/km still existed [34]. The authors also replaced the GeO_2 cladding with a silicon cladding which resulted in a reduced loss, narrowing from 50 to 13 dB/km at 1.1 μm. This was explained by a smoother interface between the core and the cladding [35]. This work was followed up in 1997 with the production of fibres with a fluorine doped cladding, predicting that a loss of 0.15 dB/km at 2 μm should be possible, though little actual improvement was made [36].

In 1988 Hosaka *et al.* evaded the problem of the high thermal expansion mismatch by using $P_2O_5-SiO_2$ for the cladding; this has a large thermal expansion coefficient [37]. A pure germania core was inserted into a drilled $P_2O_5-SiO_2$ tube, which was subsequently elongated and inserted into another drilled $P_2O_5-SiO_2$ tube. Both the core and cladding were made by the VAD method. The resulting preform was then drawn to form a fibre. The fibre was used to demonstrate a low threshold fibre Raman laser, but the fibre's losses were reported to be around 400 dB/km. This may have been due to the large amount of handling involved in the manufacturing process which consequentially leads to difficulties in maintaining a high cleanliness required for low losses.

The most common method of producing conventional silica fibres, namely the modified chemical vapour deposition (MCVD) technique, has also been used for high concentration

Property	GeO$_2$	SiO$_2$
Single bond strength, kcal/mol	108	106
Melting point (of crystals), °C	1116	1723
Heat of fusion, kcal/mol	10	2.1
Glass-transition temperature, °C	513-650	1127
Viscosity at 2000 °C, Pa.s	~25	~10^4
Viscosity at 1250 °C, Pa.s	~10^6	~10^{11}
Rayleigh coefficient a$_{RS}$, μm^{4}dB/km	2.6	0.7
Refractive index at 589 nm, n$_d$	1.605	1.4585
Wavelength of zero material dispersion λ_0, μm	1.74	1.27
Density ρ, g/cm^3	3.65	2.202
Thermal expansion coefficient, 10^{-7}K^{-1}	77	5

Table 5.1: Properties of germania and silica glasses adapted from [38].

germanium fibres. In this regime the core is heavily doped with or consists of pure GeO$_2$, while the cladding is made from SiO$_2$. The benefit of using SiO$_2$ is that it improves the refractive index contrast between core and cladding whilst enabling better compatibility with conventional fibres. The first report of GeO$_2$ fibre produced via MCVD was in 1987 [39]. The optical losses were rather high, ranging between 150 and 300 dB/km at 2.0μm. In this fibre the maximum core concentration was limited to 45 mol.% due to vaporisation of the core and diffusion of the glasses during the drawing stage. These problems arose due to the differences in the thermal expansion coefficients and by the temperature dependencies of viscosity of these glasses. These properties along with several others are listed in table 5.1. For fibre drawing, at the typical temperature of 2000 °C, there is a difference of three orders of magnitude in the viscosities. This viscosity mismatch can lead to noncircular cores which in turn can increase the optical losses, especially those related to scattering [40].

5.2.2 Pure germania fibres

With the issues of the thermal expansion and viscosity mismatch along with the small temperature range between nonsintering and evaporation of the deposited core glass, our collaborators at the Fiber Optics Research Center (FORC) re-visited the issue using MCVD. In order to try and solve these and other problems they attempted

- To control the temperature during core glass deposition, tube collapse, stretching, and jacketing of the preform.

- To control the pressure inside the tube.

- To control the speed of the torch and to use an additional torch.

(a) Typical structure

(b) Concentration profiles
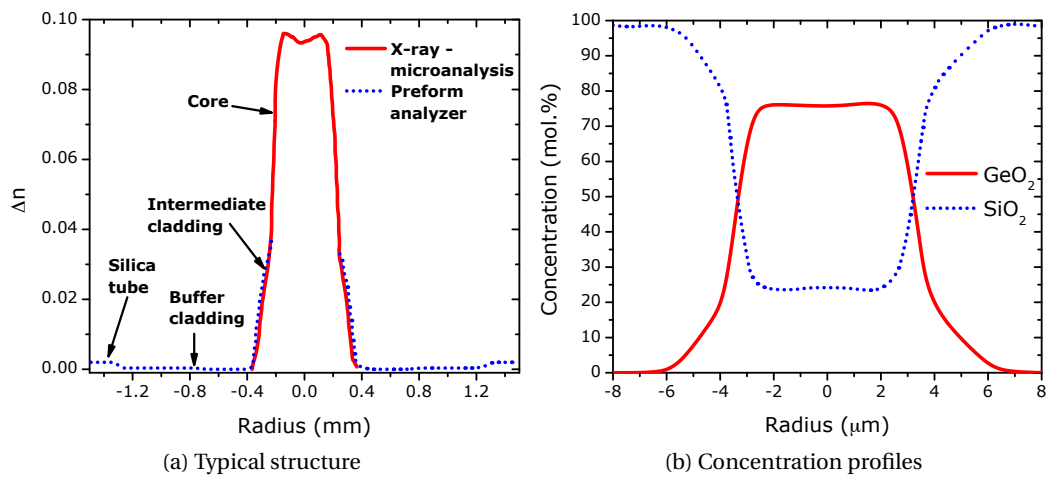
Figure 5.2: The typical structure of a germania-based glass core preform is shown in 5.2a. The preform shown is 67 mol.% GeO_2. 5.2b shows the GeO_2 and SiO_2 concentration profiles measured in a multimode fibre with 75 mol.% GeO_2. Adapted from [38].

- To vary the oxidising gas during the glass deposition.

- To create a gradual change of the thermophysical properties of the glass in the preform cross section via an intermediate layer of GeO_2 (from 4 to 30 mol.%) between the cladding and the core.

In addition to these amendments FORC wanted to develop a gradient core-refraction-index deposition without a central dip for GeO_2 concentration in the range of 50 to 100 mol.% [41]. A series of preforms with variations of the core, intermediate layer, and buffer cladding glass composition were made. The typical structure and an example concentration profile are shown in figure 5.2. The intermediate cladding is key to helping to resolve the issue of the viscosity and thermal mismatch. The preforms were drawn into a variety of single and multimode fibres ranging from 51 to 98 mol.% GeO_2. These have different losses and single mode cutoff wavelengths, the details of which can be found in [38].

5.2.3 Fibre properties

It is well established that the intrinsic IR absorption of GeO_2 glass is shifted to longer wavelengths compared with SiO_2 glass due to the greater mass of the Ge atoms; this makes GeO_2 a better candidate for the IR. The transmission losses of the fibres vary based upon the GeO_2 content and the core size. All of the fibres exhibited similar spectral features and figure 5.3 shows the loss for several single mode GeO_2 fibres. Measurements show

that the total attenuation is almost fully due to scattering, with the measured scattering loss exceeding the Rayleigh scattering in bulk GeO_2 by 10 to 100 times. The angular dependance of the scattering is intensely biased towards the direction of propagation suggesting the presence of relatively large scale optical inhomogeneities in the core region. Further work has indicated that these inhomogeneities arise from fluctuations at the fibre core-cladding interface and that they are present in the preform before drawing. However the tension of the fibre during the draw still effects the losses meaning that more than one mechanism may be responsible and further work needs to be carried out to understand this [42]. The zero dispersion wavelength of bulk GeO_2 is 1.74 μm and falls to 1.63 and 1.51 μm for concentrations of 75 and 50 mol.% respectively [43]. The zero dispersion of the fibre is governed by the material dispersion and the waveguide dispersion - this is dependent upon the core size and the index difference between the cladding and core (see section 1.2.1). For a 2 μm core 75 mol.% GeO_2 fibre the calculated zero dispersion wavelength is ~2.5 μm. Compared to a similarly sized SiO_2 fibre the losses for both the 51 and 75 mol.% GeO_2 fibres are lower in the 2 μm region.
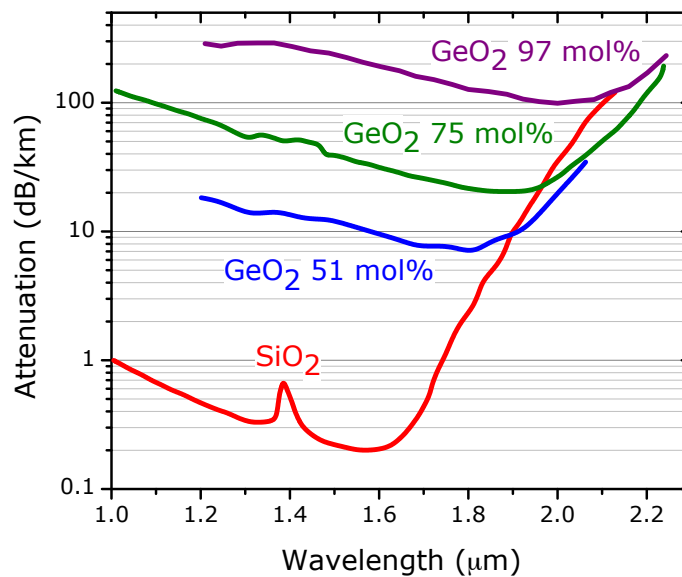
Figure 5.3: Comparison of the attenuation in dB/km between SiO_2 and various concentrations of single mode GeO_2 fibre.

It is well known that the photosensitivity of germanosilicate fibres increases with increasing GeO_2 concentration. For high concentration GeO_2 fibres the sensitivity increases to the point where no hydrogen preloading is required to write fibre Bragg gratings (FBG) into the fibre. This enhanced sensitivity, especially in the ultraviolet, has been studied [38] and may be of concern with respect to long term reliability of the fibres.

As already discussed the losses of high concentration GeO_2 fibres are lower than those

of SiO_2 fibres in the 2 μm region. Combined with the much higher Raman gain and normal dispersion these fibres would appear to be ideal as the basis of a high power Raman fibre laser in the infrared. To build such a laser we selected a 75 mol.% single mode GeO_2 fibre with a measured mode field diameter of 2.5 μm and a single mode cutoff wavelength of ~1.4 μm.

5.3 Raman fibre lasers

A low loss optical fibre is capable of guiding light over 10s of km, maintaining confinement in a small optical core with a high field intensity. As discussed in section 1.3, this makes fibre an ideal medium for nonlinear processes such as stimulated Raman scattering (SRS). If we consider a simple Raman laser as shown in figure 5.4a, one fibre Bragg grating (FBG) acts as a high reflector (HR) mirror and a second FBG acts as the output coupler (OC), i.e. a partially reflective mirror. Both FBGs are reflective at the first Stokes wavelength and when the fibre is pumped by a laser then light at the first Stokes wavelength will arise due to the stimulated Raman effect. As the pump power is increased the gain will exceed the losses in the cavity and laser oscillation will occur at the first Stokes wavelength.

(a) Simple Raman laser (b) Cascaded Raman laser
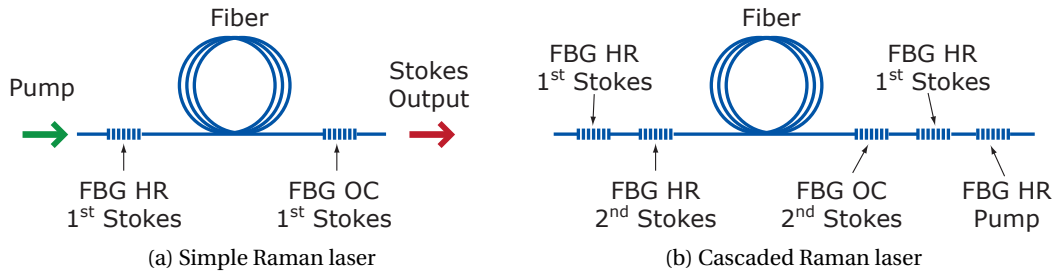
Figure 5.4: Schematics showing a 1$^{\text{st}}$ (5.4a) and 2$^{\text{nd}}$ (5.4b) order Raman fibre laser.

If we assume that the threshold for generation of the 2$^{\text{nd}}$ Stokes order is not reached, then there are three waves propagating in the fibre. A pump wave of frequency ω_p travels in the forward direction, generating two Stokes waves travelling in the forward and backward directions. These Stokes waves are frequency downshifted ω_s, from the pump and their optical powers obey the following propagation equations:

$$\frac{dP_p}{dz} = -\alpha P_p - \frac{\omega_p g}{\omega_s A} P_p (P_f + P_b) \tag{5.1}$$

$$\frac{dP_f}{dz} = -\alpha P_f + \frac{g}{A} P_p P_f \tag{5.2}$$

$$\frac{dP_b}{dz} = \alpha P_b - \frac{g}{A} P_p P_b \qquad (5.3)$$

P_p, P_f, and P_b are the forward pump wave power, forward Stokes wave power and backwards Stokes wave power respectively. The linear absorption in the fibre is denoted by α and is assumed to be identical for the pump and Stokes wave in this case. The Raman gain is given by g and the effective area of the core is denoted by A with z representing the length along the fibre. For all three equations the first term on the right hand side simply takes care of the loss due to absorption as the light propagates down the fibre. The second term describes the stimulated Raman gain and couples the three equations together. If we ignore the problem of modelling how the Stokes oscillation builds up and assume that it has, and that we are in a steady-state CW situation then it is possible to solve the coupled equations.

In the simplest case of a single cavity with identical absorption for the pump and Stokes waves, then the boundary value problem can be solved by taking boundary conditions of:

$$P_p(z = 0) \equiv P_{p0} \qquad (5.4)$$

$$P_f(z = 0) \equiv P_{f0} = R_{\mathrm{HR}} P_b(z = 0) \equiv R_{\mathrm{HR}} P_{b0} \qquad (5.5)$$

$$P_b(z = L) \equiv P_{bL} = R_{\mathrm{OC}} P_f(z = L) \equiv R_{\mathrm{OC}} P_{fL} \qquad (5.6)$$

where L is the length of the fibre between the FBGs while the reflectivity of the FBGs is given by R_{HR} and R_{OC}. Any splice losses between the FBGs and the fibre can be accounted for in R_{HR} and R_{OC}. P_{p0} represents the actual power launched into the fibre at $z = 0$ with the other subscripts denoting the power of the forward f and backward b Stokes waves at $z = 0$ and $z = L$. After several steps it is possible to derive two equations which allow you to solve for the unknowns [44], enabling accurate modelling of the pump and Stokes powers inside the RFL.

This analytical solution is only possible if the attenuation of the fibre is the same at the pump and Stokes wavelengths i.e. $\alpha_p \equiv \alpha_s$. In addition it is not possible to model cascaded Raman lasers (see figure 5.4b) using this approach. Instead a numerical method is usually invoked to solve the coupled ordinary deferential equations by applying appropriate boundary conditions. This type of problem has been well explored by mathematicians and is known as an ordinary differential equation boundary value problem. Common numerical methods include the shooting method [45–47], collocation (a particular class of Runge-Kutta methods) [48], the more general Runge-Kutta method [49] and linear multi-step methods [50]. More recently an analytical solution based upon the Lambert W function has been demonstrated [51]. Each of these methods has been shown to be in good agreement with experimental results with differences often relating to the

computational time required to run the simulation.

5.4 Experimental results

In this section we will look at a series of experimental results based upon pumping a 75 mol.% single mode GeO_2 fibre with a Tm fibre laser. A concentration of 75 mol.% was chosen as it offered the best compromise between the fibre attenuation in the infrared whilst maximising the potential Raman gain available.

5.4.1 Pump laser

Although it is perfectly feasible to use any laser source as the pump source for a Raman fibre laser, the most logical approach is to use a fibre laser. This potentially enables an all fibre format which removes the constraints of alignment and helps maintain a high overall efficiency. Fibre lasers exist based upon ytterbium, erbium and thulium centred on 1.07, 1.54 and 1.94 μm respectively. While it is perfectly feasible to cascade Stokes orders so that either an ytterbium or erbium laser would make a suitable pump source, there is an associated efficiency penalty. With the specific aim of constructing a source beyond 2 μm it would therefore seem that the best approach would be to use a thulium fibre laser to pump the GeO_2 fibre. It should be mentioned that both ytterbium and erbium based Raman fibre lasers have been demonstrated with high concentration GeO_2 fibre [38].
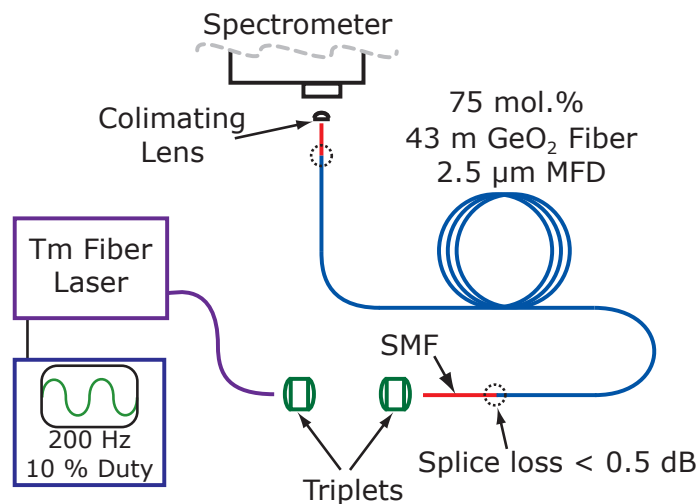
Figure 5.5: Schematic of the experimental setup for the single pass results. The Tm laser is modulated via a signal generator. The first triplet is integrated into the fibre laser whilst the second triplet is used to launch into a short length of SMF. This is spliced to 43 m of 75 mol.% GeO_2 fibre, the output of which is also spliced to a short length of SMF before being collimated and sent to diagnostic equipment.

The pump source that we utilised was an unpolarised 20 W single mode CW Tm fibre laser operating at 1.938 μm [3]. The laser has a collimated output and to maintain flexibility of the source within the lab this was left on the laser. The unpolarised pump light was coupled into a standard single mode fibre by a triplet lens with an efficiency of up to 80 %. Coupling directly into the GeO_2 fibre resulted in very poor coupling efficiencies due to the small core and high NA. Similarly, this presented difficulties in handling the output from the GeO_2 fibre. These issues were dealt with by splicing a short length of SMF to the input and output end of the GeO_2 fibre before focusing or collimating with a lens. In order to maintain alignment of the launch fibre over long periods of time, the average power was reduced to decrease the thermal drift. This was achieved by either modulating the fibre laser directly via a TTL signal or by using a chopper with a 25 % duty factor. The experimental setup for single pass pumping of the GeO_2 fibre is shown in figure 5.5.

Splicing

Due to the difficulties of launching high powers into the ~2 μm core of the GeO_2 fibre it was necessary to splice the GeO_2 fibre to a larger core SMF. Standard telecommunications fibre (SMF28) and large mode area (LMA) fibre were both used. Due to the large differences in mode field diameter (MFD), 2.5 μm versus ~ 12 μm for SMF28, standard splicing does not produce the lowest possible losses. Instead we made use of a mode field matching process specifically designed for splicing fibres with very dissimilar mode field diameters. This process takes advantage of the fact that during splicing, a fibre's dopants will diffuse into its core, decreasing its index profile. With two different fibres this can lead to a convergence of their index profiles, minimising losses. In order to implement such a scheme it is necessary to constantly monitor the fibres parameters during the splice and then terminate the fusion arc when the index profiles match. A schematic of what happens during the splicing process is shown in figure 5.6.

The splices were made using an Ericisson fusion splicer (FSU 975-PM-A). Several values such as the *pre-fuse current, current 1, current 2, gap, overlap,* and *time 1* are defined by the user. Many of the other settings are set by the splicer after performing several test splices. Using this technique it is possible to achieve splices with a loss of 0.4-0.5 dB. This is comparable to the 0.2-0.3 dB splice losses achieved between high NA silica fibres and SMF28. Splicing GeO_2 fibre to itself was possible using standard single mode splicer settings, with a typical splice loss of 0.15 dB.

5.4.2 Single pass results

Initial results were obtained by pumping the full 43 m length of 75 mol.% GeO_2 fibre with the thulium fibre laser as shown in figure 5.5. The laser was modulated at 200 Hz with
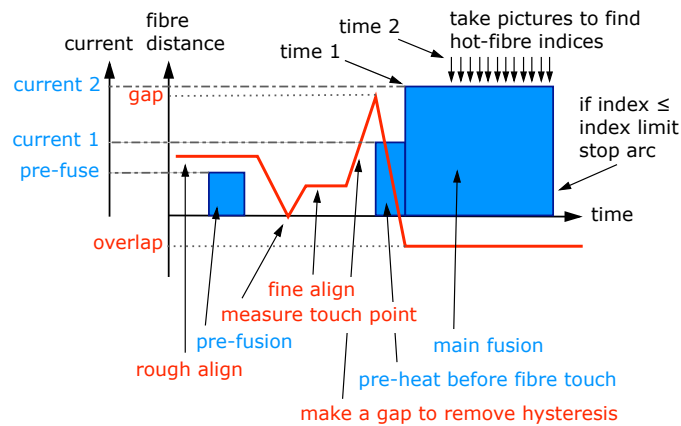
Figure 5.6: Schematic of the splicing process with time. The red line represents the distance between the two fibres while the blue boxes represent arc fusions at given current levels for a set period of time.
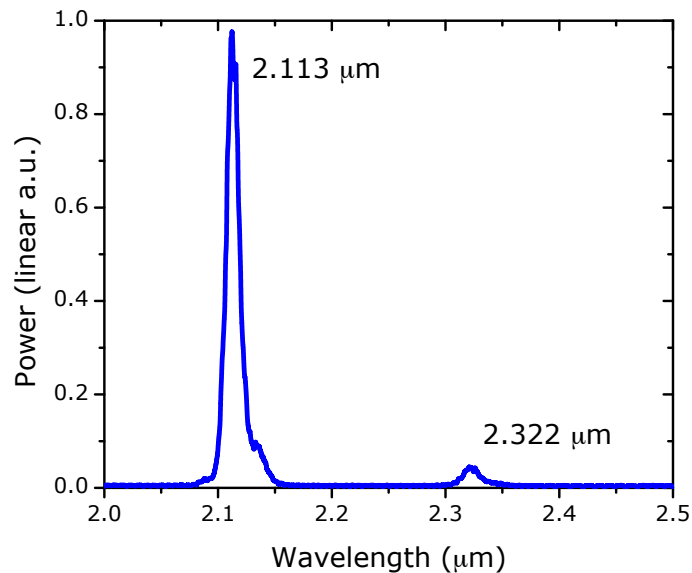

Figure 5.7: Signal from 43 m of 75 mol.% GeO_2 pumped in a single pass by a modulated Tm laser at 1.938 μm .

a duty factor of 10 via a TTL signal sent to the laser. A short length (~2 cm) of SMF was used to reduce the NA of the output to aid collimation by a lens. The resulting signal was launched into a Spex 500M spectrometer with a 600 line/mm grating blazed at 1250 nm and suitable for wavelengths upto 2.5 μm. A PbS detector was used in combination with a SRS lock-in amplifier (SR530) to measure the output signal. The detector's response curve was taken into account during data capture although it is flat over the spectral range which we were investigating. On any given sensitivity setting the lock-in amplifier

provided approximately 20 dB of dynamic range and repeating traces at higher sensitivities was used to improve overall dynamic range to 35-40 dB.

The loss was measured as 21 dB/km at 1.938 μm , increasing to 52-56 dB/km at 2.105 μm . This compares favourably with SiO_2 which has losses of ~16 and 110 dB/km at these wavelengths. The fibre was pumped at full power, 2.2 W (22 W peak), with spontaneous Raman signals at both 2.113 and 2.322 μm being recorded (figure 5.7). The signal at 2.113 μm was an order of magnitude less than the pump with the signal at 2.322 μm just detectable. This corresponds to a peak Raman gain shift of 12.8 THz in good agreement with previous measurements (figure 5.1).

5.4.3 Fibre Bragg gratings in GeO$_2$

In order to build a Raman laser cavity two FBGs were manufactured, a high reflector (HR, reflectivity > 99 %) and an output coupler (OC, reflectivity ~50 %). The gratings were written directly into the GeO_2 fibre with 244 nm laser radiation. Due to the high Ge concentration of the fibre it was not necessary to pre-load the fibre with hydrogen. Writing the gratings at 2.113 μm proved difficult due to the lack of available sources to characterise the gratings at this wavelength. Therefore during manufacture the gratings' properties were controlled by measuring the second dispersion order and taking account of the calculated dispersion.

(a) Setup for characterisation   (b) Signal from two gratings
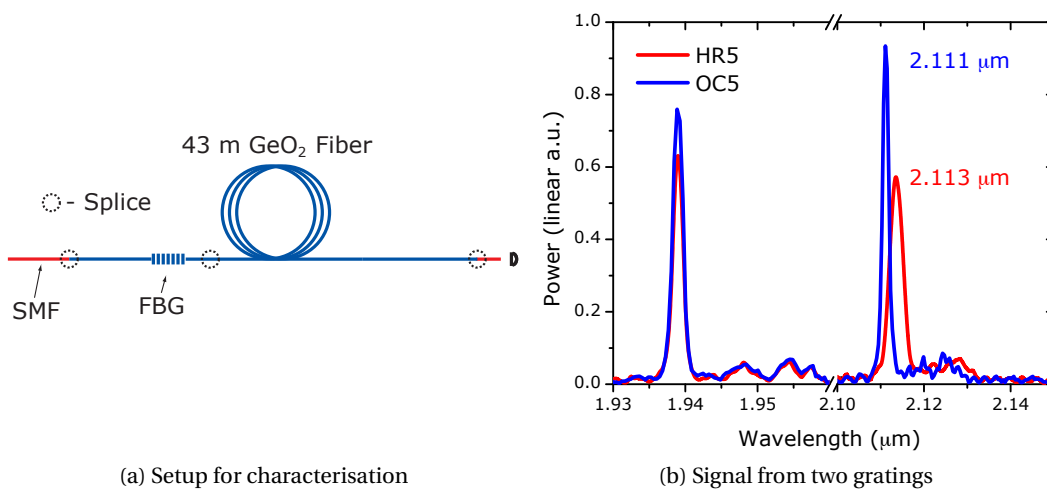
Figure 5.8: Shows the setup used to characterise the FBGs and the typical signal measured on the spectrometer.

Gratings were characterised more completely by placing one FBG at the input side of the 43 m of GeO$_2$ fibre and pumping with the thulium laser. By making use of the ~4 % back reflection from the end of the fibre, a Raman laser cavity is formed enabling the

characterisation of the central wavelength of the FBG under test. The set-up is shown in figure 5.8a with typical results for later gratings shown in figure 5.8b. Initial FBGs were slightly short of the peak Raman gain with the HR centred on 2.106 μm and the OC centred on 2.104 μm . Feeding these measurements back allowed for a later set of FBGs to be made with the HR centred at 2.111 μm and the OC centred on 2.113 μm . Gratings were also made for 1.938 μm (HR > 99 %) and 2.322 μm (HR > 99 %, OC ~50 %). It was possible to characterise the 1.938 μm FBG using a 1.5-2.0 μm supercontinuum source [52]. However to date it has not been possible to characterise the 2.3 μm gratings by either of the methods mentioned.

Typically FBGs are characterised by a white light source enabling accurate measurement of their central wavelength, bandwidth and reflectivity. It has not been possible to implement this method due to the low powers, poor coupling efficiency and high losses in the spectrometer set-up making detection of a signal all but impossible. The method used above provided measurements of the central wavelength and bandwidth but critically lacked a precise measurement of the FBG reflectivity. The HR FBGs were confirmed as having a reflectivity of >99 % by using them as a filter. Hence, uncertainly only exists for the exact reflectivity of the OC.

5.4.4 Cavities

A series of cavities were built around two FBGs. The HR was centred on 2.106 μm whilst the output coupler was centred on 2.104 μm and therefore had to be stretched in order to match the HR. To avoid any problem of additional peak power enhancement, resulting from diode modulation a chopper was used. The chopper operated at 200 Hz with a 25% duty factor. A schematic of the the Raman fibre laser is shown in figure 5.9.
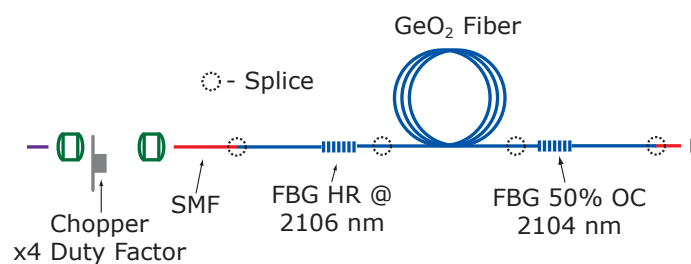
Figure 5.9: The Raman laser cavity consisting of two FBGs and a variable cavity length between 10.3 and 42.5 m.

Five cavities of lengths 10.3, 17.5, 26.3, 33.5 and 42.5 m were assembled and pumped by the thulium laser with up to 15 W (peak) launched into the Raman fibre laser cavity. The output power was measured using a thermal power meter (Molectron PM10) and the corresponding spectral trace taken on the spectrometer. The spectrum was then

(a) Output power at 2.105 μm

(b) Residual pump power at 1.938 μm

(c) Spectrum from 26.3 m cavity
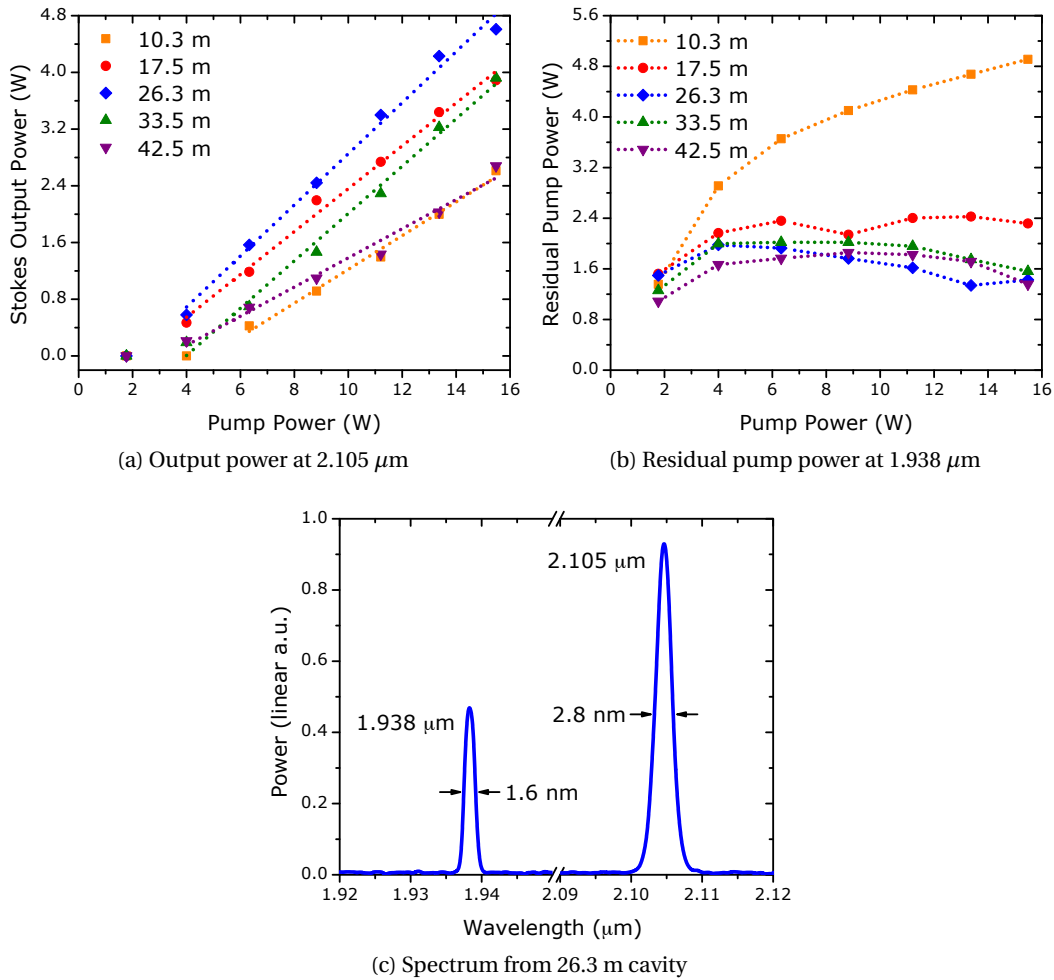
Figure 5.10: 5.10a shows the Stokes output power with pump power. The residual pump power is shown in 5.10b. Typical spectral output is shown in 5.10c.

integrated and normalised to the measured output power to enable calculation of the power in the Stokes wave and the residual pump power. Spectral measurements were made up to 2.4 μm in order to check for power transfer to the second Stokes wave; however no signal was detected beyond the first Stokes wave for any of the cavities. The output power at the first Stokes wavelength is shown in figure 5.10a along with the residual output power in figure 5.10b.

Figure 5.10a shows that the slope efficiency for the 10.3 and 42.5 m cavities are almost identical while the 26.3 m cavity has the highest efficiency. A maximum output power of 4.61 W (1.15 W average) with a full width half maximum (FWHM) line-width of 2.8 nm (figure 5.10c) was achieved. The line-width is related to the width of the FBGs as the resolution of the spectrometer was in the sub-nanometer range. The slope efficiency,

Cavity Length (m)	Fitted P_{Th} (W)	Calculated g_R (W^{-1}km^{-1})		
		Lower Fit	Fit	Upper Fit
10.3	4.9	22	27	33
17.5	2.2	29	37	49
26.3	2.1	21	27	37
33.5	4.0	10	12	14
42.5	3.3	9	12	16

Table 5.2: Calculated values of the threshold pump power and Raman gain based upon the linear fits in figure 5.10a.

defined as the output signal power over the absorbed pump power was 36 %.

For the 26.3, 33.5 and 42.5 m cavities the residual pump power remains largely saturated in the 1.5-2.0 W region (figure 5.10b). For the shorter cavities, especially the 10.3 m cavity, even less of the pump is converted which further reduces efficiency. The residual pump power of the longer cavities suggests poor extraction of the Raman gain. The Raman gain g_R, can be calculated from the threshold condition where the cavity losses L_c equal the cavity gain G_c, such that

$$G_c = \exp(2g_R P_{\text{Th}} L_{\text{eff}}) = L_c \tag{5.7}$$

$$L_{\text{eff}} = \frac{1 - \exp(-\alpha_p L)}{\alpha_p} \tag{5.8}$$

where P_{Th} is the threshold pump power and L_{eff} is the effective length as defined in equation 5.8. L is the length of the cavity and α_p is the attenuation at the pump wavelength. The total cavity losses L_c, can be calculated by summing the losses due to any splices in the cavity for a roundtrip, the output coupling and the attenuation at the Stokes wavelength α_s. The threshold pump power P_{Th}, can be determined experimentally from the measurements in figure 5.10a.

The calculated Raman gain is given for each cavity in table 5.2 and varies from 12 to 37 W^{-1}km^{-1}. The large variation can be partially explained by the uncertainity in the threshold pump power derived from the linear fits. Assuming that the Raman gain is inversely proportional to wavelength [53], the Raman gain is expected to be ~81 W^{-1}km^{-1} at 2.1 μm [54]. The difference may be due to operating at a wavelength 0.5 THz short of the Raman gain peak. From figure 5.1 the gain would be reduced by 13 % for a pure GeO$_2$ fibre. As our fibre's GeO$_2$ concentration is only 75 mol.% the expected reduction in gain would be less, especially as the gain curve is modified resulting in a broader flatter peak for a GeO$_2$-SiO$_2$ fibre [55, 56]. Even if we assume the full reduction in gain of 13 % the values derived in table 5.2 are still significantly lower than expected. The remaining explanations involve assuming a poor overlap between the OC and HR FBGs and/or damage to the
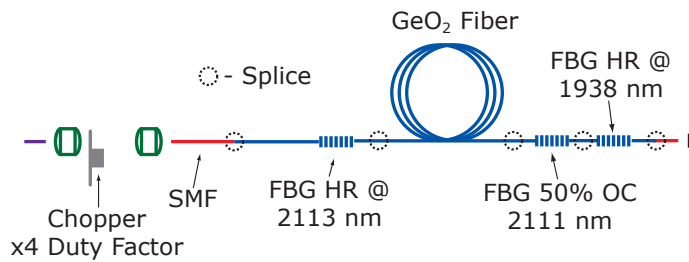
Figure 5.11: The second set of Raman laser cavities consisting of three FBGs and a variable cavity length between 6.8 and 23.2 m.

FBGs modifying their reflectivity. Initial attempts to improve the gain by stretching both gratings to 2.113 μm resulted in the gratings snapping under the strain. Furthermore, efficiency improvements may be possible by making use of the residual pump by reflecting it back into the cavity. In order to try to improve the efficiency a new set of gratings centred on 2.113 μm were made along with a HR FBG at the pump wavelength.

Double pass pumping

A second set of FBGs were manufactured based upon the inital feedback and were found to be much closer to the Raman gain peak. The HR was centred on 2.113 μm with a bandwidth of 3.6 nm whilst the 50 % OC was centred on 2.111 μm with a bandwidth of 1.6 nm. The OC was stretched to match the HR and a third HR FBG centred on the pump wavelength of 1.938 μm was used to send the residual pump light back into the cavity. The setup is similar to the previous experiment and is shown in figure 5.11.

Figure 5.12a shows the output power at 2.113 μm for four cavity lengths of 6.8, 8.4, 10.2 and 26.2 m. A maximum power of 6.84 W (1.71 W average) was achieved in the 6.8 m cavity. The results for the 6.8 and 10.2 m cavity were comparable, with the 8.4 m cavity producing slightly lower output powers. Shifting the gratings to match the peak Raman gain at 2.113 μm improved efficiency from 36 to 63 % in the best cases and dramatically reduced the residual pump power as shown in figures 5.12c and 5.12d. Double passing the 1.938 μm pump improved the output power further whilst maintaining approximately the same slope efficiency. It also had the additional benefit of removing the residual pump from the output signal.

The Raman gain was calculated from the threshold pump powers derived from the linear fits in figure 5.12a. The results are given in table 5.3 for each of the cavities. The values for g_R are much closer, with a peak value of 68 $W^{-1}km^{-1}$ for the 6.8 m cavity. Again the values should be consistent with each other and are still lower than the expected value of ~81 $W^{-1}km^{-1}$. There are many possible explanations for this, including incorrect estimation of the losses, most notably the output coupler, for which an exact reflectivity is not known.

(a) Output power at 2.113 μm

(b) Output spectrum at 2.113 μm

(c) Output power from 10 m cavities

(d) Residual pump power from 10 m cavities
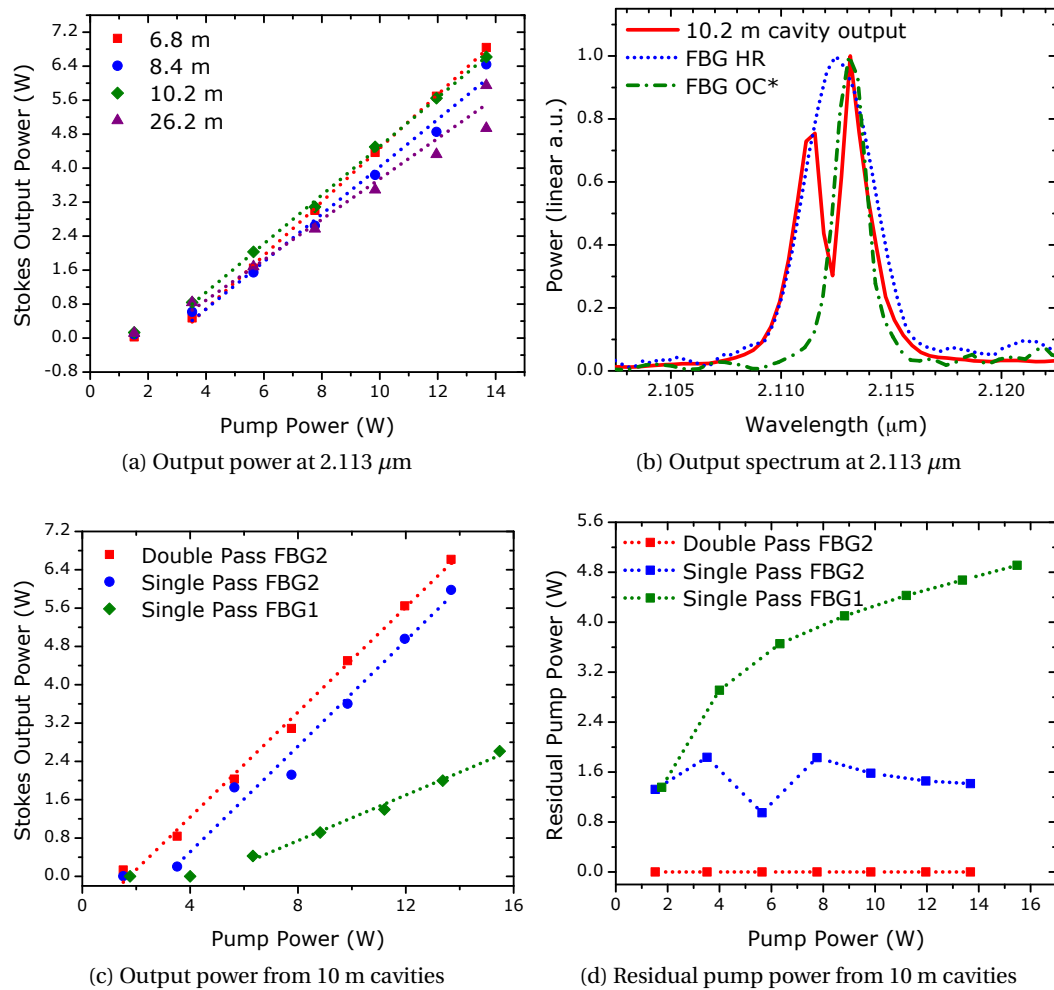
Figure 5.12: The growth in output power with pump power for cavities of length 6.8, 8.4, 10.2 and 26.2 m is shown in 5.12a using a double pass configuration as illustrated in figure 5.11. The spectral output at 2.113 μm is shown in 5.12b and compared with the bandwidth of the HR and OC. *Central wavelength adjusted to account for stretching assuming peaks align. 5.12c and 5.12d compare the three different 10 m cavities based around the two different sets of FBGs under single pass and double pass pumping.

The expected gain value is dependent upon the effective area of the fibre, which itself is not known precisely due to a slightly elliptical core and the difficulties involved in measuring this. In addition the Ge concentration was inferred from measurements on the preform and multimode fibres drawn from a similar prefrom. Thus it may be possible that in drawing a smaller core fibre there is a greater rate of diffusion and the central concentration may drop below 75 %.

Examining the spectral output from the cavity in figure 5.12b shows a double peaked

Cavity Length (m)	Fitted P_{Th} (W)	Calculated g_R (W^{-1}km^{-1})		
		Lower Fit	Fit	Upper Fit
6.8	2.9	64	68	71
8.4	2.8	46	58	75
10.2	2.1	58	63	70
26.2	1.7	23	33	60

Table 5.3: Calculated values of the threshold pump power and raman gain based upon the linear fits in figure 5.12a.

structure. All the cavities produced a similar double peaked output at maximum pump power. The laser linewidth of the output was shown to be related to the bandwidth of the FBGs. As the HR reflector is broader than the OC it determined the overall laser linewidth. The stronger signal was due to a cavity formed between the HR and OC while the weaker signal was due to a cavity being formed between the HR and the end facet of the fibre. This weaker signal only appeared at high pump power, as it was only then that the gain was high enough to support lasing between the HR and end facet. This is a clear indication of non-optimal cavity conditions. It would be expected that this issue could be resolved with the HR and OC having the same spectral profile. Furthermore, optimisation of the reflectivity could result in more energy being extracted. Thus the output power and slope efficiency of the Raman fibre laser could potentially be improved further, which we shall now examine by computational modelling.

5.5 Modelling

The coupled ordinary differential equations (ODE) and related boundary value problem (BVP) were described in section 5.3. Modelling of Raman fibre lasers has been realised by utilising both numerical [46–50, 57, 58] and analytical [44, 51] methods. The following model makes use of a Fortran based BVP solver written by Shampine *et al.* [59] for which the code is freely available. This solver uses Runge-Kutta methods to solve the ODE BVP problem. Our implementation is very similar to that used by Jackson *et al.* [49].

Simulated results were found to be in reasonable agreement with experimental measurements and are shown in figure 5.13. Given the uncertainties discussed in the previous section excellent agreement would not necessarily be expected. Simulation of any given cavity with the Raman gain value derived from the threshold pump condition set out in equation 5.7 results in numerical results with a higher Stokes power than that measured experimentally. This is illustrated in figure 5.13a. Given the uncertainty in g_R from the threshold calculation this would appear to be a good explanation for the error. However,

(a) Model of the 6.8 m cavity

(b) Output power with output coupler reflectivity and cavity length
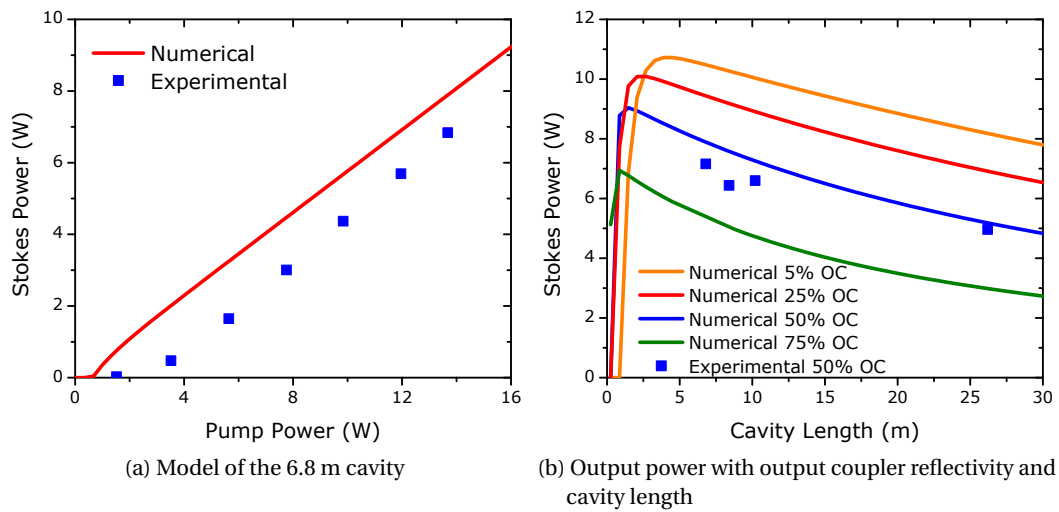
Figure 5.13: 5.13a shows the numerical simulation compared with experiment for the 6.8 m cavity with $g_R = 68$ W^{-1}km^{-1}. 5.13b shows the cavity output power with length and output coupling with $g_R = 68$ W^{-1}km^{-1}.

the exact output coupler reflectivity is unknown and is simply assumed to be the intended 50 % that was targeted during manufacture, also some uncertainty surrounds the attenuation at the Stokes wavelength as previously mentioned. In addition, the requirement to continuously monitor the FBG stretch may have lead to occasional non-optimal results which could explain the dip in output power for the 8.4m cavity.

These issues can be investigated further by considering the Stokes output power with the cavity length and output coupler reflectivity. This is shown in figure 5.13b where it can be seen that the optimal cavity length of 5 m with a 5 % output coupler reflectivity (5 % of the light reflected back into the cavity) would result in a much higher output power and improved efficiency. Again it is shown that the experimental results for each cavity length are in close agreement with the numerical calculation.

5.6 2.3 μm and beyond

In this section we will take a brief look at extending the Raman fibre laser to a cascaded regime of Stokes orders stretching to 2.3 μm and beyond. Such a cavity configuration is illustrated in figure 5.14.

An initial attempt to be build a cavity based around a 3rd set of FBGs at 2.322 μm was made. Characterisation of the gratings using the technique outlined in section 5.4.3 was attempted using the 6.8 m, 2.1 μm Raman laser to pump a single 2.322 μm grating followed by 7 m of GeO$_2$ fibre. This failed to result in any detectable signal at 2.3 μm. Indeed, by
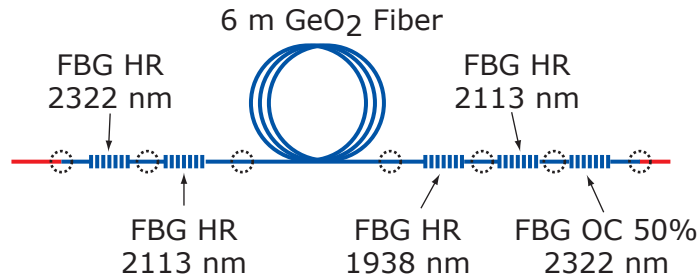
Figure 5.14: Schematic of a cascaded Raman laser for operation at 2.322 μm.

(a) GeO$_2$ fibre attenuation

(b) Simulations of a 2.322 μm cavity
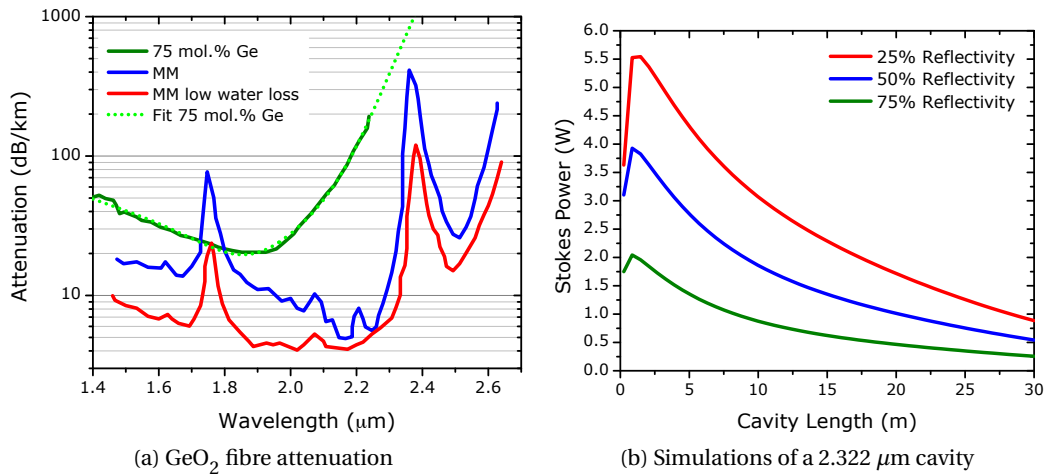
Figure 5.15: 5.15a Attenuation in dB/km for the 75 mol.% GeO$_2$ fibre and two multi-mode (MM) GeO$_2$ fibres. A polynomial fit of the loss is denoted by the dotted line. Multimode fibre data from [34]. 5.15b shows the Stokes output power at 2.322 μm with output coupler reflectivity and cavity length. g_R = 68 W^{-1}km^{-1} at 2.11 μm and g_R = 61 W^{-1}km^{-1} at 2.32 μm.

modeling such a configuration we can see that with a loss of 400 dB/km at 2.322 μm we would not expect to see a signal until the pump power power reached ~7 W. Of course this ignores any losses in the signal transmission through the spectrometer to the detector. A simple extrapolation of the loss curve in figure 5.15a would suggest a loss of ~520 dB/km at 2.32 μm, assuming the gradient doesn't increase significantly. If we examine some previous loss measurements made by Takahashi *et al.* [34] of a 70 μm core, multimode fibre (also shown in figure 5.15a) we see two significant loss peaks at 1.75 and 2.38 μm due to OH$^-$ absorption. As there is no indication of any significant loss at 1.75 μm in our GeO$_2$ fibre the calculated loss via extrapolation is probably reasonable.

Scaling the gain down by $1/\lambda$ and placing these values into the simulation we find that it should be possible to achieve several watts of output power at 2.322 μm, especially if the cavity is made exceptionally short as shown in figure 5.15b. These numbers are almost

certainly optimistic; as we saw in the last section, our model over estimated the output power. Additionally we also found that the measured gain was less than expected, perhaps suggesting a fall of greater than $1/\lambda$ which would result in a lower gain value than we used at 2.3 μm. Reducing the gain to 10 $^{-1}$km^{-1} significantly increases the threshold pump power, nevertheless a watt level Stokes output should still be possible using our pump source.

Achieving this experimentally is fraught with difficulties. The inability to characterise the gratings and fibre loss at this wavelength make the experiment difficult, not least because of the unknown wavelength mismatch of the HR and OC. A practical solution to this problem would be to use a tuneable Tm laser to enable pumping at longer and shorter wavelengths. For instance pumping close to 2.00 μm would result in a Stokes wave around 2.18 μm where the losses are lower, the gain is higher and perhaps easier to achieve experimentally. With this knowledge it may be easier to make the transition to operation at longer wavelengths. Alternatively, it is likely that in the next couple of years progress will be made in developing supercontinuum sources in the 2-3 μm region which could be used to fully characterise the fibre and gratings making it significantly easier to build the RFL.

5.7 Supercontinuum in GeO$_2$

As we previously mentioned the zero dispersion wavelength of bulk GeO$_2$ is 1.74 μm and falls to 1.63 and 1.51 μm for concentrations of 75 and 50 mol.% respectively [43]. For the small core fibres used in this work the zero dispersion is estimated as being at 2.5 μm . Modelling shows that increasing the core size shifts the zero dispersion to shorter wavelengths whilst potentially reducing the loss in the infra-red. Using a pulsed source at 1.9 μm could enable the generation of a supercontinuum up to the 2.4-2.5 μm region and possibly beyond if a suitably low loss fibre were achieved. It is likely however that this 300-400 nm improvement in continuum bandwidth in the infrared will be skipped in favour of utilising fibres with low losses further into the infrared such as ZBLAN, chalcogenide and tellurite [60, 61]. The main advantages of high concentration GeO$_2$ fibres over these soft glass fibres is the ability to splice the fibre to standard fibre based sources and their ability to handle high powers.

5.8 Future directions

As increasingly high power commercial thulium lasers appear, producing 100s of watts of output power in the 1.9-2.0 μm region, GeO$_2$ fibre may prove to be important for

extending these sources further into the infrared. Raman fibre laser operation in the 2.1-2.2 μm region is certainly possible with good conversion efficiency, and extension into 2.2-2.4 μm region should be attainable. Indeed, utilising a larger core single mode fibre, whilst increasing the single mode cut-off wavelength, would reduce losses in the 2.0-2.4 μm region potentially enabling better performance.

In theory a significant reduction of the high losses in GeO_2 fibres should be possible, if the exact causes can be fully understood and controlled [42]. It would also be necessary to insure that the high photosensitivity of the fibres does not result in photodegradration in the long term, before a commercial source could be considered. Moderate progress on the first of these issues and straight forward testing of the second could see the production of 10s-100 W RFL at 2.1 - 2.3 μm.

In order to aid understanding and modelling for future development, it would be worth revisiting and extending earlier work. This includes extending work for accurately modelling the Raman gain of low concentration Ge fibres (less than 50 mol.%) to the high concentration regime [56] and characterisation of the Raman gain using multiple techniques at multiple wavelengths [62]. This would hopefully lead to precise values for the Raman gain coefficient and allow accurate modelling.

Finally it may be worth considering pulsed pumping in the future. Not only will pulsed pumping enable higher peak powers and extension further into the infrared, but the results should help to quantify operation under the CW regime. Ideally a nanosecond or picosecond thulium laser would be used, both of which are becoming commonly available in research laboratories. Indeed a similar scheme has been demonstrated recently with lower concentration GeO_2 fibres pumped by an nanosecond erbium system showing extension to 2.4 μm [63].

5.9 Conclusions

In this chapter we demonstrated a high power Raman fibre laser source at 2.11 μm producing 6.8 W of output power. The Raman fibre laser was based upon a 75 mol.% GeO_2 fibre in a 6.8 m cavity which had a slope efficiency of 63 %. Additionally a variety of other cavities were demonstrated around the same fibre and operation at 2.3 μm was explored. Operation at longer wavelengths was shown to be possible numerically but proved impossible to implement due to an inability to characterise the exact wavelength of the fibre Bragg gratings.

As commercial thulium lasers scale to higher and higher output powers in the 100 W -1kW range GeO_2 fibre lasers may represent a practical and sensible approach to efficiently transfer this energy further into infrared, especially if progress can be made in

understanding and reducing the fibre losses.

Bibliography

[1] J. S. Sanghera, I. D. Aggarwal, L. B. Shaw, L. E. Busse, P. Thielen, V. Nguyen, P. Pureza, S. Bayya, and F. Kung, "Applications of chalcogenide glass optical fibers at NRL," J. Optoelectron Adv. Materials **3**, 627–640 (2001).

[2] M. Meleshkevich, N. Platonov, D. Gapontsev, A. Drozhzhin, V. Sergeev, and V. Gapontsev, "415 W single-mode CW thulium fiber laser in all-fiber format," in "CLEO/Europe and IQEC 2007 Conference Digest," (Optical Society of America, 2007), p. CP2_3.

[3] I.P.G. Photonics, "TLR series: 1-150 W single mode thulium fiber lasers," http://www.ipgphotonics.com/products_2micron_lasers_cw_tlr-series.htm (2008).

[4] S. D. Jackson, F. Bugge, and G. Erbert, "Directly diode-pumped holmium fiber lasers," Opt. Lett. **32**, 2496–2498 (2007).

[5] A. Kurkov, V. Paramonov, O. Medvedkov, Y. N. Pyrkov, E. M. Dianov, S. E. Goncharov, and I. Zalevskii, "Compact fiber source emitting at 2.1 μm with an output power of 2 W," Laser Physics Letters **3**, 151–153 (2006).

[6] R. H. Page, K. I. Schaffers, L. D. DeLoach, G. D. Wilke, F. D. Patel, J. B. Tassano, S. A. Payne, W. F. Krupke, K. T. Chen, and A. Burger, "Cr^{2+}-doped zinc chalcogenides as efficient, widely tunable mid-infrared lasers," IEEE J. Quant. Elect. **33**, 609–619 (1997).

[7] I. Sorokina, E. Sorokin, S. Mirov, V. Fedorov, V. Badikov, V. Panyutin, A. D. Lieto, and M. Tonelli, "Continuous-wave tunable Cr^{2+}:ZnS laser," Appl. Phys. B: Lasers and Optics **74**, 607–611 (2002).

[8] E. Sorokin, S. Naumov, and I. T. Sorokina, "Ultrabroadband infrared solid-state lasers," IEEE J. Sel. Topics Quant. Elect. **11**, 690–712 (2005).

[9] S. Mirov, V. Fedorov, I. Moskalev, and D. Martyshkin, "Recent progress in transition-metal-doped II–VI mid-IR lasers," IEEE J. Sel. Topics Quant. Elect. **13**, 810–822 (2007).

[10] B. Rosener, N. Schulz, M. Rattunde, C. Manz, K. Kuhler, and J. Wagner, "High-power high-brightness operation of a 2.25-μm (AlGaIn)(AsSb)-based barrier-pumped

vertical-external-cavity surface-emitting laser," IEEE Phot. Tech. Lett. **20**, 502–504 (2008).

[11] I. T. Sorokina and K. L. Vodopyanov, *Solid-State Mid-Infrared Laser Sources* (Springer, Berlin, 2003).

[12] K. L. Vodopyanov, O. Levi, P. S. Kuo, T. J. Pinguet, J. S. Harris, M. M. Fejer, B. Gerard, L. Becouarn, and E. Lallier, "Optical parametric oscillation in quasi-phase-matched GaAs," Opt. Lett. **29**, 1912–1914 (2004).

[13] C. Kieleck, M. Eichhorn, A. Hirth, D. Faye, and E. Lallier, "20-50 kHz mid-infrared OP-GaAs OPO," in "Conference on Lasers and Electro-Optics/Quantum Electronics and Laser Science Conference," (Optical Society of America, 2008), p. CTuII1.

[14] P. Gross, M. E. Klein, T. Walde, K.-J. Boller, M. Auerbach, P. Wessels, and C. Fallnich, "Fiber-laser-pumped continuous-wave singly resonant optical parametric oscillator," Opt. Lett. **27**, 418–420 (2002).

[15] M. E. Klein, P. Gross, K.-J. Boller, M. Auerbach, P. Wessels, and C. Fallnich, "Rapidly tunable continuous-wave optical parametric oscillator pumped by a fiber laser," Opt. Lett. **28**, 920–922 (2003).

[16] K. O. Hill, B. S. Kawasaki, and D. C. Johnson, "Low-threshold CW Raman laser," App. Phys. Lett. **29**, 181–183 (1976).

[17] J. Stone, "CW Raman fiber amplifier," App. Phys. Lett. **26**, 163–165 (1975).

[18] C. Lin, R. H. Stolen, W. G. French, and T. G. Malone, "A CW tunable near-infrared (1.085-1.175 μm) Raman oscillator," Opt. Lett. **1**, 96–97 (1977).

[19] R. K. Jain, C. Lin, R. H. Stolen, and A. Ashkin, "A tunable multiple stokes CW fiber Raman oscillator," App. Phys. Lett. **31**, 89–90 (1977).

[20] R. Stolen, C. Lin, J. Shah, and R. Leheny, "A fiber Raman ring laser," IEEE J. Quant. Elect. **14**, 860–862 (1978).

[21] C. Lin and P. Glodis, "Tunable fibre Raman oscillator in the 1.32-1.41 μm spectral region using a low-loss, low OH$^-$ single-mode fibre," Elect. Lett. **18**, 696–697 (1982).

[22] M. Nakazawa, M. Tokuda, and N. Uchida, "Continuous-wave Raman oscillation for a Nd^{3+}:YAG intracavity fiber laser," J. Opt. Soc. Am. B **1**, 86–90 (1984).

[23] S. Chernikov, N. Platonov, D. Gapontsev, D. I. Chang, M. Guy, and J. Taylor, "Raman fibre laser operating at 1.24 μm," Elect. Lett. **34**, 680–681 (1998).

[24] D. Georgiev, V. Gapontsev, A. G. Dronov, M. Y. Vyatkin, A. B. Rulkov, S. V. Popov, and J. R. Taylor, "Watts-level frequency doubling of a narrow line linearly polarized Raman fiber laser to 589nm," Opt. Express **13**, 6772–6776 (2005).

[25] R. Fugate, D. Fried, G. Ameer, B. Boeke, and S. Browne, "Measurement of atmospheric wavefront distortion using scattered light from a laser guide-star," Nature **353**, 144–146 (1991).

[26] E. M. Dianov, M. V. Grekov, I. A. Bufetov, V. M. Mashinsky, O. D. Sazhin, M. Prokhorov, G. G. Devyatykh, A. N. Guryanov, and V. F. Khopin, "Highly efficient 1.3 μm Raman fibre amplifier," Elect. Lett. **34**, 669–670 (1998).

[27] I.P.G. Photonics, "RAR series Raman amplifiers," http://www.ipgphotonics.com/telecom_rar-series-fiber-amplifiers.htm (2008).

[28] A. S. Grabtchikov, V. A. Lisinetskii, V. A. Orlovich, M. Schmitt, R. Maksimenka, and W. Kiefer, "Multimode pumped continuous-wave solid-state Raman laser," Opt. Lett. **29**, 2524–2526 (2004).

[29] S. D. Jackson and G. Anzueto-Sanchez, "Chalcogenide glass Raman fiber laser," App. Phys. Lett. **88**, 221106 (2006).

[30] R. D. Maurer and P. C. Schultz, "Germania containing optical waveguide," US Patent 3884550 (1975).

[31] F. L. Galeener, J. C. Mikkelsen, R. H. Geils, and W. J. Mosby, "The relative Raman cross sections of vitreous SiO_2, GeO_2, B_2O_3, and P_2O_5," App. Phys. Lett. **32**, 34–36 (1978).

[32] Y. Zhao and S. Jackson, "Highly efficient first order Raman fibre lasers using very short Ge-doped silica fibres," Opt. Commun. **253**, 172–176 (2005).

[33] H. Takahashi and I. Sugimoto, "Decreased losses in germanium-oxide glass optical fiber prepared by VAD method," Jpn. J. Appl. Phys. **22**, L139–L140 (1983).

[34] H. Takahashi and I. Sugimoto, "A germanium-oxide glass optical fiber prepared by a VAD method," J. Lightwave Tech. **2**, 613–616 (1984).

[35] H. Takahashi and I. Sugimoto, "Silicone-resin-clad germanium-oxide glass optical fiber," Jpn. J. Appl. Phys. **22**, L313–L314 (1983).

[36] S. Sakaguchi and S. Todoroki, "Optical properties of GeO_2 glass and optical fibers," Appl. Opt. **36**, 6809–6814 (1997).

[37] T. Hosaka, S. Sudo, H. Itoh, and K. Okamoto, "Single-mode fibres with extremely high-Δ and small-dimension pure GeO$_2$ core for efficient nonlinear optical applications," Elect. Lett. **24**, 770–771 (1988).

[38] E. M. Dianov and V. Mashinsky, "Germania-based core optical fibers," J. Lightwave Tech. **23**, 3500–3508 (2005).

[39] A. Peder-Gothóni and M. Leppihalme, "GeO$_2$-Core/SiO$_2$-cladding optical fibers made by MCVD process for stimulated Raman applications," Appl. Phys. B: Lasers and Optics **42**, 45–49 (1987).

[40] E. G. Rawson, "Analysis of scattering from fiber waveguides with irregular core surfaces," Appl. Opt. **13**, 2370–2377 (1974).

[41] M. M. Bubnov, S. L. Semjonov, M. E. Likhachev, E. M. Dianov, V. F. Khopin, M. Y. Salganskii, A. N. Guryanov, J. C. Fajardo, D. V. Kuksenkov, J. Koh, and P. Mazumder, "On the origin of excess loss in highly GeO$_2$-doped single-mode MCVD fibers," IEEE Phot. Tech. Lett. **16**, 1870–1872 (2004).

[42] M. E. Likhachev, M. M. Bubnov, S. L. Semenov, V. F. Khopin, M. Y. Salganskii, A. N. Gur'yanov, and E. M. Dianov, "Study of the radiation scattering indicatrix in fibres heavily doped with germanium oxide," Quant. Elect. **36**, 464–469 (2006).

[43] J. W. Fleming, "Dispersion in GeO$_2$–SiO$_2$ glasses," Appl. Opt. **23**, 4486–4493 (1984).

[44] J. AuYeung and A. Yariv, "Theory of CW Raman oscillation in optical fibers," J. Opt. Soc. Am. **69**, 803–807 (1979).

[45] Y. JA, "Using the shooting method to solve boundary-value problems involving nonlinear coupled-wave equatons. Part 1 Degenerate two-wave mixing," Opt. Quant. Elect. **15**, 529–538 (1983).

[46] X. Liu and B. Lee, "Effective shooting algorithm and its application to fiber amplifiers," Opt. Express **11**, 1452–1461 (2003).

[47] K. Huang, X. Zhou, Z. Qin, H. Wu, and Z. Zhou, "A novel fast numerical algorithm for cascaded Raman fiber laser using the analytic approximate solution," Opt. Commun. **271**, 257–262 (2007).

[48] M. Rini, I. Cristiani, and V. Degiorgio, "Numerical modeling and optimization of cascaded CW Raman fiber lasers," IEEE J. Quant. Elect. **36**, 1117–1122 (2000).

[49] S. D. Jackson and P. H. Muir, "Theory and numerical simulation of nth-order cascaded Raman fiber lasers," J. Opt. Soc. Am. B **18**, 1297–1306 (2001).

[50] X. Liu, H. Zhang, and Y. Guo, "A novel method for Raman amplifier propagation equations," IEEE Phot. Tech. Lett. **15**, 392–394 (2003).

[51] J. Zhou, J. Chen, X. Li, G. Wu, and Y. Wang, "Exact analytical solution for Raman fiber laser," IEEE Phot. Tech. Lett. **18**, 1097–1099 (2006).

[52] A. B. Rulkov, A. A. Ferin, J. C. Travers, S. V. Popov, and J. R. Taylor, "Broadband, low intensity noise CW source for OCT at 1800 nm," Opt. Commun. **281**, 154–156 (2008).

[53] G. P. Agrawal, *Nonlinear Fiber Optics* (Springer, 2001), 3rd ed.

[54] E. M. Dianov, I. A. Bufetov, V. M. Mashinsky, A. V. Shubin, O. I. Medvedkov, A. E. Rakitin, M. A. Mel'kumov, V. F. Khopin, and A. N. Gur'yanov, "Raman fibre lasers based on heavily GeO_2-doped fibres," Quant. Elect. **35**, 435–441 (2005).

[55] S. T. Davey, D. L. Williams, B. J. Ainslie, W. J. M. Rothwell, and B. Wakefield, "Optical gain spectrum of GeO_2-SiO_2 Raman fibre amplifiers," IEE Proceedings: Part J Optoelectronics **136**, 301–306 (1989).

[56] J. Bromage, K. Rottwitt, and M. Lines, "A method to predict the Raman gain spectra of germanosilicate fibers with arbitrary index profiles," IEEE Phot. Tech. Lett. **14**, 24–26 (2002).

[57] B. K. Min, W. J. Lee, and N. Park, "Efficient formulation of Raman amplifier propagation equations with average power analysis," IEEE Phot. Tech. Lett. **12**, 1486–1488 (2000).

[58] F. Leplingard, C. Martinelli, S. Borne, L. Lorcy, D. Bayart, F. Castella, P. Chartier, and E. Faou, "Modeling of multiwavelength Raman fiber lasers using a new and fast algorithm," IEEE Phot. Tech. Lett. **16**, 2601–2603 (2004).

[59] L. Shampine, P. Muir, and H. Xu, "A user-friendly Fortran BVP solver," Journal of Numerical Analysis, Industrial and Applied Mathematics **1**, 201–217 (2006).

[60] C. Hagen, J. Walewski, and S. Sanders, "Generation of a continuum extending to the midinfrared by pumping ZBLAN fiber with an ultrafast 1550-nm source," IEEE Phot. Tech. Lett. **18**, 91–93 (2006).

[61] J. Price, T. Monro, H. Ebendorff-Heidepriem, F. Poletti, P. Horak, V. Finazzi, J. Leong, P. Petropoulos, J. Flanagan, G. Brambilla, X. Feng, and D. Richardson, "Mid-IR supercontinuum generation from nonsilica microstructured optical fibers," IEEE J. Sel. Topics Quant. Elect. **13**, 738–749 (2007).

[62] F. Koch, S. A. E. Lewis, S. V. Chernikov, and J. R. Taylor, "Broadband Raman gain characterisation in various optical fibres," Elect. Lett. **37**, 1437–1439 (2001).

[63] P. T. Rakich, Y. Fink, and M. Soljacic, "Efficient mid-IR spectral generation via spontaneous fifth-order cascaded-Raman amplification in silica fibers," Opt. Lett. **33**, 1690–1692 (2008).

6 Conclusion and Outlook

Over the last twenty years there has been rapid progress in the development of fibre lasers in laboratories around the world. At the beginning of the twenty-first century, many research groups joined in a race to produce the highest power, single mode, CW fibre laser. Scaling from 10's to 100's of watts was initially seen as a daunting prospect, but today 1000's of watts are available in commercial systems. As we saw in chapter 1 fibre lasers have come from almost nowhere to represent a significant segment of the laser market, all in the last ten years. Their rise in popularity is due to their low cost, high efficiency and generally robust, straightforward design. This trend is almost certain to continue. However, wavelength selection is currently limited to a handful of rare earth lasing lines- for instance there are no watt level visible fibre lasers. In order to continue the rapid progression, new gain media for fibre must be found and their strength as a nonlinear medium should be capitalised upon. In this thesis we have developed and demonstrated sources which extend the range of available wavelengths accessible by fibre sources, both through the use of a new gain medium, and nonlinear processes.

In chapter 2 we made use of bismuth doped fibre, a new fibre gain medium, to demonstrate CW lasing at 1178 nm. We also showed that while bismuth doped fibre currently suffers from several hindrances, such as low gain and high unsaturable losses, these can be reduced considerably by cooling the fibre to 77 K. As a gain medium, bismuth is extremely promising due to its broad bandwidth, demonstrated as over one hundred nanometers. Bismuth also sits in a wavelength region for which there is currently no rare-earth doped fibre gain media available. These early results, combined with a variety of applications for fibre lasers and amplifiers in this wavelength region, suggest that bismuth fibres may have a bright future ahead.

Chapters 3 and 4 concentrated on CW supercontinuum generation to create sources with a high spectral power density that span hundreds of nanometers of bandwidth. We demonstrated the highest spectral power densities from a supercontinuum to date as well as the first results to show short wavelength generation from a 1 μm pumped CW continuum. This is possibly a first step towards high power broadband visible sources. In supercontinuum generation the new wavelengths are generated via a variety of nonlinear processes, often making it difficult to establish which processes are driving the evolution of any given part of the continuum. By simulating a variety of fibres and tying this to a series

of experimental results, we were able to build upon the base of knowledge established for pulse pumped continuum generation. This allowed us to describe the key processes in depth and describe how further improvements could be made by engineering suitable PCFs.

Finally in chapter 5 we made use of the high Raman gain available in an almost pure GeO$_2$ fibre to build a 6.8 W Raman laser at 2.1 μm. The Raman laser was pumped by a 20 W thulium fibre laser allowing for an all fibre format. We also showed that operation further into the infrared up to 2.3 μm should be possible. With the powers available from commercial thulium fibre lasers beginning to scale to hundreds of watts, high power sources in the 2.1-2.3 μm region will be possible via this technique. Indeed, we suggested that with further work on the GeO$_2$ fibre, it should be possible to reduce the losses and enable operation further into the infrared.

Much of the work in this thesis is based upon nonlinear optics. The advent of photonic crystal fibres and the first supercontinuum result in a PCF in 1999 reinvigorated the field of nonlinear optics and led to a decade of advances [1]. The control offered by PCFs is still being extended to new areas, with recent advances such as solid-core band-gap fibres [2] and lower loss, broader bandwidth air-core band-gap fibres [3] yet to be fully exploited. The commercialisation of supercontinuum sources is already well under way, and the first lasers based upon large mode area PCFs are beginning to appear. It is likely that in the fullness of time PCF will become as common as fibre is today, possibly even making inroads into telecommunications. Other novel uses for PCF, such as filling them with gases [4] or liquids [5] to study nonlinear effects, or the development of soft glass PCFs [6], will no doubt keep the optics community busy.

The development of supercontinuum sources is likely to continue with researchers likely to focus on: the infra-red in the 2-10 μm region; higher power levels in the visible; the creation of polarised continuum sources; and engineering the sources to be flat on a linear scale. It is probably only a matter of time before one of the many academic uses for supercontinuum sources breaks out of the research lab and into mainstream medical or industrial use.

Fibre has dominated nonlinear optics research in many respects, not least due to the long interaction lengths available. Looking forward it is likely that there will be an increasing focus on nonlinear optics in bulk media, for example nonlinear processes in wave-guiding chips. These chips may be aimed at replacing current electronic components with optical components in telecommunication and computing based equipment. The development of bulk photonic crystals also makes many nonlinear processes, such as soliton formation, possible in bulk materials which can be engineered to control these effects. Finally, in the longer term, it is reasonably to assume that as metamaterials mature,

and become more widely available at optical wavelengths, researchers will begin to study and capitalise upon their unique properties to drive a new generation of nonlinear devices [7].

With any research-based work, predictions should always be viewed with some caution. However, there has been consistent progress in the fields of fibre lasers and nonlinear optics for the last thirty years. It is hard to imagine that further progress will not be made, given the number of ideas and ingenuity within the research community.

Bibliography

[1] J. M. Dudley and J. R. Taylor, "Ten years of nonlinear optics in photonic crystal fibre," Nat. Phot. **3**, 85–90 (2009).

[2] F. Luan, A. K. George, T. D. Hedley, G. J. Pearce, D. M. Bird, J. C. Knight, and P. S. J. Russell, "All-solid photonic bandgap fiber," Opt. Lett. **29**, 2369–2371 (2004).

[3] R. Amezcua-Correa, F. Gèrôme, S. G. Leon-Saval, N. G. R. Broderick, T. A. Birks, and J. C. Knight, "Control of surface modes in low losshollow-core photonic bandgap fibers," Opt. Express **16**, 1142–1149 (2008).

[4] F. Benabid, F. Couny, J. C. Knight, T. A. Birks, and P. S. J. Russell, "Compact, stable and efficient all-fibre gas cells using hollow-core photonic crystal fibres," Nature **434**, 488–491 (2005).

[5] A. Bozolan, C. J. S. de Matos, C. M. B. Cordeiro, E. M. dos Santos, and J. C. Travers, "Supercontinuum generation in a water-core photonic crystal fiber," Opt. Express **16**, 9671 (2008).

[6] J. S. Sanghera, L. Brandon Shaw, and I. D. Aggarwal, "Chalcogenide glass-fiber-based mid-IR sources and applications," IEEE J. Sel. Topics Quant. Elect. **15**, 114–119 (2009).

[7] N. Litchinitser and V. Shalaev, "Photonic metamaterials," Laser Physics Letters **5**, 411–420 (2008).

List of publications

Journal publications

[1] B. A. Cumberland, J. C. Travers, R. E. Kennedy, S. V. Popov, and J. R. Taylor, "2 W/nm peak-power all-fiber supercontinuum source and its application to the characterization of periodically poled non-linear crystals," Opt. Commun. **277**, 134–137 (2007).

[2] J. C. Travers, J. M. Stone, A. B. Rulkov, B. A. Cumberland, A. K. George, S. V. Popov, J. C. Knight, and J. R. Taylor, "Optical pulse compression in dispersion decreasing photonic crystal fiber," Opt. Express **15**, 13203–13211 (2007).

[3] B. A. Cumberland, S. V. Popov, J. R. Taylor, O. I. Medvedkov, S. A. Vasiliev, and E. M. Dianov, "2.1 μm continuous-wave Raman laser in GeO_2 fiber," Opt. Lett. **32**, 1848–1850 (2007).

[4] J. Travers, A. Rulkov, B. Cumberland, S. Popov, and J. Taylor, "Non-linear applications of microstructured optical fibres," Opt. Quant. Elect. **39**, 963–974 (2007).

[5] B. A. Cumberland, J. C. Travers, S. V. Popov, and J. R. Taylor, "29 W high power CW supercontinuum source," Opt. Express **16**, 5954–5962 (2008).

[6] B. A. Cumberland, J. C. Travers, S. V. Popov, and J. R. Taylor, "Toward visible CW-pumped supercontinua," Opt. Lett. **33**, 2122–2124 (2008).

[7] J. C. Travers, A. B. Rulkov, B. A. Cumberland, S. V. Popov, and J. R. Taylor, "Visible supercontinuum generation in photonic crystal fibers with a 400W continuous wave fiber laser," Opt. Express **16**, 14435–14447 (2008).

Conference publications

[1] B. A. Cumberland, J. C. Travers, R. E. Kennedy, S. V. Popov, and J. R. Taylor, "Application of a 2W/nm all-fiber supercontinuum source to the characterization of nonlinear crystals," in "Conference on Lasers and Electro-Optics," (2006), p. JThC53.

[2] J. C. Travers, B. A. Cumberland, S. V. Popov, J. R. Taylor, N. Traynor, and A. Monteville, "Pump format influence on noise characteristics and spectral extent of CW continuum generation in new low-water-loss holey fibers," in "Conference on Lasers and Electro-Optics," (2006), p. CMGG5.

[3] R. E. Kennedy, B. A. Cumberland, S. V. Popov, and J. R. Taylor, "Aircore fiber based spectral compression of an all fiber integrated ultrashort pulse source," in "Conference on Lasers and Electro-Optics," (2006), p. CMC3.

[4] B. A. Cumberland, A. Ferin, A. B. Rulkov, J. C. Travers, S. V. Popov, and J. R. Taylor, "Nonlinear optics and frequency conversion: fiber lasers in IR, VIS and UV," in "Fiber Lasers IV: Technology, Systems, and Applications, Lase, Photonics West," (2007).

[5] B. A. Cumberland, J. C. Travers, S. V. Popov, J. R. Taylor, O. I. Medvedkov, S. A. Vasiliev, and E. M. Dianov, "2.1 μm CW Raman source in GeO$_2$ fiber," in "Conference on Lasers and Electro-Optics," (2007), p. CML7.

[6] J. C. Travers, B. A. Cumberland, A. B. Rulkov, S. V. Popov, J. R. Taylor, J. M. Stone, A. K. George, and J. C. Knight, "Pulse compression in dispersion decreasing photonic crystal fiber," in "Conference on Lasers and Electro-Optics," (2007), p. CFK1.

[7] J. C. Travers, A. B. Rulkov, B. A. Cumberland, S. V. Popov, and J. R. Taylor, "Non-linear applications of microstructured optical fibres," in "International Conference on Materials for Advanced Technologies," (2007), pp. F–3–IN4.

[8] S. V. Popov, J. C. Travers, A. B. Rulkov, B. A. Cumberland, and J. R. Taylor, "Versatile all-fibre lasers for bio-imaging applications," in "Ultrafast Optics VI, Applications of High Field Short Wavelength Sources XII, Lase, Photonics West," (2007).

[9] J. M. Stone, A. K. George, J. C. Knight, J. C. Travers, B. A. Cumberland, A. Rulkov, S. V. Popov, and J. R. Taylor, "Pulse compression at 1.06 μm in dispersion decreasing photonic crystal fibre," in "Non-linear Photonics Conference," (2007), p. NThB2.

[10] B. A. Cumberland, J. C. Travers, S. V. Popov, and J. R. Taylor, "High-power continuous wave supercontinuum," in "Fiber Lasers V: Technology, Systems, and Applications, Lase, Photonics West," (2008), pp. Paper 6873–46.

[11] B. A. Cumberland, J. C. Travers, S. V. Popov, and J. R. Taylor, "Short wavelength extension of CW-pumped supercontinuum at 1 mircon," in "Conference on Lasers and Electro-Optics," (2008), p. CFC2.

[12] B. A. Cumberland, J. C. Travers, S. V. Popov, and J. R. Taylor, "High power 29 W CW supercontinuum source," in "Conference on Lasers and Electro-Optics," (2008), p. CMDD1.

[13] J. C. Travers, A. B. Rulkov, B. A. Cumberland, S. V. Popov, and J. R. Taylor, "Spectral extension and temporal manipulation of high power fibre lasers," in "4th International Symposium on High Power Fiber Lasers and their Applications," (2008).

[14] J. C. Travers, A. B. Rulkov, B. A. Cumberland, S. V. Popov, and J. R. Taylor, "Optical pulse propagation in tapered photonic crystal fibers," in "The seventeenth annual International Laser Physics Workshop (LPHYS'08)," (2008).

[15] J. C. Travers, A. B. Rulkov, B. A. Cumberland, S. V. Popov, and J. R. Taylor, "High power fibre integrated supercontinuum sources," in "1st Workshop on Specialty Optical Fibers," (2008).

[16] A. Kudlinski, B. A. Cumberland, J. C. Travers, G. Bouwmans, Y. Quiquempois, and A. Mussot, "CW supercontinuum generation in photonic crystal fibres with two zero-dispersion wavelengths," in "1st Workshop on Specialty Optical Fibers," (2008).

[17] J. C. Travers, A. B. Rulkov, B. A. Cumberland, S. V. Popov, and J. R. Taylor, "Supercontinuum sources," in "Photon 08," (2008).

[18] J. C. Travers, A. B. Rulkov, B. A. Cumberland, S. V. Popov, and J. R. Taylor, "Optical pulse propagation in tapered photonic crystal fibers," in "3rd EPS-QEOD Europhoton Conference," (2008).

[19] A. Kudlinski, B. A. Cumberland, J. C. Travers, G. Bouwmans, Y. Quiquempois, and A. Mussot, "Dynamics of CW supercontinuum generation in photonic crystal fibres with two zero-dispersion wavelengths," in "EOS Topical Meeting on Nonlinear Optics: Materials, Devices and Spatio-Temporal Effects," (2008), p. TOM 6.

[20] J. C. Travers, A. B. Rulkov, B. A. Cumberland, S. V. Popov, and J. R. Taylor, "High power ultrabroad band supercontinuum generation," in "Asian Optical Fibre Communications and Optoelectronics Conference," (2008).

Acronyms

While we have attempted to keep the use of acronyms to a minimum, there are still a reasonable number within this thesis. To make life as easy as possible for the reader we have defined them at the point of first use in each chapter. As a further aid, the common acronyms are listed below in alphabetical order.

AC	Alternating current or Angle cleave
ASE	Amplified spontaneous emission
BVP	Boundary value problem
CNRS	Centre National de la Recherche Scientifique, France
CW	Continuous wave
DC	Direct current
DWDM	Dense wavelength division multiplexing
ESA	Excited state absorption
FBG	Fibre Bragg grating
FC	Flat cleave
FORC	Fiber Optics Research Center at General Physics Institute, Moscow
FWHM	Full width half maximum
FWM	Four-wave mixing
GNLSE	General nonlinear Schrödinger equation
GVD	Group velocity dispersion
HF	Holey fibre
HNLF	Highly nonlinear fibre
HR	High reflector
IR	Infrared
IRCICA	Institut Recherche sur les Composants logiciels et matériels pour l'Information et la Communication Avancée at the University of Lille
LASER	Light amplification by stimulated emission of radiation
LIDAR	Light detection and ranging
LMA	Large mode area
MASER	Microwave amplification by stimulated emission of radiation
MCVD	Modified chemical vapour deposition
MFD	Mode field diameter
MI	Modulation instability
MIT	Massachusetts Institute of Technology
MM	Multi-mode

MOPFA	Master oscillator power fibre amplifier
NA	Numerical aperture
NIR	Near-infrared
OC	Output coupler
OCT	Optical coherence tomography
ODE	Ordinary differential equation
OPO	Optical parametric oscillator
OSA	Optical spectrum analyser or Optical Society of America
OVD	Outside vapour deposition
PCF	Photonic crystal fibre
RF	Radio frequency
RFL	Raman fibre laser
RIN	Relative intensity noise
SBS	Stimulated Brillouin scattering
SEM	Scanning electron microscope
SESAM	Semiconductor saturable absorber mirror
SMF	Single mode fibre
SPCVD	Surface-plasma chemical vapour deposition
SPD	Spectral power density
SPM	Self-phase modulation
SRS	Stimulated Raman scattering
SSFS	Soliton self-frequency shift
VAD	Vapour-phase axial deposition
VB	CW supercontinuum model based on work by Vanholsbeeck and Barviau (see section 3.3.2)
VECSEL	Vertical external cavity surface emitting laser
WDM	Wavelength division multiplexing
XPM	Cross-phase modulation
ZDW	Zero dispersion wavelength

Index